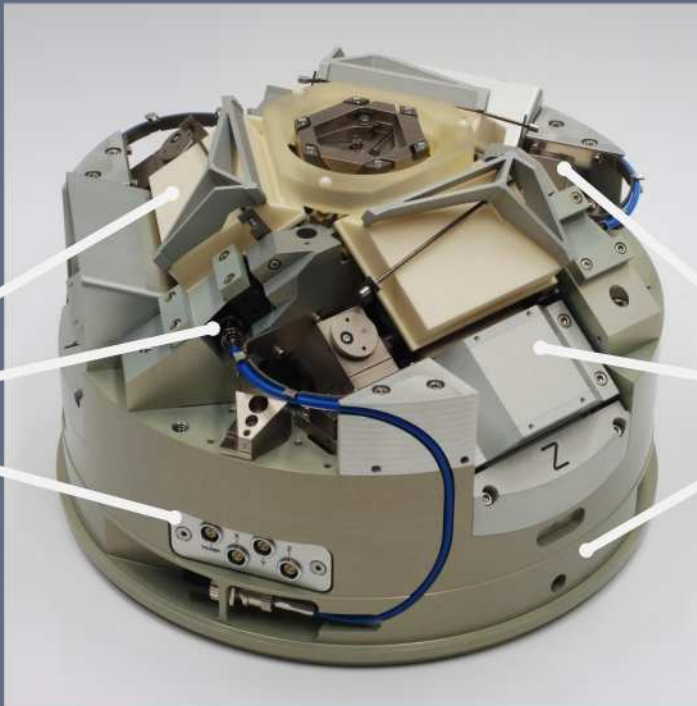


A 3D translation stage for metrological AFM



Chris Werner



This research was supported by NanoNed, a national nanotechnology program coordinated by the Dutch Ministry of Economic Affairs.

A 3D translation stage, for metrological AFM / by Chris Werner –
Eindhoven : Technische Universiteit Eindhoven, 2010 - Proefschrift

A catalogue record is available from the Eindhoven University of Technology Library.
ISBN: 978-90-386-2391-7
NUR: 978

Key words: metrological Atomic Force Microscope / elastic straight guide /
Lorentz actuator / stiffness compensation / thermal center /
differential plane mirror interferometer.

Trefwoorden: metrologische Atomic Force Microscope / elastische geleiding /
Lorentz actuator / stijfheidcompensatie / thermisch centrum /
differentiële vlakke-spiegel interferometer.

Reproduction: Ipskamp Drukkers bv, Enschede, The Netherlands.

The photographs in this thesis are available in color on <http://www.nanostage3D.nl>

Copyright © 2010 by C. Werner. All rights reserved.

A 3D translation stage for metrological AFM

PROEFSCHRIFT

ter verkrijging van de graad van doctor
aan de Technische Universiteit Eindhoven,
op gezag van de rector magnificus, prof.dr.ir. C.J. van Duijn,
voor een commissie aangewezen door het College voor Promoties
in het openbaar te verdedigen
op donderdag 16 december 2010 om 16.00 uur

door

Christian Werner

geboren te Dussen

Dit proefschrift is goedgekeurd door de promotor:

prof.dr.ir. M. Steinbuch

Copromotor:

dr.ir. P.C.J.N. Rosielle

Contents

1	Introduction	1
1.1	Atomic Force Microscopy (AFM)	1
1.2	AFM components	3
1.3	State of the art metrological AFMs	6
1.4	Thesis contributions	12
1.5	Thesis outline	13
2	Instrument overview	15
2.1	Design considerations	15
2.2	Instrument layout	18
2.3	AFM head - considerations	19
2.4	Sample stage design	21
2.4.1	Straight guide	21
2.4.2	Actuation	23
2.4.3	Measurement system	24
2.5	Design overview	26
3	Sample table and straight guide	29
3.1	Sample table	29
3.2	Struts	35
3.3	Parallelograms	36
3.4	Sample table rotations	39
3.5	Concluding remarks	43
4	Actuation	45
4.1	Actuator	45
4.1.1	Concept	45
4.1.2	Design	50
4.1.3	Control	55
4.2	Stiffness compensation and weight compensation	57
4.2.1	Stiffness compensation	57
4.2.2	Weight compensation	62
4.2.3	Design	66
4.3	Validation	78
4.3.1	Experimental set up	78

4.3.2	Actuator measurements	82
4.3.3	Stiffness and weight compensation measurements	83
4.3.4	Dynamics	87
4.4	Concluding remarks	90
5	Measurement system	91
5.1	Introduction	91
5.2	Interferometer optics	95
5.2.1	The optical layout	95
5.2.2	Interferometer design	100
5.2.3	Assembly procedure	105
5.2.4	Optics support box	113
5.3	Interferometer target and reference mirror	118
5.3.1	Moving target mirror	118
5.3.2	Stationary reference mirror	121
5.4	Beam delivery	125
5.5	Measurement electronics	132
5.6	Concluding remarks	134
6	Conclusions	135
Appendices		
A	Current mAFMs and transfer standards	139
B	AFM head design	143
C	Base material and instrument base	147
D	Intermediate optimization	153
E	Actuator details	155
F	Interferometer assembly	157
G	Transport accessories	165
Bibliography		173
Nomenclature		179
Summary		183
Samenvatting		185
Dankwoord		187
Curriculum Vitae		189

CHAPTER ONE

Introduction

Abstract / The Atomic Force Microscope (AFM) is a widely used, high resolution surface imaging instrument. Making accurate nanometer-scale measurements with an AFM requires calibration of the instrument against the standard of length. In this calibration, transfer standards are used, these standards are in turn calibrated using traceable, metrological AFMs. Extending the range of metrological AFMs from the current tens of micrometers to the millimeter range, while maintaining nanometer range uncertainty, reduces the calibration uncertainty through better measurement statistics and therefore helps to improve nanometer scale metrology.

The Atomic Force Microscope (AFM) [9] can make topographical images of surfaces with up to atomic resolution. The AFM and its predecessor, the Scanning Tunneling Microscope (STM) [10], are part of the Scanning Probe Microscopy (SPM) instrument family [34].

Figure 1.1 [96] on the next page, compares the SPM with other high-resolution surface topography analysis techniques like Scanning Electron Microscopy (SEM) and profilometers.

The SPM combines the high planar resolution of SEMs with the high vertical resolution of optical methods. Additionally, the SPM can make high-resolution measurements in ambient conditions, unlike most SEMs. This makes the SPM a versatile, and therefore popular, instrument.

The next section discusses the AFM technique in more detail. Section 1.2 describes the components in a typical AFM, followed by a few remarks on the calibration procedure necessary for accurate AFM measurements (Page 5). The AFMs used in this calibration procedure are described in Section 1.3. From Page 12 onward, the objectives of this project are discussed, followed by the thesis outline in Section 1.5.

1.1 Atomic Force Microscopy

AFMs use a small, elastically suspended probe as a sensor to measure the atomic forces present at the sample surface [9]. As the probe approaches the surface, the tip of

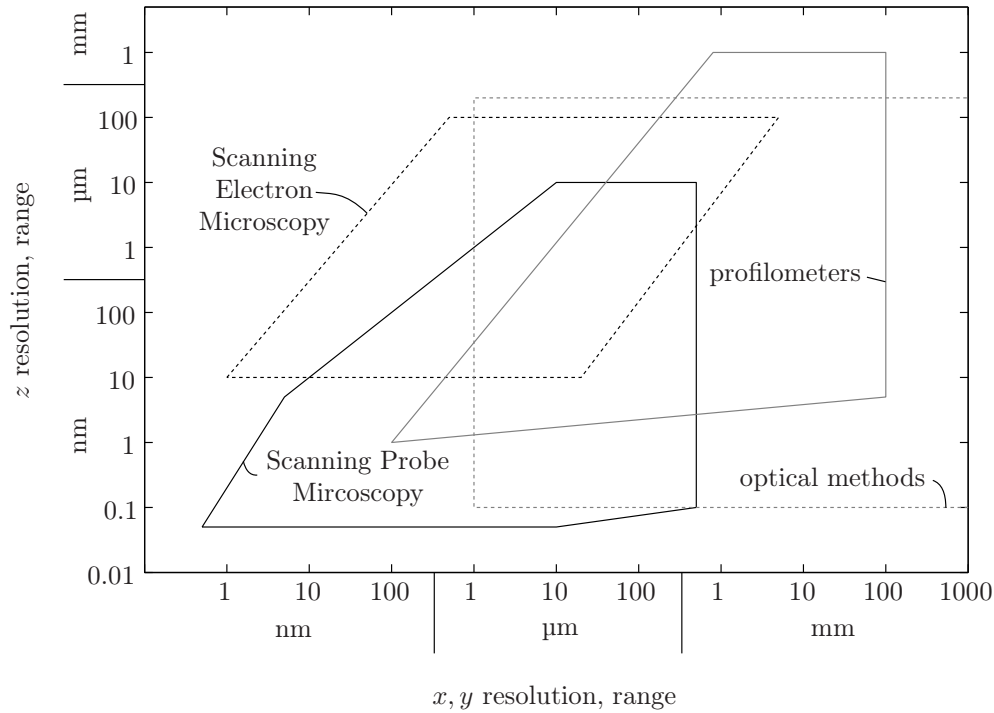


Figure 1.1 / From [96]. Comparison of several high-resolution imaging techniques. Generally, the range and resolution on the sample surface (x, y) differs from the range and resolution perpendicular to the surface (z).

the probe starts to interact with the sample surface, resulting in a force on the tip and subsequently a vertical probe displacement. As the probe is scanned across the sample surface, this vertical displacement is measured and either converted directly into topographical data (constant height mode, CHM) or used as a feedback signal to keep the vertical displacement constant (constant force mode, CFM).

In most AFM measurements, the probe stays in constant contact with the sample surface. This contact mode AFM (c-AFM) works very well in normal laboratory conditions and gives true topographical data [35] but is only suitable for relatively hard samples as the tip force can get quite large.

To reduce the force on the tip and sample, non-contact mode AFM (nc-AFM) has been developed [68]. Here the probe is made to vibrate above the sample surface, variations in the force on the tip result in an amplitude or a phase change in the probe oscillation. Since there is no contact between the tip and the sample there is no tip wear or sample damage. This technique is, however, not easy to use in ambient conditions [114] and the measurement results can be difficult to interpret [35].

A third method is intermittent contact mode AFM or Tappingmode[®] [114]. Like

nc-AFM, the probe is made to vibrate but now the tip does touch the sample during the lower portions of the oscillation. During contact a fraction of the probe's kinetic energy transfers to the sample, resulting in a reduction of probe's oscillation amplitude.

The intermittent contact mode combines the stability and the robustness of c-AFM with the minimal tip wear and the low sample damage of nc-AFM. Tappingmode[®] is therefore well suited to image delicate biological samples [42].

1.2 AFM components

A typical AFM contains at least the following components [34]:

- a probe and a probe suspension,
- a sensor to measure the probe's vertical displacement,
- actuators and straight guides to generate the scanning motion,
- sensors to measure the relative displacements of the probe and the sample.

Figure 1.2(a) shows an electron micrograph of a typical AFM probe. The probe is located at the free end of a cantilever which acts as the elastic suspension for the probe. Most commercially available probes are made from silicon or silicon nitride and are integral with the cantilever.

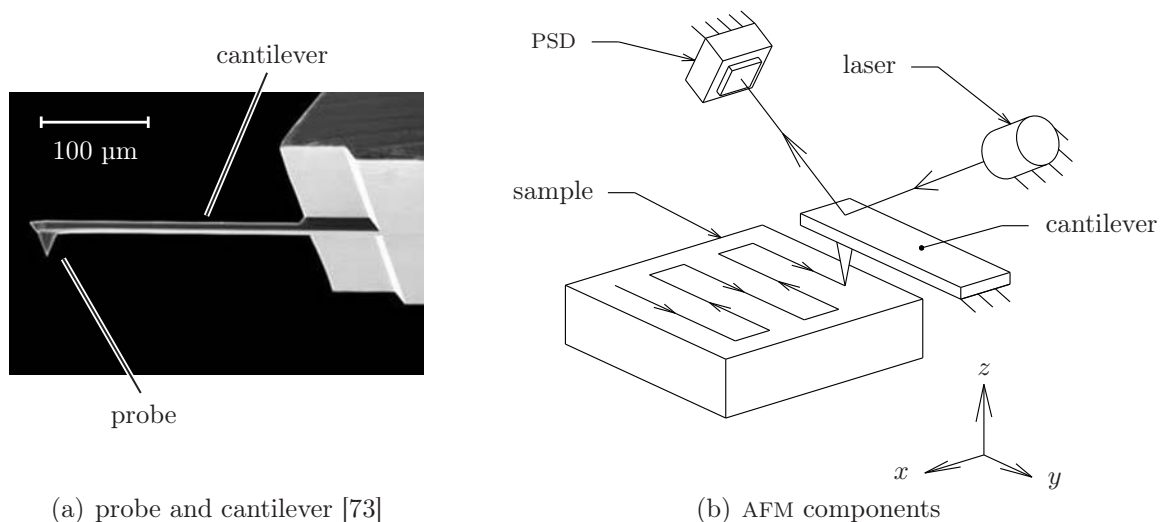


Figure 1.2 / Micrograph of a contact mode AFM cantilever. Figure (b) shows the AFM components with optical beam deflection (OBD) measurement (Figure not to scale).

Many AFMs use the optical beam deflection (OBD) method to measure the vertical displacement of the probe [72, 94, 95]. With this method, see Figure 1.2(b), a laser beam is focussed on the rear side of the cantilever, directly behind the probe, and is then reflected onto a position sensitive detector (PSD). Any vertical movement of the probe leads to a rotation of the free end of the cantilever and subsequently results in an amplified translation of the laser beam spot on the PSD.

The OBD method has a high resolution and is relatively easy to use. A disadvantage is that the relation between the vertical probe movement and the subsequent laser spot displacement depends on the cantilever stiffness. The cantilever stiffness must therefore be known for accurate constant height mode measurements. However, when the AFM is used as zero-sensor, as in constant force mode, no cantilever stiffness measurement is necessary.

Nearly all AFMs use piezoelectric actuators to generate the relative scanning motion. This motion is either guided by the actuator itself or by additional straight guides. An example of the former is the tubescanner. This cylindrical piezoelectric actuator makes three-dimensional movements through a combination of axial contraction and sideways bending. It is mechanically simple but suffers from cross-talk between the translation axes, has a range limited to tens of micrometers and has large straight guide errors [37]. The use of a separate flexure guide reduces the straightness error and the cross-talk significantly but adds complexity and moving mass to the instrument.

Not all instruments actually measure the relative displacements of the probe and the sample, some merely estimate the displacement from the actuator input. Most tubescanner AFMs use this displacement reconstruction [110] as it requires no additional sensors. At the downside, the piezoelectric actuator's creep, hysteresis and non-linear behavior make the reconstruction complex and potentially inaccurate.

Alternatively, the relative displacements can be measured with, for example, capacitive position sensors (CPSs) [38]. Although this is more direct than the displacement reconstruction method, neither method is actually reliable until the AFM has been calibrated. The next section discusses this.

AFM calibration

If absolute displacement measurements are required, then the AFM must be checked or calibrated against a standard which is traceable to the international definition of the meter [40].

Most commercial AFMs are calibrated towards the length standard using transfer standards [13, 24, 31]. These physical standards are made from silicon and typically have a one-dimensional or two-dimensional grating or step pattern (Figure 1.3). The grating dimensions are traceably determined by a national metrology institute (NMI).

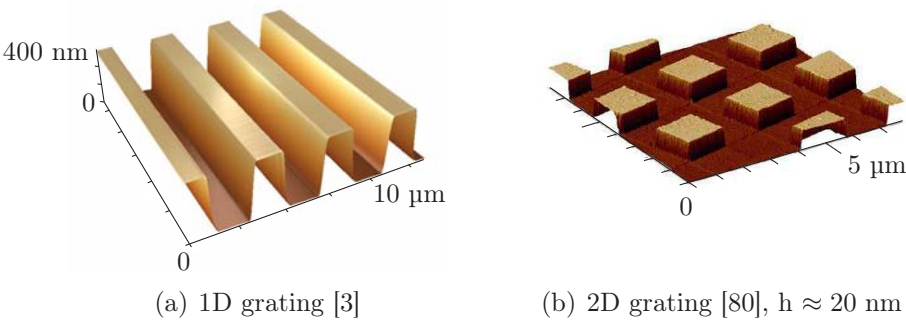


Figure 1.3 / Typical transfer standard patterns for AFM.

Table 1.1 summarizes the typical dimensions of transfers standards. Appendix A gives a more detailed list.

pattern		1D-steps, 2D-steps
pitch	μm	0.2 to 10
height	nm	20 to 500
sample		
effective area	mm	0.1×0.1 to 6×6
sample size	mm	3×4 to 10×10
thickness	mm	0.5 to 1

Table 1.1 / Typical dimensions of transfer standards for AFM. See Table A.2 on Page 141 for more information and the references.

The AFM that needs calibration, scans the transfer standard and the scan results are compared with the NMI-provided data to estimate the instrument errors. The calibration of the transfer standard itself is usually done with laser diffractometers [57, 70], metrological SEMs [44], profilometers [64, 65] and, increasingly, with dedicated metrological AFMs (mAFMs) [20, 31].

Table 1.2 briefly summarizes the advantages and disadvantages of the different measurement principles.

	advantages	disadvantages
diffractometer	fast measurement, non-contact	pitch only (no height), no local information
SEM	fast measurement	no 3D information, time consuming preparation
profilometer	readily available, pitch and height	2D (line) information, contact (wear)
mAFM	pitch and height, local information	contact (wear)

Table 1.2 / Advantages and disadvantages of several transfer standard (grating) calibration methods.

The mAFM can, unlike the other instruments, measure the local pitch and height variations over an area of the sample surface and is therefore a suitable instrument for transfer standard calibrations.

Figure 1.4 shows the traceability chain between the length standard and the user's commercial AFM when a mAFM is used to calibrate the transfer standard.

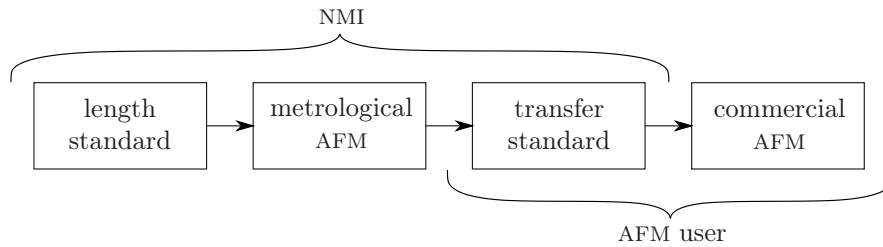


Figure 1.4 / Traceability chain. The transfer standard is calibrated towards the primary length standard using a metrological AFM at a national metrology institute (NMI). The AFM user scans the transfer standard and compares the measurement results with the transfer standard specifications.

The next section discusses the currently available and the near-future appearing metrological AFMs.

1.3 State of the art metrological AFMs

The development of metrologically more advanced AFMs [5, 102] started almost immediately after the invention of AFM. The first modern mAFM was realized in 1994 [98] and since then many more have been developed. Table 1.3 summarizes the specifications of the more recent instruments, and of the instruments currently under development.

nr	institute	scan volume (μm)	DOF ^a	scan motions		sample	displ.	source
				actuator	tip		meas.	
1	iNRiM	$30 \times 30 \times 18$	5	PZT	fixed	x,y	DMI ^b	[81]
						z, φ , ψ	CPS ^c	
2	LNE	$50 \times 50 \times 5$	3	PZT	fixed	x,y,z	DMI	[86–88]
3	PTB	$70 \times 15 \times 15$	3	PZT	fixed	x,y,z	DMI	[21]
4	NPL	$100 \times 100 \times 5$	3	PZT	z	x,y	DMI	[45, 64]
5	KRISS	$100 \times 100 \times 12$	3	PZT	z		CPS	[54]
						x,y	DMI	
6	MIKES	$100 \times 100 \times 12$	4	PZT	z	x,y,z	DMI	[58, 59]
7	NMIJ	$100 \times 100 \times 12$	3	PZT	fixed	x,y,z	DMI	[74]
8	VSL	$100 \times 100 \times 20$	3	PZT	fixed	x,y,z	DMI	[26, 56]
9	NMIA	$100 \times 100 \times 25$	3	PZT	fixed	x,y,z	DMI	[47, 62]
10	FPS-SMD	$100 \times 100 \times 100$	3	PZT	fixed	x,y,z	DMI	[82–84]
11	NIM	$200 \times 200 \times 6$	9	-	x,y,z	x,y,z φ , ψ , θ	DMI	[67]
12	CMI	$200 \times 200 \times 10$	4	PZT	z	x,y,z	DMI	[63]
13	METAS	$800 \times 800 \times 200$	7	PZT	z		-	[69]
						x,y,z	DMI	
						φ , ψ , θ	-	
14	TU/e ^d	$1 \times 1 \times 1$ mm	3	lorentz	fixed	x,y,z	DMI	[107–109]
15	PTB	$25 \times 25 \times 5$ mm	6	lorentz + PZT	fixed	x,y,z φ , ψ	DMI AC	[22, 23]
16	NRC	$40 \times 40 \times 6$ mm	12	PZT	z		CPS	[33]
						x,y,z	DMI	
						φ , ψ , θ	AC	
17	NIST	50×50 mm $\times 5$ μm	3	PZT	y	x	DMI	[60, 102]
					z		CPS	

^adegrees of freedom, ^bdisplacement measuring interferometer, ^ccapacitive position sensor, ^dfor VSL

Table 1.3 / Summary of current and near-future appearing metrological AFMs (mAFMs). More information and additional references are given in Table A.1 on Page 140.

Most mAFMs have a scanning range of about $100 \times 100 \times 10$ to $20 \mu\text{m}$, use mechanical guides with linear piezoelectric actuators (PZTs) to move the sample in three degrees of freedom (DOFs) relative to a stationary AFM probe and measure the relative movements with displacement measuring interferometers (DMIs). None of the instruments use a, for commercial AFM common, piezoelectric tubescanner to generate the scanning motion.

Because of the similarities between the mAFMs, only two instruments are discussed in detail.

A typical mid-range instrument is NPL's mAFM (Figure 1.5) [45, 64]. The instrument uses, like many mAFMs, a commercial AFM head and a commercial flexure translation

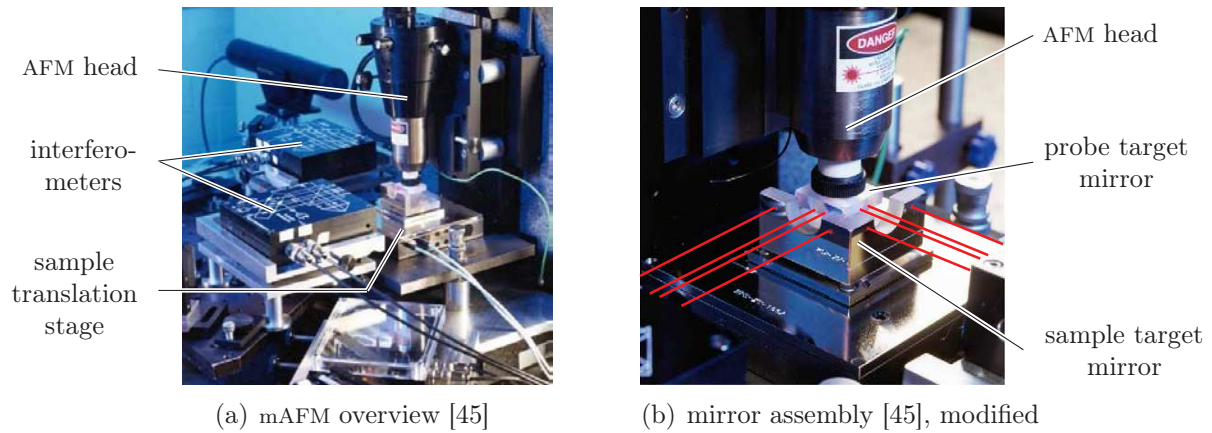


Figure 1.5 / NPL’s mAFM with Jamin interferometers. The beams of the interferometer are indicated schematically in (b). Table 1.3 summarizes the instrument characteristics.

stage. The piezoelectric tubescanner in the AFM head is used to move the probe only vertically, the sample’s horizontal scanning motion is generated with the two-DOF, PZT-driven, sample translation stage.

Three differential plane-mirror Jamin interferometers [27–29] measure the relative probe and sample displacements. Figure 1.5(b) gives a view detail of the target mirrors. A target mirror with three mutually orthogonal reflective surfaces is connected to the AFM probe while a second, similar shaped target mirror is attached to the sample translation stage. The interferometers are nominally aligned with the AFM probe for Abbe-error free measurements (Section 2.1).

Using a commercially available AFM head is presumably convenient. The AFM head has a cantilever deflection measurement system with sufficient resolution, built-in signal processing electronics and comes with user-friendly software. However, the AFM is probably not designed for maximum thermal stability. This lower thermal stability can make the mAFM susceptible to drift because the AFM head is, even with the differential interferometer layout, part of the metrology loop from the probe target mirror to the AFM probe.

The NPL mAFM’s DOFs are physically separated into one fast probe motion (vertical) and two much slower sample motions (horizontal). Due to the differences in moving mass, this layout requires smaller actuator forces than the moving sample-stationary probe layout and is therefore used in several other mAFMs (instruments 5, 6, 11, 12, 13 and 16 in Table 1.3). The dynamical advantage in the NPL instrument is slightly reduced by the probe target mirror’s mass.

The moving probe layout has a metrological disadvantage. The AFM probe moves away from the virtual intersection point of the three interferometers when the AFM probe

moves vertically to follow the sample topography. This introduces an Abbe offset and subsequently increases the sensitivity to straight guide rotations [14]. Although this is admittedly of little practical importance with a 5 μm scanning range, it does become important for larger scanning ranges. For example, a 50 μm Abbe offset and a 5 arcsec stage rotation gives an error of more than one nanometer.

The PZT-driven sample translation stage uses flexures to guide the sample and the sample target mirror with minimal rotations. In the NPL instrument, the combined center of gravity (COG) of the sample and the sample target mirror is well above the translation stage's horizontal midplane. This leads to non-reproducing or random sample rotations during acceleration and these rotations ultimately limit the instrument's measurement speed. Remarkably, actuating the translation stage in the COG to minimize the rotations is mentioned in none but one (instrument 14) of the mAFM descriptions.

The NPL mAFM's measurement results are made traceable to the international definition of the meter by calibrating the DMI's laser source wavelength against an iodine-stabilized reference laser of an NMI [36, 45]. This procedure is relatively practical compared to the calibration of other, non-interferometrical sensors like capacitive position sensors [40, 58, 98] and is therefore used by every mAFM in Table 1.3.

The Jamin interferometer's differential layout results in a short metrology loop from the AFM probe to the sample. This helps to minimize the instrument's sensitivity to temperature variations. Despite this metrological advantage, only a few of the current mAFMs use differential interferometers (Table 1.3: instruments 2, 7, 9, 13, 14 and 17).

The displacement measurement system with the NPL mirror layout is sensitive to environmental changes because the laser beams reflected by the probe target mirror travel a different distance through the air than the beams reflected by the sample target mirror. This dead path error [113] is minimal when the probe target mirror and sample target mirror are nominally in the same plane (instruments 2 and 14) or when the instrument is operated in vacuum (instruments 9 and 17).

Figure 1.6(a) gives a photograph of PTB's metrological Large-Range SPM (LR-SPM) [19, 22, 23]. The instrument has a stationary AFM and moving sample layout. Table 1.3 summarizes the instrument's properties.

PTB's LR-SPM uses a commercial translation stage (NanoMeasuringMachine, NMM) with a stroke of $25 \times 25 \times 5$ mm. On top of the NMM's sample table there is a second, one-DOF translation stage which holds the sample. This PZT-driven sample stage has a 2 μm stroke.

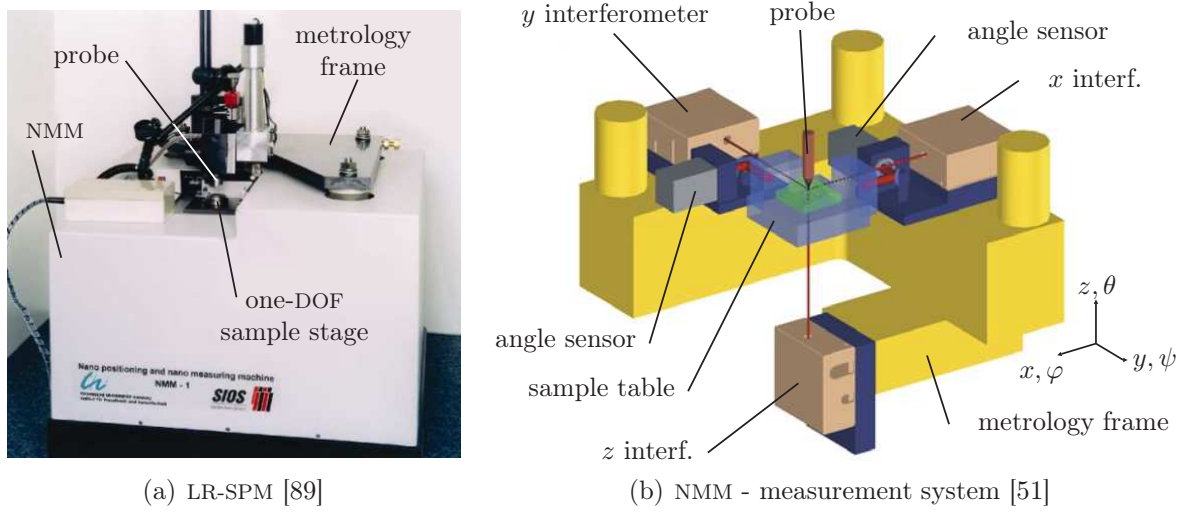


Figure 1.6 / PTB's metrological Large-Range SPM (LR-SPM) with the NMM translation stage and extra one-DOF, PZT-driven sample stage. The metrology frame's top plate is only visible in Figure (a). Table 1.3 summarizes the instrument specifications.

The NMM has three orthogonally stacked ball bearing guides [51]. The ball bearing guides give the sample table three translational DOFs and two rotational DOFs (φ, ψ). The two rotations are measured and close-loop controlled towards minimal sample table rotations. The one-DOF sample stage has no straight guide other than the three PZTs.

Three homodyne, single-beam interferometers, measure the NMM's sample table translations (Figure 1.6(b)). The three interferometer beams virtually intersect at the AFM probe position for minimal Abbe error. A low-expansion Zerodur® metrology frame connects the three interferometers, this frame also holds the two autocollimation-based angle sensors [97]. A CPS measures the one-DOF sample stage's movements along the z direction.

The AFM connects directly to the NMM's Zerodur® metrology frame. For the cantilever deflection measurement an unusual optical detection method was initially used but this system has been replaced by a more common OBD measurement system [23]. The LR-SPM measures in the constant force mode.

The LR-SPM has a larger than average scanning range. With this extended range, larger parts of the sample can be measured in one continuous scan. This improves the measurement statistics [20] and sample uniformity estimate [20, 33].

The NMM actively corrects for angular misalignments in its straight guides. This reduces the straight guide requirements so relatively compact and low-cost ball-bearing guides can be used [51]. Disadvantageous compared to a purely mechanical three-DOF

translation stage are the extra actuators and sensors needed to control the rotational DOFs. These actuators increase the instrument's mass and complexity. Furthermore, every actuator and sensor is a heat source and consequently affects the instrument's thermal stability.

The actuators in the NMM are not aligned with the translation stage's COG. Although accelerations do not lead to sample table rotation, they do lead to extra power dissipation and subsequent heat production within the stage.

The NMM's metrology frame supports the three interferometers, the two angle sensors and the AFM head and is made from Zerodur[®]. The Zerodur's near-zero coefficient of thermal expansion (CTE) makes the frame practically insensitive to temperature variations. The stacked-beam design of Figure 1.6(b) is appropriate for a material like Zerodur[®] but does not provide the highest stiffness possible. This relatively low stiffness increases the metrology frame's sensitivity to vibrations.

Two other instruments (3 and 16) use Zerodur[®] for the metrology frame while instruments 6, 8 and 10 use Invar[®] instead. Invar[®] is better machineable than Zerodur[®] but its specific stiffness (E/ρ) is only about two-thirds of the specific stiffness of aluminium [104]. This makes it difficult to design a mechanically stable metrology frame.

Zerodur[®] and Invar[®] have much lower volumetric thermal diffusivity coefficients ($\lambda/(\rho c_p)$) than, for example, aluminium. Metrology loop components made from Zerodur[®] or Invar[®] therefore respond much slower to temperature variations and subsequently take longer to settle than similar aluminium parts. This is disadvantageous for the instrument's thermal stability.

The LR-SPM operates in the constant force mode so the sample's vertical position is controlled to keep the cantilever deflection constant. With the stacked-stages design, the sample's vertical motion is generated with the fast one-DOF sample stage instead of with the slower NMM. This increases the measurement speed and consequently reduces the influence of temperature variations on the measurement result. Furthermore, in the stacked-stages design, the CPS can conveniently be calibrated against the NMM's traceably calibrated z -interferometer.

The NMM's large moving mass, estimated at 40kg [99], negatively affects the instrument's mechanical stability. Furthermore, the large moving mass also influences the thermal stability through the actuator power losses.

Three interferometers measure the NMM's sample table translations while the CPS measures the sample's vertical motions relative to the NMM's sample table. Sideways motions of the sample relative to the NMM's sample table, caused by temperature variations, drift or straight guide errors in the one-DOF sample stage, are not measured. Additionally, the NMM's measurement system complies with the Abbe principle but

the one-DOF sample stage's CPS clearly does not. Both factors are considerable disadvantages of the LR-SPM's stacked-stages design.

1.4 Thesis contributions

Extending the measurement range of mAFMs to the millimeter range while maintaining nanometer range uncertainty, reduces the calibration uncertainty through better measurement statistics and therefore helps to improve nanometer scale metrology. Additionally, increasing the scanning range makes mAFMs better suited for, for example, semiconductor critical dimension metrology. For these reasons, a new long-range mAFM is developed for VSL, the NMI of The Netherlands. Table 1.4 summarizes the instrument requirements, adapted from [6]. The instrument is developed within the Metrology Stages Cluster of NanoNed [77], a national nanotechnology program.

range	$1 \times 1 \times 0.1 \text{ mm}$
resolution	$< 1 \text{ nm}$
uncertainty	$\leq 10 \text{ nm}$

Table 1.4 / Instrument specifications.

Achieving nanometer range uncertainty over millimeter range strokes requires instrument characteristics that the current long-range mAFMs lack, such as:

low hysteresis so the instrument behavior is reproducible. This is a requirement for accurate instrument calibration and subsequent low-uncertainty measurements,

high resonance frequency for minimal sensitivity to external vibrations and high maximum scanning speeds. This requires high stiffness and low moving mass (e.g. 100 g instead of the LR-SPM's 40 kg),

statically determined design so the instrument reacts predictably to temperature changes and disturbance forces,

minimal internal heat sources to minimize the temperature variations and gradients within the instrument. Using efficient actuators and minimizing the actuator loads also improve the instrument's temperature stability,

minimal instrument errors (e.g. Abbe error) because the measurement uncertainty is likely to be lower if less errors need to be calibrated [105]. High quality straight guides and properly aligned actuators are necessary to eliminate (dynamic) rotations.

These aspects are taken into account in the new mAFM.

1.5 Thesis outline

Chapter 2 discusses the design considerations and explains the mAFM's moving sample-stationary AFM probe layout. The new mAFM has a three-DOF sample translation stage and a separate, kinematically mounted AFM head. In the next chapters, the sample translation stage design is explained, the AFM head design [92] is briefly explained in Appendix B.

The sample translation stage's straight guide design is explained in Chapter 3, followed by a description of the actuation system in Chapter 4. Chapter 5 addresses the displacement measurement system and Chapter 6 gives the conclusions.

CHAPTER TWO

Instrument overview

Abstract / This chapter discusses the metrological AFM's layout. The new instrument has a three-DOF translation stage to move the sample relative to the stationary AFM head. The AFM uses optical beam deflection to measure the cantilever's deflection. The translation stage has three, identical, elastic parallel guides, each driven by a Lorentz actuator. Three stiffness compensation mechanisms and three weight compensation mechanisms reduce the actuator's power loss. The sample motions are measured with three differential plane mirror interferometers.

The first section gives some design aspects that affect the instrument performance. Section 2.2 discusses the possible instrument layouts, followed by a few remarks on the AFM head design in Section 2.3. The translation stage concept is discussed from Page 21 onward. Section 2.5 gives an overview of the translation stage design.

2.1 Design considerations

Atomic Force Microscopes (AFMs) image a sample by scanning a small probe across the sample surface and measuring the probe movements as it follows the surface topography. In a perfect instrument these movements are measured without errors while only movements necessary to follow the sample topography are made.

In practice, however, measurement errors and deviations between the required and actual movements, caused by friction, external disturbances and temperature variations, limit the instrument's metrological performance. These limitations, and how to prevent or minimize them, are the topic of the following sections.

measurement errors

The potentially largest measurement error in metrological AFMs (mAFMs) is the Abbe error [24]. This error occurs when the displacement measurement axis is not aligned with the actual measurement point or probe [1] and the probe rotates during translation (Figure 2.1 on the next page).

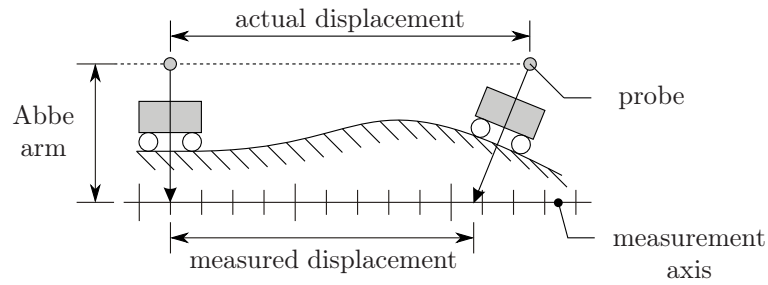


Figure 2.1 / The offset between the measurement axis and the measurement probe results in an Abbe error when the probe rotates.

Aligning the measurement axis to the probe or translating the probe without rotations, minimizes the error. If this is not possible, then the rotations must be measured and the displacement measurement results corrected for this rotation [14].

Accurate correction for the probe rotation requires a high resolution, low uncertainty angle measurement system. Additionally, the Abbe arm must be accurately known. These requirements make an out-of-Abbe displacement measurement system which corrects for probe rotations, less practical than a measurement system in Abbe.

Nevertheless, the probe rotations must be minimized, even with the measurement system nominally in Abbe, because some misalignment between the probe and the measurement axis is practically inevitable.

friction and external disturbances

Friction in the instrument causes hysteresis. Hysteresis limits the positioning accuracy as the output motions cannot be accurately predicted from the actuator inputs.

Preventing friction and assuring high (actuation) stiffness in the motion direction helps to reduce the hysteresis [93]. Conversely, the difficulties in accurately predicting hysteresis makes it practically impossible to improve the positioning accuracy by merely introducing advanced motion controllers.

Other mechanical factors that affect the positioning accuracy are external disturbances like acoustic loads and floor vibrations [110]. Maximizing the instrument stiffness minimizes the deflection caused by external loads. Keeping the moving mass low reduces the dynamic forces and subsequent deflections and further improves the positioning accuracy.

The instrument's sensitivity to (floor) vibrations decreases when its resonance frequency increases [105]. Furthermore, an increase in eigenfrequency allows for a higher control bandwidth, which improves the controller's disturbance attenuation. Another advantage of a high eigenfrequency is the higher allowable scanning speed. Scanning at high speeds shortens the measurement time and thereby reduces the influence of temperature variations on the measurement results.

temperature variations

Changes in the instrument temperature often result in unmeasured displacements. These displacements are prevented when the temperature variations are eliminated altogether or when the instrument itself is insensitive to temperature changes.

Temperature variations are minimal when the power dissipation within the instrument is minimized, the instrument is shielded from external heat sources and the ambient temperature is kept constant.

The instrument's largest internal heat source is the actuator. Using an efficient actuator and minimizing the actuator load reduces the dissipated power. The actuator's dynamic load can be reduced by minimizing the instrument's moving mass and friction. The static load caused by residual stiffness in the actuation direction and by gravity, can be decreased with stiffness compensation and weight compensation mechanisms.

During sample loading and alignment, a large amount of heat is transferred (through radiation) from the instrument operator to the instrument. This thermal disturbance and subsequent equalization time can be minimized by fast sample loading and alignment.

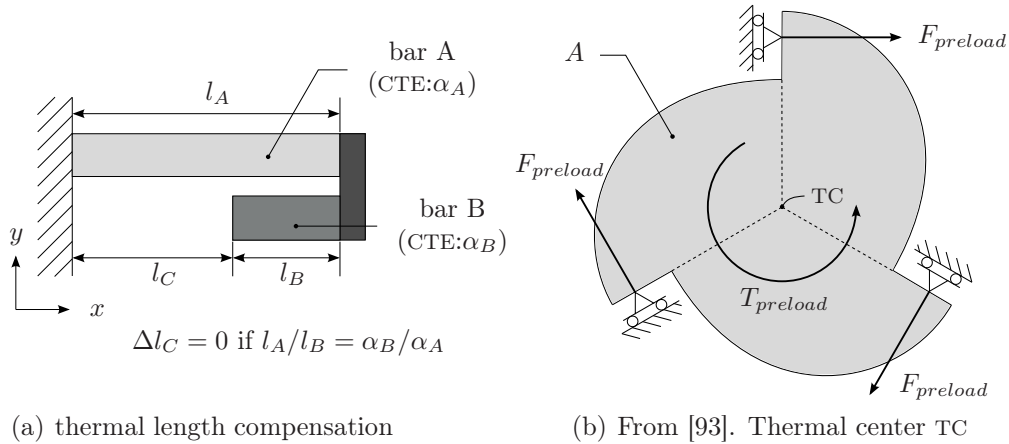


Figure 2.2 / Thermal length compensation and thermal center. Figure (a) shows how thermal length compensation results in zero thermal expansion. The thermal center TC in Figure (b) remains stationary during uniform temperature changes and is independent of material properties.

One way of reducing the instruments sensitivity to temperature variations is the use of thermal length compensation (Figure 2.2(a)). In this passive compensation concept, the thermal expansion of bar A is compensated by the equal but oppositely directed expansion of bar B. The difference in the coefficient of thermal expansion (CTE) between bars, determines their length ratio.

Another passive compensation method is the thermal center of expansion (TC) (Figure 2.2(b)). In this two-dimensional example, the position of body *A* is fully constrained by three preloaded tangential supports. The three supports move radially if the body expands or contracts but the central point (TC) remains stationary.

Passive compensation corrects only for uniform temperature changes so any temperature gradient must be quickly equalized. The temperature settling time is determined by the instrument thermal capacity and the thermal resistance. Minimizing both results in a short settling time [104, 105].

2.2 Instrument layout

The AFM probe moves across the sample surface during measurement. The way this relative motion is generated, has a large influence on the instrument design.

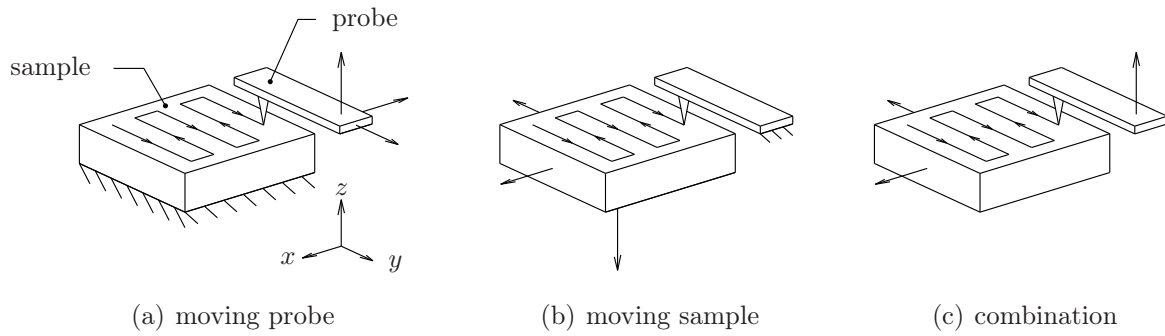


Figure 2.3 / Relative motion of the probe and the sample.

Figure 2.3 gives three possible configurations for the relative motion. In the first variant, Figure 2.3(a), the probe moves and the sample remains stationary. Translating the lightweight AFM probe instead of the heavy sample, helps to minimize the moving mass of the instrument. Furthermore, there are no limitations on the sample size, weight or shape that can be scanned, which makes the instrument versatile. Unfortunately, it is difficult to measure the probe's movements without Abbe error as this requires that the axes of the measurement system remain aligned with the probe when it moves across the sample, or that the probe moves without rotations. Measuring the probe's rotation and afterwards correcting the measurement results for the Abbe error is considered to be too complex (Section 2.1).

Moving the sample and keeping the probe and the displacement measurement system stationary, as shown in Figure 2.3(b), fulfills the Abbe principle and is mechanically simpler. As a consequence, the moving mass now depends on the mass of

the sample which makes the dynamical behavior of the instrument somewhat sample dependent.

Compared to the moving sample layout, the dynamics of the instrument improve if the fast vertical movements, necessary to follow the sample topography, are made with the AFM probe while the sample makes the much slower horizontal scanning motion (Figure 2.3(c)). The metrological disadvantage of no longer measuring in Abbe may be acceptable for short scan ranges, but leads to considerable errors when millimeter-range motions are made.

The samples that must be scanned with the new instrument are very similar in shape and weight (Table 1.1). Combined with the large required scanning range, the moving sample layout of Figure 2.3(b) is selected.

The instrument can now be divided into two more or less independent components. The first component is the AFM head which holds the cantilever and the cantilever deflection measurement system (Section 2.3). The second part is the sample translation stage with straight guides, actuators and displacement measurement system necessary to generate and measure the sample's scanning motions (Section 2.4).

2.3 AFM head - considerations

The requirements for mAFMs differ slightly from those for commercial AFMs because accuracy, not speed, is the most important factor. These differences are reflected in the AFM measurement mode and feedback type.

Most mAFMs make either contact-mode or intermittent-contact mode measurements [24], non-contact mode is rarely used because it is less suited for measurements in ambient conditions.

In intermittent-contact mode measurements, the cantilever vibrates to minimize the tip and sample contact time. Compared to contact mode measurements, the oscillation reduces the tip wear but does require an additional actuator. This actuator negatively affects the AFM head's thermal and mechanical stability so contact mode is the preferred measurement mode here.

In constant force mode (CFM) feedback, the cantilever deflection is kept constant by controlling the sample's vertical position during scanning. When the cantilever deflection is at the preset target value, the sample stage displacement sensors are read and the relative position of the probing point recorded.

Unlike constant height mode (CHM) feedback, which converts the cantilever deflection

directly into topographic information, CFM measurements require less calibration of the cantilever deflection measurement system as it is used only as a zero-sensor. Conversely, CHM continuously measures the sample topography while CFM only measures the topography when the cantilever deflection is at the preset value, which results in discrete measurement points. Furthermore, the spacing of the CFM measurement points depends on the position controller's performance. This can result in irregularly spaced measurements (Figure 2.4(a)). Oscillating the sample vertically with a small (≈ 10 nm) amplitude, results in more equidistantly spaced measurement points (Figure 2.4(b)).

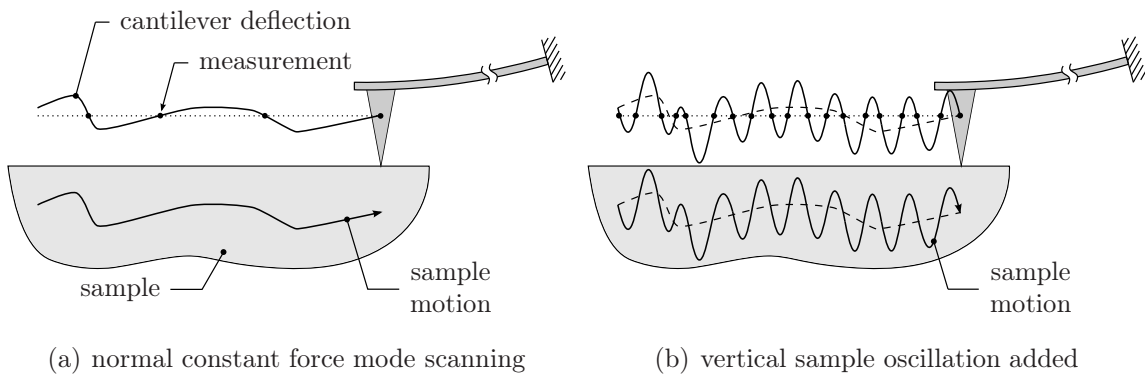


Figure 2.4 / Sample motion controlled to constant cantilever deflection (CFM). Tracking errors result in deflection variations and subsequently irregularly spaced measurement points. Adding a small vertical oscillation to the sample motion increases the number of measurement points. Figures not to scale.

The metrological advantage of using the cantilever deflection measurement system merely as a zero-sensor makes CFM the most appropriate feedback method.

The AFM head for the new mAFM is described in [92] and uses the optical beam deflection (OBD) method to measure the cantilever deflection (Figure 2.5).

A high-efficiency laser diode generates the light beam, this beam is then focussed onto the cantilever by several beam shaping optics. The cantilever reflects the now diverging beam onto a four-quadrant position sensitive detector (PSD) which measures the beam movements.

The AFM's TC coincides with the AFM probe position for maximum thermal stability. Three ball and v-groove contacts kinematically locate the AFM head on the translation stage's solid world / frame. This kinematic mount minimizes the alignment effort during reinstallation of the AFM head onto the stage after sample changes.

A kinematic cantilever holder simplifies the cantilever loading and alignment on the AFM head. Appendix B gives more information on the AFM head design.

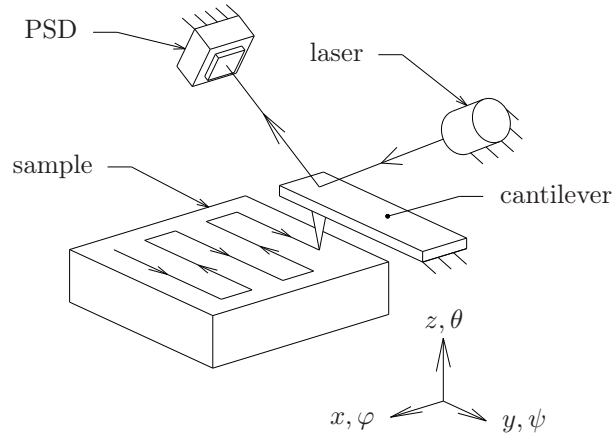


Figure 2.5 / Measuring the cantilever deflection with optical beam deflection (OBD). Figure not to scale.

2.4 Sample stage design

The sample stage moves the sample within a volume of $1 \times 1 \times 0.1$ mm centered around the stationary AFM probe. The sample stage has straight guides to constrain the sample's rotations, actuators to generate the translation and a traceable, three-dimensional displacement measurement system.

2.4.1 Straight guide

The sample stage minimally needs three translational degrees of freedom (DOFs), e.g. x, y, z in Figure 2.5. The three sample stage rotations (φ, ψ, θ) are mechanically constrained. Conversely, the sample stage can also have more than three DOFs, for example six: x, y, z and φ, ψ, θ in Figure 2.5. The additional rotational DOFs are measured and actuated, and controlled towards minimal sample stage rotation [51].

A six-DOF stage requires a more extensive and complex measurement system than a three-DOF translation stage, even when the displacement measurement is in Abbe. Furthermore, the additional actuators are potential sources for heat and electrical noise. Because of these disadvantages, a three-DOF layout is preferred over a six-DOF design.

The ideal straight guide is frictionless and combines high stiffness against external disturbances with minimal residual stiffness in the actuation direction for low actuator loads. Elastic straight guides have no friction [93] and provide a high stiffness ratio between the constrained and unconstrained motions and are therefore used.

The kinematic design for the three-DOF sample stage can be either serial or parallel. In

a serial layout, three separate one-DOF translation stages are stacked onto each other to form a three-DOF sample stage. This layout is mechanically straightforward and decouples, at least theoretically, the three translations. A disadvantage is the large moving mass which also varies for each direction. The long mechanical loop between the sample and the solid world results in low stiffness in the constrained directions.

In a parallel configuration, all the sample table's DOFs are directly constrained towards the solid world. Figure 2.6 gives an example how three identical parallel guides, each with one parallelogram and two struts, suspend the sample table and allow it to translate without rotation.

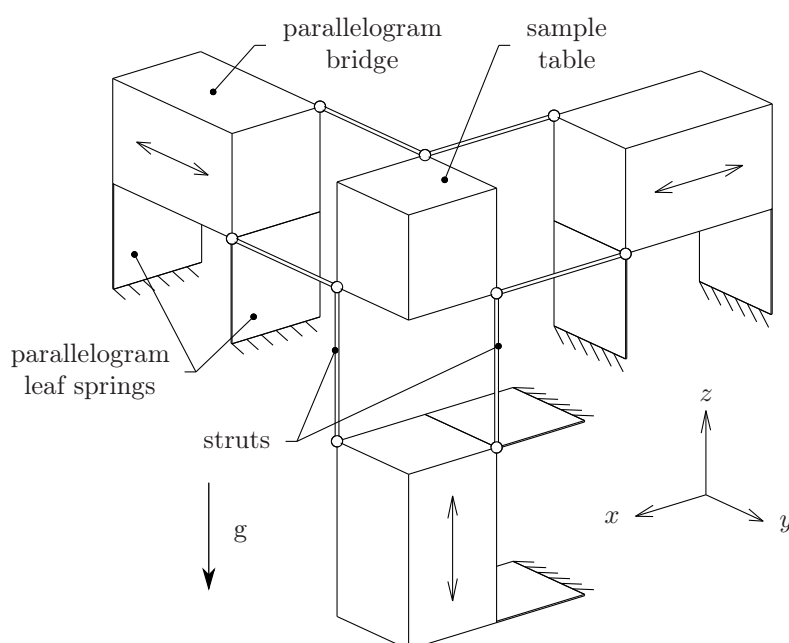


Figure 2.6 / Three identical, elastic, parallel guides. All the sample table's DOFs are directly constrained towards the solid world. This leads to equal stiffness and moving mass in all directions.

Unlike the serial layout, the motions of the stage are no longer decoupled so a straight line motion requires simultaneous actuation of the three parallelograms. Conversely, the moving mass is considerably lower and equal in all directions. Furthermore, the mechanical loop between sample and solid world is much shorter and the rotation stiffness therefore higher.

With three identical parallel guides, the instrument's scanning range can easily be increased from $1 \times 1 \times 0.1$ mm to $1 \times 1 \times 1$ mm. This increased scanning range eases the sample set-up.

A drawback of the layout in Figure 2.6 is that gravity, aligned parallel to the z axis, affects the individual parallel guides differently. This is remedied by rotating the stage so that each guide makes an identical angle with the vertical (Figure 2.7). A further advantage is the reduced sensitivity to vertical temperature gradients as each guide is now equally affected.

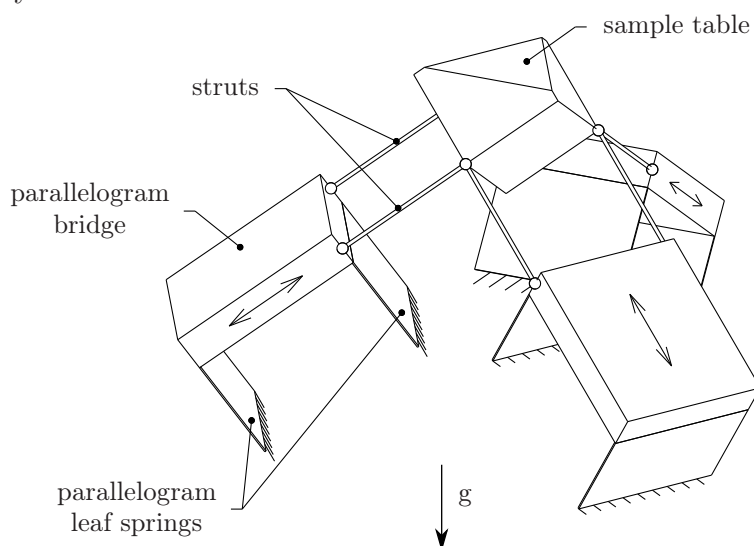


Figure 2.7 / The layout of Figure 2.6 is rotated so each parallel guide is now equally affected by gravity and vertical temperature gradients.

2.4.2 Actuation

Three Lorentz actuators generate the sample table motions. Unlike piezoelectric actuators, these electromagnetic motors provide a constant linear relation between the actuator input and the sample table motion which simplifies the stage position control.

Placing the actuator in the parallelogram bridge, aligns it with the struts and the sample table's center of gravity (COG). The former maximizes the stiffness in the actuation direction while the latter results in minimal residual moments on the straight guide. Furthermore, integration of the actuator into the parallelogram places the actuator at the outer and lower edge of the instrument. This results in a short mechanical loop to the solid world and maximizes the distance between the sample table and the heat-generating actuator.

The actuators are the instrument's largest heat sources. Low power dissipation within the actuators requires efficient actuators and minimal actuator loads.

The actuator load has a static component, originating from gravity and the residual straight guide stiffness, and a dynamic component (acceleration forces). Using stiffness compensation and weight compensation, minimizes the static actuator load. Minimizing the instrument's moving mass, reduces the force needed for acceleration. Chapter 4 explains the actuator design and compensation modules in more detail.

2.4.3 Measurement system

The measurement system traceably measures the sample movements within the instrument's cubic millimeter scanning range. For normal AFM measurements a sub-nanometer position resolution is required [24]. Practically, only laser interferometers can provide such high resolution over millimeter range motions [12].

A laser interferometry system has at least a frequency-stabilized laser, a beamsplitter, two mirrors and a detector. The beamsplitter divides the incoming laser beam into a measurement beam and a reference beam. After reflecting of their respective target mirror, the beams are recombined by the beamsplitter and reflected towards the detector. Optical interference at recombination makes the beam intensity dependant on the optical path difference (OPD) between both paths. Moving one mirror relative to the other results in an OPD, which the photosensitive detector measures as a light intensity variation. The measurement electronics convert the detector's output signal into a displacement signal.

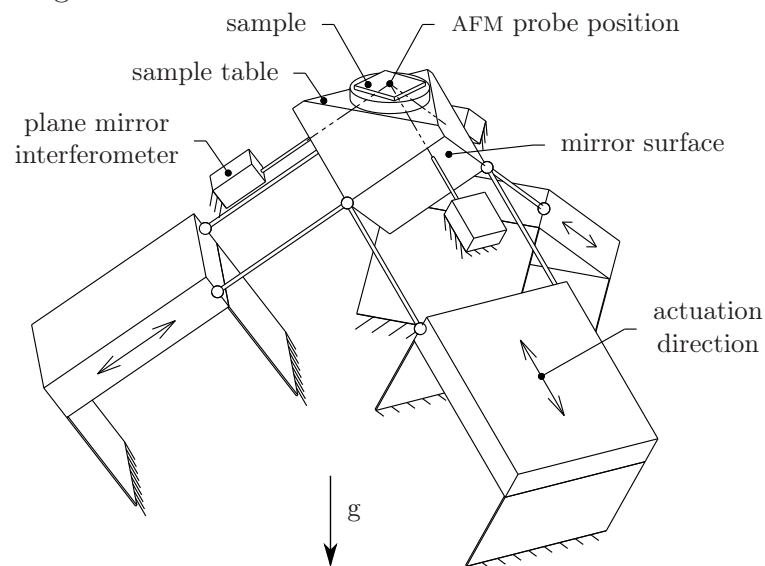


Figure 2.8 / Three-dimensional interferometric displacement measurement in Abbe using three, identical, plane mirror interferometers.

Figure 2.8 shows a simple three-dimensional interferometric displacement measurement system which uses three separate, identical, plane mirror interferometers (PMIs). The interferometers align with the AFM probe position to minimize Abbe measurement errors and are parallel to the actuator for collocated control.

The interferometers measure only the displacements of the sample table's mirror surfaces, variations in the mirror to AFM probe distances are not detected and thus lead to measurement errors. To minimize these errors, the mirror surfaces are as close as possible to the AFM probe position. Fabricating the mirror from nearly zero-expansion Zerodur[®] further improves the metrology loop stability.

The reference mirror of most PMIs is mounted directly onto the interferometer's beamsplitter. Consequently, the metrology loop from the reference mirror to the AFM probe position differs considerably from the sample table's moving target mirror metrology loop. This difference makes the displacement measurement sensitive to temperature variations.

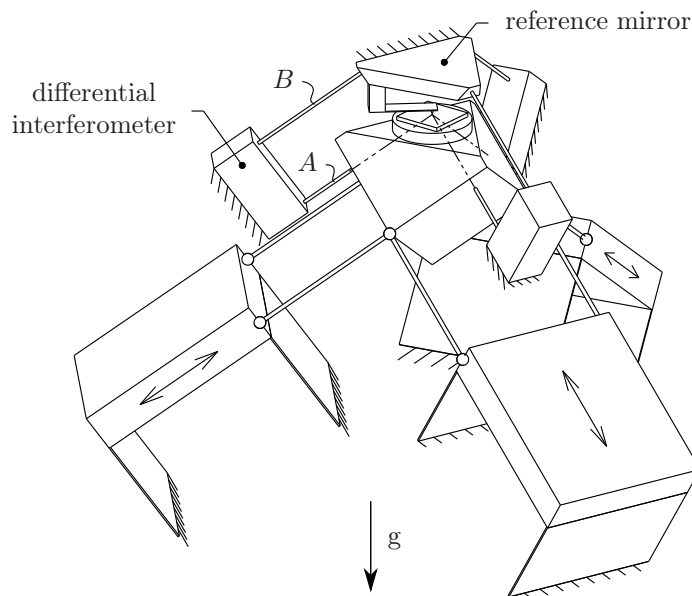


Figure 2.9 / Differential displacement measurement. Translations of the differential interferometer itself, have no influence on the measured displacement. In the actual instrument, the measurement beam (*A*) and reference beam (*B*) travel equal distances through air for a reduced influence of air temperature variations and air pressure variations (explained in Section 5.2.1).

Connecting the reference mirror directly to the AFM head reduces the length difference between the measurement metrology loop and the reference metrology loop and accordingly improves the thermal stability. Figure 2.9 schematically shows this

differential plane mirror interferometer (DPMI) [113] layout.

The layout in Figure 2.9 forms the basis for the new metrological translation stage.

2.5 Design overview

Table 2.1 summarizes the instrument's characteristics. Figure 2.10 on the next page shows an exploded view. A photograph of the assembled instrument is given in Figure 2.11 on Page 28.

instrument layout
<ul style="list-style-type: none"> - moving sample, stationary AFM - thermal center in AFM probe - minimal Abbe-error in displacement measurement
AFM head
<ul style="list-style-type: none"> - contact mode, constant force mode - constant force mode AFM - optical beam deflection for cantilever deflection measurement
sample stage
<ul style="list-style-type: none"> - stroke $1 \times 1 \times 1$ mm (spec: $1 \times 1 \times 0.1$ mm) - layout symmetrical around vertical - overall dimensions $\varnothing 250 \times 170$ mm - all parts fabricated from the same bar stock
straight guide
<ul style="list-style-type: none"> - three identical, elastic parallel guides
actuation
<ul style="list-style-type: none"> - Lorentz actuators - weight and stiffness compensation
measurement system
<ul style="list-style-type: none"> - three mutually orthogonal, plane mirror interferometers - differential layout - Zerodur[®] mirrors

Table 2.1 / Summary instrument characteristics.

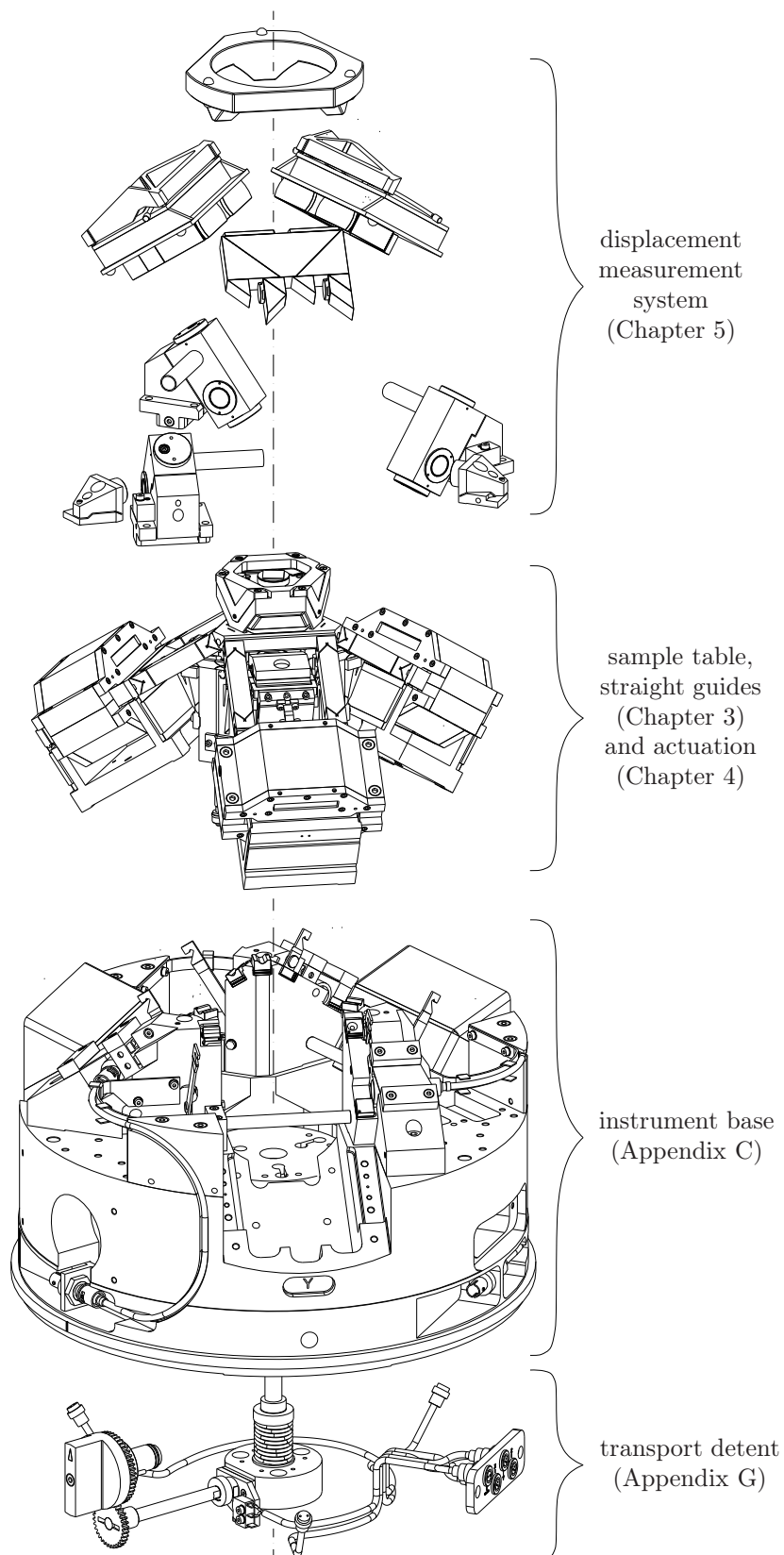


Figure 2.10 / Instrument components.

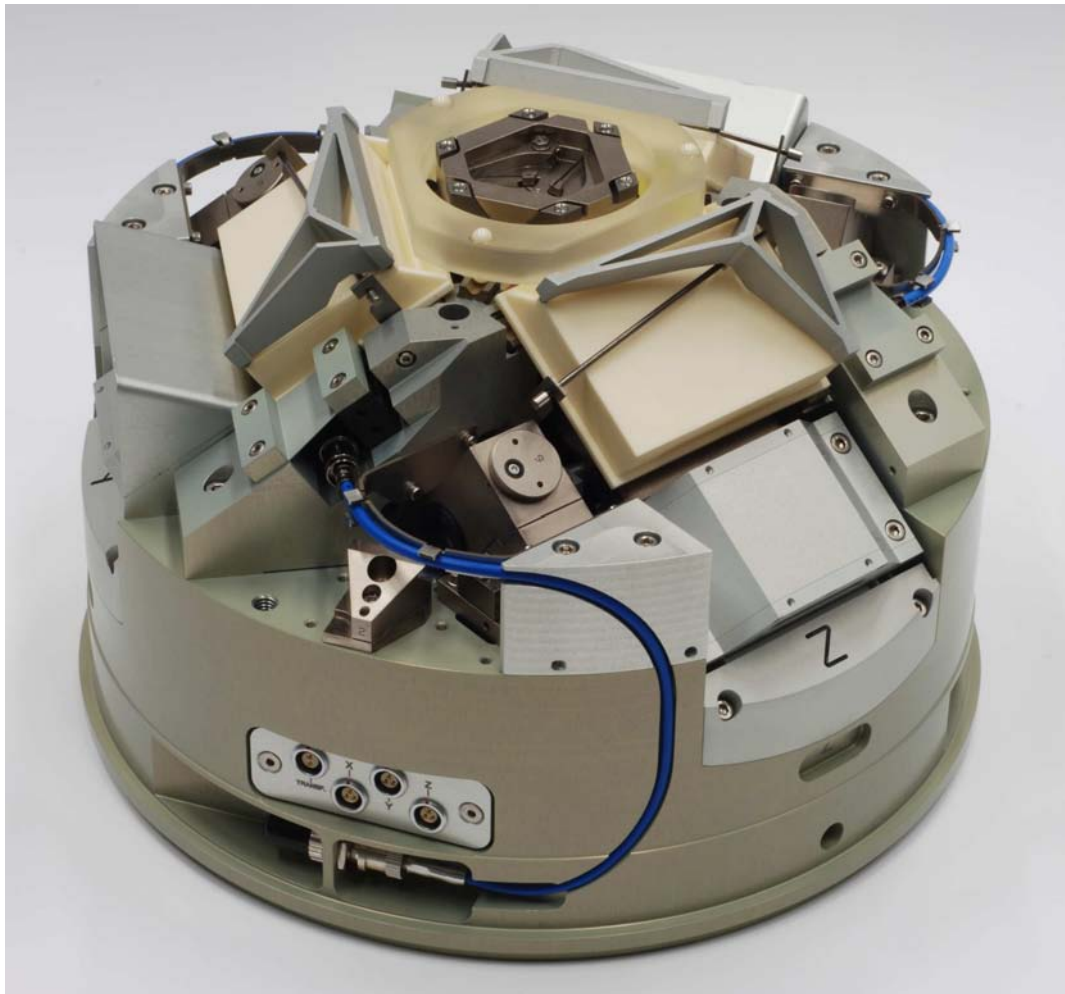


Figure 2.11 / The new translation stage. The overall dimensions are $\varnothing 250 \times 170$ mm.

CHAPTER THREE

Sample table and straight guide

Abstract / A kinematic sample holder fixes the sample to the translation stage's sample table. The sample table design is optimized towards maximum eigenfrequency. Six, cross-hinge struts, support the sample table. Each pair of two parallel struts connects to a stiffened leaf spring parallelogram.

The estimated maximum errors resulting from sample table rotations are within the specified nanometer-range.

The new long-range metrological AFM (mAFM) has a stationary AFM head and a separate, three-DOF sample translation stage. The translation stage's sample table, holds all components that actually move over the instrument's $1 \times 1 \times 1$ mm scanning range. Three identical, elastic, parallel guides, support the sample table. Each guide has two parallel struts which connect to one stiffened leaf spring parallelogram.

The sample table, struts and parallelograms are machined from the same aluminium bar stock to minimize the differences in thermal and mechanical material properties between the components (Figure C.1 in Appendix C).

The first part of this chapter discusses the sample table design, followed by a description of the struts (Section 3.2) and parallelograms (Section 3.3). From Page 39 onward, the sample table rotations are discussed.

3.1 Sample table

A kinematic sample holder fixes the sample to the translation stage's sample table. The sample table also holds the interferometric displacement measurement system's monolithic, Zerodur[®] moving target mirror. A frame connects the sample, the sample holder and the moving target mirror to the three parallel guides.

sample and sample holder

Most transfer standards have a patterned area which is considerably larger than the stage's measurement range (Table 1.1 on Page 5). Aligning the sample's region of interest with the measurement range, requires coarse adjustment of the sample's horizontal position relative to the sample stage. Vertical coarse position adjustments are necessary so samples with different thicknesses can be accommodated.

A simple and thermally stable way to adjust the sample's horizontal position is to slide the sample over the sample stage. Placing the sample on top of a spacer instead of directly onto the stage, allows vertical position adjustments. To simplify the alignment, the sample and the spacer are not fixed directly onto the sample stage but are mounted on a separate sample holder instead.

The sample holder is kinematically fixated to the sample table, so the sample holder's position is reproducibly defined relative to the AFM probe position. Alignment of the sample is now reduced to alignment of the sample relative to the sample holder, which can be done at a separate location using a second, identical kinematic mount and an optical cross-hair microscope. Most importantly, the time needed to place and remove the sample from the instrument is reduced considerably. This, in turn, reduces the operator induced thermal load on the instrument.

The sample, the spacer and the sample holder are part of the metrology loop between the AFM probe and the displacement measurement system's moving target mirror. Any variation in the length of this loop, caused by a temperature change, is not measured and therefore directly results in a displacement measurement error.

To minimize this error, the metrology loop is thermal length compensated (see Figure 2.2). Accordingly, the spacer is made from silicon to ensure that a change in sample thickness does not affect this thermal length compensation (the spacer thickness is adjusted to keep the combined sample and spacer height constant).

Figure 3.1(a) gives an exploded view of the sample holder assembly. The sample and the spacer are joined to the sample holder by three small spots of fast setting glue. The sample holder, in turn, is kinematically fixated to the sample holder frame by three tangentially oriented ball and v-groove contacts. The kinematic sample holder's thermal center of expansion (TC), coincides with the center line.

The ball and v-groove contacts are preloaded for maximum contact stiffness. A high contact stiffness reduces the sample holder movements during sample table accelerations and minimizes hysteresis.

Three low-stiffness wire springs generate the preload force. Each wire meshes at right

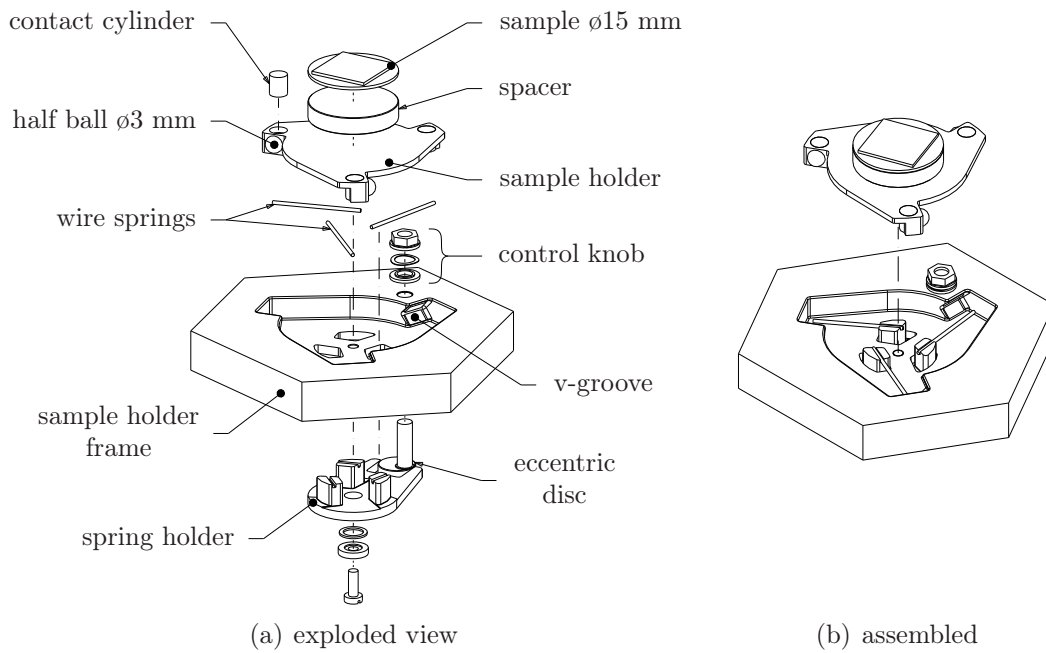


Figure 3.1 / The kinematic sample holder is designed for the largest commercial calibration sample (NanoDevices 1646x-series, Table A.2). Full-surface scans are possible for samples $\leq \varnothing 11$ mm, the maximum sample thickness is 4 mm.

angles with a cylinder in the sample holder, their contact point is directly behind the half ball's center for minimal sample holder bending. Using low-stiffness springs results in large deflections of the springs, which reduces the preload force sensitivity to sample holder and v-groove fabrication tolerances. Furthermore, the slip between the wire spring and cylinder resulting from the large deflection, eliminates unwanted out-of-plane preload force components [93] and minimizes hysteresis.

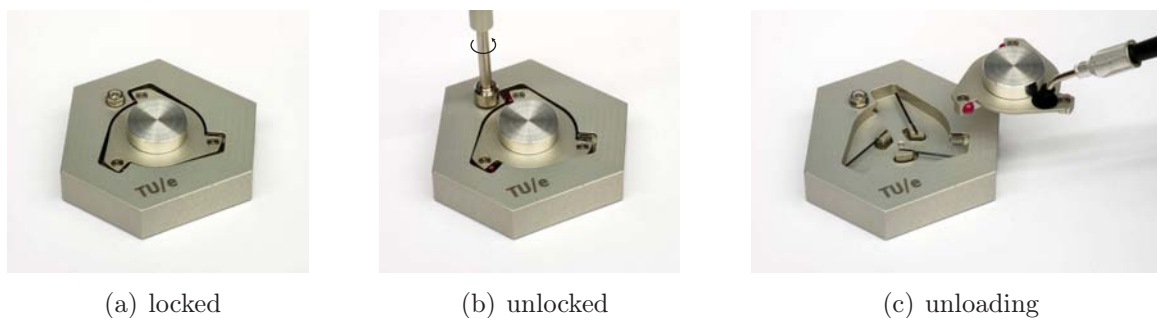


Figure 3.2 / Unloading the sample holder with a bellow-type vacuum gripper (Pen-VAC®). The sample holder is loaded with a dummy mass ($\varnothing 15 \times 4.5$ mm) equivalent to the maximum sample and spacer mass.

The wire springs are fixed onto the rotating spring holder for synchronous operation. During locking, the wire springs first fully locate the sample holder in its kinematic mount before applying the preload force. This, again, minimizes hysteresis.

An eccentric disc rotates the spring holder and decouples the preload force from the required operation or actuation torque. Figure 3.2 on the previous page shows the procedure of unlocking and subsequent removal of the sample holder from the kinematic mount using a vacuum gripper.

mirror support

Three Invar[®] A-frames [93] connect the monolithic, Zerodur[®], moving target mirror to the aluminium sample holder frame (Figure 3.3).

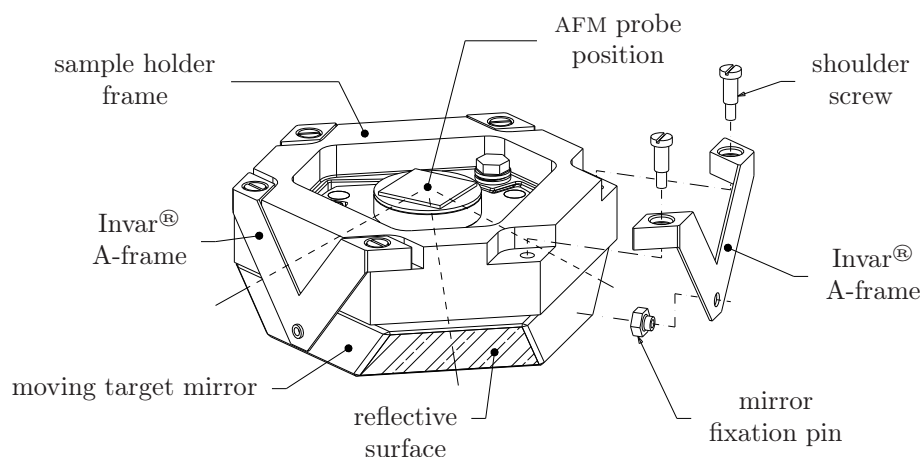


Figure 3.3 / Three Invar[®] A-frames connect the moving target mirror to the sample table frame.

The A-frames minimize the bending moments on the mirror while the high stiffness of the connection reduces the relative mirror and sample holder movements. Additionally, the support keeps the sample holder frame centerline and the moving target mirror centerline aligned, independent of the temperature. The thermal stability is further improved by vertical, thermal length compensation which places the mirror's effective TC directly at the AFM probe position, both radially and axially. This thermal length compensation requires A-frames made from low-expansion Invar[®].

The A-frames have a large surface to volume ratio for fast settling after a temperature change. Two shoulder screws fix each A-frame to the sample table frame, an Invar[®] pin connects the mirror to the A-frame. The pin is first glued axially onto the mirror, after curing the pin is glued radially to the A-frame. This two-step procedure minimizes the influence of glue shrinkage [93].

sample table frame

The sample table frame connects the sample holder and the moving target mirror to the straight guides. The sample table frame's main components are the sample holder frame and the strut frame (Figure 3.4).

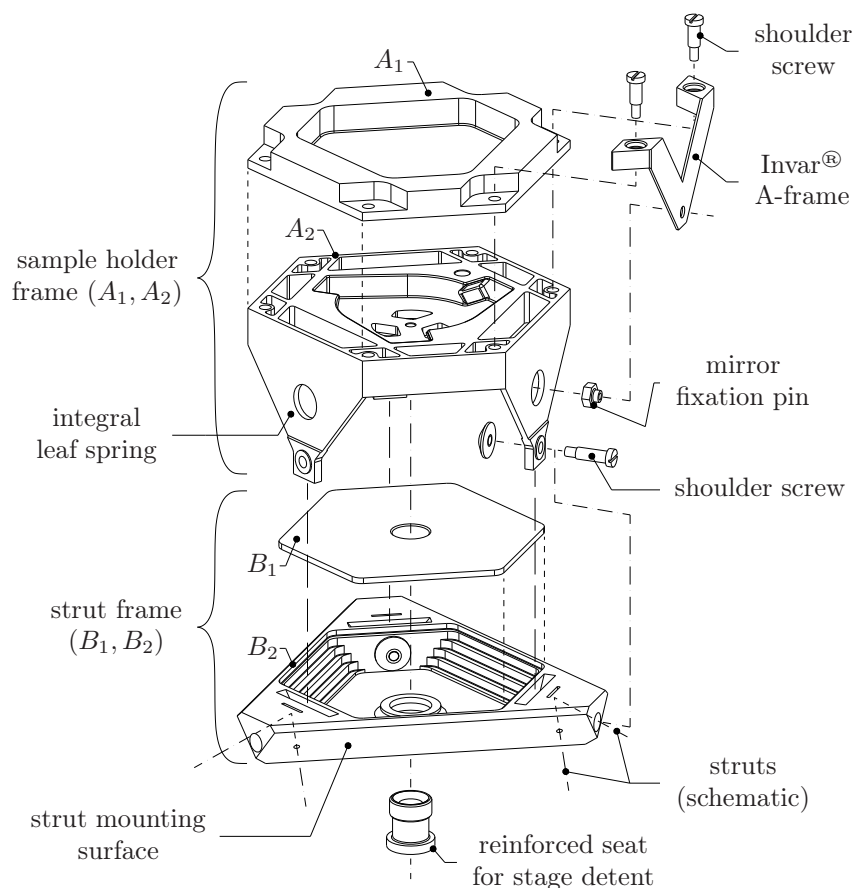


Figure 3.4 / Exploded view of the sample table frame. The sample table frame is assembled from the sample holder frame and the strut frame. The moving target mirror and the sample holder are not shown.

The sample holder frame, in turn, is made from parts A_1 and A_2 which are glued together to form a ring of thin walled, box-shapes. These ventilated boxes ensure high stiffness with minimal mass. Furthermore, the resulting low thermal capacity and nearly constant cross-section allows fast settling after temperature variations. Three integral leaf springs and three, double-shear, shoulder screws, connect the sample holder frame to the box-shaped strut frame.

The sample holder frame is part of the moving target mirror's vertical, thermal length compensation. To ensure accurate thermal length compensation, the sample

holder frame base material's coefficient of thermal expansion (CTE) is measured at VSL.

The strut frame connects directly to the straight guide struts and consequently determines the actuation forces' orientation relative to the sample table's center of gravity (COG). This orientation affects the sample table rotations and the position controller stability.

Reducing the misalignment between the actuation force and the COG, decreases the residual moments on the straight guide during acceleration and subsequently minimizes the sample table rotations. Unfortunately, a perfect alignment in the central position places the actuation force either above or below the sample table's COG during vertical movements (see also Figure 3.11 on Page 40). When the actuation force moves past the COG, the sample table's rotation direction reverses which destabilizes the position controller [91]. The strut frame is therefore designed to keep the actuation force between the sample table's COG and the displacement measurement system at all times. Machining the strut mounting surfaces on the strut frame in one fixture, maximizes the mutual orthogonality of the surfaces.

A detent constrains the sample table movements during transport. The conical seat for this transportation detent is integrated into the strut frame. The transport detent mechanism is described in Appendix G (Page 165).

The sample table frame and the parallel guide's struts (described in Section 3.2) are optimized towards maximum eigenfrequency using the finite element analysis (FEA) package NX Nastran[®] 4. The first, optimized, sample table resonance occurs at 1.7 kHz. Appendix D summarizes the intermediate optimization steps.

Figure 3.5 gives photographs of the sample table frame, before and after assembly.

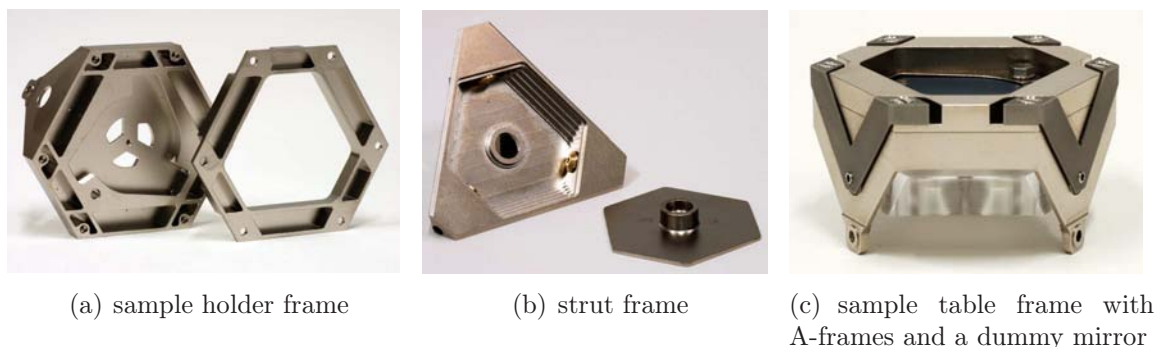


Figure 3.5 / Sample table frame components. In the assembled view (c), a dummy-mirror is temporarily installed.

3.2 Struts

Six struts fully constrain the sample table's position and orientation. Increasing the strut's axial stiffness decreases the sample table's sensitivity to external disturbances. The sideways stiffness, on the other hand, must be as low as possible since it leads to forces and moments on the sample table which, in turn, result in unwanted sample table rotations.

Elastic hinge struts as shown in Figure 3.6(a) allow for a higher axial over lateral stiffness ratio than classic, single-diameter struts or constricted struts (Figure 3.6(b)). However, even with equal distances between the elastic hinges, i.e. $\|\overline{A_1A_2}\| = \|\overline{B_1B_2}\|$ in Figure 3.6(a), there is a difference between the lateral stiffness in the y and the z direction. Conversely, the cross-hinge type strut of Figure 3.6(c) have the same stiffness in either lateral direction and are therefore chosen.

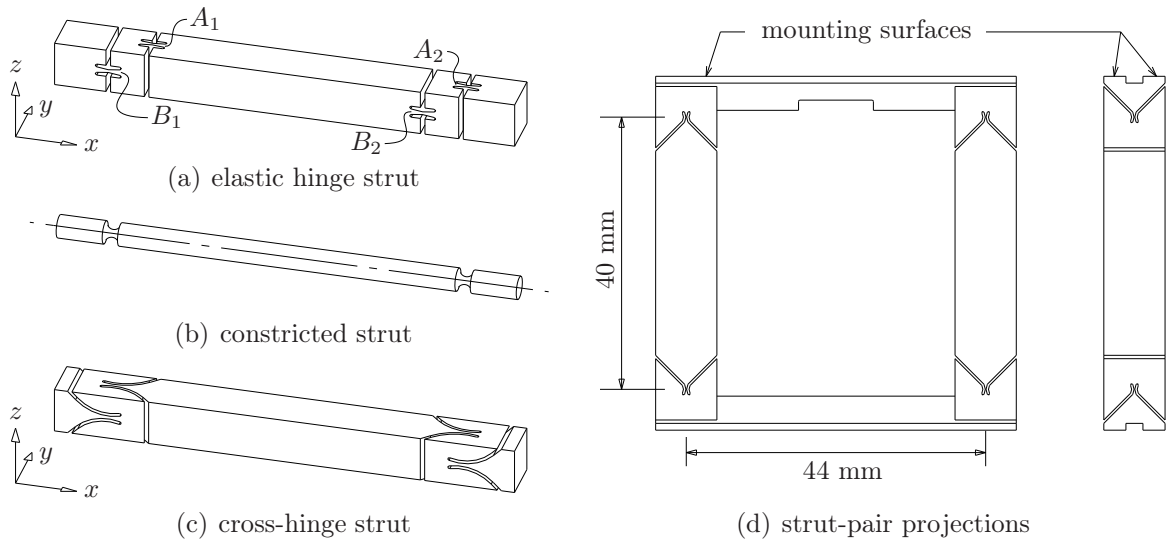


Figure 3.6 / Cross-hinge struts have a higher axial over lateral stiffness ratio than constricted struts. Additionally, the cross-hinge strut's lateral stiffness is equal in all directions, unlike the elastic hinge strut in (a). Two struts are fabricated in one pair for high strut parallelism. The strut cross-section is 9×9 mm with 0.1 mm thick hinges.

The struts are fabricated in pairs of two (Figure 3.6(d)). This way, the hinges of both struts can be cut in one operation, without re-setting of the part on the wire-EDM machine, which results in two nearly identical and parallel struts. The 0.1 mm thick hinges are as close as possible to the strut's mounting surfaces for high stiffness. The strut's mounting faces are pocketed to reduce the strut's moving mass.

Each strut pair is glued to its respective parallelogram and to the sample table's strut frame, dowel pins provide the alignment. The joints can be pried apart with a flat tool inserted in the groove between the two mounting surfaces (Figure 3.6(d)).

The dimensions of the struts and their center distances are determined in the sample table frame eigenfrequency optimization (Appendix D). With these dimensions, the first eigenmode of the strut occurs at about 2.5 kHz (torsion around the centerline). Table 3.1 summarizes some properties of the struts, a photograph of the struts is given in Figure 3.7.

	axial	c_a	N/m	$2.15 \cdot 10^7$
stiffness ^a	lateral	c_l	N/m	750
	ratio	c_a/c_l	-	1 : 28,500
mass ^a		m	g	25.5
strut eigenfreq.		f_{eig}	kHz	2.5
^a per pair				

Table 3.1 / Properties of the struts (FEA).

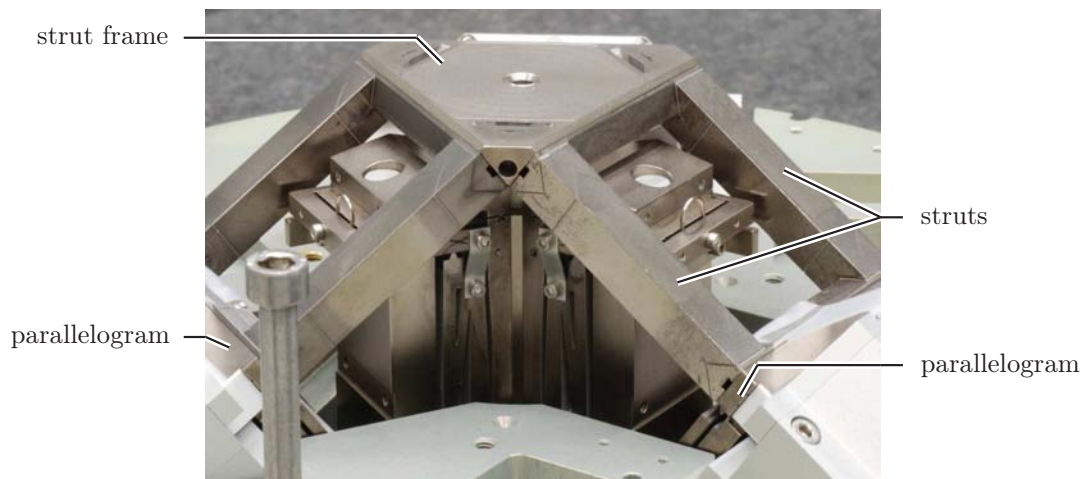


Figure 3.7 / Struts assembled to the strut frame and the (partially visible) parallelograms.

3.3 Parallelograms

Figure 3.8 gives a side view of the straight guide's parallelogram and the struts. The parallelogram's stiffened leaf springs are integral with the parallelogram base. The leaf springs end in the bridge end parts, the two bridge end parts are connected by a ceramic, box-shaped bridge. The ceramic bridge is assembled from two 2×2 inch,

0.64 mm thick aluminium oxide (Al_2O_3) plates (Figure 3.9(a)) and two similar, 2 inch \times 9 mm side plates (Figure 3.9(b)).

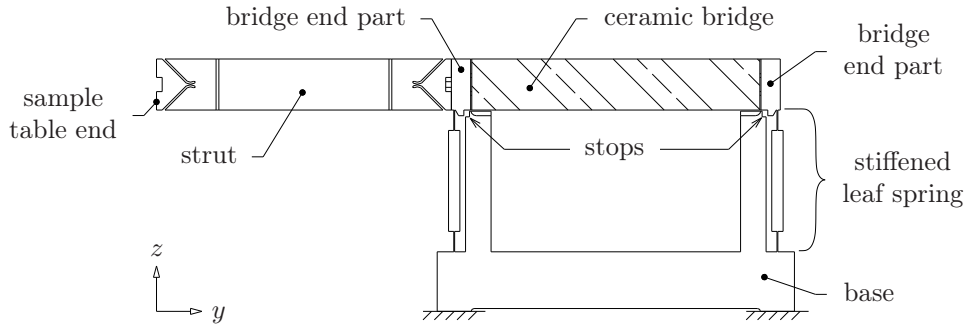


Figure 3.8 / Side view of the parallelogram and the struts. The parallelogram's aluminium, stiffened leaf springs are integral with the parallelogram's base. A ceramic (Al_2O_3) bridge connects the two leaf springs.

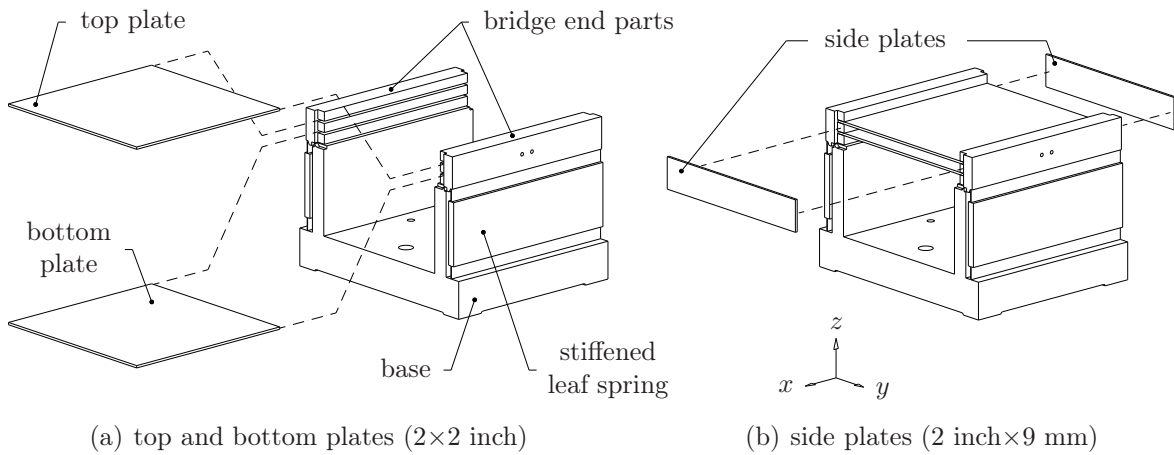


Figure 3.9 / The parallelogram's bridge is assembled from Al_2O_3 plates. The plates are glued before the leaf springs are cut to ensure leaf spring parallelism.

The top and bottom plates are glued into parallel grooves in the bridge end parts (Figure 3.9(a)). The large glue area and the small layer thickness result in a high-stiffness connection between the ceramic plates and the bridge end parts.

The Al_2O_3 plates are glued to the bridge end parts before the leaf springs are machined (wire-EDM) to ensure leaf spring parallelism.

Stops within the parallelogram base, limit the parallelogram's motion to ± 1 mm to protect the parallelogram during fabrication and assembly.

The specific stiffness (E/ρ) of Al_2O_3 is about 3.2 times higher than the specific

stiffness of aluminium [104]. Consequently, using Al_2O_3 instead of aluminium for the parallelogram bridge, results in a lower moving mass for a similar stiffness. Additionally, the magnetic properties of Al_2O_3 allow integration of the actuator coil (Section 4.1) into the parallelogram bridge. This aligns the actuator with the struts and results in a high stiffness in the actuation direction.

The parallelogram's stiffness around the z -axis (Figure 3.9), determines the stiffness against sample table rotations and consequently affects the straight guide eigenfrequency. Increasing the leaf spring thickness increases this rotation stiffness but also leads to a larger unwanted residual stiffness in the motion direction.

The relation between the residual stiffness and the straight guide resonance frequency is estimated with a FEA model (Figure 3.10). Based on this analysis the leaf spring thickness is set to 0.15 mm which results in a 1.4 kHz eigenfrequency and a residual stiffness of 1600 N/m. The first resonance of the parallelogram itself is at about 3.7 kHz (FEA).

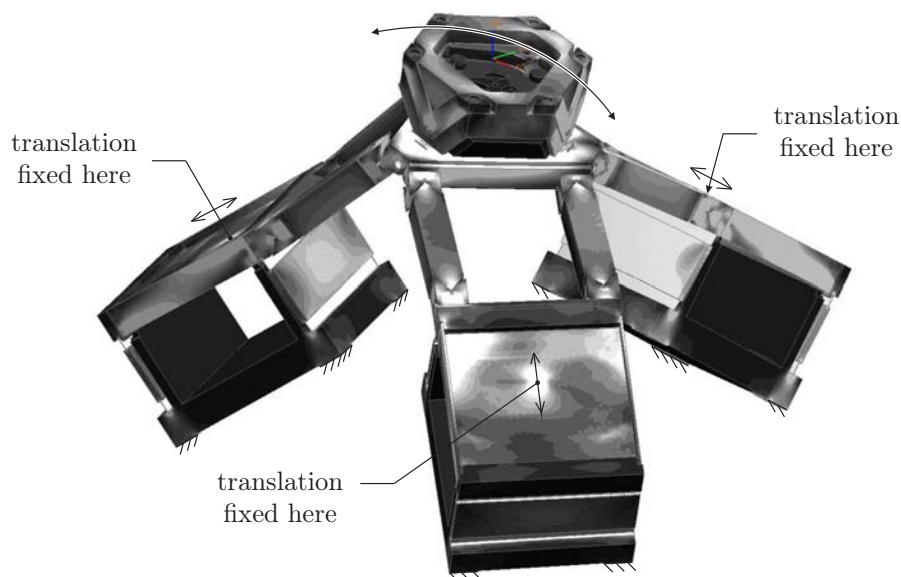


Figure 3.10 / The first straight guide resonance is estimated at 1.4 kHz. The parallelogram bridges are only constrained in the indicated (actuation) direction, the shade represent the stress level. Modes 1 through 10 (1.4 to 3.4 kHz) do not affect the sample table to mirror alignment.

Stiffness measurements on the realized parallelograms, agree to within one percent with the FEA estimated stiffness.

3.4 Sample table rotations

Sample table rotations give an Abbe measurement error when the displacement measurement system axes are not perfectly aligned with the AFM probe position. This Abbe error can be corrected when the sample table rotations are reproducible. Conversely, non-reproducing or random rotations, caused by, for example, actuation forces or temperature gradients, cannot be accurately corrected.

The next section discusses the reproducing rotations. The random rotations are described from Page 40 onward.

Reproducible rotations

There are three sources for reproducible rotations:

- lateral stiffness of the struts leading to moments on the straight guides,
- fabrication tolerances on the straight guide components,
- misalignments during assembly.

The effect of the strut's lateral stiffness is estimated analytically (forces and moments balance) and with (non-linear) FEA. In these estimates, the sample table is moved over ± 1 mm in the parallelogram's translation direction. At these extreme positions, the conservatively estimated rotation is ± 1.2 arcsec. With an estimated (worst-case) Abbe arm of 0.5 mm, this leads to a ± 3 nm systematic measurement error.

The rotations resulting from fabrication tolerances and alignment errors are difficult to estimate (e.g. the estimation is similar to the forward kinematics problem of a Stewart platform [71]) and must therefore be experimentally determined. In this experiment, the sample table rotations are measured at different positions within the instrument's motion range with, for example, an autocollimator. Because the sample table displacement measurement system (described in Chapter 5) was not available at the time of writing, these experiments have not been done.

The reproducing sample table rotations can be calibrated to within ± 0.1 to ± 0.2 arcsec [103]. This calibration reduces the systematic (Abbe) measurement errors to a ± 0.5 nm position measurement uncertainty, which is within the specified nanometer range.

Random rotations

Actuation forces and temperature gradients can lead to random sample table rotations. First the effect of actuation forces is discussed. The influence of temperature gradients is explained on Page 41.

actuation forces

Figure 3.11(a) gives a side view of the straight guide and the sample table. The actuator generates a reaction force F_r on the sample table, this force aligns with the struts. Any misalignment between the line of action A of force F_r and the sample table's COG, leads to a moment and a subsequent rotation of the sample table.

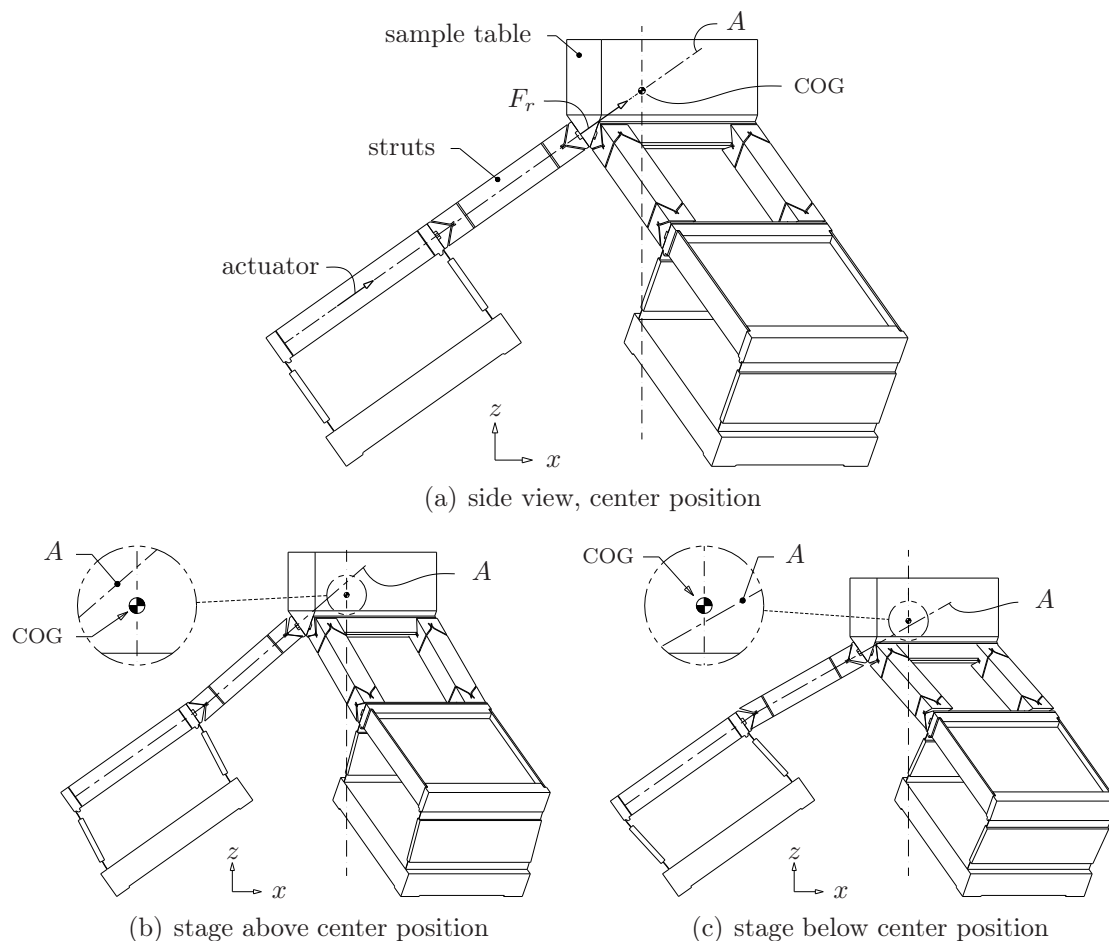


Figure 3.11 / Aligning the actuator's reaction force F_r with the sample table's COG when the stage is in the center position (a), minimizes the sample table rotations. However, the direction of rotation then depends on the position of the stage (b,c). Displacements exaggerated, sample table simplified.

For minimal rotations, the misalignment must be minimal, e.g. the struts align with the sample table's COG when the sample stage is in the nominal or center position (as in Figure 3.11(a)). This, however, results in position dependent behavior. If the sample table moves upwards (Figure 3.11(b)), then the reaction force's line of action A passes above the COG. Conversely, the line of action passes under the sample table's COG when the sample table is below the center position (Figure 3.11(c)). The direction of rotation therefore depends on the sample table position which is unfavorable for the position controller stability [91], i.e. it might induce non-minimum phase behavior.

The rotation direction reversal is prevented by aligning the struts slightly above the sample table's COG when the sample table is in the center position. The rotations resulting from this misalignment are estimated by calculating the sample table's deflection (analytically as well as with FEA) under a moment which is equivalent to the maximum actuator force times maximum misalignment. This maximum estimated rotation is ± 0.3 arcsec, which corresponds to a ± 0.7 nm error with an estimated (worst-case) Abbe arm of 0.5 mm.

Fortunately, the actuator forces are considerably smaller during normal measurements. For example, scanning at $100 \mu\text{m/s}$, which is about five times above the average AFM scanning speed [49], with <100 nm turnaround distances, results in less than ± 0.01 arcsec sample table rotations ($< \pm 0.02$ nm).

Additionally, vertical movements do not result in sample table rotations at all because the required vertical force, which is a combination of three equal actuator forces, aligns with the sample table COG.

temperature gradients

Uniform temperature changes do not lead to sample table rotations. Similarly, a temperature gradient along the instrument's symmetry axis (z axis in Figure 3.11) does not result in a sample table rotation either because the instrument's three parallel guides are equally affected by the temperature gradient. However, a gradient in the horizontal plane (x, y plane in Figure 3.11) can lead to a rotation.

Figure 3.12(a) shows a temperature difference or temperature front passing in the x -direction through the instrument. In the figure, struts B_2 and C_1 are at a different temperature than struts A_1, A_2, B_1 and C_2 . This results in different strut lengths and consequently leads to a sample table rotation in ψ .

Air temperature variations in a metrology laboratory are typically 70 to 80 mK over 150 minutes [99]. Enclosing the measurement set up within a polystyrene box, reduces the air temperature variation to about 12 to 20 mK over a 150 min period. The worst-case, analytically estimated sample table rotation, resulting from a ± 10 mK

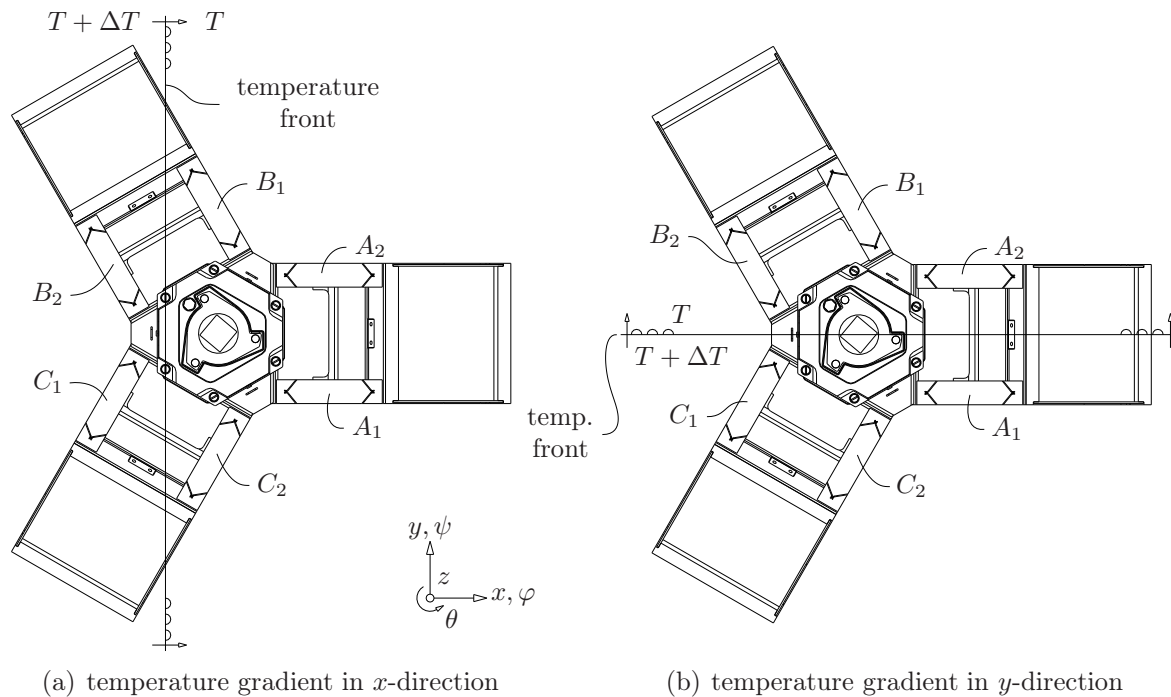


Figure 3.12 / Top view of the instrument. Horizontal (x, y plane) temperature gradients result in sample table rotations. Vertical gradients do not lead to rotations.

temperature change is ± 0.1 arcsec. With an estimated maximum Abbe arm of 0.5 mm, this leads to an acceptable ± 0.2 nm worst-case Abbe error.

If the temperature front passes in the y -direction through the instrument (Figure 3.12(b)), then struts A_1, C_1 and C_2 are at a different temperature than struts A_2, B_1 and B_2 . This leads to a sample table rotation (practically) around the normal of the plane through struts A_1 and A_2 . With a temperature variation of ± 10 mK, this rotation is less than ± 0.05 arcsec.

Table 3.2 summarizes the sample table rotations and the subsequent systematic (Abbe) errors. All errors are within the specified nanometer-range.

	rotation (arcsec)		error (nm)
stiffness	max	± 1.2	$\pm 3.0^a$
	typical	$< \pm 0.01$	$< \pm 0.02$
temperature ^b	max	± 0.1	± 0.2

^awithout calibration, ^b $\Delta T = \pm 10$ mK

Table 3.2 / Summary of the estimated maximum and typical rotations. The subsequent Abbe errors are based on an Abbe arm of 0.5 mm.

3.5 Concluding remarks

The sample table holds the sample and the displacement measurement system's moving target mirror. The sample is fixed to a sample holder, this sample holder, in turn, is kinematically connected to the sample table. The kinematic sample holder allows off-line sample alignment and fast sample loading and thereby minimizes the thermal disturbances on the instrument.

Three A-frames connect the moving target mirror to the sample table frame. The mirror's thermal center of expansion coincides radially and axially with the AFM probe position for minimal sensitivity to uniform temperature changes.

The sample table design is optimized towards maximum eigenfrequency. The sample table's low thermal capacity minimizes the settling time after temperature variations. Six, cross-hinge struts, support the sample table. The struts are fabricated in pairs of two to ensure strut parallelism.

Each pair of two struts connects to a stiffened leaf spring parallelogram. The parallelogram has a ceramic, high-stiffness bridge which holds part of the actuator.

The straight guide's first eigenfrequency is predicted at 1.4 kHz. The estimated, maximum reproducing sample table rotation leads to a worst-case estimated (Abbe) position measurement error of ± 3 nm. After calibration, this systematic error expectedly reduces to a ± 0.5 nm position measurement uncertainty. Similarly, the estimated maximum, random, position measurement errors caused by actuator forces and temperature gradients are ± 0.7 nm and ± 0.2 nm respectively. These errors are well within the specified range.

Figure 3.13 shows the instrument design as discussed in this chapter.

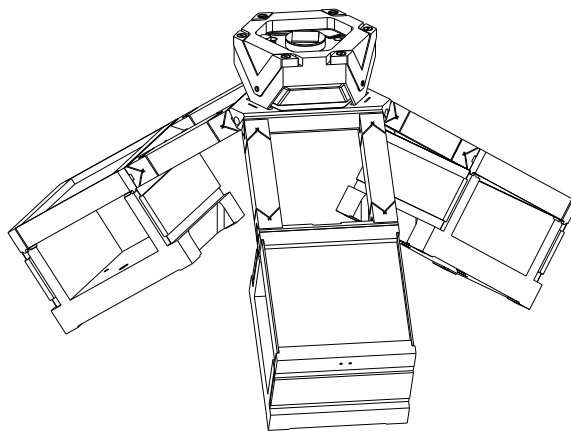


Figure 3.13 / Instrument design as discussed in this chapter.

CHAPTER FOUR

Actuation

Abstract / The actuation system generates the sample's movements relative to the stationary AFM probe. Each of the three identical parallel guides has a Lorentz actuator, a stiffness compensation mechanism and a weight compensation mechanism. The former delivers the sample table acceleration forces, the two compensation mechanisms reduce the actuator's static load for minimal power dissipation in the actuator.

The actuation system uses three identical systems for similar actuation stiffness' in each translation direction. Subsequently, the resonance frequencies seen in each axis are similar and the instrument's overall eigenfrequency is maximized for the given actuation stiffness. Additionally, the identical dynamical behavior simplifies the stage position control. The mechanical and the thermal similarity of the actuators helps to maintain symmetry in the instrument. This symmetry is advantageous for the instrument's thermal stability. Finally, the design and production of three identical actuation systems presents a small economical advantage over the development of different systems.

Section 4.1 discusses the actuator, the compensation mechanisms are explained in Section 4.2. The experimental validation is described in the last section.

4.1 Actuator

Moving the sample within the instrument's cubic millimeter measurement volume, requires an actuator stroke of about two millimeters. Combining this with the nanometer-scale movements necessary for AFM, results in a large required dynamic range. The next section briefly discusses two possible actuator types.

4.1.1 Actuator concept

Most mAFMs with mechanical straight guides (Section 1.3) use linear piezoelectric actuators (PZTs) to generate the sample movements [110]. These actuators commonly consist of several ceramic discs axially stacked together. When the discs are subjected

to a large electrical field, the discs expand or contract. PZTs are fast, mechanically simple, have a relatively high stiffness and are capable of sub-nanometer movements. Conversely, the creep and hysteresis in PZTs complicates the position control. For reliable operation, the PZT's stroke to length ratio is limited to about one part in one thousand (0.1%). Consequently, millimeter range movements with normal, commercial PZTs requires an unpractically large mechanical leverage (e.g. 1:50 to 1:200).

An alternative to the PZT is a Lorentz type electromechanical actuator. A Lorentz actuator uses electrically conducting wires placed within a magnetic field to generate the actuation force. This Lorentz force is proportional to the current passing through the wires, the wire length within the field and the magnetic field strength.

The Lorentz actuator has inherently no hysteresis and no creep so the actuator control is simplified compared to a PZT. Furthermore, its application is not limited to micrometer-range movements, the required two millimeter stroke is easily achievable in direct drive, i.e. without a mechanical lever or ratio. For these reasons a Lorentz type actuator is chosen instead of PZT-drive.

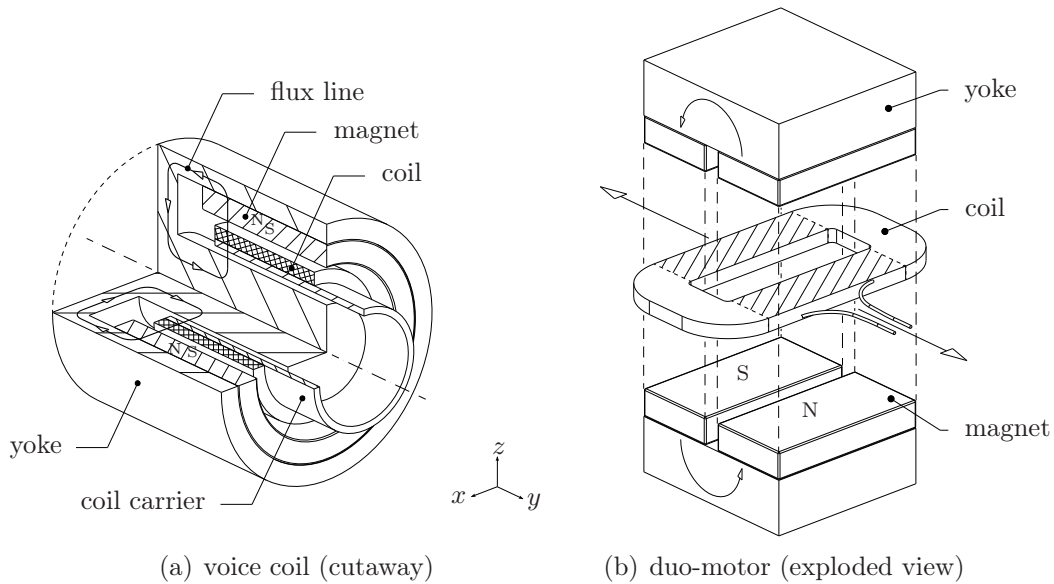


Figure 4.1 / A voice coil and a duo-motor. The voice coil delivers forces in the y direction, the magnetic field in the air gap is radially oriented. The duo-motor's rectangular coil also moves in y direction, its rectangular magnets are stationary. The hatched parts of the duo-motor's coil are in the magnetic field and deliver the force. Figures not to scale.

Figure 4.1(a) shows a voice coil type Lorentz motor. The motor has an axially moving coil placed within a radially oriented magnetic field. A cylindrical permanent magnet creates the field, a soft iron yoke closes the magnetic circuit.

All coil wires are within the actuator's magnetic field, which gives a high efficiency.

The coil's cylindrical shape, however, complicates the actuator integration into the straight guide parallelograms (described in Section 3.3). Another Lorentz motor type, the duo-motor, is better suited for this.

The duo-motor shown in Figure 4.1(b) uses a flat, rectangular coil placed between two yoke and magnet assemblies. Each yoke holds two rectangular magnets with opposing magnetization directions. The magnetic circuit formed by the yokes and the magnets, is perpendicular to the plane of the coil. The coil's two long straight coil sections, generate the actuation force. The two shorter coil sections do not add to the actuation force so their length is minimized.

The actuator linearity depends on the magnetic field variations over the coil's stroke. Extending the magnets beyond the actuator stroke, homogenizes the field and consequently improves the actuator linearity. Alternatively, the linearity increases when the coil extends well beyond the magnetic field but this results in a heavier and less efficient actuator.

The next section discusses how the duo-motor design influences the actuator's efficiency.

duo-motor dimensioning

The actuator coil has N turns of average length l_c (m), each turn has a section l_e (m) within the magnetic field. The Lorentz force F (N) generated by the actuator coil is linearly related to the magnetic flux density B_g (T) in the air gap, the current i (A) through the coil wire as well as the length and the number of wire sections within the field:

$$F = B_g N l_e i \quad (4.1)$$

The actuator's efficiency is expressed through the steepness S (N²/W) [15]. The steepness is defined as the ratio between the squared maximum required actuation force F_{max}^2 (N²) and the corresponding power loss P_{diss} (W) in the coil's resistance R (Ω):

$$S = \frac{F_{max}^2}{P_{diss}} = \frac{(B_g N l_e)^2}{R} \quad (4.2)$$

Introducing the wire material's specific electrical resistance ϱ_w (Ω m) and the wire conducting cross section A_w (m²) gives:

$$\begin{aligned} R &= \varrho_w \frac{l_w}{A_w} = \varrho_w \frac{N l_c}{A_w}, \\ S &= \frac{l_e}{l_c} \left(\frac{V_{w,e}}{\varrho_w} \right) B_g^2 \end{aligned} \quad (4.3)$$

with $V_{w,e}$ (m³) the coil's volume of conducting wire within the air gap. According to Equation (4.3), the actuator's efficiency improves when:

- there is more of the coil's wire within the magnetic field ($l_e = l_c$),
- the volume of conducting wire within the magnetic field increases (largest possible coil within the available air gap, high space factor),
- when the coil wire's specific resistance decreases (e.g. copper wire instead of aluminium wire),
- when the magnetic flux density in the air gap increases.

The magnetic flux density is related to the air gap's area A_g (m²) and the magnetic circuit flux φ (Wb) within the actuator's magnetic circuit (Figure 4.2).

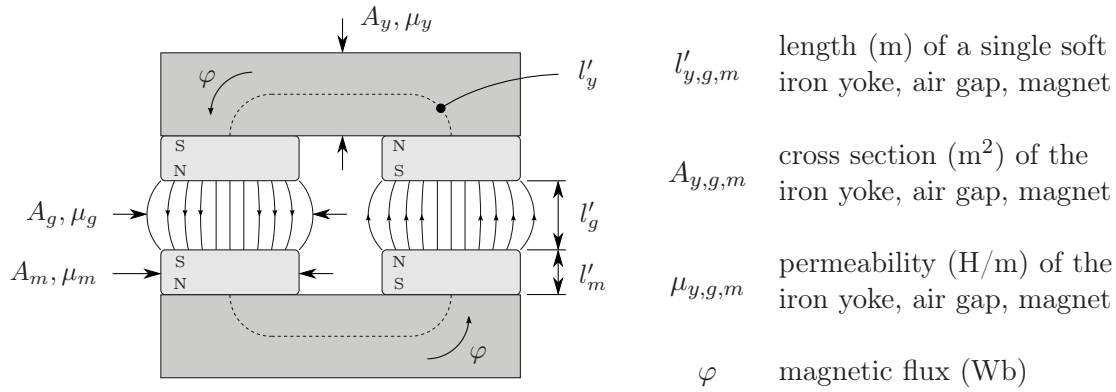


Figure 4.2 / Duo-motor's simplified magnetic circuit. Coil not shown, Figure not to scale.

How much flux flows through the circuit, depends on the magnetic resistance of each component within the circuit and the strength of the magnets. For the closed circuit in Figure 4.2 with samarium-cobalt (SmCo) or neodymium-iron-boron (NdFeB) magnets and no flux leakage, the air gap's average flux density B_g is calculated with the following equations [41]:

$$\oint H dl = 0 \rightarrow H_y l_y + H_g l_g + H_m l_m = 0 \quad (4.4)$$

$$l_y = 2l'_y, \quad l_g = 2l'_g, \quad l_m = 4l'_m$$

$$\varphi = B_g A_g = B_m A_m = B_y A_y \quad (4.5)$$

$$H_g = \frac{B_g}{\mu_g} = \frac{\varphi}{\mu_g A_g}, \quad H_y = \frac{B_y}{\mu_y} = \frac{\varphi}{\mu_y A_y} \quad (4.6)$$

$$H_m = \frac{H_c B_m}{B_r} - H_c = \frac{B_m}{\mu_m} - H_c \quad (4.7)$$

$$B_g = \frac{A_m}{A_g} \frac{H_c \mu_m l_m}{\mu_m A_m \left(\frac{l_y}{\mu_y A_y} + \frac{l_g}{\mu_g A_g} \right) + l_m} \quad (4.8)$$

with

$H_{y,g,m}$	A/m	coercive field strength in yoke, gap and magnet respectively
$A_{y,g,m}$	m ²	area or cross-section
$B_{y,g,m}$	T	flux density
$l_{y,g,m}$	m	total length
$\mu_{y,g,m}$	H/m	magnetic permeability
φ	Wb	circuit flux
B_r	T	magnet's remanence
H_c	A/m	magnet's coercivity

Without flux fringing, the air gap's cross section within a duo-motor is equal to the magnet's cross section. To account for some fringing, the air gap area is (arbitrarily) chosen fifty percent larger than the magnet cross-section. Furthermore, the permeability of the magnets is nearly equal to the air gap's permeability and much smaller than the yoke's permeability. Using these simplifications, Equation (4.8) reduces to:

$$B_g = \mu_{air} H_c \left(\frac{l_m}{l_g + 1.5 l_m} \right) \quad (4.9)$$

$$(\mu_g = \mu_{air}, \quad \mu_m \approx \mu_{air}, \quad \mu_y \gg \mu_{air}, \quad A_g = 1.5 A_m)$$

Using magnets with a high coercivity value helps to increase B_g . This means that NdFeB instead of SmCo magnets should be used.

The equation part between brackets represents the actuator's magnetic circuit geometry. Increasing the magnet length, reducing the air gap length and minimizing fringing all improve the air gap's flux density and thus the actuator efficiency.

The validity of Equation (4.9) is checked by comparing the predicted flux density in the designed duomotor (discussed in the next section) with the results obtained with the magnetic and electrical finite element analysis (FEA) package Ansoft Maxwell®. Equation (4.9) underestimates the magnetic flux density with about 10% (Ansoft: 0.60 T, Equation (4.9): 0.55 T). Conversely, the predicted influence of the magnet length and the air gap length on B_g , correspond well with the FEA estimates. The underestimation is probably caused by the conservative estimate for the flux fringing.

4.1.2 Actuator design

Figure 4.3 gives an exploded view of the Lorentz motor. The following sections describe the coil, the yokes, the magnets and the support frames in more detail.

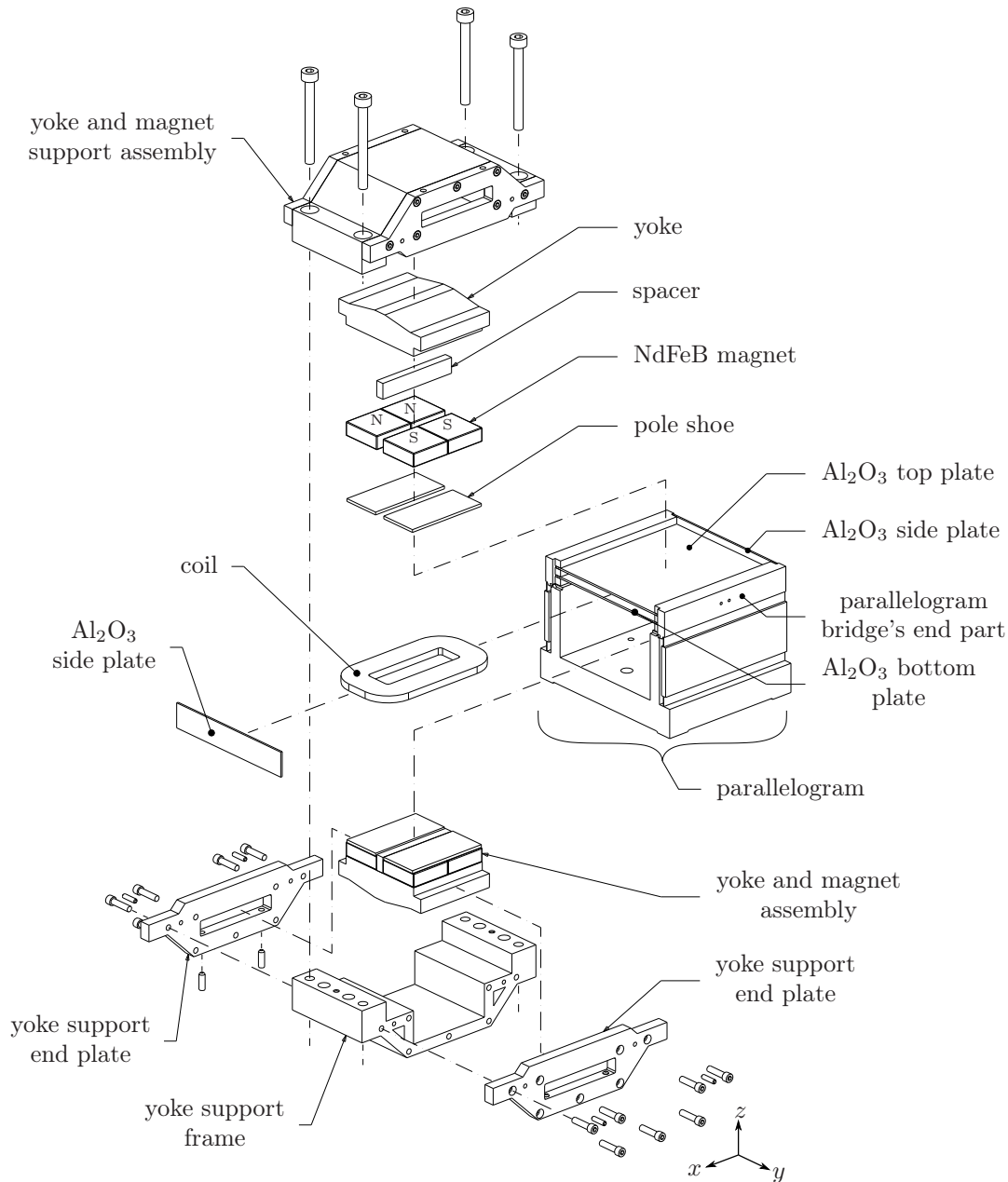


Figure 4.3 / Exploded view of the actuator. The rectangular coil is sandwiched between the parallelogram bridge's Al₂O₃ plates. Two yoke and magnet support assemblies constrain the magnets and yokes to the instrument base.

actuator coil

The actuator coil is sandwiched between the parallelogram bridge's top and bottom Al_2O_3 plate and its plane is aligned with the respective parallel guide struts centerlines for maximum actuation stiffness. The high specific stiffness of Al_2O_3 helps to minimize the parallelogram bridge's mass (Section 3.3 on Page 36). Additionally, the ceramic's insensitivity to magnetic fields prevents eddy currents and unwanted magnetic attraction within the coil support.

The coil is fabricated by orthocyclically winding self-bonding enameled copper wire onto a rectangular mandrel between endplates. After winding, the coil is heated in an oven, this cures the bond between the wires and results in a self supporting coil. The coil is then slid between the two Al_2O_3 plates and its effective wires are aligned parallel to the parallelogram's leaf springs. This aligns the actuation force with the parallelogram's motion direction and subsequently minimizes the unwanted sideways force components on the parallelogram. An epoxy adhesive bonds the coil to the top and bottom Al_2O_3 plates. The large glue areas and the small glue layer thickness, result in a stiff connection.

Both free ends of the coil wire, feed through holes in the parallelogram bridge's end part and connect to a modified IC-socket near the parallelogram's base. Pre-shaped insulation jackets are added to protect the fragile wires.

The coil is designed for a maximum continuous actuation force of about ± 1.25 N at a moderate 3 A/mm^2 [99] and with $B_g \approx 0.55$ T. The relatively low maximum current density gives low losses and allows for (relatively) safe short term actuator overloading. The coil wire diameter is chosen such that the maximum coil current is within the current range of the foreseen analog, linear current amplifier [52]. Table E.1 on Page 155 summarizes the coil properties.

Integrating the actuator coil into the parallelogram, eliminates the need for a separate coil straight guide and therefore minimizes the moving mass, the straight guide stiffness and the instrument complexity. Additionally, the coil stays parallel to the yoke and magnet assemblies (Figure 4.3) during translations so minimal clearance between the coil and the yokes is needed. Minimizing this clearance increases the air gap's magnetic flux density, and subsequently improves the actuator efficiency.

Introducing a heat source directly into the parallelogram's bridge could negatively affect the sample table's rotation suppression. Indeed, if the actuator coil heats up, the Al_2O_3 bridge expands and subsequently reduces the leaf spring parallelism. Translating the parallelogram bridge now leads to a rotation around the x -axis (Figure 4.3). Fortunately, this rotation has, by design, no effect on the sample table orientation.

yokes and magnets

The coil moves in the air gap between the two yoke and magnet assemblies. Each assembly holds four identical, square NdFeB magnets arranged in pairs with opposing magnetization directions. The NdFeB's high coercivity maximizes the magnetic circuit flux and therefore improves the air gap's flux density. A nickel coating protects the magnets against oxidation.

The magnets are sorted to thickness to ensure a constant and parallel air gap. In addition to the attractive magnetic forces between the magnets and the yoke, glue is used to fixate the magnets on the yoke. Table E.1 in Appendix E gives some magnet details.

The nickel-plated, soft iron (Armco®) yoke, guides the magnetic field with minimal magnetic resistance and flux leakage. Containing the magnetic flux within the actuator also reduces the unwanted attraction of magnetic particles and debris onto the actuator. The flux density and flux lines within the yoke are estimated with Ansoft Maxwell®. Based on these analyses, the sections of the yoke that do not contribute to the air gap's flux density are removed to minimize the yoke's weight. With a local maximum of 2.0 T, the flux density is below the soft iron's 2.15 T saturation limit.

Nickel-plated Armco® pole shoes are added to the magnets to homogenize the air gap's magnetic flux field (Figures E.1 and E.2 on Page 156). This reduces the variation in the motor force constant K_f over the actuator's stroke and subsequently simplifies control. Additionally, the pole shoes reduce the effect of the small air gap between the two square magnets in each pair and minimize the influence of inhomogeneities within the magnets. Finally they protect the brittle magnets against chipping.

The pole shoes also result in some magnetic short circuiting between the pole shoes and the yoke and between the pole shoes from the same yoke. This decreases the circuit flux somewhat and increases the flux stray field outside the air gap. The former merely reduces the actuator efficiency slightly, the latter could result in eddy currents with subsequent resistive losses and unwanted Lorentz forces.

Eddy currents exist when the magnetic flux density in an electrically conducting component changes [41]. This flux density variation either originates from a displacement within an inhomogeneous flux field or from a change in the magnetic circuit.

The only moving components near the actuator's inhomogeneous stray field are the parallelogram's ceramic bridge and its bridge end parts (Figure 4.4(a)). Clearly, the Al_2O_3 is unaffected by the field, the aluminium end parts are too far away to be influenced by the stray field.

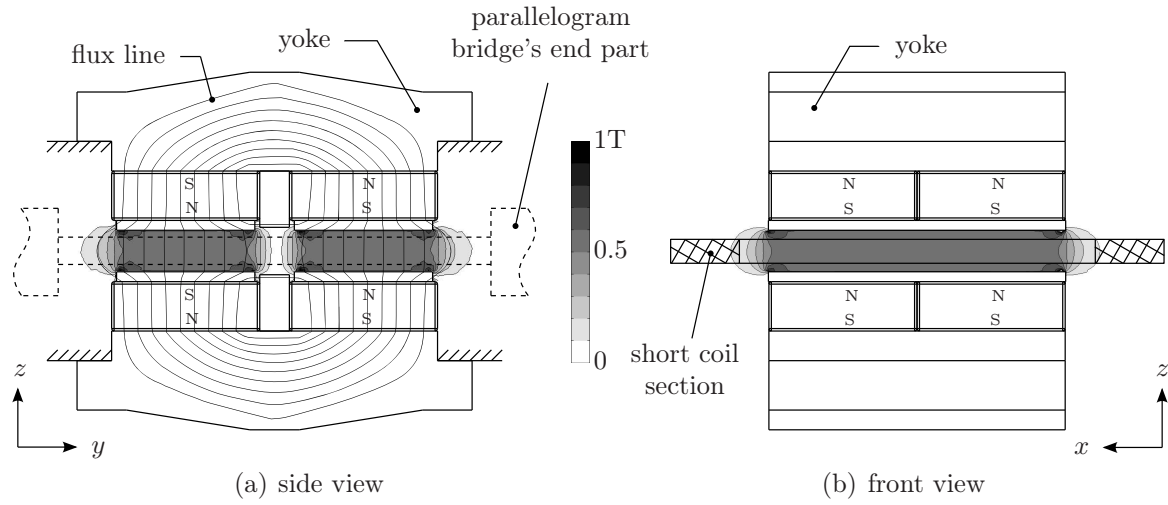


Figure 4.4 / Magnetic field and flux lines in the actuator ($B_g \approx 0.60$ T). The parallelogram bridge's end parts stay clear from the magnetic stray field to prevent eddy current losses. The yoke's shape follows the flux lines for minimal mass.

The stray field perpendicular to the parallelogram's motion direction, generates Lorentz forces in the coil's short sections (Figure 4.4(b)). Because these forces are, at least theoretically, symmetrical and mutually opposing, they have no effect on the parallelogram's straight guide motion.

The current forced through the actuator coil, leads to a self induced flux field around the coil. This field can change the flux density in the actuators' magnetic circuit. Ansoft simulations show that the coil current induced flux only passes through the pole shoes. In the worst case situation the pole shoe's flux density variation is much less than one percent so significant eddy currents are not expected. Furthermore, because the flux density in the yoke is constant, there is no need to use a complex laminated yoke.

yoke and magnet support assembly

The stiffness of the yoke and magnet support assembly affects the overall actuation stiffness. In addition to the actuator's reaction forces (up to ± 1.5 N), the upper and lower magnet assemblies also magnetically attract each other with approximately 120 N.

Each yoke and magnet assembly is supported on lugs protruding from either side of the yoke (Figure 4.4(a)). The lugs mesh with rectangular slots in the aluminium yoke support end plates (Figure 4.3), these end plates screw onto the aluminium yoke support frame. By fastening both yoke support frames together, the mutual magnetic attraction force loop length is minimized (Figure 4.5). For high actuation stiffness both

yoke supports are attached directly to the instrument base, this interface is as close as possible to the actuator coil's midplane to avoid bending moments.

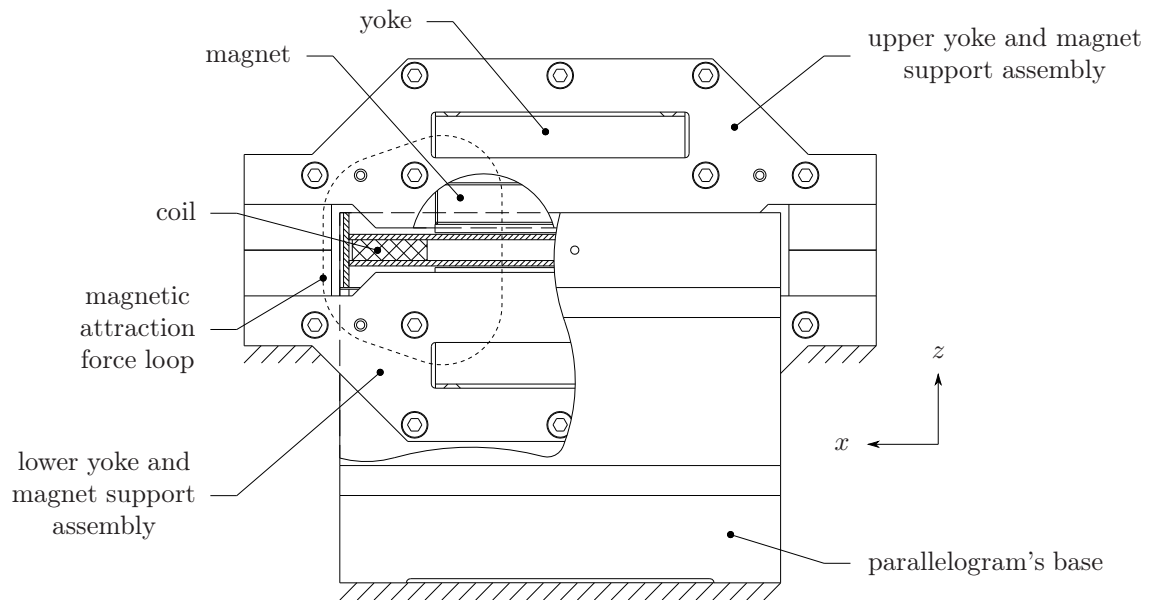
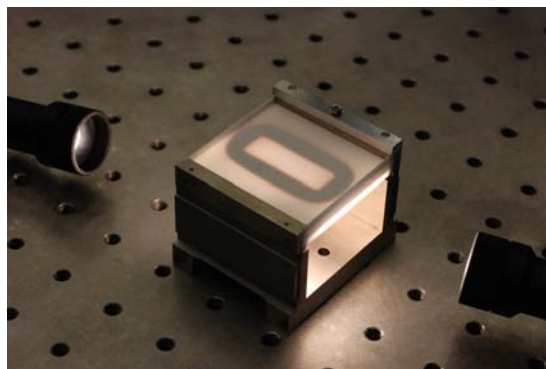
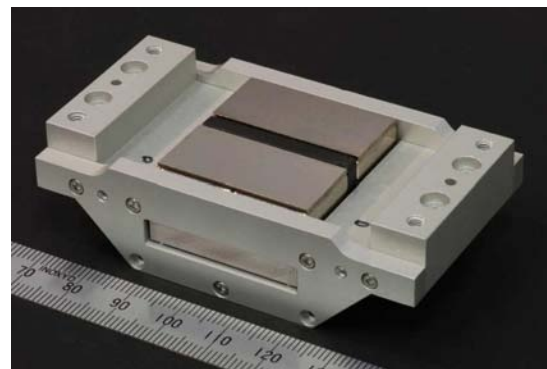


Figure 4.5 / Breakout view along the parallelogram's motion direction. The magnetic attraction force loop is closed over the two yoke and magnet support assemblies. The indicated magnet, the lower yoke and magnet support assembly and the coil are normally hidden by the parallelogram.

Figure 4.6 gives two photographs of the actuator components.



(a) coil inside the parallelogram's bridge



(b) magnets, yoke and support bridge

Figure 4.6 / The actuator coil's outline is just visible through the parallelogram's opaque Al_2O_3 plates (a). Figure (b) shows the lower yoke support with yoke, magnets and pole shoes.

4.1.3 Actuator control

Each actuator is powered by one analog, linear, current amplifier [52]. A digital-to-analog converter (DAC) converts the instrument control system's [100] signal to an amplifier input voltage.

digital-to-analog converter

The DAC resolution determines the actuator's dynamic range. To estimate the required DAC resolution, a one-dimensional dynamic model with a lead/lag feedback controller is made¹. The model simulates the scanning of a typical grating sample for different DAC resolutions and control bandwidths. Figure 4.7 shows the subsequent maximum tracking error for an (over-dimensioned) ± 60 mA amplifier.

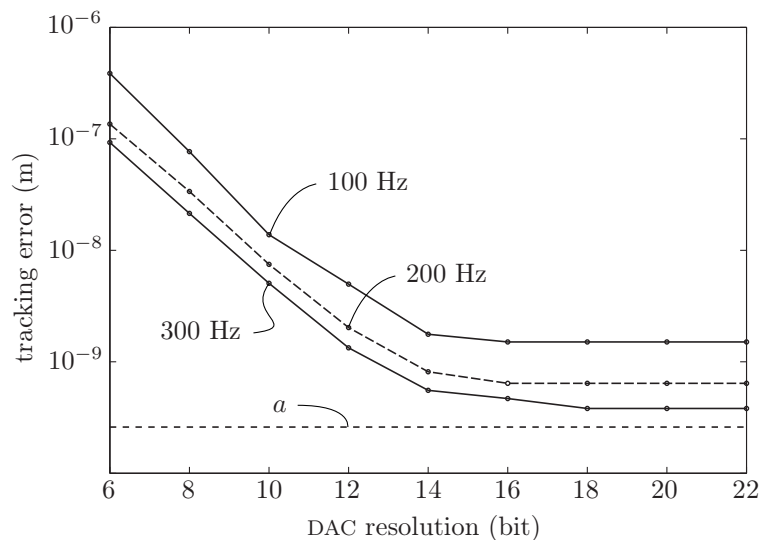


Figure 4.7 / Estimated maximum tracking error during sample scanning as a function of different DAC resolutions and for three control bandwidths. *a*: displacement measurement system resolution (3D, 0.26 nm). Maximum amplifier output current: ± 60 mA. Sample: 200 nm step height, 2 μ m pitch. Scan speed: 10 μ m/s. Sample frequency: 4 kHz.

With the translation stage's first mechanical resonance at approximately 1.4 kHz (Figure 3.10 on Page 38), a control bandwidth of 300 Hz is considered realistic.

Increasing the DAC resolution reduces the tracking error. However, increasing the resolution beyond 18-bit does not further reduce the tracking error.

An 18-bit DAC gives the required sub-nanometer tracking error as well as some safety margin and is therefore chosen.

¹R.J.E. Merry, CST-TU/e

Each of the three 18-bit DACs is assembled from four, commercially available 16-bit DACs. The three 18-bit DACs and the three amplifiers are installed in a closed box of perforated steel which, in turn, is placed within the electronics box (Figure 4.8). The closed, steel box shields the DACs and the amplifiers against electromagnetic interference.

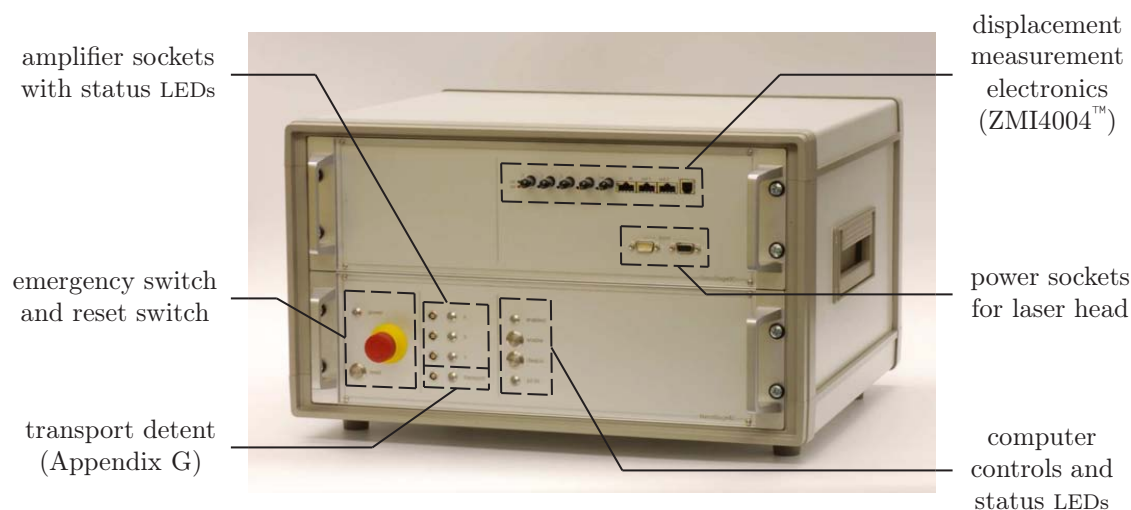


Figure 4.8 / Electronics box with PC/104 control system, amplifiers, DACs and Zygo® ZMI4004™ measurement electronics. The space to the left of the ZMI4004™ is reserved for the AFM head electronics.

The amplifier's measured maximum output current is ± 60 mA, the measured amplifier resolution is 0.46 ± 0.05 μ A [100]. This is the equivalent of 18 bit so the amplifier's resolution is within specification.

instrument control system

A dedicated, PC/104-based control system² [100], operates the actuators and reads out the commercial displacement measurement electronics (Zygo® ZMI4004™, Section 5.5). The control system has several 16-bit analog-to-digital converters (ADCs) to read out the AFM head's position sensitive detector (PSD) and laser power sensor.

The control system is operated through a remote workstation to minimize the heat production within the measurement room. Several safety measures in the control system protect the instrument against, for example, mains voltage failure and (basic) operator-errors.

The control computer is installed in the lower compartment of the electronics box (Figure 4.8). The delicate ZMI4004™ measurement board is in the electronic box' upper compartment for improved electromagnetic shielding.

²R. Solberg, IME Technologies

4.2 Stiffness compensation and weight compensation

The following two sections discuss the stiffness compensation and weight compensation concepts. The last section presents the weight and stiffness compensation mechanism's construction details.

4.2.1 Stiffness compensation

The concept of stiffness compensation or negative stiffness is explained using a simplified one-degree of freedom (DOF) sample stage. This sample stage represents one of the three translation axes of the instrument's three-DOF stage and has a motion stiffness c_s (Figure 4.9(a)).

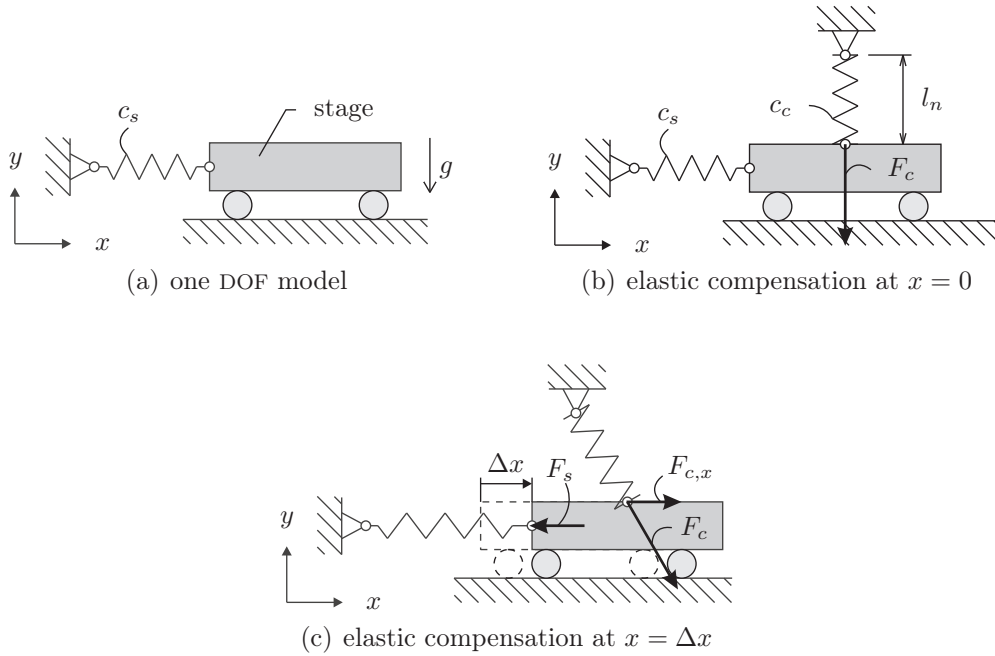


Figure 4.9 / Stiffness compensation of a stage with stiffness c_s . A preloaded compression spring delivers the compensation force $F_{c,x}$ to counteract the stiffness force F_s . Ideally, the total potential energy in the system is constant at all positions.

Moving the stage away from its nominal position requires a force to overcome the stage's stiffness c_s , the work done by this force is stored as elastic energy in the stiffness. Normally a stage actuator delivers this work but only at the cost of power dissipation within the actuator.

Conversely, a stiffness compensation mechanism uses energy stored in an additional spring to deliver the required work. The energy is transferred from the additional spring to the stage's stiffness and the other way round with minimal losses. The

maximum static actuator force is considerably reduced and with it the actuator's dissipation and subsequent heat production.

Figure 4.9(b) shows a preloaded compression spring c_c arranged perpendicular to the stage's motion direction. At the center position, the preload force F_c is exactly perpendicular to the motion direction so no driving force is exerted on the stage. As the stage now moves away from the center in either direction, as shown in Figure 4.9(c), the preload force rotates and generates a force component $F_{c,x}$ parallel to the motion direction and away from the center position. This force component increases with increasing displacement and therefore behaves as a negative stiffness.

The preloaded compression spring can also be replaced by a buckled leaf spring. Both spring types allow stiffness compensation of 98 to 99% [32, 93, 99]. However, the buckled leaf spring is, in practice, less easily tuned towards the required degree of compensation and is larger in size than the preloaded compression spring compensation for a similar compensation level so a preloaded compression spring is used instead.

The next section discusses how the elastic stiffness compensation mechanism of Figure 4.9(b) can be dimensioned.

elastic stiffness compensation: dimensioning

The elastic compensation mechanism is designed for a stage with known stiffness c_s (N/m) and stroke $\pm x_s$ (m). In addition to being sufficiently low, the effective residual stiffness $c_r(x)$ (N/m) must be zero or slightly positive over the stage's full stroke to prevent local open-loop instabilities.

The compensation mechanism's force and stiffness characteristics are calculated using the system's energy balance. These relations are then used to estimate the compensation spring's required stiffness, its nominal length and the preload force for a given degree of compensation.

The residual force needed to keep the stage at position x (m) after the compensation mechanism is set up and adjusted, equals $F_r(x)$ (N). Moving the stage from the center position ($x = 0$) to position x requires work from force $F_r(x)$, this work is stored as elastic energy in the stage's stiffness and in the compression spring. With $E_s(x)$ (J) and $E_c(x)$ (J) the elastic energy stored in the stage and the compression spring respectively, the balance becomes:

$$W_r(x) = \int_0^x F_r(x) dx = E_s(x) + E_c(x) \quad (4.10)$$

The force $F_r(x)$ and the momentary residual stiffness $c_r(x)$ (N/m) can be calculated by differentiating Equation (4.10):

$$F_r(x) = \frac{d}{dx} (E_s(x) + E_c(x)) \quad (4.11)$$

$$c_r(x) = \frac{dF_r(x)}{dx} = \frac{d^2}{dx^2} (E_s(x) + E_c(x)) \quad (4.12)$$

Considering the stage stiffness c_s and compression spring stiffness c_c constant, gives:

$$E_s(x) = \frac{1}{2} c_s x^2, \quad (4.13)$$

$$E_c(x) = \frac{1}{2} c_c (\Delta l)^2, \quad \Delta l = l_o - l(x) = l_o - \sqrt{x^2 + l_n^2} \quad (4.14)$$

with l_o (m) the spring's free length, l_n the nominal length indicated in Figure 4.9(b) and $l(x)$ the momentary length ($l_n \leq l(x) \leq l_o$).

With a positive effective stiffness, the largest force after compensation is needed at the stage's end position ($x = \pm x_s$). This force is specified as a fraction a of the maximum force without compensation:

$$F_r(x = \pm x_s) = \pm a c_s x_s = \pm \left(c_s - c_c \frac{l_o - \sqrt{x_s^2 + l_n^2}}{\sqrt{x_s^2 + l_n^2}} \right) x_s \quad (0 \leq a \leq 1) \quad (4.15)$$

Additionally, the stiffness at the center position must be zero or positive for open-loop stability. Defining the effective stiffness at the center position as a fraction b of the stage's uncompensated stiffness c_s gives:

$$c_r(x = 0) = b c_s = c_s - \left(\frac{l_o - l_n}{l_n} \right) c_c \quad (0 \leq b < a) \quad (4.16)$$

Fraction b must be equal or larger than zero for stability. A b value larger than a implies maximum negative stiffness at $x = \pm x_s$ instead of at the center position. As this is physically not possible with the compensation mechanism of Figure 4.9(b), b must be smaller than a .

An additional equation is needed to solve the spring properties towards the required compensation level and midpoint stiffness. This third equation links the required elastic energy to practical spring dimensions by introducing a limit to the spring's compression. A normal coil spring cannot be compressed beyond about 70% of its free length without significantly reducing its expected lifetime, therefore:

$$\frac{l_n}{l_o} = r \quad (r \geq 0.7) \quad (4.17)$$

Substituting Equation (4.17) in (4.16) and solving for c_c gives the required compensation spring stiffness. Solving Equation (4.15) for l_n gives the nominal length, combination

with Equation (4.17) gives the spring's free length. The equations below summarize the result.

$$c_c = \left(\frac{1-b}{1-r} \right) r c_s \quad (4.18)$$

$$l_n = x_s \sqrt{\frac{((1-a)c_s + c_c)^2}{((1-b)c_s + c_c)^2 - ((1-a)c_s + c_c)^2}} \quad (4.19)$$

$$l_o = \frac{l_n}{r} \quad (4.20)$$

The calculations above are based on the elastic energy in the mechanism and estimate the required spring dimensions for a given degree of compensation and midpoint stiffness. Subsequently, the resulting compression spring force is based only on the required compensation.

The compression spring's horizontal force component counteracts the stage's stiffness c_s . Conversely, the compression spring's vertical force component merely stresses the stage and its straight guide.

Ideally, the ratio between the horizontal and vertical force component is as large as possible. The vertical component F_v (N) and the horizontal component F_h (N) are given by:

$$\begin{aligned} F_v &= c_c \Delta l \cos \alpha \\ F_h &= c_c \Delta l \sin \alpha \\ \frac{F_h}{F_v} &= \tan \alpha = \frac{x}{l_n} \end{aligned}$$

with α the angle between the compression spring and the vertical and Δl the compression spring's momentary length change (Equation 4.14). Clearly, reducing the nominal length l_n reduces the vertical load for a required horizontal compensation force.

A compression spring with the properties according to Equations (4.18) to (4.20) can be added to each of the instrument's three straight guide parallelograms (Section 3.3). Integrating the spring with the already available parallelogram minimizes the number of extra components needed for the compensation mechanism. Additionally, any spring force component perpendicular to the parallelogram's motion direction is directly diverted towards the instrument base by the parallelogram and subsequently has minimal influence on the sample stage's position.

Combining the sample stage's residual stiffness with the required compensation ($a < 0.05, b \approx a$) leads to a considerable compression spring load on the parallelogram, even with the shortest possible spring. This load significantly reduces when the compression spring is replaced by a mechanism similar to Figure 4.10(a).

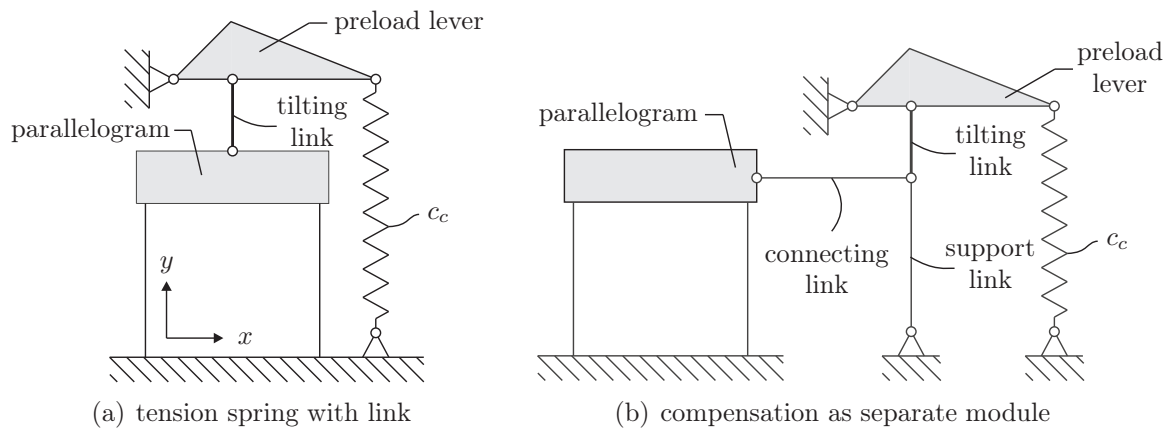


Figure 4.10 / Stiffness compensation as a separate mechanism. In the left figure, the preload force acts directly on the parallelogram. Separating the stiffness compensation from the parallelogram eliminates this load (b). Figure not to scale.

The mechanism has a rigid tilting link, a tension spring and a pivoting preload lever. The tilting link converts the tension spring's vertical force into an effective horizontal compensation force. Because the tilting link's length is not limited by any spring compression limit, it can be kept short for a high horizontal to vertical force ratio.

Although the mechanism is more complex, it introduces little extra moving mass because the pivoting preload lever and tension spring move over only a fraction of the parallelogram's stroke. Furthermore, the tension spring is easier to connect with low hysteresis than the compression spring, and has no tendency to buckle. The latter simplifies the spring preload adjuster.

Converting the schematic two-dimensional mechanism of Figure 4.10(a) into a real-world, three-dimensional mechanism, introduces the risk of overconstraining the parallelogram with the rigid tilting link. This overconstraining deteriorates the parallelogram's straight guide motion. Additionally, the space needed for the mechanism is already taken by the actuator (Section 4.1.2)

Both concerns are remedied by combining the tilting link, preload lever and tension spring into a separate module (Figure 4.10(b)). The tension spring and the preload lever push the tilting link onto an extra support link. A connecting link attaches the support link to the now stress-free parallelogram.

Connecting the mechanism to the parallelogram's bridge, aligns the compensation force with the actuator and the struts. This ensures high stiffness in the actuation direction. Both the parallelogram and the support link deflect vertically while translating horizontally. Matching these vertical movements keeps the connecting link exactly

parallel to the parallelogram's bridge and therefore to the motion direction. Consequently, the compensation force has no vertical component acting on the parallelogram. Additionally, the hinge which connects the link to the parallelogram does not rotate and therefore exerts no bending moment on the parallelogram's bridge. Inevitably, the mechanism adds some stiffness and mass to the actuation direction, but due to the geometry, the influence is very small.

In the next section, weight compensation is added to the stiffness compensation mechanism.

4.2.2 Weight compensation

Preventing gravity from pulling the sample table and the parallelograms downward, requires a constant upward compensation force. This weight compensation force can work directly on the sample table. Alternatively, three smaller, mutually perpendicular, forces which each act directly on one of the three parallelograms, can together also generate one single, upward compensation force.

The sample table's three-dimensional movements make it difficult to apply the compensation force directly on the sample table without introducing unwanted moments or horizontal forces. Conversely, any misalignment between the three smaller compensation forces and the parallelograms, affects the sample table position only indirectly. This makes weight compensation through the three parallelograms the more practical option.

The three Lorentz actuators already integrated into the parallelograms can easily generate the required compensation forces. Using the actuators is mechanically simple but results in unwanted heat production through power losses within the actuator.

An alternative is adding a preloaded spring to each parallelogram to generate the weight compensation force. This concept is simple and introduces little hysteresis and moving mass but has a few drawbacks. Firstly, the weight compensation force varies when the parallelograms translate. Secondly, the springs also adds some stiffness to the actuation direction. The variations in compensation force increase the actuator load, the higher actuation stiffness requires either a larger actuation force or an increase in stiffness compensation.

Lowering the weight compensation spring stiffness reduces the spring force variation over the parallelogram's stroke, and results in less additional stiffness in the actuation direction. Unfortunately, lowering the stiffness also reduces the spring's eigenfrequency and increases its stretched length. This makes the spring susceptible to slinky mode

vibrations and complicates the integration into the instrument.

Conversely, a much stiffer spring combined to a lever (Figure 4.11) can also generate a nearly constant weight compensation force.

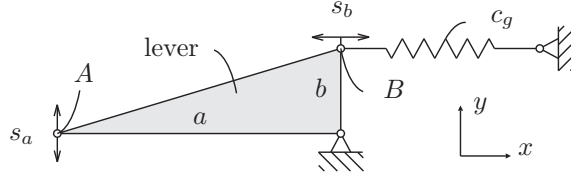


Figure 4.11 / The lever reduces the effective spring stiffness at point A.

The parallelogram connects to point A, the weight compensation spring to point B. The lever reduces the spring's motion s_b to a fraction of the parallelogram's motion s_a . The spring's effective stiffness $c_{g,a}$ at the parallelogram end of the lever reduces to:

$$c_{g,a} = c_g \left(\frac{b}{a} \right)^2 = \frac{c_g}{i^2}, \quad i \gg 1$$

Compared to the compensation spring without lever, the levered compensation spring can be i^2 times stiffer for a similar compensation force variation. This higher spring stiffness improves the spring's dynamics. The ratio can reduce the compensation force variation to less than is practically possible without the lever.

The lever and its support add some mass and stiffness to the sample stage. This added mass and stiffness is minimal when the lever is integrated into the already available stiffness compensation's support link (Figure 4.12(a) on the next page).

Each parallel guide needs one stiffness compensation mechanism and one weight compensation mechanism. Placing the mechanisms between the parallelograms and the instrument's centerline, results in a compact instrument.

Unfortunately, the mechanism of Figure 4.12(a) is horizontally too large to fit between the parallelogram and the instrument's center line. Adding a rocker and orienting the compensation mechanism vertically (Figure 4.12(b)), reduces the size just enough to make the mechanism fit in the available space. All weight compensation springs and stiffness compensation springs are now parallel, this simplifies the instrument base design and makes the spring preload adjustment more practical.

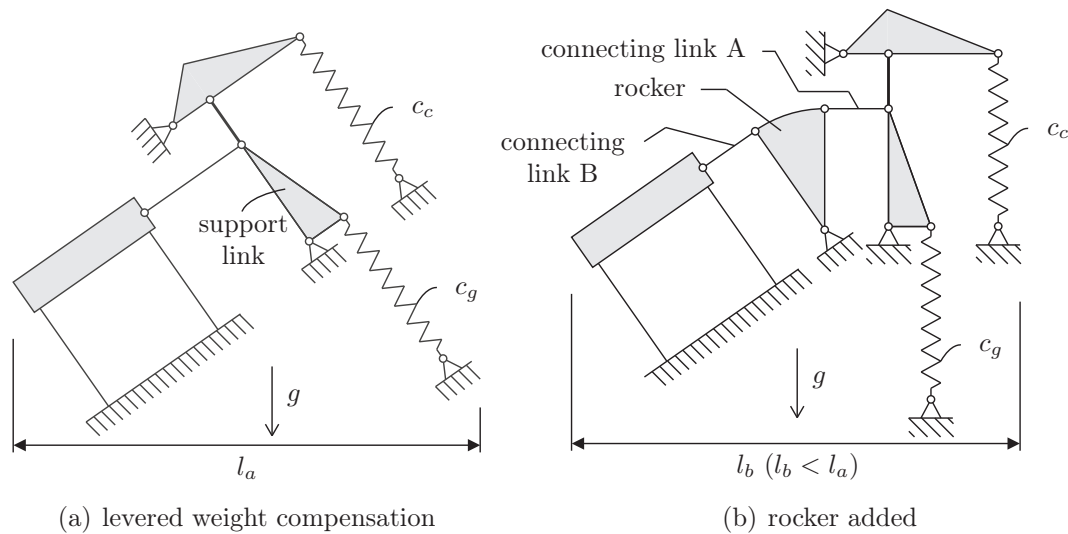


Figure 4.12 / The spring c_g generates the weight compensation force, the stiffness compensation's (modified) support link connects the spring via a 1:10 ratio to the parallelogram. Adding a rocker between the mechanism and the parallelogram reduces the horizontal length $l_{a,b}$ ($l_b < l_a$) for easier integration into the instrument.

compensation characteristic

The compensation characteristic of the mechanism in Figure 4.12(b) is analytically predicted (Figure 4.13). The stiffness of the parallelogram, compensation mechanism and connecting links, straight guide struts and both compensation springs are included in the estimate. The tilting link length, the preload lever length, the support link length etc, correspond with the design discussed in Section 4.2.3.

Curve 2 in Figure 4.13 gives the residual force-displacement for a lightly preloaded stiffness compensation spring. Increasing the spring preload (3), reduces the residual force. Further increasing the preload (4) gives too much compensation and leads to overall negative stiffness.

Comparing line 3 with a hypothetical symmetric residual force characteristic (5), shows a difference in the mechanism's maximum residual force at the positive and the negative end of the stroke. This asymmetry results from the asymmetry in the compensation mechanism's kinematics (Figure 4.14). The tilting link rotates in both directions from the center position as the parallelogram moves from one end to the other. Conversely, the preload lever rotates to one side only. This leads to different angles between the preload lever and the tilting link at the mechanism's end positions and thus gives some asymmetry in the residual force characteristic.

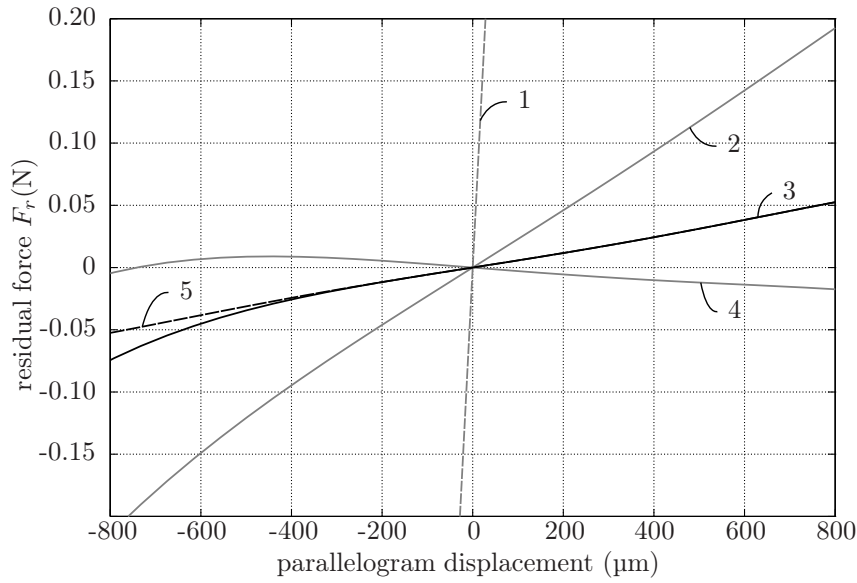


Figure 4.13 / Force-displacement curves for different spring preload settings. Starting without compensation (1) the preload is increased (2). A further increase (3) reduces the stiffness but at some point the stiffness becomes negative (4). Line (5) shows a symmetric compensation characteristic.

Because the compensation characteristic is reproducible, it is, when necessary, possible to electronically correct for the asymmetry with a position-dependent actuator gain.

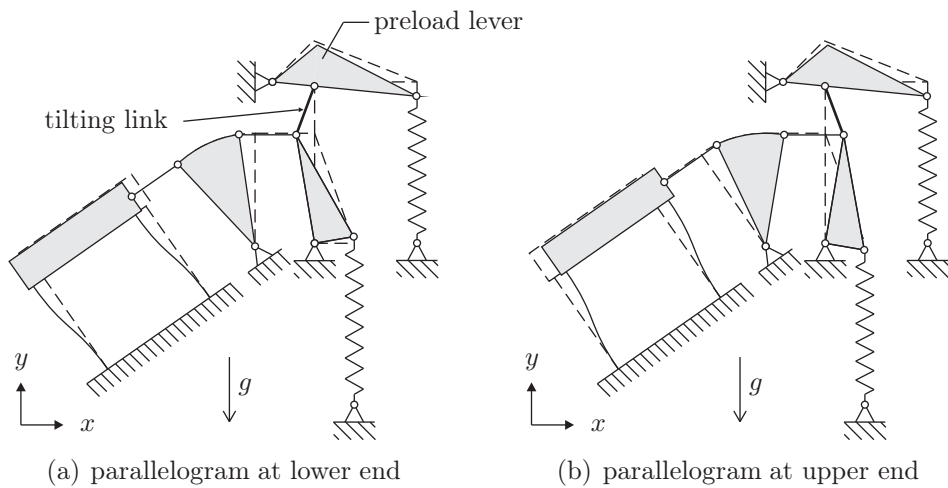


Figure 4.14 / Compensation mechanism asymmetry. The maximum angle between the preload lever and the tilting link differs for the parallelogram's lower and the upper end positions. This difference gives an asymmetric compensation force characteristic. Figure not to scale, motion exaggerated.

4.2.3 Design

Figure 4.15(a) gives a side view of the stiffness compensation and weight compensation mechanism without the rocker and connecting links attached. The mechanism's kinematics are identical to the schematic mechanism of Figure 4.14 although the stiffness compensation spring is now at the other side of the tilting link for a more compact and stiffer mechanism.

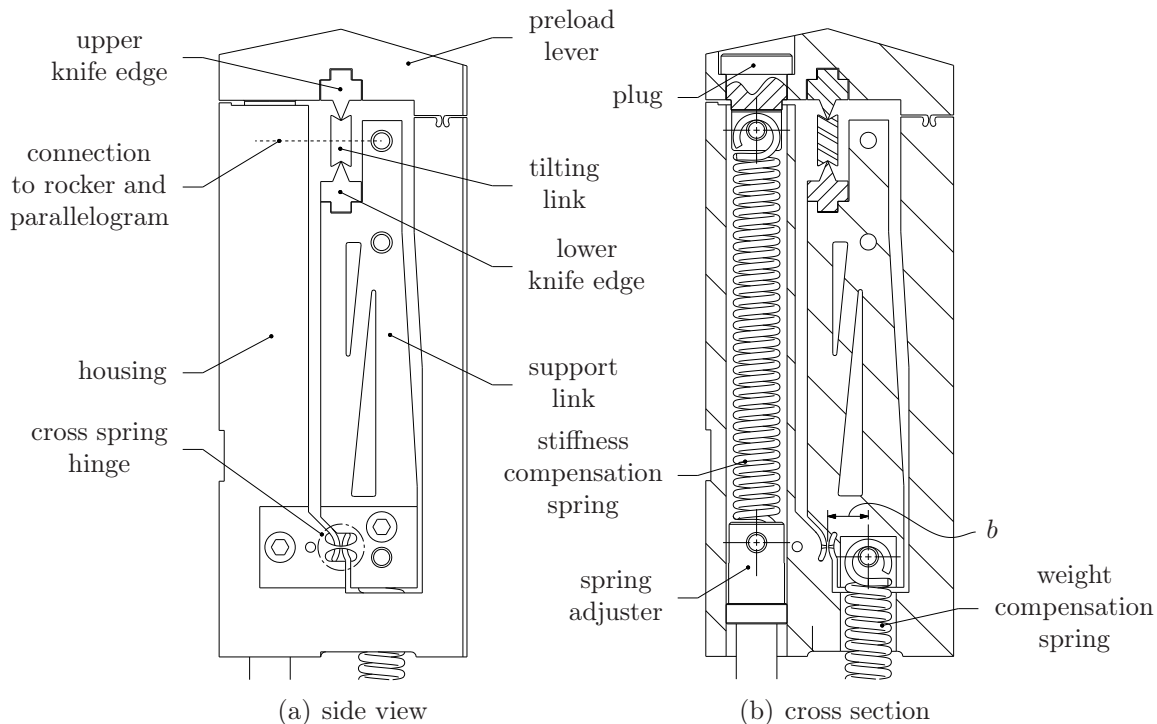


Figure 4.15 / Stiffness compensation and weight compensation mechanism without rocker and both connecting links.

The compensation mechanism's housing encloses the stiffness compensation spring and the weight compensation spring for minimal influence of acoustic vibrations and draught (Figure 4.15(b)). Similarly, the lower part of the weight compensation spring is enclosed by the compensation assembly base (explained later).

The small offset b in Figure 4.15(b) between the weight compensation spring and the support link's hinge, results in a one-in-ten ratio between the weight compensation spring's movement and the parallelogram's movement. Consequently, only one percent (Section 4.2.2) of the weight compensation spring's 1780 N/m stiffness is added to the parallelogram's 1600 N/m motion stiffness. Furthermore, the small movements of the weight compensation spring result in a nearly constant weight compensation force, e.g. the force variation is less than $\pm 1\%$.

The support link and preload lever have elastic hinges. Conversely, the tilting link uses knife edge bearings because its $\approx \pm 15^\circ$ rotations are too large for elastic hinges. The knife edges and the tilting link are made from a much harder and stronger material than the mechanism's aluminium.

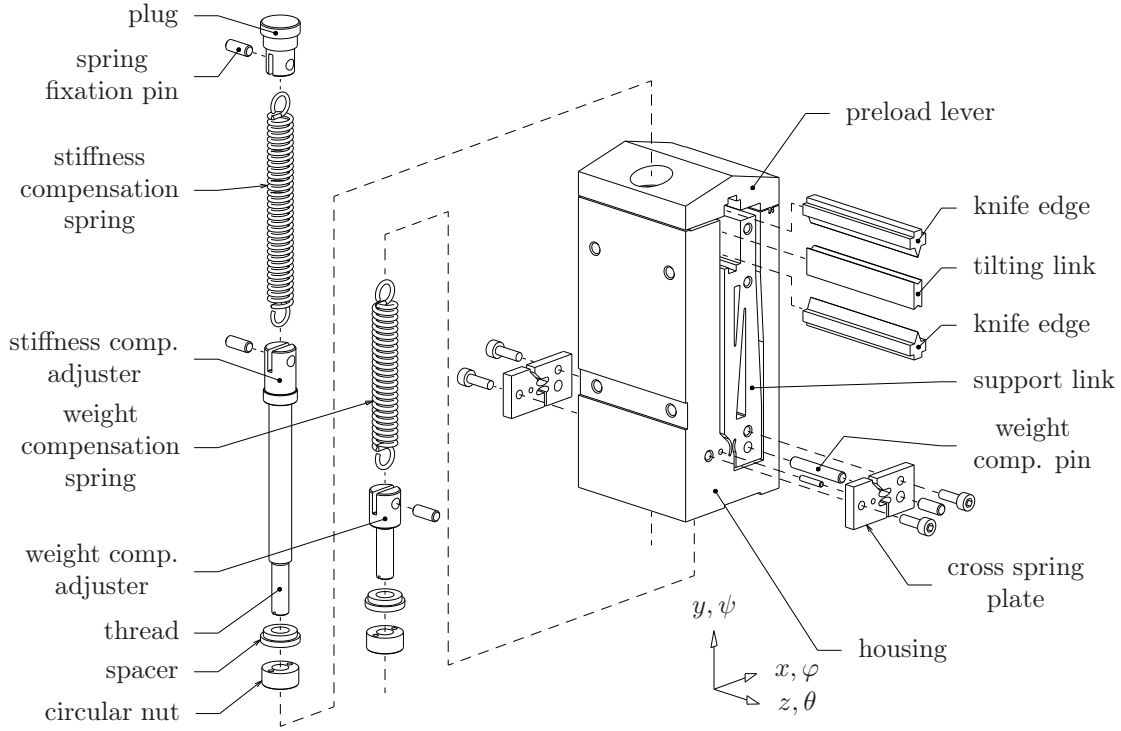


Figure 4.16 / Exploded view of the compensation module. The housing measures $25 \times 26 \times 62$ mm.

Figure 4.16 gives an exploded view of the compensation mechanism. The support link hinge and preload lever hinge are machined directly into the mechanism's housing with wire-EDM. Stops in the housing limit the support link's motion to ± 1.2 mm.

Two cross spring plates constrain the support link's ψ rotation and prevent the support link's hinge from buckling. Each cross spring plate is positioned on two precision pins. Stress-free assembly is possible by drilling the holes in the spring plates and housing in one fixture before creating the hinge.

The spring loops of both compensation springs mesh with symmetrically supported, steel pins (Figure 4.16). The fixations comply with the pivot rule [93] for minimal hysteresis. Additionally, the rotation in the contacts is minimized by making the contact-to-hinge lines (line A-B in Figure 4.17 for the stiffness compensation spring) perpendicular to the spring centerlines.

The frame ends of both springs are adjustable over a small distance to fine-tune the

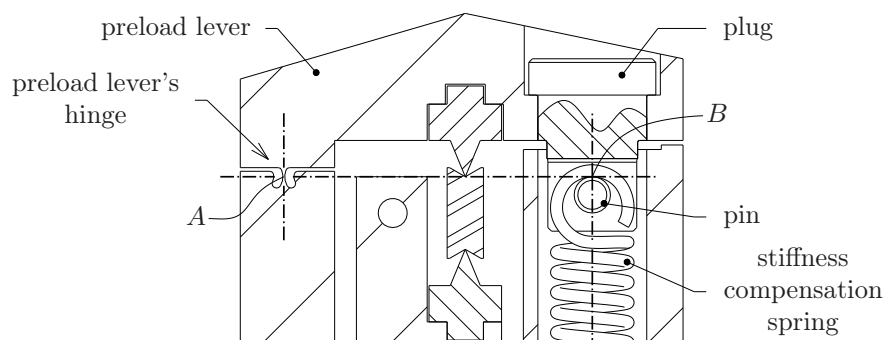


Figure 4.17 / Stiffness compensation spring fixation. The line $A - B$ is perpendicular to the spring's centerline for minimal rotation in the spring-to-pin contact. The weight compensation spring fixation is similar.

spring preload forces. Each spring attaches to its respective adjuster, these adjusters feed through holes in the compensation assembly base (explained later) and are secured by a spacer and finely-threaded circular nut at the hole's other end.

The spacer centers the adjuster and the spring in their bore to prevent contact and subsequent friction between the spring and the hole's wall.

The adjuster's range is too small to stretch the spring from its free length to its nominal length. To get the spring stretched to within the adjuster's range, a threaded rod is temporarily inserted into the concentric hole in the adjuster's lower end face. This rod is then pulled downwards to make the adjuster extend enough beyond its hole to start the circular nut.

Rotating the circular nut changes the adjuster's axial position and therefore the spring preload force. A spade-like tool meshes with slots in the adjuster's lower end face to prevent the spring from twisting during adjustment. Small spots of glue secure each nut against rotation after adjustment.

knife edge bearings

Knife edge bearings are very suitable for limited rotations with extremely low motion losses [85] and are common in high-accuracy mechanical scales. Figure 4.18(a) gives a view detail of the tilting link's upper knife-edge bearing. The knife attaches directly to the preload lever and interfaces with the tilting link's cushion. The preload lever delivers the compressive stiffness compensation force F_c to the tilting link.

The losses in the bearing are minimal when the cushion rolls over the knife's edge without slip [85] (Figure 4.18(b)). This rolling is only possible when the compensation force's tangential component F_t is smaller than the friction μF_n within

the contact. Both components start to slip when the tangential force exceeds the friction force, this slip damages the knife's edge and changes the mechanism's geometry and therefore limits the bearing's maximum rotation angle.

How much the bearing can rotate before it starts to slip, depends on the friction coefficient, the knife-edge radius, the cushion radius and the bearing's configuration. For example, the configuration in Figure 4.18(a) complies with the pivot rule [93] and can rotate up to $\approx \pm 50^\circ$ without slipping. Conversely, in the configuration of Figure 4.18(c) slip occurs at an unpractically low $\approx \pm 6^\circ$ angle.

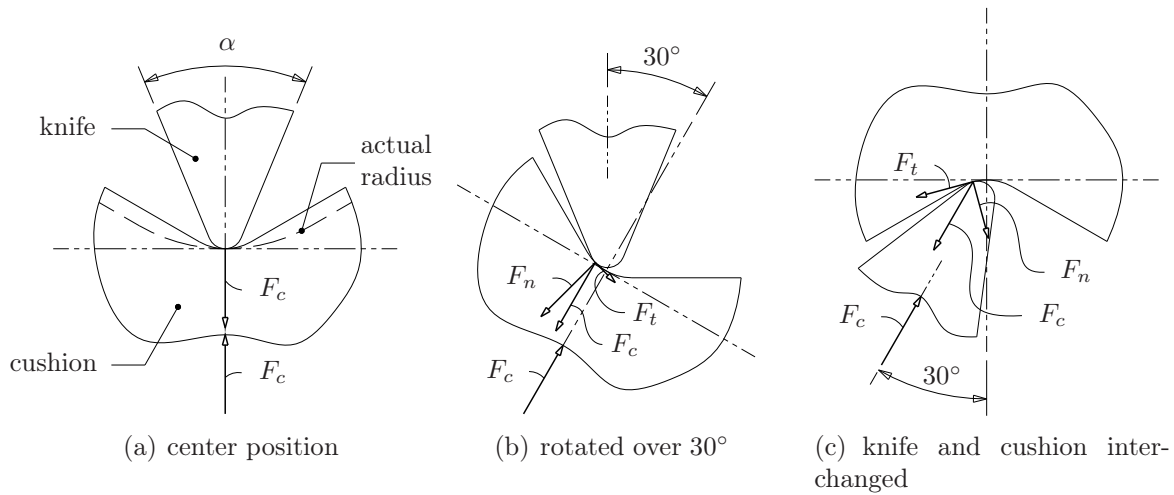


Figure 4.18 / View detail of the tilting link's upper knife-edge bearing. The cushion's radius and the bearing angle are exaggerated for clarity. In the contact (b), the compensation force F_c decomposes in a normal force F_n and tangent force F_t . Rolling is possible as long as $F_t < \mu F_n$. At what angle the components start to slip depends also on the configuration (c).

Material hysteresis and micro-slip cause rolling resistance within the knife-edge bearing [53]. These losses are minimal when the knife's radius is as small as possible [85]. A consequence of a very sharp knife is the high maximum Hertzian stress within the contact. To withstand this high stress, a hard material with a high compressive yield strength is necessary for both the knife and the cushion.

Knives are typically made from either ceramics like sapphire (Al_2O_3) and silicon carbide (SiC) or from metals like high-carbon steel and tool steel. A metal knife can be considerably narrower than a ceramic knife; the knife's angle α defined in Figure 4.18(a) is between 30° to 90° for metals and about 60° to 120° for ceramics.

The large required rotation angle ($\approx \pm 15^\circ$) makes a wider ceramic knife less practical than a narrower steel knife. Additionally, a steel knife gives more freedom in designing the knife's support on the preload lever as it is better machineable. Finally, there is

less difference in the coefficient of thermal expansion (CTE) between a steel knife and the aluminium compensation's housing than there is between any ceramic and the aluminium.

The knife must always be softer than the cushion to prevent the knife from damaging the cushion's surface. If the knife is harder, it digs into the cushion's surface, resulting in a groove with a radius similar to the knife's edge. This groove makes rolling impossible.

A bonus of having a relatively hard cushion is the simplified fabrication procedure for the knife. Instead of machining the knife's edge directly to the required micrometer-range radius, which is difficult and therefore costly, the knife is made as sharp as possible. Afterwards, the knife is placed on the cushion and pivoted back and forth under normal preload. The knife's sharp edge deforms into a cylinder with just enough radius to keep the Hertzian stresses at or below the yield stress. This gives the smallest possible edge radius and ensures contact along the knife's full length. Because the knife and cushion are now made to fit, they must be kept together and properly oriented.

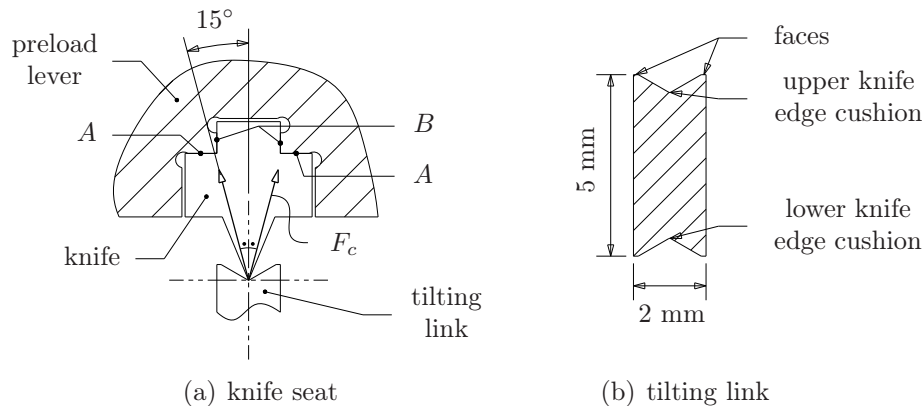


Figure 4.19 / View detail of the upper knife edge seat and tilting link. The compensation force F_c stays between the knife's support surfaces A . Horizontal alignment is through a precision fit, glue permanently fixates the knife to the preload lever.

The knife edge (Figure 4.19(a)) meshes with two horizontal surfaces A on the preload lever. The rotating compensation force acting on the knife's edge, stays between these horizontal faces A , this keeps both faces compression loaded and minimizes the knife edge bending. Two vertical faces B , machined in the same set-up as the two horizontal faces, locate the knife sideways through a precision fit. Finally, glue fixates the knife permanently to the preload lever.

The influence of the knife edge's fabrication tolerances on the compensation mechanism's kinematics are kept to a minimum by measuring the knife edges before machining their

seats in the mechanism. The seats in the preload lever and in the support link are machined in one set-up for high knife edge parallelism.

The cushion of Figure 4.19(b) is made from fine-grained tungsten carbide. The flat surfaces at either side of the v-groove reduces the risk of chipping and simplify the cushion's fabrication.

Table 4.1 summarizes the knife edge and cushion properties, a photograph of both components is given in Figure 4.20.

		knife edge	cushion
material		ASP30 steel	HM GT30
hardness	HRC	62	70
radius ^a	μm	< 5 (5)	70 ± 2 (50)
knife, v-groove angle		45°	120°

^ameasured at VSL, values between brackets are design values

Table 4.1 / Knife edge and cushion properties.

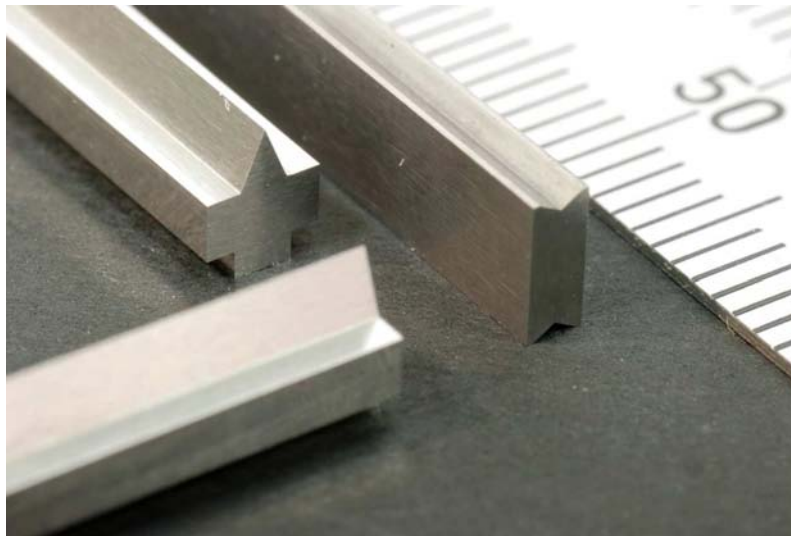


Figure 4.20 / Close-up of the knife edges and cushion. The scale at the right has millimeter spaced lines.

rocker and connecting links

Figure 4.21 shows the compensation mechanism, the rocker, the connecting links and the parallelogram.

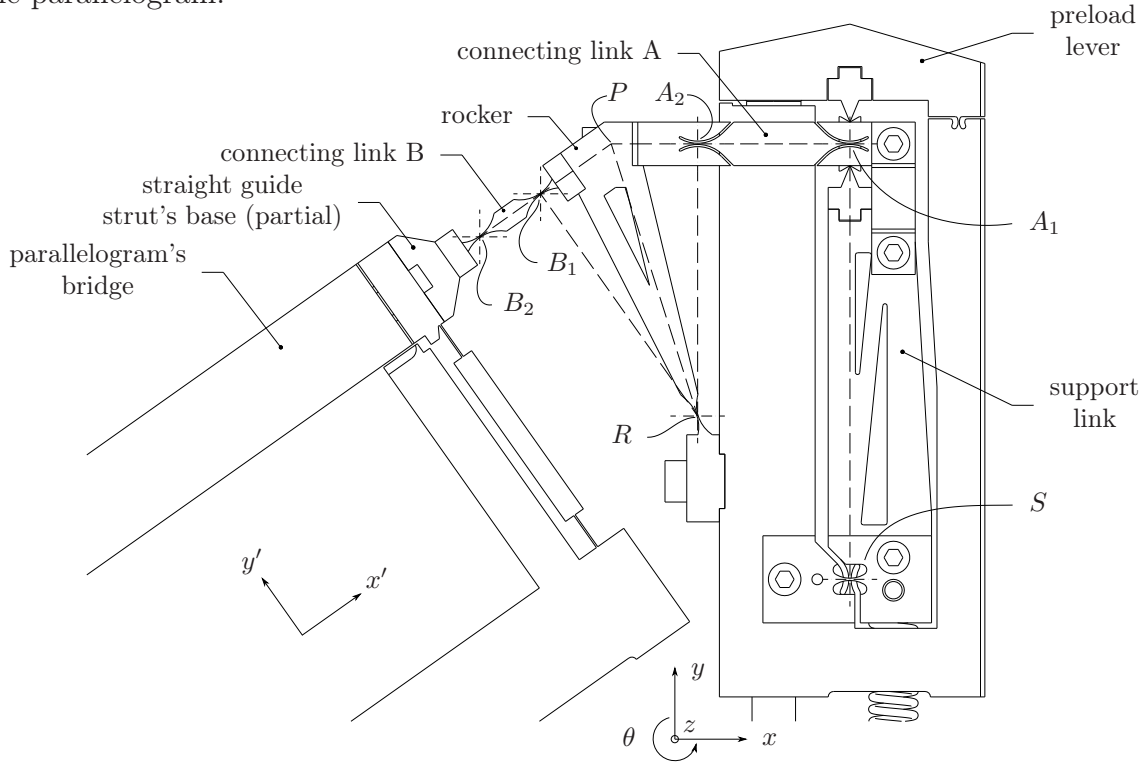


Figure 4.21 / Rocker and connecting links side view. A_1 , A_2 , B_1 , B_2 , S and R identify the hinges. Some parts (struts, several screws) are missing for clarity.

Connecting link A connects the compensation mechanism's support link to the rocker while connecting link B attaches the rocker to the parallelogram.

The hinges in both connecting links coincide with the kinematic points of minimal sideways deflection. This results in symmetrical behavior around the mechanism's center position and minimizes the forces on the hinges.

Hinge B_1 and the parallelogram practically deflect the same amount (in $-y'$ direction) during translation. The connecting link B therefore stays parallel to the parallelogram. This keeps the compensation force aligned with the parallelogram's motion direction and minimizes the bending moments from hinge B_2 on the parallelogram's bridge. Additionally, link B can be relatively short, which helps to keep the mechanism compact.

The rocker joins both connecting links with a one-to-one ratio, i.e. $\|\overline{RA_2}\| = \|\overline{RB_1}\|$. The compensation force on connecting link A works along the line A_1 - A_2 . Similarly, for connecting link B the force aligns with line B_1 - B_2 . Both forces combined give a

reaction force on the rocker along line $P-R$ because links A and B are at an angle (about 35.3°). Consequently, the stiffness along line $P-R$ affects the stiffness between the parallelogram and the compensation mechanism. Aligning the rocker's hinge with the reaction force, maximizes this stiffness.

Connecting link A rotates up to 0.5 mrad (support link rotation: $\pm 25 \text{ mrad}$) when the parallelogram translates over $\pm 1 \text{ mm}$. Although this connecting link A rotation affects the rocker's input-output ratio, it has little practical influence on the compensation force characteristic.

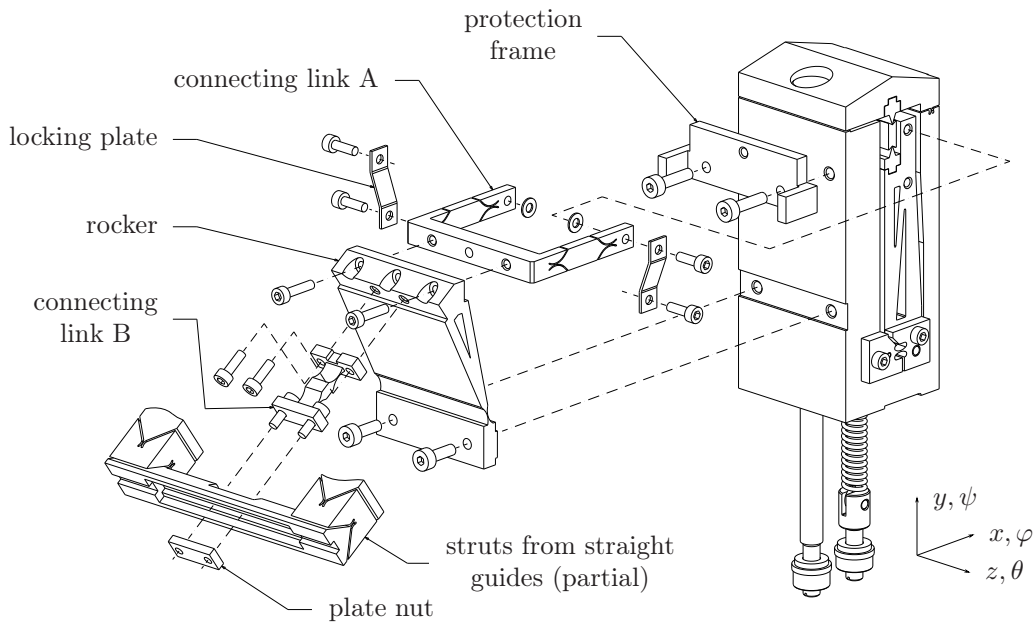


Figure 4.22 / Exploded view showing the compensation mechanism, the rocker and the connecting links.

Figure 4.22 gives an exploded view of the rocker assembly. The U-shaped connecting link A attaches symmetrically to the compensation mechanism's support link with two screws. Spacer rings between the two components keep the connecting link A clear from the compensation mechanism's housing and increase the contact pressure for less hysteresis. Locking plates between the screw heads and the connecting link, prevent twisting of the link during screw tightening.

The other end of connecting link A interfaces with the rocker. This interface is normal to the force direction for high stiffness and minimal hysteresis. Two screws go through the rocker and screw into the connecting link A, a small ridge locates link A vertically (y) and in rotation (φ). A frame fixed to the compensation mechanism's housing, protects the fragile connecting link A during assembly and installation in the instrument.

Screws fasten the rocker to the compensation mechanism's housing while a groove and flange determine the relative position and orientation. The rocker itself is pocketed for minimal moving mass.

Both mounting surfaces of connecting link B are normal to the force direction for minimal hysteresis. Two screws at either end fixate the connecting link, a flange on the rocker determines the link's position and orientation. At the rocker's side the screws go directly into the rocker while the screws at the parallelogram end go into a plate nut. The plate nut fits into a pocket in the straight guide struts' base, this pocket is closed-off by the parallelogram's bridge end face (Figure 3.8).

The compensation mechanism and the parallelogram are separately installed into the instrument. Consequently, any misalignment makes that the compensation mechanism and the parallelogram are not at their center position at the same time. To prevent this, the connecting link B is machined to length after the compensation mechanism and the parallelogram are installed. Machining only the interface at the parallelogram side keeps hinge B_1 at the kinematically right position (Figure 4.21).

The eigenfrequency of the compensation mechanism and connecting links is about 3 kHz (Figure 4.23).

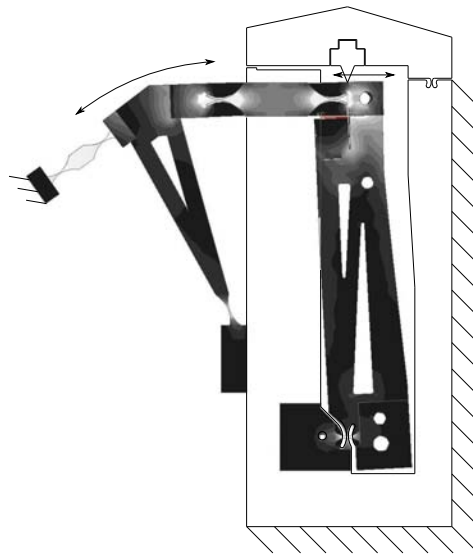


Figure 4.23 / First eigenmode at 3 kHz, the shade represents the stress level. The analysis includes the mechanism's housing and the preload lever, upper knife edge and stiffness compensation spring effective masses. Modes 2 through 5 are internal modes of the compensation mechanism, starting at 3.5 kHz.

installation in the instrument

The compensation mechanisms are installed back-to-back around the instrument's center line. Unfortunately, the access to the mechanisms at this position is restricted by the sample table assembly and the struts. This limited access makes the mechanism's assembly, alignment and installation difficult.

To simplify these steps, the mechanisms are not mounted directly to the instrument base but on a separate compensation mechanism assembly base instead. This separate assembly base also isolates the instrument base from the relatively large spring reaction forces and thereby helps to keep the instrument base deflection to a minimum.

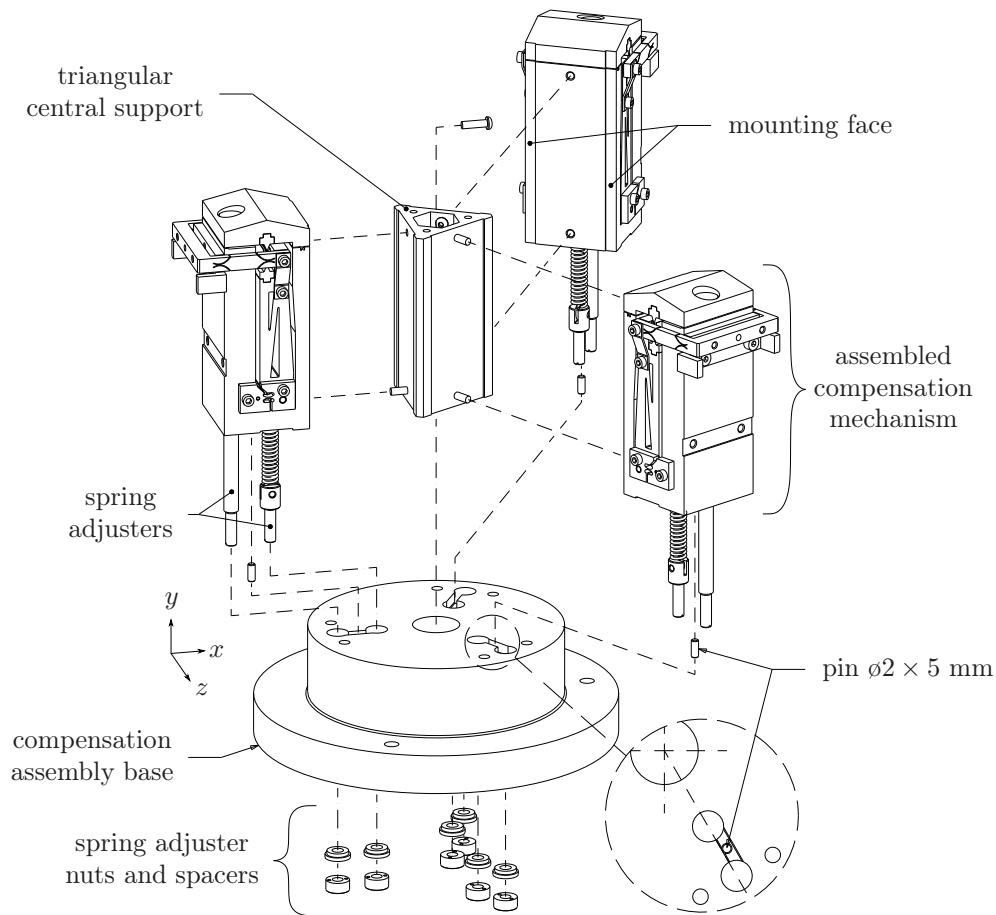


Figure 4.24 / Exploded view of the compensation mechanisms assembly. The three compensation mechanisms are first attached to the triangular central support and then installed on the compensation assembly base. Three pins and three radial grooves orient the components.

First, each compensation mechanism is assembled separately and away from the instrument. At this time the connecting link A (Figure 4.22) is installed but not the rocker and connecting link B, these are added later. Then the three compensation mechanisms are fastened to the triangular central support (Figure 4.24). Next, this subassembly is placed on the compensation assembly base and the spring adjuster nuts and spacers are installed. The compensation mechanism assembly is now inserted from below into the instrument (Figure 4.25) while the rockers and remaining connecting links are installed from above.

Finally, the stiffness compensation springs and the weight compensation springs are adjusted to give the required compensation.

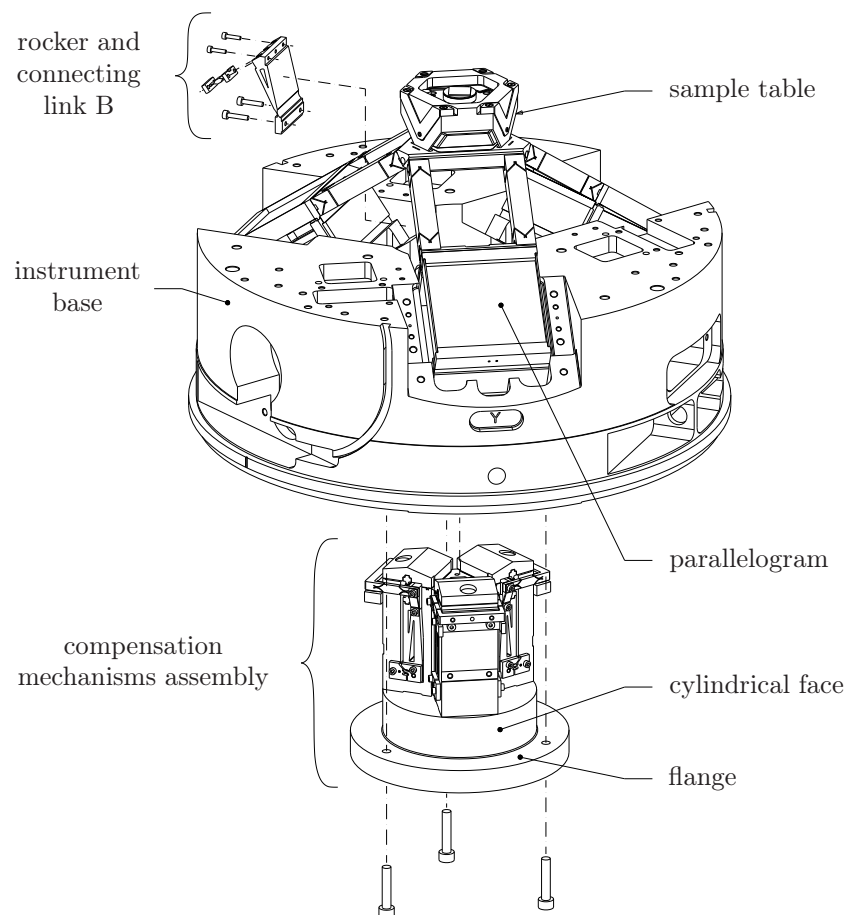
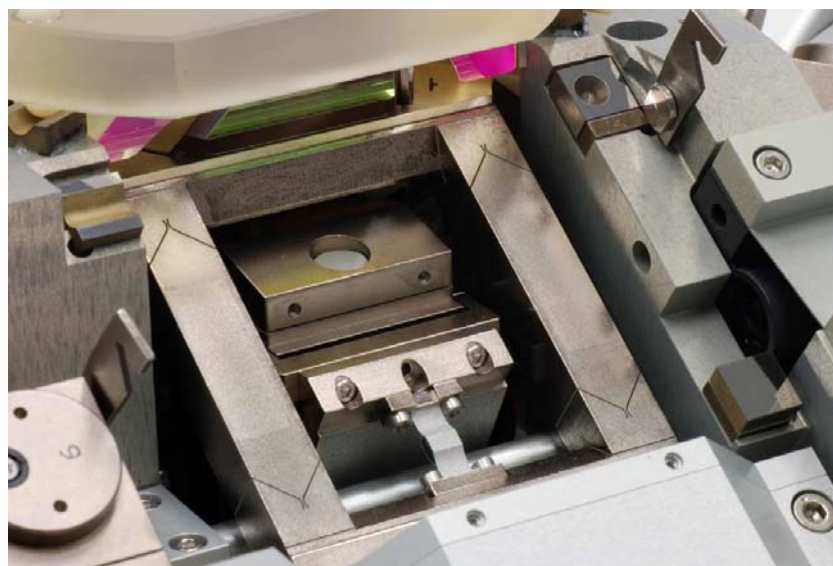
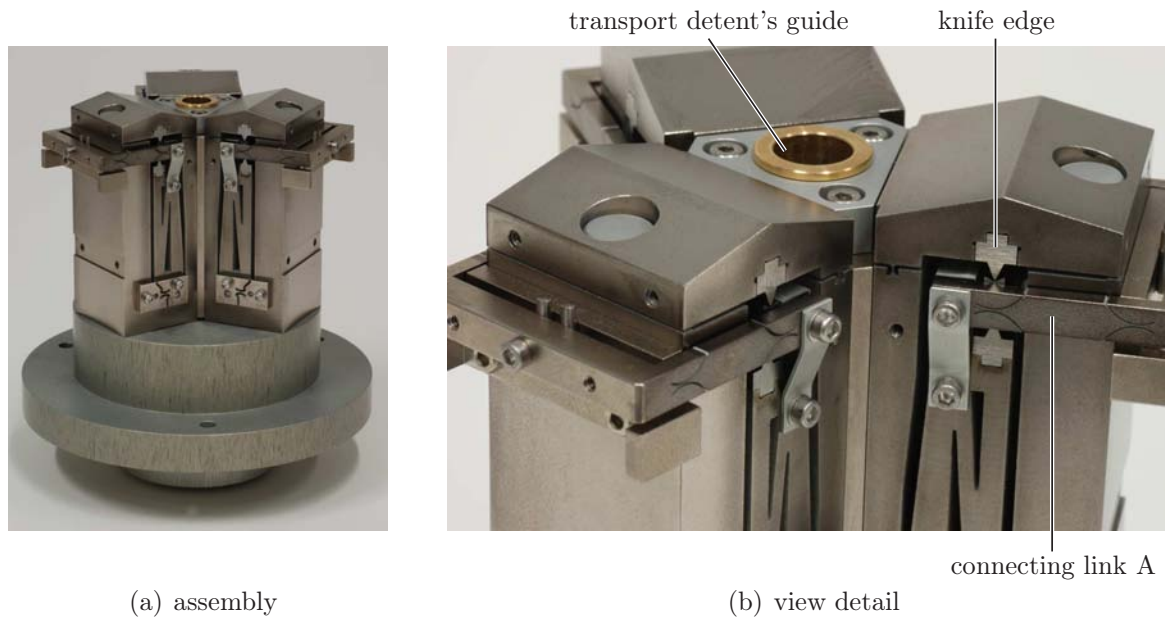


Figure 4.25 / The compensation mechanisms assembly is installed from below into the instrument. The rockers and connecting links are added from above. Only one rocker and one connecting link are shown, the actuator's yoke and magnet assemblies (Section 4.1.2) are not displayed.

Figure 4.26 show photographs of the compensation mechanisms.



(c) installed in the instrument

Figure 4.26 / The compensation mechanisms. Figure (b) shows the knife edges, connecting link A and the transport detent's guide (Appendix G). The individual compensation mechanism is difficult to reach after installation in the instrument (c).

4.3 Validation

This section discusses the actuation system's experimental validation. First the experimental set up is described, followed by a description of the actuator measurements. Section 4.3.3 discusses the stiffness measurements on the compensation mechanism and gives some remarks on the hysteresis. The dynamical behavior is evaluated in the last section.

4.3.1 Experimental set up

Figure 4.27 gives an exploded view of the experimental set up without sensors. The parallelogram, the actuator and the compensation mechanism are identical to the ones in the actual instrument for reliable results. Similarly, the components' orientation within the set up is exactly the same as in the instrument. Additionally, using the same components makes the set up assembly a rehearsal for the actual instrument assembly procedure, which is particularly useful for the actuator magnet installation.

First the parallelogram and actuator assembly and the compensation mechanism are installed from above into the base part (Figure 4.27). The connecting link B is installed next. At the parallelogram end, the link connects to the straight guide strut's base (see Figure 4.22), here only part of the strut is installed.

The actuator coil cables plug into electrical socket A in the base. The shielded cable at the base's underside, connects socket A to the larger socket B at the back of the instrument. The current amplifier's cable (not shown) plugs into socket B.

Three rectangular feet support the solid aluminium base, three pockets in the base's sides are used to clamp the base to the table surface. The cover at the underside protects the spring adjuster nuts and the cables while a transparent cover (not shown) shields the parallelogram and compensation mechanism during measurements and during transport.

Figure 4.28 shows the assembled experimental set up.

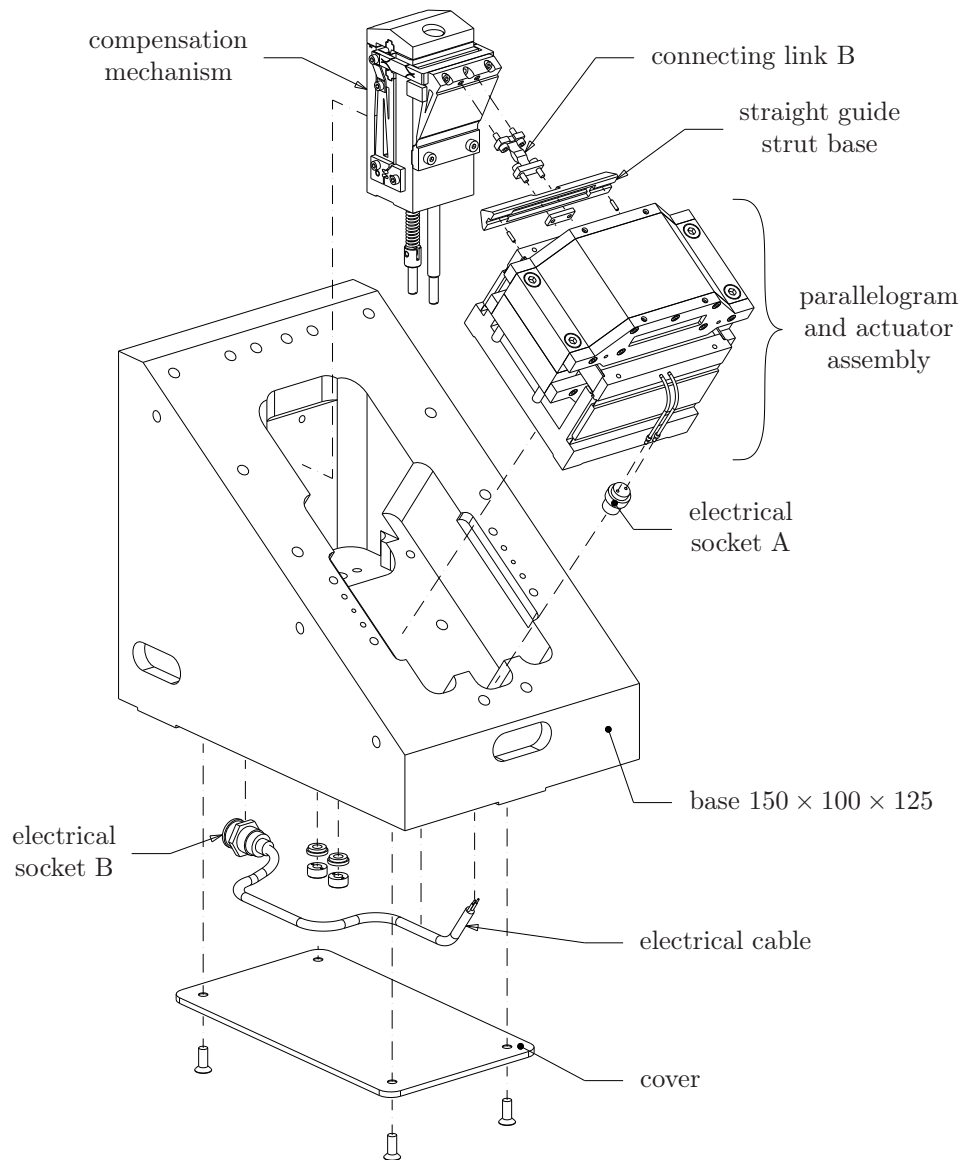
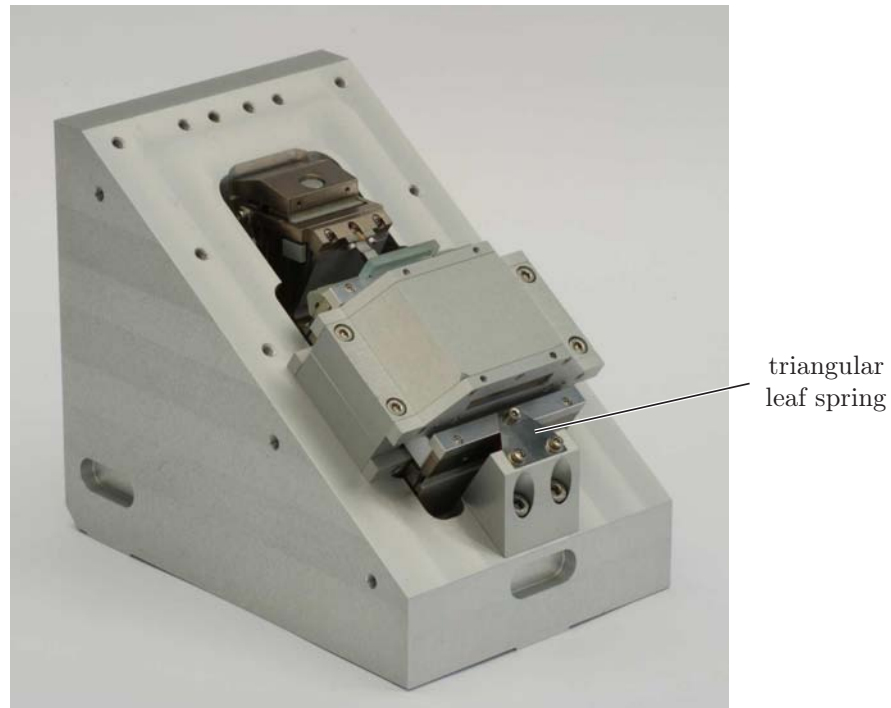


Figure 4.27 / Exploded view of the experimental set up. The base holds one parallelogram and actuator assembly and one compensation mechanism under exactly the same angle as in the instrument. Connecting link B connects to the straight guide strut base.



(a) experimental set up



(b) close-up compensation mechanism



(c) side view

Figure 4.28 / Assembled experimental set up (without sensors). The triangular leaf spring secures the parallelogram during transport.

The parallelogram movements are measured with a Zygo® double-pass plane mirror interferometer fixed to the base (Figure 4.29). A Zygo® model 7705 laser head generates the $\varnothing 4.2$ mm laser beam while a fiber optic pickup and cable transfer the interferometer's optical interference signal to the ZMI510 measurement electronics.

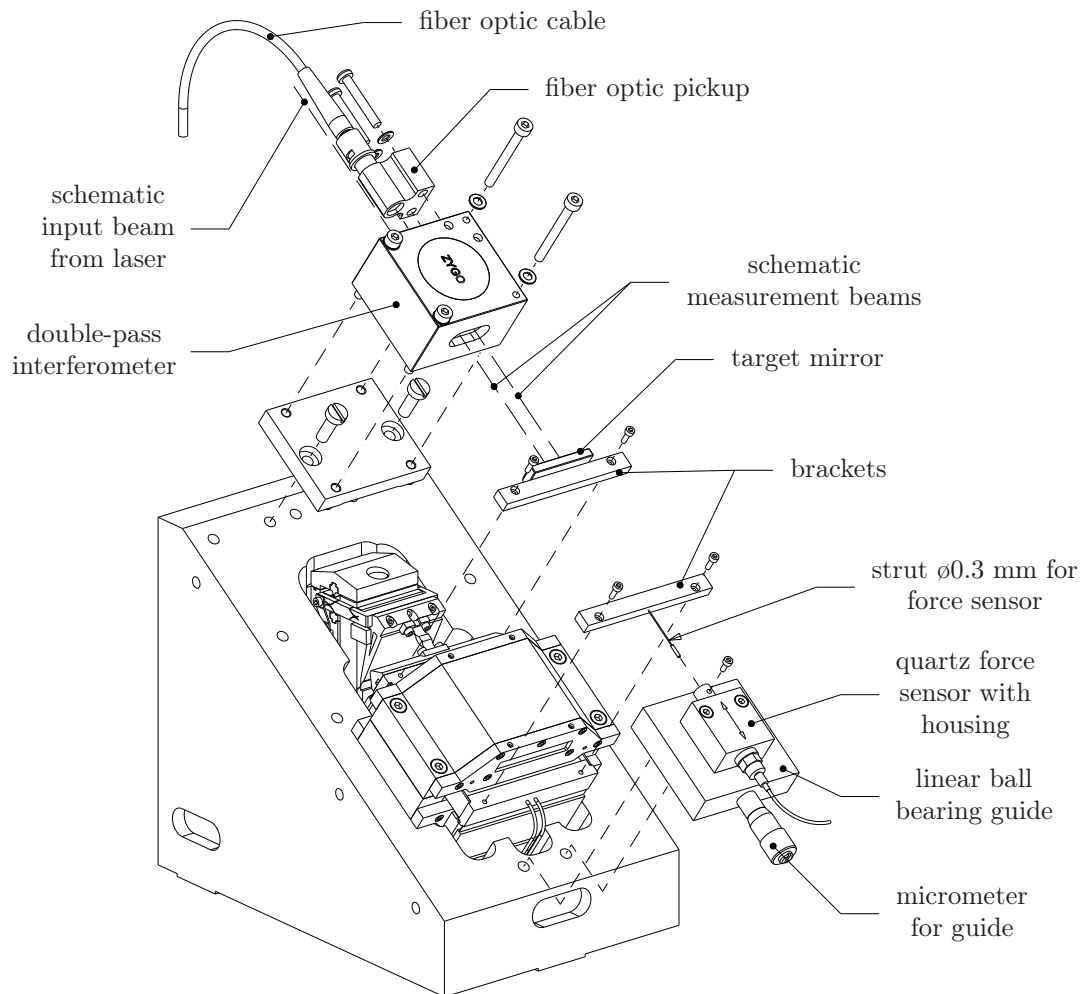


Figure 4.29 / Exploded view of the displacement and force measurement set up. A double-pass interferometer measures the displacement of the target mirror fixed to the parallelogram. The quartz force sensor measures the forces in the motion direction.

The interferometer's target mirror is glued onto an aluminium bracket, two screws fasten this bracket to the parallelogram bridge. The interferometer's reference mirror is integral with the interferometer optics [115].

A quartz force sensor (Kistler® type 9203 sensor with a type 5011 charge amplifier) measures the forces along the translation direction on the parallelogram. The force sensor is mounted on the moving part of a linear ball bearing guide, a steel

strut $\varnothing 0.3 \times 15$ mm connects the force sensor to the parallelogram. At the parallelogram end the strut is glued into a bracket similar to the target mirror bracket. A compression spring preloads the linear ball bearing guide and force sensor onto a micrometer, turning this micrometer translates the guide.

The displacement measurement axis and the force sensor's strut are collinear and as close as possible to the actuator's mid plane for accurate displacement measurements and minimal residual moments on the parallelogram.

With the moveable force sensor it is possible to measure the forces over the parallelogram's full stroke and measure the actuator's force constant K_f at different parallelogram positions.

An analog, current amplifier powers the actuator. The amplifier input voltage is generated with a 15-bit DAC linked to a computer with Matlab Simulink®. The amplifier can generate ± 100 mA, this is four times more than the designed maximum coil current. This gives some amplifier overcapacity and therefore some flexibility if the actuator performs less than expected. A disadvantage is the reduced current resolution. The 15-bit DAC is part of a TUEDACs AQI signal interface box. This signal interface also digitizes the force sensor's voltage signal and the ZMI510's quadrature displacement signal with a sample rate of 4 kHz. Table 4.2 summarizes the resolutions.

interferometer	nm	9.89
force sensor ^a	μN	15
coil current	μA	3
^a at highest sensitivity		

Table 4.2 / Resolution of the interferometer, the force sensor and the amplifier's output current.

4.3.2 Actuator measurements

In this section the ratio between the actuator's input current and the actuator's output force is experimentally determined.

The first step is attaching the force sensor to the parallelogram and removing the transport detent leaf spring. Both compensation mechanisms are not set up at this time. Then the current through the coil is increased linearly while measuring the resulting actuator force. After reaching the maximum of about 25 mA (or 3 A/mm²) the current reduces gradually and the same procedure is repeated in the opposite direction.

Each automated measurement takes about one second. This is fast enough to eliminate the influence of the charge amplifier's time constant on the force measurement but slow enough to prevent the coil's electrical time constant from affecting the force buildup.

The force sensor constrains the parallelogram with high stiffness ($\approx 4 \cdot 10^7$ N/m) so the parallelogram remains practically stationary during actuator force measurements ($F_{max} \approx \pm 1.5$ N). The force measurements are therefore not affected by inertia or the weight compensation and stiffness compensation mechanisms.

Dividing the measured actuator force by the coil current gives the actuator's force constant K_f (N/A). Measurements at different parallelogram positions showed no measurable variation in force constant over the parallelogram's stroke.

Table 4.3 summarizes the measured actuator properties. Several other actuator properties are given in Table E.1 on Page 155.

			measurement	predicted ^b
max force ^a	$F_{max,c}$	N	$\pm 1.5 \pm 0.1$	± 1.25
force constant	K_f	N/A	57.6 ± 1.8	54.0
motor constant	K_m	N/ \sqrt{W}	3.0 ± 0.1	2.85
^a continuous, ^b with design-value $B_g = 0.55$ T				

Table 4.3 / Measured and predicted actuator properties.

The actuator performs slightly better than expected. This difference is most likely caused by the underestimation of the air gap's flux density B_g and the effective wire length l_e . Using $B_g = 0.60$ T (as Ansoft suggests) and a 10% larger effective wire length (e.g. the magnetic field extends a reasonable 1.5 mm (Figure E.2) beyond the air gap) gives a maximum force of ± 1.5 N.

4.3.3 Stiffness and weight compensation measurements

This section describes the stiffness measurements on the stiffness compensation and weight compensation mechanism. Additionally, the compensation adjustment procedure is explained and a few remarks on hysteresis are made. The adjustment procedure is identical to the procedure for setting up the instrument's three compensation mechanisms.

stiffness

The laserinterferometer measures the parallelogram's movements during the stiffness or force-displacement measurements. Because the interferometer is an incremental position sensor rather than an absolute sensor it needs zeroing, preferably when the parallelogram is in its center position.

The first step is therefore to move the parallelogram to the center position and zero or initialize the interferometer. The force sensor's strut is attached so the parallelogram can be moved with the micrometer. The parallelogram reaches its center position when the gaps between the parallelogram's bridge and its two internal motion stops are equal (see Figure 3.8). An optical alignment telescope measures both gap sizes with high resolution.

Next, the stiffness compensation spring is preloaded just enough to keep the knife edges and cushion in contact when the parallelogram moves over its full stroke. Similarly, the weight compensation spring is tightened to eliminate the play within the spring adjuster and to center the spring in its hole.

Now the force needed to move the parallelogram and compensation mechanism is measured, line 1 in Figure 4.30 gives the result.

The next step is adjusting the weight compensation spring tension. To this end, the parallelogram is disconnected from the force sensor's strut so the parallelogram and compensation mechanism can move freely under the gravity load. Then the weight compensation spring tension is increased until the parallelogram returns to its center position.

Because of the relatively high uncompensated stiffness (≈ 2820 N/m) and low weight (effectively ≈ 30 g) the displacement under gravity is only small. With this small displacement it is difficult to accurately adjust the weight compensation spring. Alternatively, reducing the stiffness by slightly increasing the stiffness compensation spring tension, increases the displacement under gravity load and makes the weight compensation adjustment more sensitive.

The next step is increasing the stiffness compensation spring preload until the parallelogram and compensation mechanism are at the edge of (open-loop) instability but are still stable. This stability is checked by gently moving the parallelogram away from the center position and observing the resulting free motion with the interferometer. If the system is stable it returns to the center position, if it moves to a different resting position it is unstable (bistable).

Reconnecting the force sensor's strut and measuring the force on the parallelogram over the full stroke gives line 2 in Figure 4.30. The stiffness added by the weight compensation spring is included in this measurement. Vibrations in the system caused

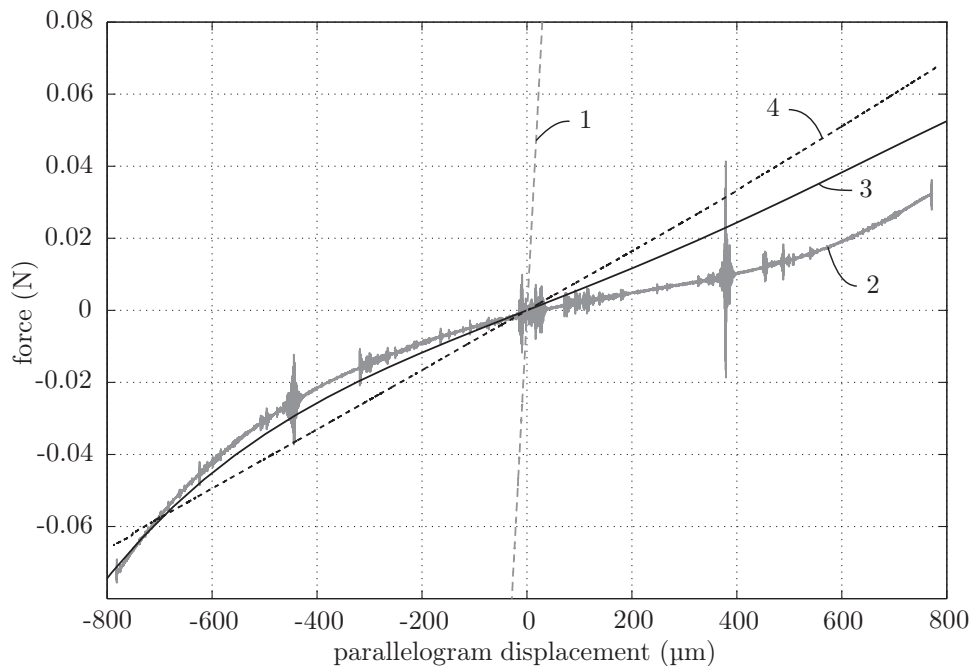


Figure 4.30 / Measured force - displacement curves: no stiffness compensation (1), with maximum compensation (2), estimated or predicted value (3), 97% compensation (4). The spikes are vibrations introduced through the manually turned micrometer. The prediction is adjusted towards similar compensation force at the stroke's end.

the spikes in the force measurement signal. These vibrations are a consequence of rotating the micrometer by hand over several turns - the distance between the spikes corresponds roughly with the micrometer's 0.5 mm per turn ratio.

Line 3 in Figure 4.30 shows the estimated or predicted force-displacement curve (Figure 4.13 on Page 65). This prediction is based on the nominal or catalog values for the stiffness compensation and weight compensation springs stiffness' and the initial loads, e.g. the forces needed to separate the tension spring's contacting windings from each other. Conversely, the stiffness compensation spring's nominal length is tuned so the predicted curve and the measurement results agree at the parallelogram's end position.

The prediction agrees in shape with the measurement results but the predicted stiffness at the end positions is higher than the measured stiffness. This is probably caused by a difference between the nominal spring properties and the actual spring properties. The actual spring stiffness and initial load can vary up to $\pm 10\%$ from the catalog value.

The maximum force after compensation corresponds with a 97% effective stiffness reduction (line 4 in Figure 4.30). This is more than the actuator's design value of 90%

so the compensation mechanism performs better than required. Additionally, the compensation mechanism reduces the actuator's maximum static dissipation at the parallelogram end position from 0.48 W to 0.54 mW (-99.7%).

Table 4.4 summarizes the compensation mechanism's measured properties.

		stiffness compensated	
		<i>no</i>	<i>yes</i>
stiffness	N/m	2820	50 ^a to 210 ^b
maximum force ^b	N	± 2.10	± 0.07
eigenfrequency ^a	Hz	35	4.5
^a center position, ^b at end of stroke (maximum)			

Table 4.4 / Measured compensation mechanism properties. The weight compensation spring's stiffness is included in both measurements.

hysteresis

Hysteresis in a mechanism is detectable using force-displacement measurements. The force versus displacement is measured over the mechanism's full stroke and in both motion directions. Hysteresis shows up as a difference between the forward measured and backward measured force-displacement curves.

To minimize the influence of accelerations (and vibrations) on both measurements, it is necessary to move the parallelogram slowly and with a nearly constant velocity. This, of course, increases the measurement time and subsequently the sensitivity to drift in the force and the displacement sensors. Unfortunately the force sensor's drift proved too large for reliable measurements of the small differences between the forward and backward force displacement curves.

An alternative and more indirect method of measuring the hysteresis uses the actuator and a closed-loop position controller.

The free-moving parallelogram makes a controlled motion over its full stroke while the displacement is recorded. If there is hysteresis in the system this shows up as a steady-state difference between the controller's trajectory and the measured parallelogram position.

The position controller parameters depend on the parallelogram and compensation mechanisms' dynamics. These dynamics and the actual closed-loop hysteresis measurements are the topic of the next section.

4.3.4 Dynamics

The first step is to measure the frequency response function (FRF) from the actuator's output force to parallelogram's displacement. Based on this FRF a position controller is designed. The parallelogram then makes a close-loop controlled motion, if there is any hysteresis in the system this will show up as a steady-state tracking error.

The stiffness compensation and weight compensation mechanisms are both already adjusted towards maximum compensation.

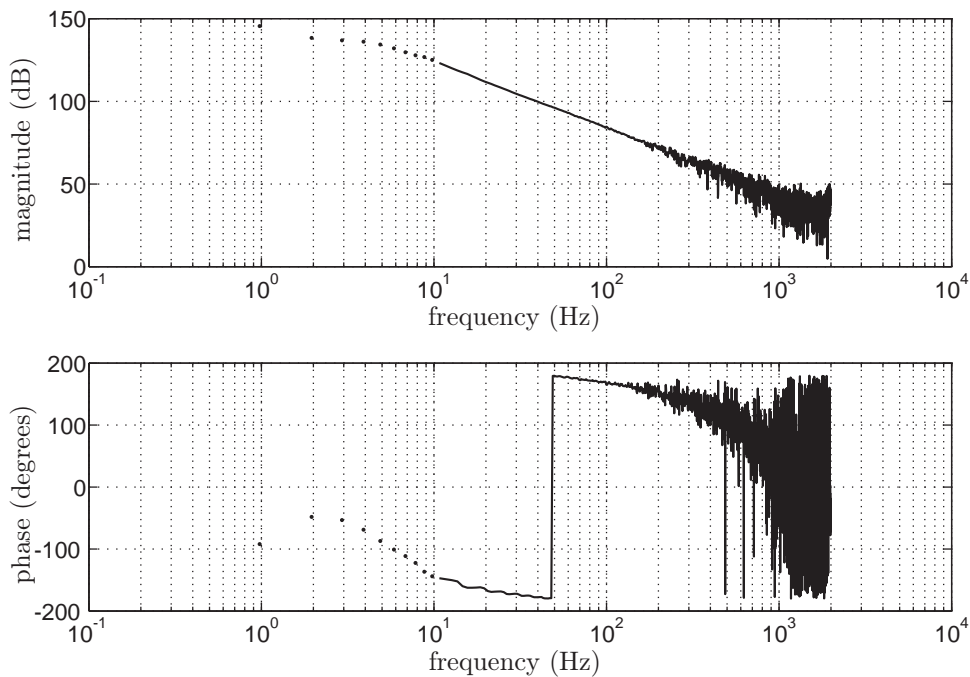


Figure 4.31 / Frequency response function (FRF) from actuator force to parallelogram displacement. Sample frequency $f_s = 4$ kHz, PI-controller with 0.1 Hz bandwidth. The actuator force is calculated from the measured amplifier's input voltage.

Figure 4.31 shows the FRF from the actuator force to the parallelogram displacement. The actuator force is calculated from the measured amplifier input voltage. The amplifier's output current is assumed proportional to the input voltage because the measurement's 4 kHz sample frequency is considerably lower than the amplifier's 55 kHz bandwidth [52].

The measurement's sensitivity plot indicates that the measurements below about 10 Hz are unreliable (coherence < 0.6). Similarly, the low signal-to-noise ratio makes the measurements over about 200 Hz noisy. Between 10 Hz and 200 Hz the system behaves

as one rigid mass with no internal eigenmodes.

Based on the FRF measurement, a lead controller with weak integrator is designed³. This controller uses position, velocity and acceleration feedforward and has a bandwidth of 100 Hz.

Figure 4.32 gives the measurement results of a controlled motion over $\pm 800 \mu\text{m}$. The upper figure gives the third-order motion profile with a maximum velocity of 1.6 mm/s while the lower figure shows the difference between the motion profile and the measured position in interferometer counts.

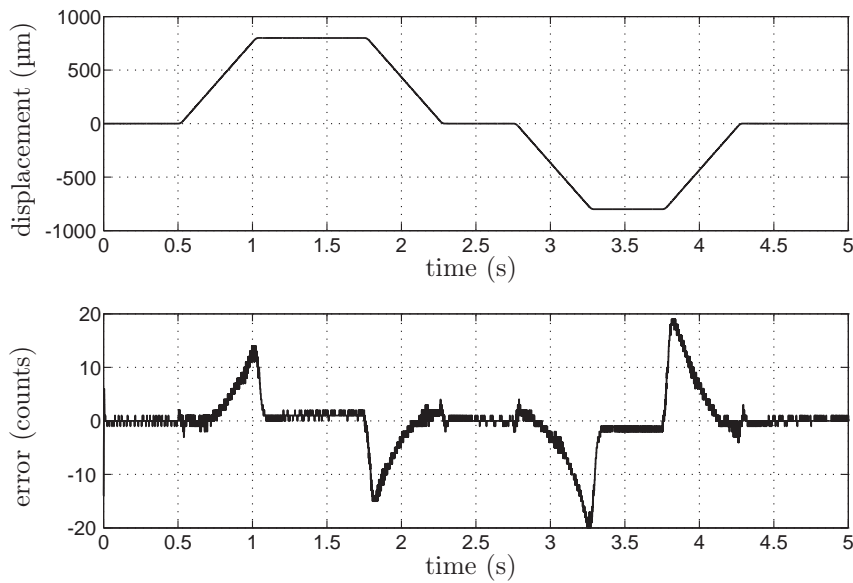


Figure 4.32 / Controlled motion over $\pm 800 \mu\text{m}$, $f_s = 4 \text{ kHz}$. The non-linearity in the compensated stiffness leads to some tracking error when the stage moves away from the mid position, this error reduces again to \pm one interferometer count ($\pm 10 \text{ nm}$) when the stage returns to the center position. The changing average around zero suggests less than one count (10 nm) hysteresis.

Close inspection of the \pm one count ($\pm 10 \text{ nm}$) errors in the first half second of the measurement show that the spikes actually span several sample intervals and are unevenly spaced in time. Additionally, the controller responds to the displacement signal with a varying actuator force, again during several sample intervals. This suggests actual parallelogram movements rather than merely interferometer measurement noise. These small movements are presumably caused by external disturbances and control electronics noise or drift.

After half a second the parallelogram starts to move in the positive direction. As the displacement increases the non-linear stiffness increases more than the linear position feedforward expects. This leads to an increasing tracking error. The controller's integrating action reduces this error to about one to two counts once the parallelogram has stopped at approximately 800 μm from the center position.

Returning to the center gives a similar but opposite tracking error. The parallelogram stops again within \pm one interferometer count from the center position.

The parallelogram then moves about 800 μm in the negative direction. The asymmetry in the compensated stiffness (Figure 4.30) leads to a larger underestimation of the stiffness compared to the positive direction. This subsequently leads to a larger tracking error.

After returning to the center, the tracking error reduces to \pm one count. The changing average suggest a position accuracy equal to or better than one count or 10 nm. The hysteresis must therefore be \leq 10 nm, which is expected to be sufficiently low.

³design and implementation R.J.E. Merry, CST-TU/e

4.4 Concluding remarks

Three Lorentz actuators drive the straight guide's three translational degrees of freedom to move the sample relative to the stationary AFM probe. Three identical, elastic, stiffness compensation and weight compensation mechanisms reduce the actuator's static load to minimize the power dissipation.

The duo-motor type actuator has a moving, copper coil, the heavy rare-earth magnets are stationary. The actuator is designed towards maximum efficiency, e.g. minimal power dissipation within the actuator per generated unit of actuation force.

The actuator is tested in an one-DOF experimental set up. The measured maximum (continuous) actuator force is about ± 1.5 N with a force constant of 57.8 ± 1.8 N/A. Linear, analog, current amplifiers, power the actuators. The amplifiers are controlled by a dedicated, PC/104 based, control system through 18-bit digital-to-analog converters. The weight compensation mechanism uses a low-stiffness tension spring and a 1:10 ratio to generate a nearly constant gravity opposing compensation force.

The elastic stiffness compensation mechanism measurably reduces the required maximum (static) actuator force from ± 2.10 N to ± 0.07 N. Consequently, the maximum power dissipation within the actuator reduces by over 99% from 0.48 W to below 0.6 mW. The (closed-loop) estimated hysteresis is ≤ 10 nm, which is expected to be sufficiently low.

Figure 4.33 shows the instrument design as discussed up to here.

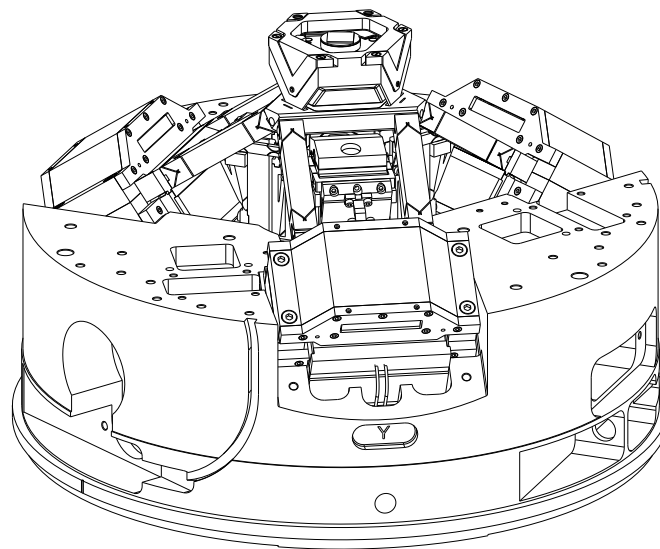


Figure 4.33 / Instrument design as discussed in Chapters 3 and 4.

CHAPTER FIVE

Measurement system

Abstract / Three custom, compact, differential plane mirror interferometers measure the sample's displacements relative to the stationary AFM probe. The moving target mirror surfaces for the three interferometers are integrated into one monolithic, Zerodur® component for maximum thermal and mechanical stability. The stationary reference mirror surfaces are combined into one single component as well. Beam delivery optics distribute the laser input beam over the three interferometers. Commercial fiber optic receivers and measurement electronics complete the translation stage's measurement system.

5.1 Introduction

The measurement system measures the sample's displacements relative to the stationary AFM probe in three orthogonal directions. The system has three identical displacement sensors, each measures the displacement in one direction.

For high-resolution AFM measurements, the displacement sensor's resolution and accuracy must be below one nanometer. Secondly, the sensor has to measure the displacement over the instrument's cubic millimeter measurement volume and stay aligned with the AFM probe for measurements in Abbe (see Figure 2.1 on Page 16). Additionally, the measurement system's traceability chain towards the national length standard should be as short as possible. Finally, sensors based on well known and proven principles are preferred over experimental sensors for practical reasons.

Capacitive position sensors (CPSs) have sub-nanometer resolution, are mechanically simple and are readily available [46]. Although they can provide the resolution, the required measurement range of nearly two millimeters is too much for this sensor type.

An alternative to capacitive position sensors is the displacement measuring interferometer (DMI). There are two types of this non-contact optical displacement sensor, the homodyne or single-frequency and the heterodyne or two-frequency system. Both types are briefly explained before the advantages and disadvantages of DMIs are discussed.

Figure 5.1 shows a homodyne plane mirror DMI. The system has a single frequency laser, a plane mirror interferometer (PMI) [113], a moving target mirror and two detectors.

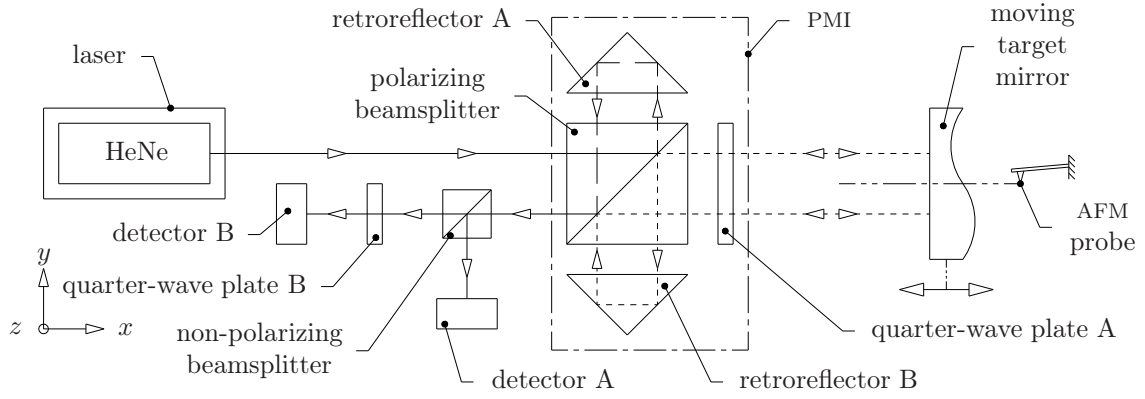


Figure 5.1 / Homodyne displacement measuring interferometer (DMI) with a plane mirror interferometer (PMI) [113]. The laser's output beam is split in a reference beam and a measurement beam by the polarizing beamsplitter. The reference beam is reflected once by retroreflector A. The moving target mirror reflects the measurement beam twice so this is a double-pass interferometer. Both beams recombine at the polarizing beamsplitter and interfere at the detectors A and B.

The frequency stabilized helium-neon laser generates a single-frequency beam polarized at 45 degrees with the horizontal [12, 18]. This beam is split into two equal parts with mutually perpendicular polarizations by the PMI's polarizing beamsplitter. The beam reflected by the polarizing beamsplitter forms the reference beam, the transmitted beam is the measurement beam.

The reference beam is reflected towards the non-polarizing beamsplitter by retroreflector A and the polarizing beamsplitter. Conversely, the measurement beam reflects twice from the moving target mirror and once from retroreflector B before being recombined with the reference beam at the polarizing beamsplitter. At this point there is no interference between the two beams because both are differently polarized.

The non-polarizing beamsplitter reflects one half of each beam towards detector A, the other half is transmitted towards detector B. A linear polarizer in each detector combines the differently polarized measurement beam and reference beam fractions into one interference signal [4]. The intensity of this interference signal changes periodically as the target mirror moves, the periodicity depends on the DMI's optical configuration (single-pass, or as in Figure 5.1, double-pass) and the laser source's wavelength.

The quarter-wave plate B between the non-polarizing beamsplitter and detector B

optically shifts the interference signal's phase by $\pi/2$ or 90 degrees [4]. With this phase difference between the two detectors, the mirror's motion direction is detectable (phase quadrature) [90].

The heterodyne DMI [30] shown in Figure 5.2 uses a two-frequency laser source and a different detection scheme compared to the homodyne DMI. The PMI optics on the other hand, are identical for both types.

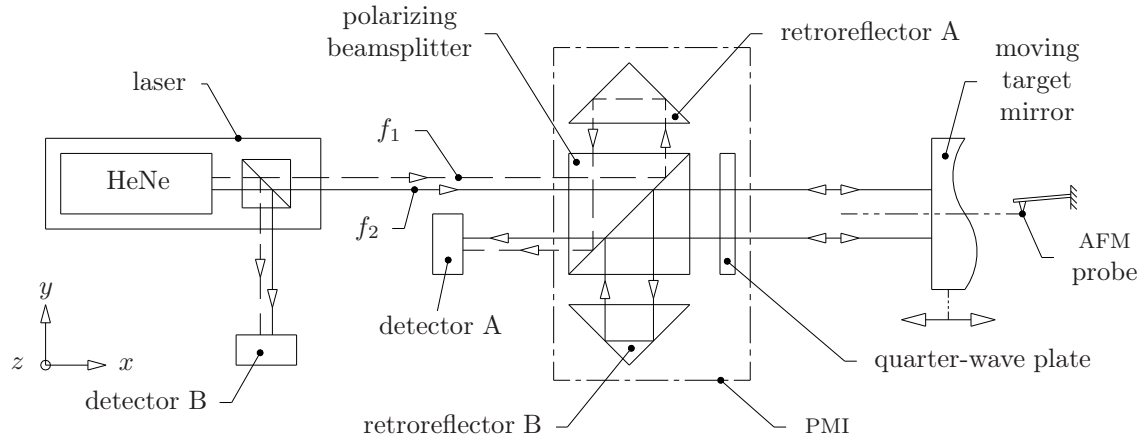


Figure 5.2 / Heterodyne displacement measuring interferometer (DMI) with a plane mirror interferometer (PMI). The laser's single output beam has two different polarization components at different frequencies, these components are drawn separately for clarity. The polarizing beamsplitter separates, and after reflection, recombines the components to give an optical beat signal. Moving the mirror changes the interference beat signal at detector A compared to detector B.

The laser's output beam has two collinear and orthogonally polarized components with slightly different frequencies f_1 and f_2 [101]. The component with frequency f_1 is the interferometer's reference beam, the other component is the measurement beam.

The polarizing beamsplitter reflects the incoming reference beam towards retroreflector A. The beam is then reflected towards detector A by retroreflector A and the polarizing beamsplitter. The measurement beam is transmitted through the polarizing beamsplitter towards the moving target mirror. After being reflected twice by the moving target mirror and once by the retroreflector B, the measurement beam exits the beamsplitter and hits detector A.

A polarizer in detector A combines the collinear measurement beam and reference beam into one optical interference signal while the detector converts the optical signal in an electrical measurement signal.

The frequency difference between the reference beam and measurement beam gives

a beat signal with a component $f_1 - f_2$ on detector A. This beat frequency changes when the target mirror moves. If the target mirror moves with speed v , then the reflected measurement beam's frequency at the detector changes to $f_2 + \Delta f$ with $\Delta f = 4(v/\lambda)f_2$, λ the laser's wavelength and c the speed of light [25]. The resulting change in beat frequency is compared to the unchanged beat frequency measured by detector B. The measurement electronics detect the phase difference between the two beat signals and convert this phase difference into position and velocity data [25, 101].

The DMI's resolution depends on the laser's wavelength, the interferometer's optical configuration (single-pass, double-pass etc) and the measurement electronics interpolation resolution. With laser sources, interferometers and electronics from commercial manufacturers like Agilent®, Zygo® or Renishaw®, sub-nanometer resolution is achievable.

Non-linearities in the interferometer limit the accuracy of these systems to just under one nanometer [111]. These non-linearities originate from mixing of the measurement beam and the reference beam [12, 113] and stray reflections within the interferometer [27].

The laser beam's coherence reduces as the distance to the laser source increases. This reduced coherence limits the DMI's measurement range [12]. Fortunately, a frequency-stabilized helium-neon laser beam is typically sufficiently coherent for sub-nanometer resolution measurements over at least a meter from the laser source [115]. This gives the DMI a sufficiently large measurement range.

Both interferometer types depend on the laser source's wavelength to convert the detector signal to actual mirror displacements. This laser source wavelength is made directly traceable to the international definition of the meter by calibrating the laser source against an iodine stabilized reference laser of the national metrology institute [36, 45].

The DMIs in Figures 5.1 and 5.2 measure the mirror's translations in the x direction. If the moving target mirror is perfectly flat, any lateral (y, z) mirror motion is not measured. This makes it possible to combine three separate and mutually orthogonal DMIs into one three-dimensional, compact and Abbe-error free displacement measurement system [11].

In addition to the interferometer optics and mirrors, the three-dimensional measurement system also needs an optical beam delivery system to distribute the laser source's output beam over the three measurement axes.

The large number of high-quality components in a DMI make it a complex, bulky and

rather expensive displacement sensor. Conversely, the measurement range, resolution and accuracy correspond well with the instrument requirements so DMIs are used.

The next section discusses the interferometer optics design in detail, followed by a description of the interferometer target mirrors in Section 5.3. The beam delivery components are explained in Section 5.4. From Page 132 onward, the measurement electronics are briefly addressed. Section 5.6 concludes this chapter.

5.2 Interferometer optics

The first part of this section describes the interferometer's optical layout, followed by a description of the design (Page 100). Section 5.2.4 discusses the interferometer support frame and fixation on the instrument.

5.2.1 The optical layout

Figure 5.3 gives a detailed view of the heterodyne plane mirror interferometer [113] discussed earlier.

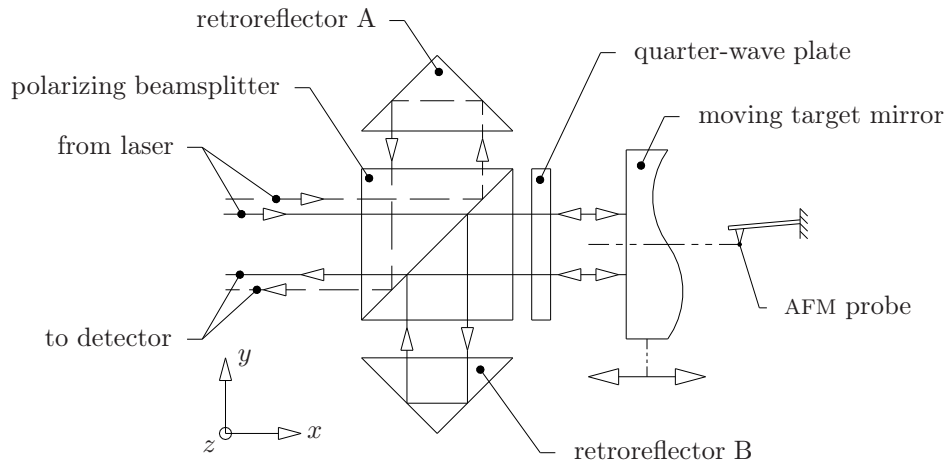


Figure 5.3 / Plane mirror interferometer (PMI). The reference beam (dashed) and measurement beam (solid) are orthogonally polarized and do overlap but are drawn separately for clarity. The path lengths of both beams differ, which leads to a high sensitivity to uniform temperature variations.

This interferometer's measurement beam reflects twice from the moving target mirror (double-pass) before being recombined with the reference beam. The optical resolution

is therefore two times the resolution of a single-pass interferometer. Additionally, mirror rotations around the z axis have no effect on the displacement measurement. Unfortunately, the measurement beam and reference beam travel different distances through the interferometer components. This path length difference makes the interferometer sensitive to (uniform) temperature variations as the measurement beam path and the reference beam path are differently affected [113].

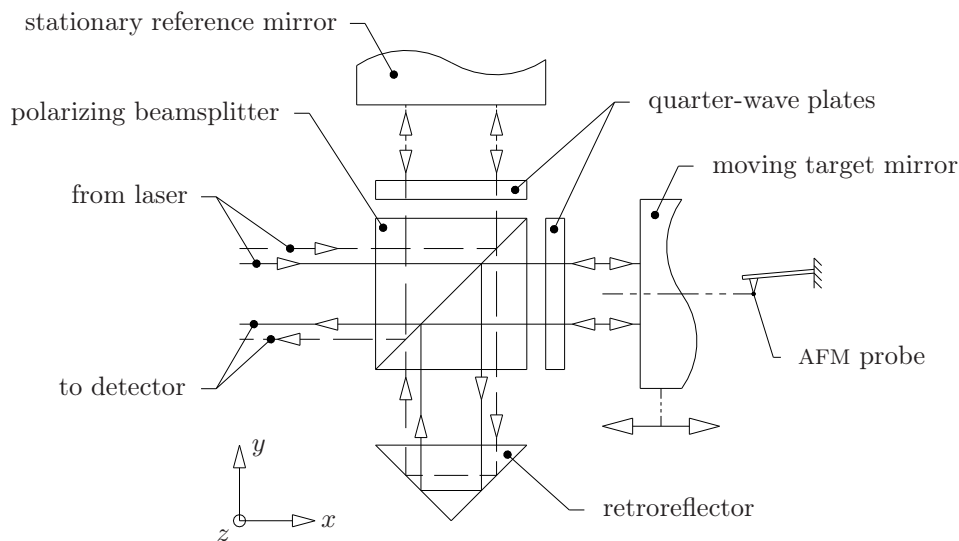


Figure 5.4 / High stability plane mirror interferometer (HSPMI) [7]. The reference beam and measurement both reflect twice of their respective mirror and have equal optical path lengths. For clarity both beams are drawn separately but actually coincide.

Balancing the path lengths within the interferometer, reduces the sensitivity to uniform temperature variations. Figure 5.4 shows such balanced high stability plane mirror interferometer (HSPMI) [7]. Like the PMI, this interferometer is also insensitive to mirror rotations.

The interferometer measures the moving target mirror displacement relative to the flat, stationary reference mirror. The moving target mirror is close to the sample and the interferometer's measurement axis aligns with the AFM probe for Abbe-error free measurements. Conversely, the stationary reference mirror is perpendicular to the interferometer's measurement axis and quite a long distance away from the AFM. This leads to a long metrology loop between the stationary reference mirror and the AFM. Additionally, if the interferometer optics move while both mirrors are stationary, an erroneous displacement is measured.

The long metrology loop and sensitivity to interferometer optics movements increases the measurement system's sensitivity to temperature changes.

The metrology loop's reference path is considerably shorter if a differential interferometer like NPL's Jamin interferometer [29] is used. Figure 5.5 shows this homodyne differential plane mirror interferometer (DPMI).

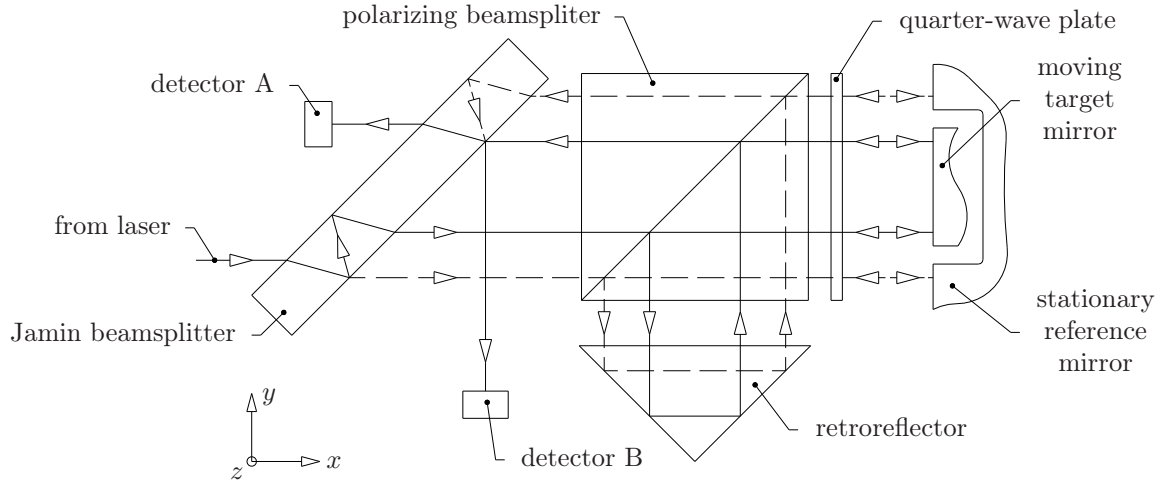


Figure 5.5 / NPL's Jamin interferometer. Due to the differential layout, movements of the interferometer optics have no influence on the mirror displacement measurement. The Jamin beamsplitter splits the incoming beam into two parallel beams and recombines the reflected beams. The coating on the Jamin beamsplitter phase shifts both beams by nearly 90 degrees for phase quadrature. The interferometer's overall size with detectors is $98 \times 96 \times 56$ mm.

The Jamin beamsplitter separates the laser's input beam into two parallel and similarly polarized beams. Both beams reflect twice from their respective mirror before being recombined again at the Jamin beamsplitter. At recombination both beams interfere optically, this interference signal is split and sent towards the two detectors. A thin metal film coating on the Jamin beamsplitter gives a near 90 degrees phase shift between the two beams (phase quadrature). This coating therefore replaces the quarter-wave plate B in the homodyne PMI of Figure 5.1.

The differential interferometer measures only relative translations of the mirrors, small mirror rotations and movements of the interferometer optics are not detected. This reduces the metrology loop length considerably compared to normal HSPMIs and therefore improves stability and accuracy.

The measurement beam and reference beam travel equal distances through the interferometer optics for minimal temperature dependence. Furthermore, the distance both beams travel through air when the interferometer is initialized is also equal. This minimizes the sensitivity to changes in the environmental conditions during the measurement (dead path error) [113].

The interferometer's sub-nanometer measurement accuracy has been demonstrated using dedicated signal processing electronics with cyclic error compensation routines [28]. This accuracy, the differential layout, the compactness of the optics and the commercial availability make the Jamin interferometer a suitable displacement sensor for the instrument.

Interferomet Ltd, a NPL-affiliated company, offers the Jamin interferometer as the AIMSTM (Adaptive Interferometric Metrology System) interferometer [50]. Unfortunately, this company went out of business in 2005. For a short time the interferometer was offered by Queensgate Instruments Ltd but is no longer available since early 2006 [112].

Other commercially available DPMIs are considerably larger in size and optically much more complex [113]. Because the differential layout is so advantageous for the metrology loop length and the subsequent accuracy, a new and simple DPMI is designed.

The new interferometer is loosely based on NPL's Jamin design but is optically much less sophisticated. Additionally, to keep the fabrication cost low, it is built from basic catalogue plane-optics.

Using commercial signal processing electronics instead of custom electronics minimizes the DMI's development time. These electronics are readily available for heterodyne systems so for the new DPMI a heterodyne detection scheme is used.

Figure 5.6 gives the new DPMI's optical layout. The HeNe laser source's beam is split by polarizing beamsplitter A into a horizontally polarized measurement beam (solid line) and a vertically polarized reference beam (dashed line). The half-wave plate (HWP) between polarizing beamsplitter A and prism A rotates the polarization direction of the reference beam over 90 degrees so both beams are horizontally polarized as they enter polarizing beamsplitter B. This beamsplitter transmits both beams towards their respective mirror and, after reflection from the mirrors and two passes through the quarter-wave plates (QWPs), directs the beams to polarizing beamsplitter C. This third beamsplitter makes both beams reflect a second time from the stationary reference mirror and moving target mirror before sending the beams to prism B and polarizing beamsplitter D. Half-wave plate B rotates the measurement beam's polarization over 90 degrees, so the beam reflects of polarizing beam splitter D. At this beamsplitter, the measurement beam and the reference beam recombine and travel together to the detector.

The optical path lengths within the interferometer and through the air are identical for the measurement beam and the reference beam. The polarizing beamsplitters B and C

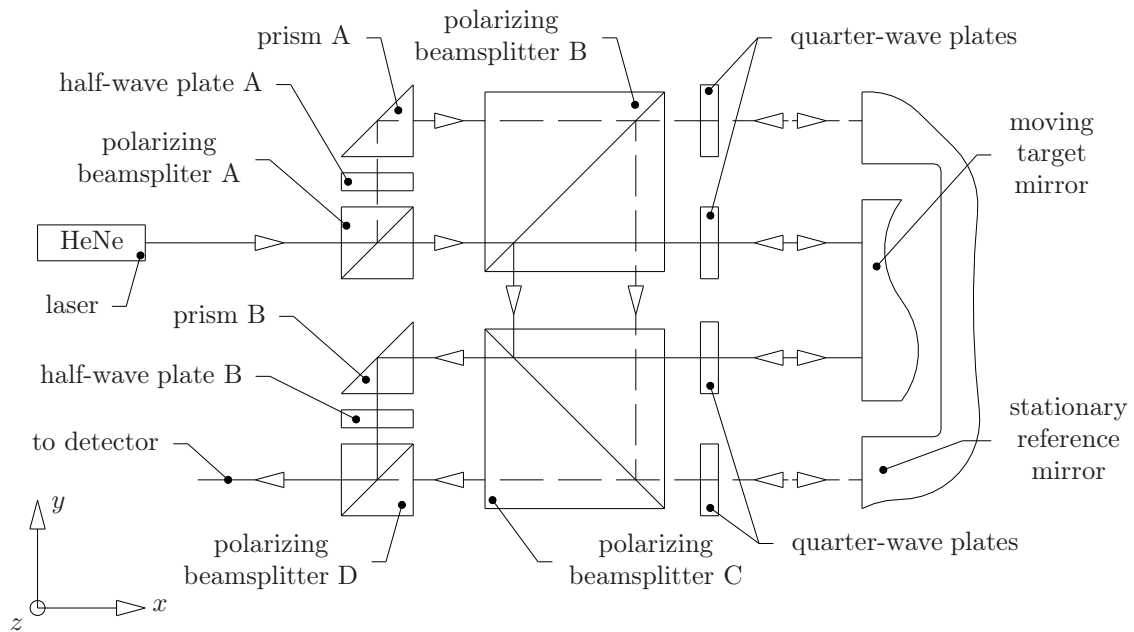


Figure 5.6 / New design for a differential plane mirror interferometer (DPMI). Polarizing beamsplitter A divides the laser's input beam, polarizing beamsplitter D recombines the beams after reflecting of the moving target mirror and the stationary reference mirror. The measurement beam and the reference beam travel equal distances.

together form a right-angle prism, this prism reduces the interferometer's sensitivity to mirror rotations somewhat, although not as much as the retroreflector in the Jamin interferometer. With all beams in the same plane, the interferometer's thickness is kept to a minimum. This simplifies the integration into the instrument.

A practical advantage of this design over the Jamin design is the flexibility in beam spacing. The spacing of the measurement beams and reference beams is easily adjustable by changing the position of the two prisms and the beamsplitters A and D. Conversely, changing the beam spacing in the Jamin interferometer requires a different thickness Jamin beamsplitter.

With no suitable commercial DPMI available, and because of the equal length beam paths, compactness and flexibility in beam spacing, the differential layout of Figure 5.6 is chosen for the stage's interferometers. In the next section this optical layout is translated into actual optical components.

5.2.2 Interferometer design

Figure 5.7 shows the DPMI fabricated from mainly standard catalog components. The measurement beams are 14 mm apart, the reference beam spacing is 48 mm while the overall dimensions are $58 \times 48 \times 10$ mm.

All components are joined together into one optical assembly for maximum thermal and mechanical stability. Another advantage of the integration is the lower number of glass-air-glass interfaces and subsequent reduction in stray reflections.

Compared to the schematic layout in Figure 5.6, two prisms C and D are added so the laser beam enters and exits the interferometer at the sides. This allows the use of a more compact beam delivery system (Section 5.4).

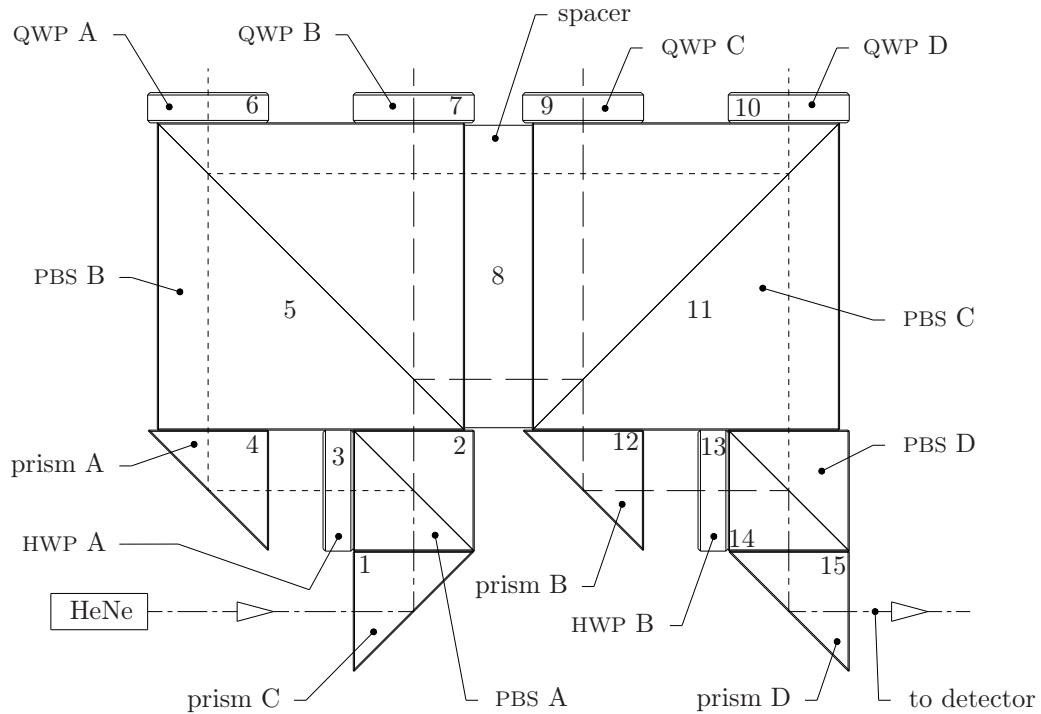


Figure 5.7 / Differential plane mirror interferometer, size: $58 \times 48 \times 10$ mm. Polarizing beamsplitters (PBSs) B and C and the spacer together form the main polarizing beamsplitter. HWP: half-wave plate, QWP: quarter-wave plate.

The prisms, wave plates and the smaller polarizing beamsplitters (PBSs) A and D are standard, unmodified 10 mm optics. Conversely, the larger polarizing beamsplitters B and C are 10 mm thick sections machined out of one single commercial one-inch polarizing beamsplitter. The bottom section of this one-inch cube forms beamsplitter B, the upper section is flipped upside down and becomes beamsplitter C. Fabricating both large beamsplitters out of one component, ensures that both components are optically identical so uniform temperature changes affect both components equally. A 5.6 mm

thick plane-parallel spacer joins beamsplitters B and C to form the interferometer's main polarizing beamsplitter. The other smaller components attach to this main polarizing beamsplitter with index-matched optical cement.

The interferometer design was discussed with several optical workshops and these discussions led to two conclusions. Firstly, the estimated fabrication cost for three interferometers significantly exceeds the available budget. Secondly, the cost of assembling the interferometer's fifteen components into a functioning interferometer is considerably higher than the cost of fabricating the components.

An alternative to buying ready-for-use interferometers is to obtain only the interferometer components from an optical workshop and assemble the interferometers in-house. This assembly is then not based on joining the components to within predetermined tolerances [43] but on a functional assembly. So instead of using one component as a mechanical reference for the alignment of a second component, the component's influence on the actual output beam alignment is used to position the component. This approach has several advantages. Firstly, the errors in the optical components are automatically taken into account when assembling the components. Secondly, with proper alignment tools and jigs, it is possible to fully assemble and test the interferometer before the components are permanently joined. This temporarily assembled interferometer can then be used to experimentally determine the interferometer's sensitivity to individual component misalignments. A third reason is the expected lower cost because there is no technical risk fee and no profit required.

The interferometer of Figure 5.7 is redesigned to simplify the interferometer assembly procedure. The polarizing beamsplitters B and C and the spacer in the first version are integrated into one, custom made, three-piece beamsplitter (Figure 5.8).

Additionally, the four $\varnothing 10$ mm QWPs are replaced by two 10 mm high sections cut from two, one-inch diameter, QWPs. Figure 5.9 shows the integration of QWPs A and B into one larger component.

The prism C and the polarizing beamsplitter A of Figure 5.10(a) are integrated into one input beam polarizing beamsplitter as shown in Figure 5.10(b). Similarly, the polarizing beamsplitter D and prism D of Figure 5.10(c) are also combined into one component (Figure 5.10(d)).

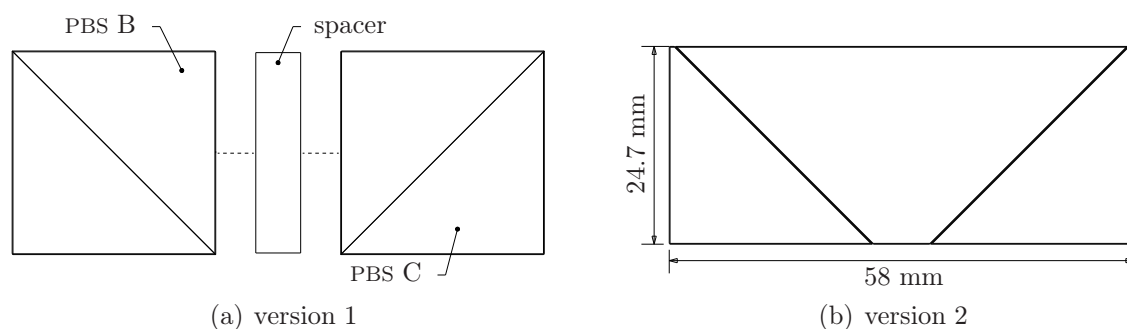


Figure 5.8 / The two 10 mm thick PBSs and the spacer of the first version (Figure 5.7) are integrated into one three-part component in the second version. This reduces the alignment effort, the number of optical interfaces and the material differences along the beam.

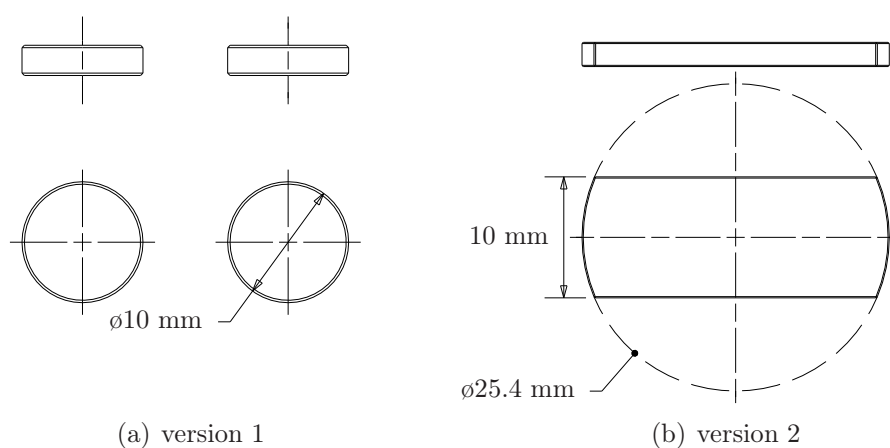


Figure 5.9 / Each set of two $\phi 10$ mm QWPs (A and B or C and D) are integrated into one 10 mm high section of a $\phi 1$ inch QWP.

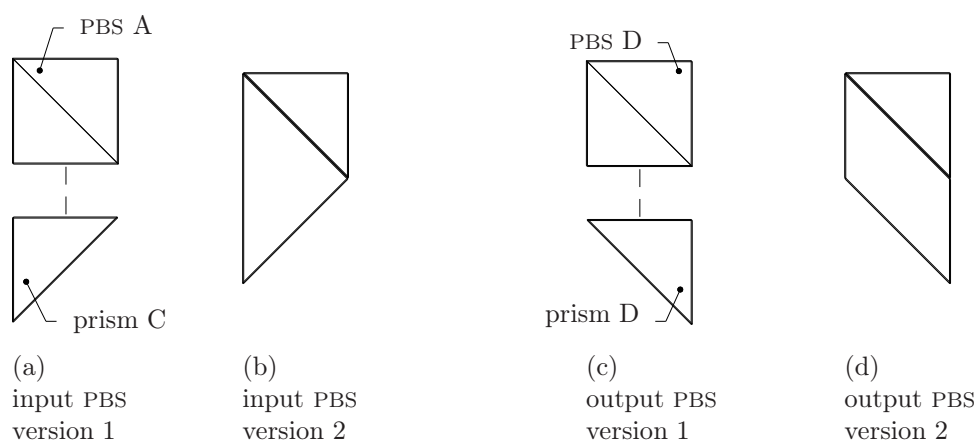


Figure 5.10 / The input prism and PBS A are combined into one preassembled component. The output prism is similarly modified.

Figure 5.11 shows an exploded view of the simplified design, the assembled interferometer is shown in Figure 5.12 on the next page. The new design has nine instead of fifteen components so less alignment work is needed. Additionally, the reduced number of optical interfaces within the interferometer also decreases the number of possible sources for beam distortions and stray reflections.

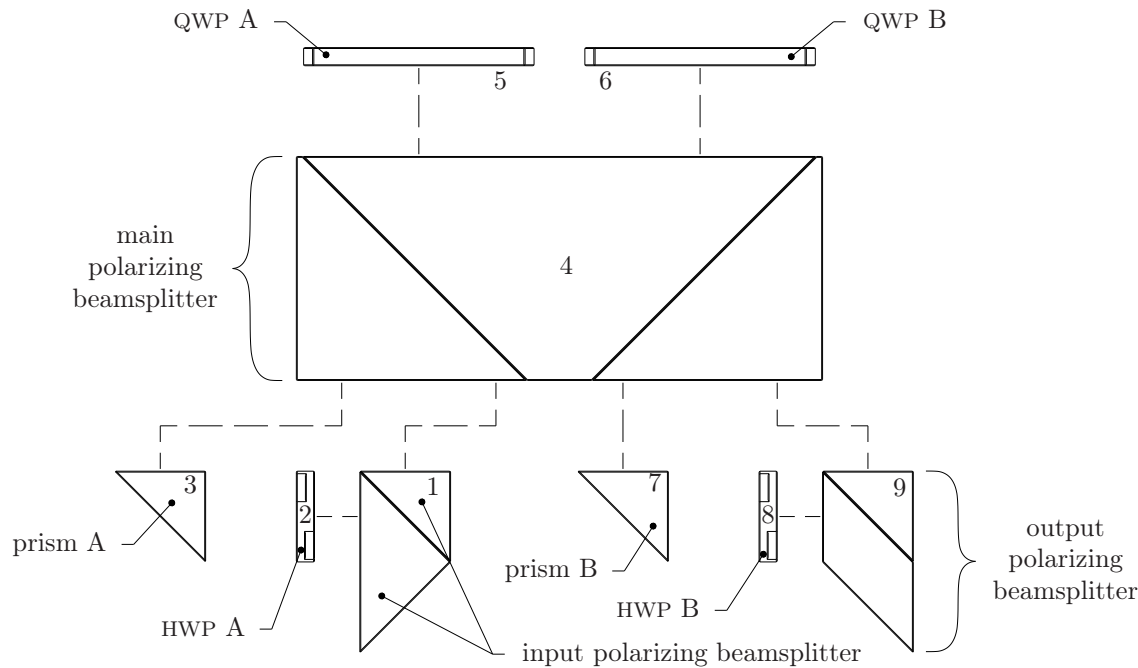


Figure 5.11 / Exploded view of the simplified DPML. Compared to version 1 this new design has nine instead of fifteen components.

Table 5.1 summarizes the interferometer component specifications. The values are typical for high-precision laser optics. All beam entrance and beam exit surfaces are anti-reflection (AR) coated, as suggested by [111].

material	BK7
flatness	$\lambda/10$ @ 633 nm
angular tolerance ^a	± 5 arcsec
surface quality	scratch/dig: 40/20
AR coating	$R < 0.25\%$ @ 633 nm
polarizing coating	$T_p > 95\%$, $T_n < 0.5\%$

^apolished surface to polished surface

Table 5.1 / Summary specifications interferometer components.

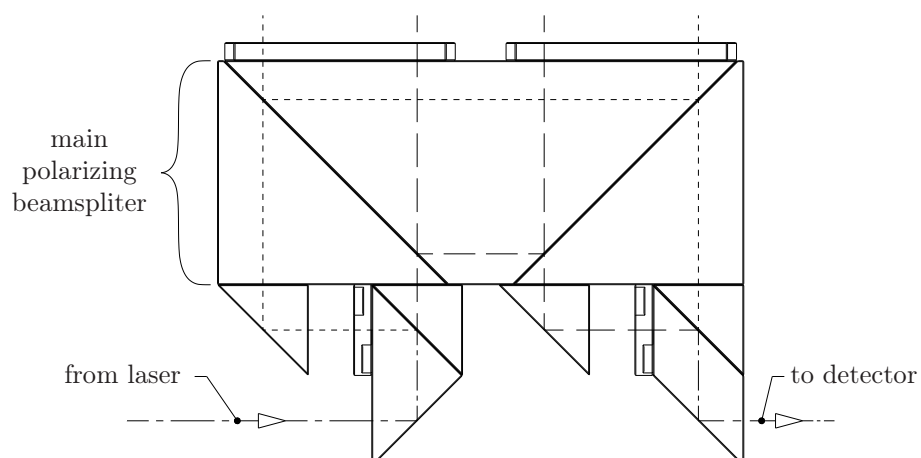


Figure 5.12 / The simplified DPML. The overall dimensions are $58 \times 46.6 \times 10$ mm. Figure 5.11 gives an exploded view.

Figure 5.13 gives a photograph of the parts. The assembly procedure is discussed in the next section.

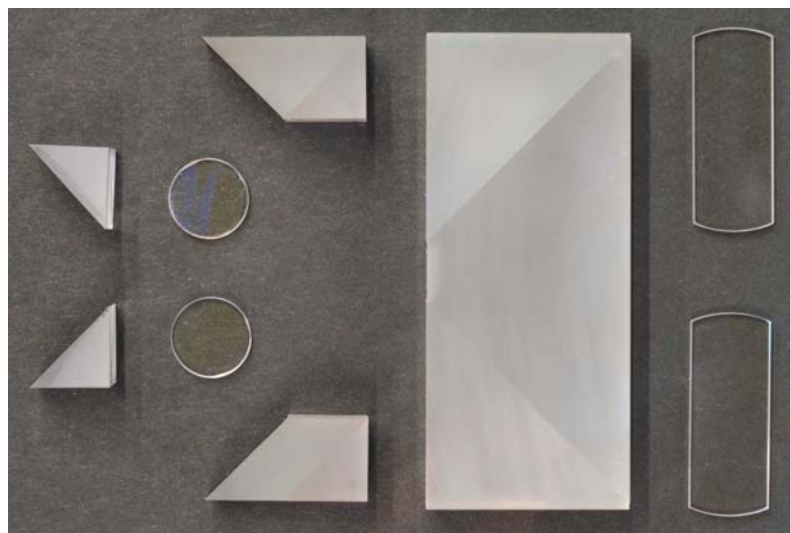


Figure 5.13 / Optical components for one interferometer. From left to right: prisms, HWPs, input beamsplitter (top) and output beamsplitter (bottom), main polarizing beamsplitter and QWPs.

5.2.3 Assembly procedure

The interferometer is assembled around the main polarizing beamsplitter (MPBS). All components are joined to the MPBS with UV-curing, index-matched, optical cement. The components are added in the same order as the laser beam travels through the interferometer. This makes it possible to correct for beam path deviations caused by already installed components with the installation and alignment of the next optical component. Once a component is properly aligned, the optical cement is cured so the component is permanently fixed to the MPBS.

All components are positioned such that the beam exiting the component is properly oriented. The spatial orientation of this exiting beam is determined by measuring the beam's position with a position sensitive detector (PSD) at two fixed positions along the beam.

This assembly method is only practical when using some sort of jig to align and hold the interferometer's nine components. Figure 5.14 gives a schematic view of such interferometer assembly jig.

The assembly jig constrains the MPBS's movements and has manipulators for the other optical components. These manipulators hold the optical components against the MPBS. Each has a mechanism to adjust the component's position and orientation. This not only simplifies the component alignment but also makes it possible to fully assemble the interferometer before curing or even applying the glue. With this temporarily assembled interferometer, the sensitivity to individual component misalignments can be tested. Additionally, it provides an opportunity to test and perfect the assembly procedure.

Next to the assembly jig is the mirror and PSD block. The rectangular mirror fixed to this mirror and PSD block, is large enough to reflect all reference beams and measurement beams simultaneously. Additionally, the block has four individual kinematic mounts for the PSD, the distances between these mounts correspond with the interferometer's reference beam and measurement beam spacing. The PSD mounts place the sensor in front of the mirror.

The mirror and PSD block itself connect with either of two kinematic mounts at positions A and B. These two kinematic mounts are fixed to the solid world and reference the PSD's position to the position of the MPBS. This reference is necessary to measure the beam position and the beam orientation relative to the optical components.

Finally, a two frequency helium-neon laser source, three other kinematic mounts for the PSD and several additional optics like a pentaprism and a linear polarizer, complete the interferometer assembly jig.

step 1 - input polarizing beamsplitter

In the first step, the input polarizing beamsplitter is added to the MPBS (Figure 5.15).

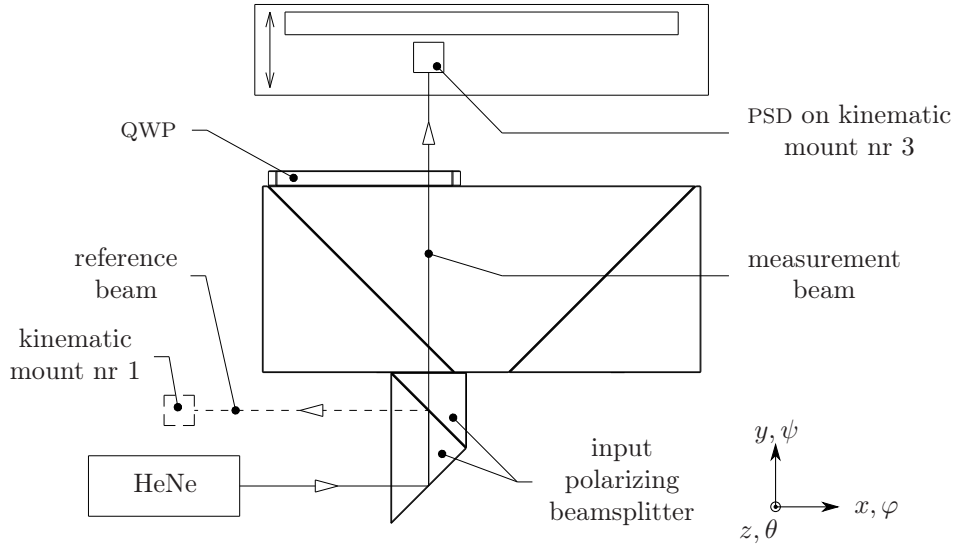


Figure 5.15 / Interferometer assembly procedure - step 1. The contact between the input polarizing beamsplitter and the MPBS constrains the y, φ and θ DOFs, the manipulator constrains the x and z translations and ψ rotation. Figure not to scale, this step corresponds with step 8 in Appendix F.

The MPBS, the assembly jig, the mirror and PSD block mounts and the laser are already aligned in previous steps. The first QWP is temporarily installed so its influence on the beam path is taken into account.

Next, the input polarizing beamsplitter is placed against the MPBS, the contact of both components constrains the y translation as well as the φ and the θ rotations. The manipulator constrains the remaining two translational DOFs and the ψ rotation.

The manipulator translates the component to get the measurement beam centralized on the PSD at both positions of the mirror and PSD block. This aligns the measurement beam with the interferometer's nominal measurement axis.

For the input beamsplitter's ψ alignment the PSD is moved to the previously aligned kinematic mount 1. The beamsplitter is then rotated until the reference beam aligns with the PSD's center. Step 2 discusses the reference beam's polarization orientation.

step 2 - orientation half-wave plate A

In this step half-wave plate (HWP) A is installed (Figure 5.16). This component rotates the reference beam's polarization parallel to the measurement beam's polarization.

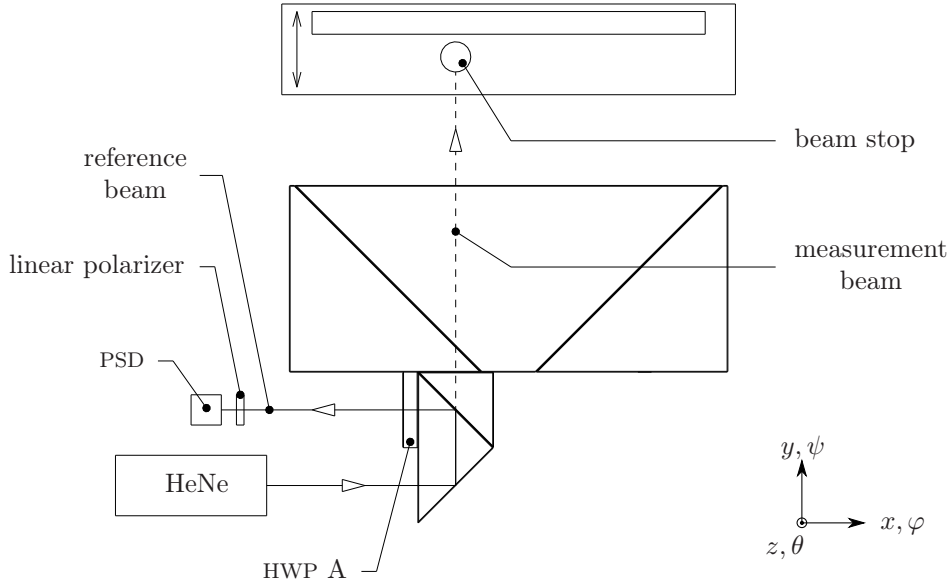


Figure 5.16 / Interferometer assembly procedure - step 2. The linear polarizer is set up to transmit only the light that is polarized parallel to the measurement beam. Rotating HWP A in φ changes the reference beam intensity measured by the PSD, the intensity is maximum when the reference beam polarization is parallel to the measurement beam polarization. The beam stop prevents unwanted measurement beam reflections. Figure not to scale, this step corresponds with step 11 in Appendix F.

The PSD and the linear polarizer are temporarily installed into the reference beam. The linear polarizer's optical axis is aligned parallel to the measurement beam's polarization direction at an earlier stage in the assembly procedure. Consequently, the polarizer only transmits light that is polarized parallel to the measurement beam. Next, the HWP A is placed against the input polarizing beamsplitter and rotated (φ) until the reference beam intensity measured by the PSD is maximal. A simpler photodiode detector could replace the PSD here because no beam position information is needed.

step 3 - prism A

Now the first prism (A) is added to the interferometer assembly (Figure 5.17).

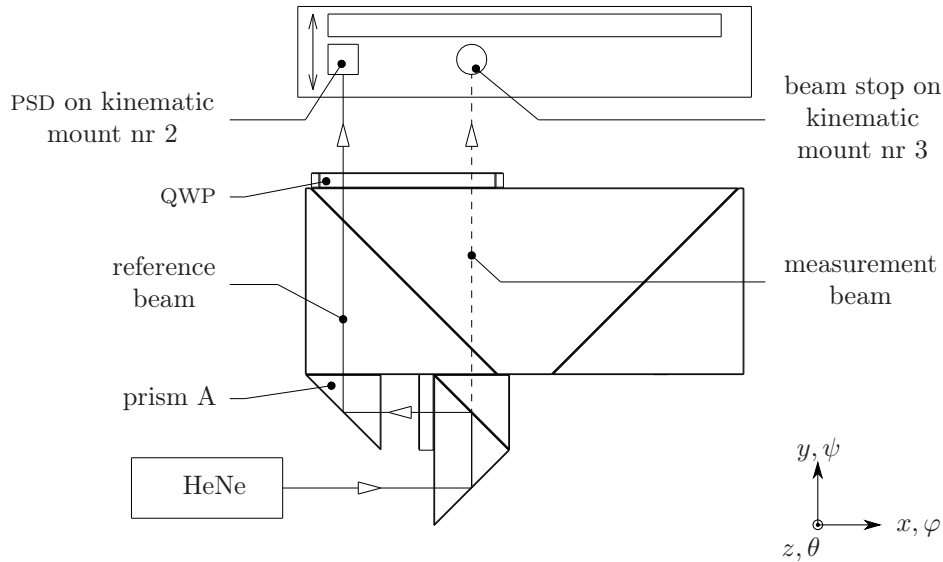


Figure 5.17 / Interferometer assembly procedure - step 3. The PSD on kinematic mount 2 defines the reference beam position. The prism A position is tuned so the measurement beam and reference beam are as parallel as possible. Figure not to scale, this step corresponds with step 12 in Appendix F.

The PSD is moved to kinematic mount number 2, this mount physically refers the reference beam position to the measurement beam position and consequently determines the beam spacing. Prism A is then installed and manipulated (x, z, ψ) until the reference beam centers on the PSD. This alignment is checked with the mirror and PSD block at position B.

The prism's φ and θ rotations and the y translation are constrained in the prism-to-MPBS contact and are therefore not directly adjustable. If small adjustments are necessary in these DOFs for proper reference beam and measurement beam parallelism, the prism itself can easily be replaced by another and inevitably slightly different prism. Additionally, some adjustments can be made within the prism to MPBS joint but this clearly must be avoided if possible.

step 4 - output polarizing beamsplitter

At the end of step 3, one half of the interferometer is assembled. In step 4 the output polarizing beamsplitter is added (Figure 5.18). This component combines the measurement beam and reference beam into one collinear beam and directs this beam towards the measurement electronic's detector.

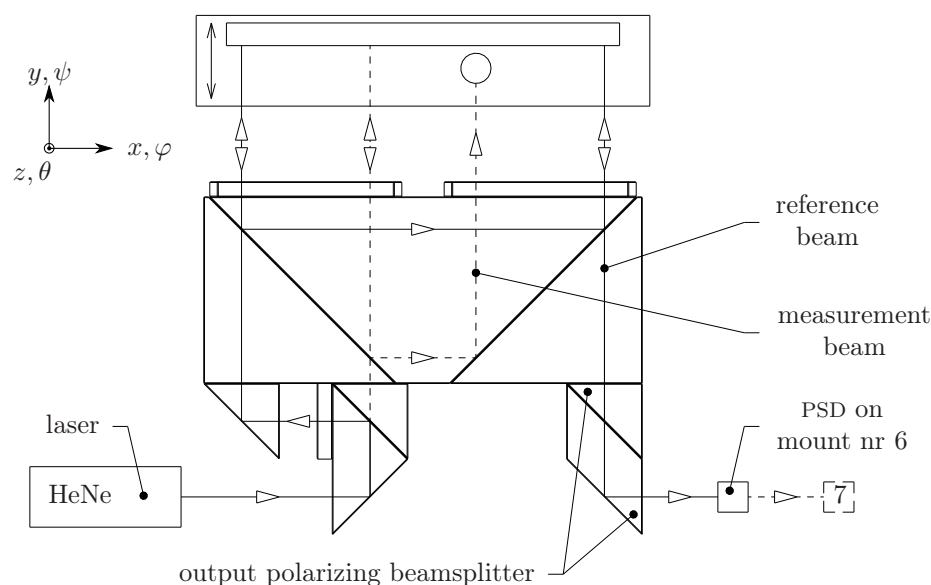


Figure 5.18 / Interferometer assembly procedure - step 4. The reference beam reflects twice of the jig's mirror before the output polarizing beamsplitter reflects it towards the PSD on mount nr 6. Kinematic mounts 6 and 7 center the PSD on the interferometer's input beam. Figure not to scale, this step corresponds with step 17 in Appendix F.

Before installing the output beamsplitter, the PSD is moved to kinematic mount nr 6. This mount aligns the PSD's center with the interferometer's input beam. Then the beamsplitter is installed and its position adjusted until the reference beam is centered on the PSD. The output beam's orientation is checked by moving the PSD to the earlier aligned kinematic mount nr 7 and measuring the beam deflection.

step 5 - prism B and HWP B

Prism B and HWP B are added to the interferometer in the fifth and final assembly step. This is a critical step in the interferometer assembly because the alignment of both components ultimately affects the measurement beam and reference beam overlap and parallelism. If both beams do not sufficiently overlap, then the interference

signal's intensity becomes too small for accurate measurements. Additionally, an angular misalignment between the two beams results in an optical path difference (OPD) which varies across the interfering beam region. This OPD changes the interference signal contrast, i.e. the intensity difference between the maximum and minimum occurring interference intensity. Without sufficient interference contrast the measurement electronics cannot detect the interference beat frequency so the interferometer doesn't function. With the $\varnothing 3$ mm laser beam the contrast is zero at about ± 45 arcsec misalignment.

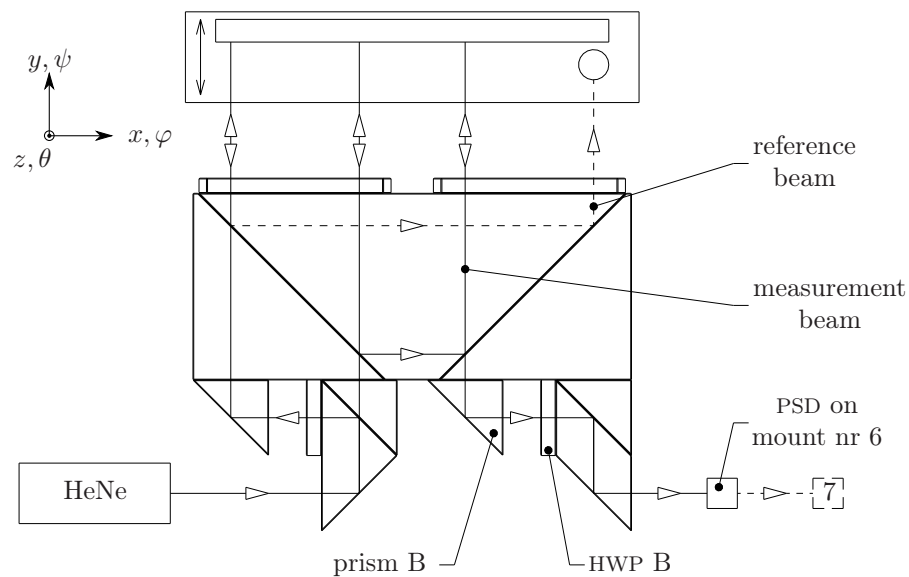


Figure 5.19 / Interferometer assembly procedure - step 5. This is the last assembly step before testing the interferometer. Prism B and HWP B are aligned so the measurement beam and reference beam overlap and are collinear. The procedure for the HWP alignment is similar to the one discussed in step 2. Figure not to scale, this step corresponds with step 19 in Appendix F.

The prism B and the HWP B are installed simultaneously so the influence of both components on the output beam's alignment is taken into account. The alignment procedure for HWP B is identical to the procedure for HWP A (step 2, Figure 5.16). Prism B is manipulated until the measurement beam fully overlaps the reference beam and, more importantly, both beams are collinear to within at least ± 10 arcsec for about 90% interference contrast.

With prism B and HWP B aligned, the interferometer is fully assembled and ready for testing. This is briefly discussed in the last step.

step 6 - interferometer testing

Figure 5.20 shows the preliminary set up to test the interferometer's resolution and stability.

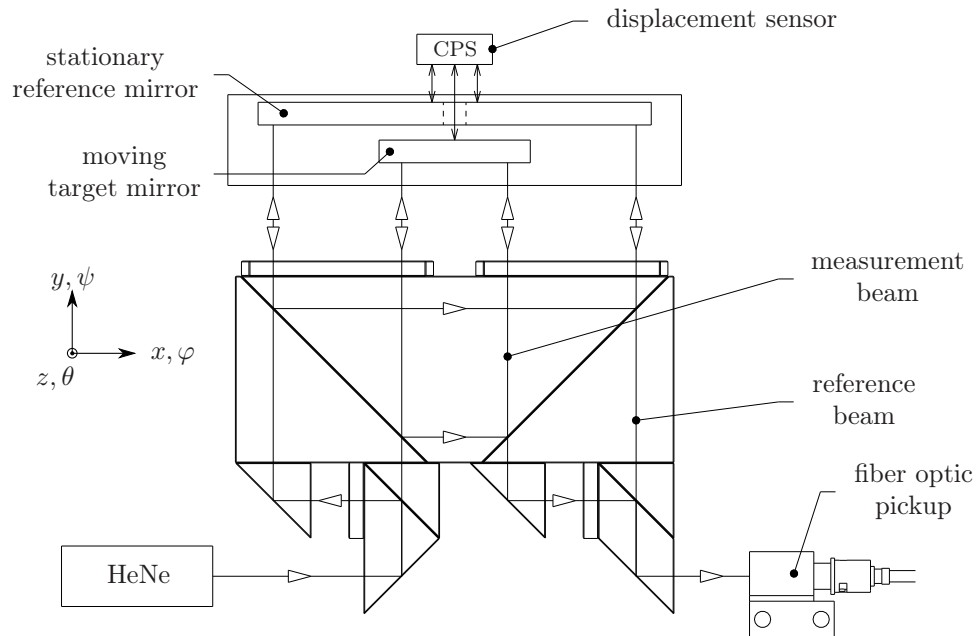


Figure 5.20 / Interferometer assembly procedure - step 6. The interferometer assembly is complete, here the performance is tested. The moving target mirror can translate in the y direction. The additional displacement sensor measures the target mirror's movements relative to the stationary reference mirror. Comparing the interferometer's output with the additional sensor's signal yields the interferometer's non-linearity. The interferometer stability is tested by reflecting the measurement beams and the reference beams all of the same stationary reference mirror. Figure not to scale, this step corresponds with step 22 in Appendix F.

A commercial fiber optic pickup is aligned to the interferometer's output beam. This pickup has a linear polarizer which combines the orthogonally polarized measurement beam and reference beam into one interfering beat signal. A fiber optic cable transports this optical interference signal to a detector on the measurement electronics board where the optical signal is converted into electronic displacement data.

An extra mirror, the moving target mirror, is installed on the mirror and PSD block, this mirror reflect the interferometer's two measurement beams. The moving target mirror can translate over a small distance along the y direction while the reference mirror on the block remains stationary. A suitable capacitive position sensor (CPS) or an extra DMI measures the moving target mirror's displacement in Abbe through a small hole in

the stationary reference mirror.

The interferometer's non-linearity is visible when comparing the interferometer's output with the CPS output while moving the target mirror [28]. This non-linearity limits the interferometer's resolution [21].

For the interferometer stability measurements, the moving target mirror is removed so the stationary reference mirror reflects the reference beams as well as the measurement beams. Any measured displacement is now caused by either interferometer instability or measurement electronics drift. Movements of the reference mirror have no influence on the measurement due to the interferometer's differential layout.

The interferometer assembly jig design is not complete at the time of writing. The interferometers have therefore not been assembled.

5.2.4 Optics support box

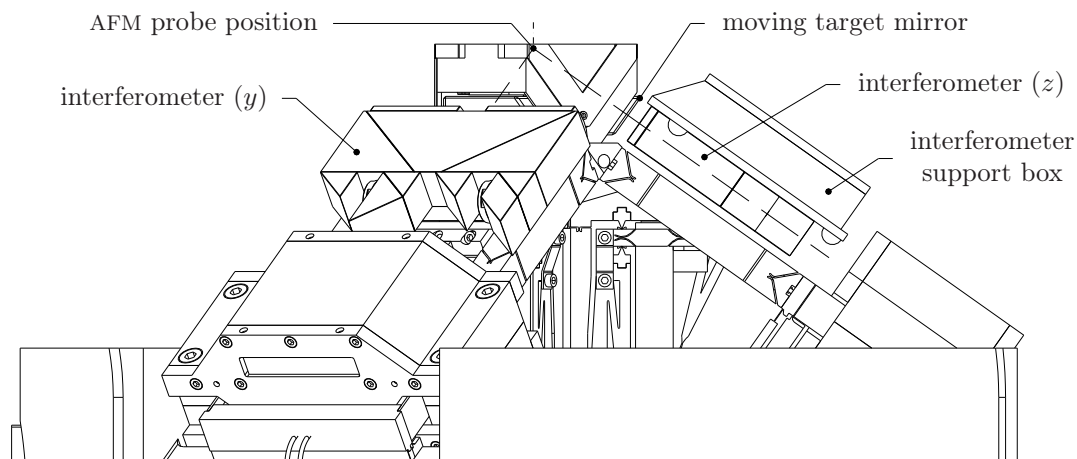


Figure 5.21 / Side view of the instrument. The interferometer optics are above the struts and are connected to the interferometer support box. The box is kinematically fixed to the instrument. The kinematic mount and the y -interferometer's support box are not shown.

Figure 5.21 shows the interferometers in the instrument. Each interferometer is attached to the underside of an interferometer support box. These support boxes are, in turn, kinematically mounted on the instrument. With this kinematic mount, the interferometer can be easily removed from the instrument for inspection or cleaning and can be re-installed without requiring extensive realignment.

The interferometer optic support box is made from seven, 2 mm thick, laser cut Al_2O_3 plates (Figure 5.22).

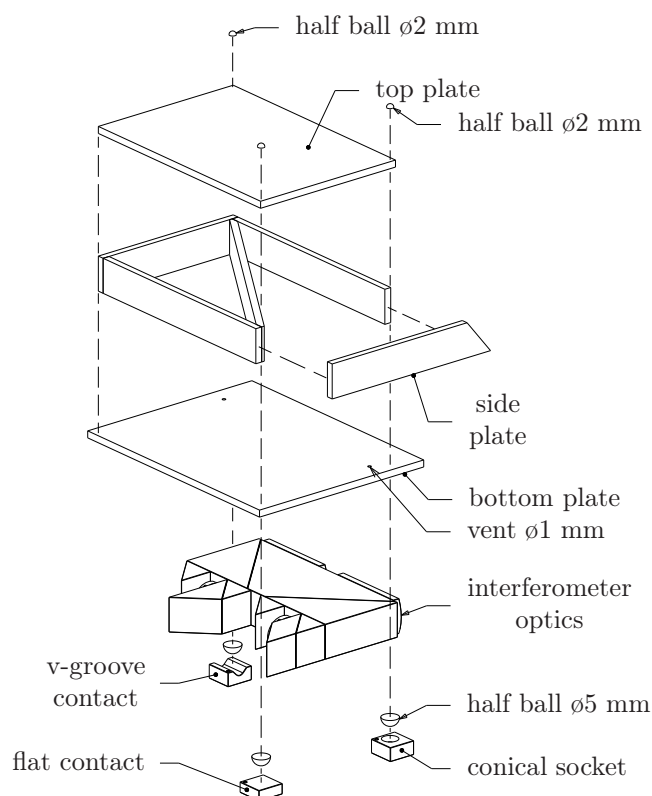


Figure 5.22 / The interferometer support box ($56 \times 72 \times 14$ mm, 78.6 g) is assembled from seven Al_2O_3 plates. The box is kinematically connected to the instrument. Both cambers in the box are ventilated.

Three Al_2O_3 half balls $\varnothing 5$ mm are glued to the underside of the bottom plate. The half balls mesh with a conical socket, a v-groove contact and a flat contact on the instrument and together form a kinematic mount for the interferometer support box. The top plate holds three hardened steel half balls $\varnothing 2$ mm, these half balls mesh with the interferometer support box preload frame (Figure 5.23). The steel half balls are directly above the Al_2O_3 half balls for minimal bending of the interferometer support box.

The shape of the box and the position of the kinematic contacts is optimized towards maximum eigenfrequency. The combined center of gravity (COG) of the interferometer optics and the support box lies within the triangle spanned by the contact points. This simplifies the interferometer installation on the instrument because the interferometer stays in position even without the preload frame.

The high specific stiffness (E/ρ) of Al_2O_3 helps to maximize the support box eigenfrequency. Additionally, the coefficient of thermal expansion (CTE) of Al_2O_3 is practically identical to the CTE of the interferometer glass (BK7) so there is minimal thermal stress in the interferometer-to-support connection.

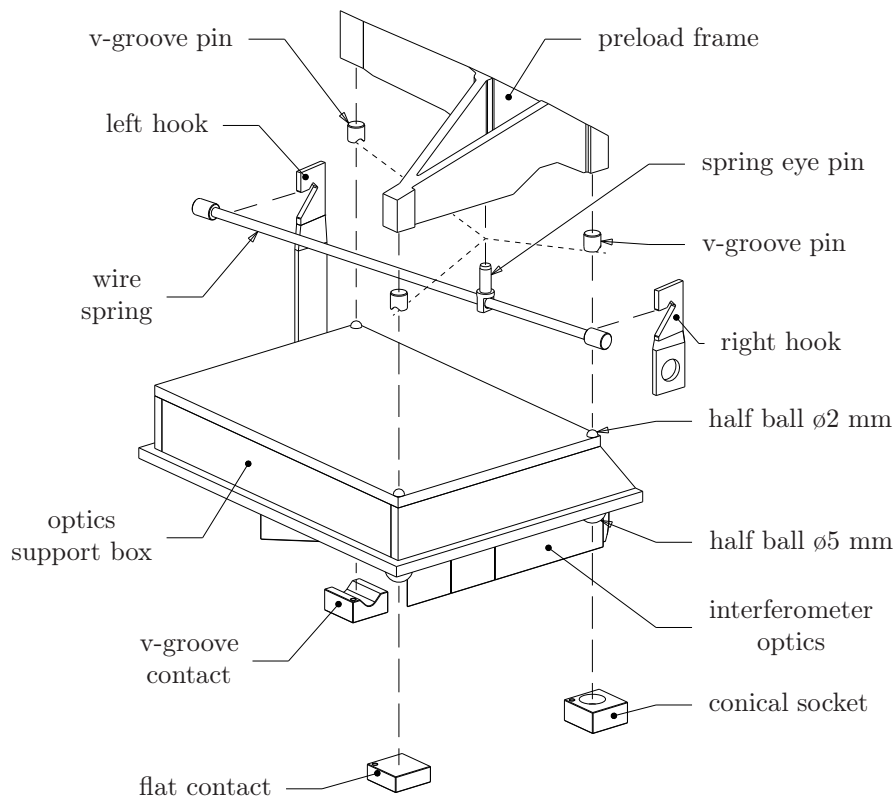


Figure 5.23 / Exploded view of the support box' preload assembly. The preload frame's three v-grooves mesh with the half balls on the optics support box. The wire spring $\phi 1.7 \times 96$ mm delivers the preload force.

Figure 5.23 shows the interferometer support box' preload assembly. Three tungsten carbide v-groove pins in the aluminium preload frame, mesh with the steel half balls $\phi 2$ mm on the interferometer support box. A steel wire spring threaded through the preload frame's spring eye, generates the preload force. Two hooks fix the wire spring to the instrument base.

The grooves in the preload frame's v-groove pins align with the spring eye so the preload force alignment is independent of temperature. Similarly, the low stiffness wire spring is considerably deflected to make the preload force practically insensitive to temperature variations. The left hook and the right hook transfer the spring forces to the instrument base with minimal bending moments while the pivot-rule [93] compliant design minimizes the hysteresis. Notches in the hooks simplify the preload assembly installation and spring preloading.

The eigenfrequency of the interferometer support box with the interferometer optics mass and the contact stiffness' taken into account, is about 2.6 kHz.

To align the interferometer to the moving target mirror, some adjustment of the interferometer's position and orientation is necessary. Because the Al_2O_3 half balls cannot be moved without introducing bending stresses in the interferometer support box, the kinematic mount on the instrument base is adjusted instead.

The position and the orientation of the interferometer's kinematic mount is adjusted using spacers (Figure 5.24). Although this is a more time-consuming procedure than, for example, adjustment with an elastic mechanism, it is simple, mechanically stable and potentially unlimited in range and is therefore used here.

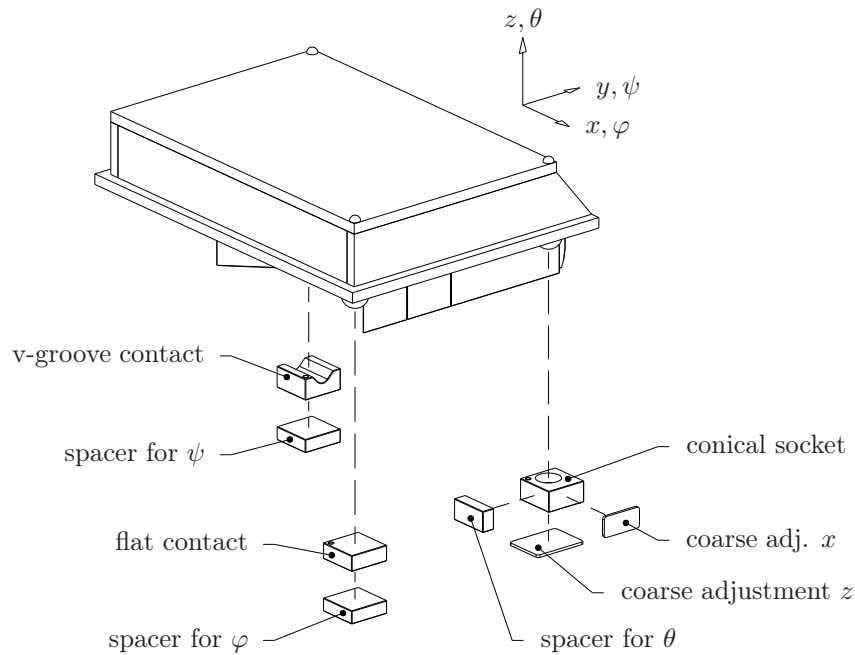


Figure 5.24 / The interferometer's position and orientation is adjusted using spacers. The rotations are independently adjustable, the (less important) position is not.

The three rotational DOFs can be adjusted independently by changing one spacer at a time. Conversely, changing the, less important, translational DOFs can require simultaneous changes to more than one spacer.

Initially, the spacers are made by stacking up to four gauge block sections together. Exchanging one or more gauge block sections in the stack conveniently changes the spacer thickness. This gives a minimal rotation change of less than 4 arcsec while the smallest increment for translation adjustments is 0.025 mm.

When the interferometer is properly aligned, the spacer stack is measured and replaced by a one-piece spacer made to the required thickness for increased mechanical stability. The kinematic mount's conical socket, the v-groove contact and the flat contact are machined (EDM) from tungsten carbide gauge blocks.

A photograph of the optics support box and the preload assembly is given in Figure 5.25. Figure 5.26 shows a photograph of the kinematic mount.

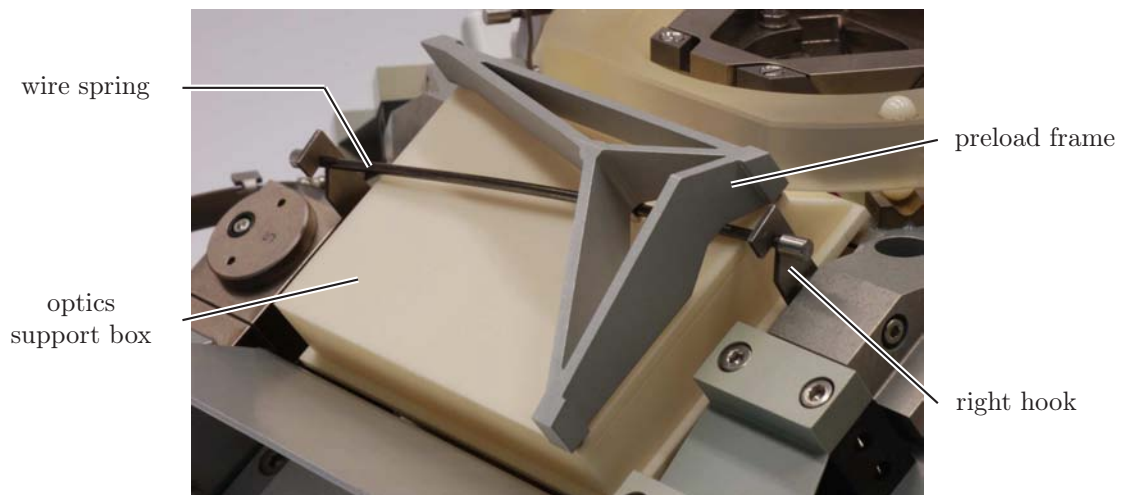


Figure 5.25 / Interferometer support box and preload assembly on the instrument.

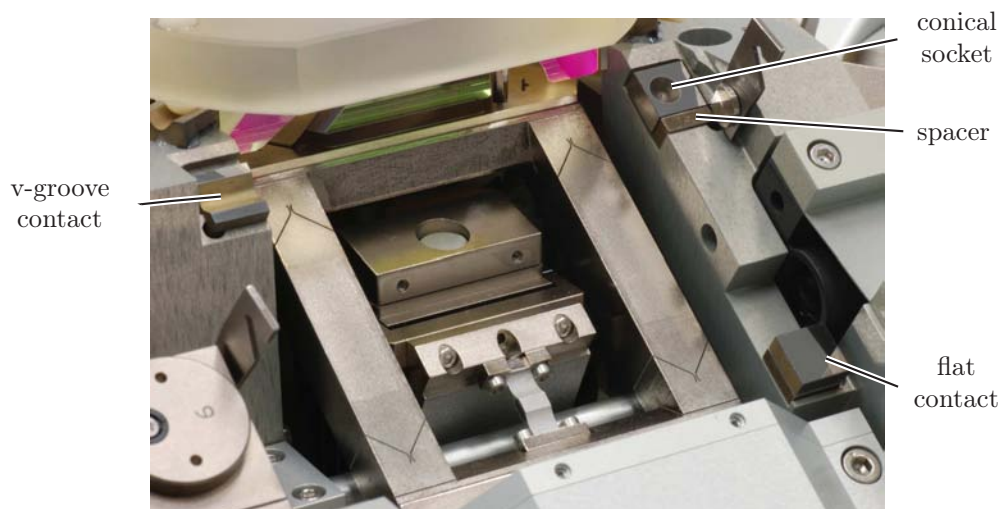


Figure 5.26 / The interferometer's kinematic mount is adjusted using spacers. The conical socket, v-groove and flat contact are machined from tungsten carbide gauge blocks.

5.3 Interferometer target and reference mirror

The interferometric displacement measurement system uses a moving target mirror and a stationary reference mirror. The moving target mirror is connected to the sample table while the stationary reference mirror is directly attached to the AFM head.

The moving target mirror is discussed in the next section. Section 5.3.2 discusses the stationary reference mirror.

5.3.1 Moving target mirror

Figure 5.27 shows the top view, side view and bottom view of the moving target mirror.

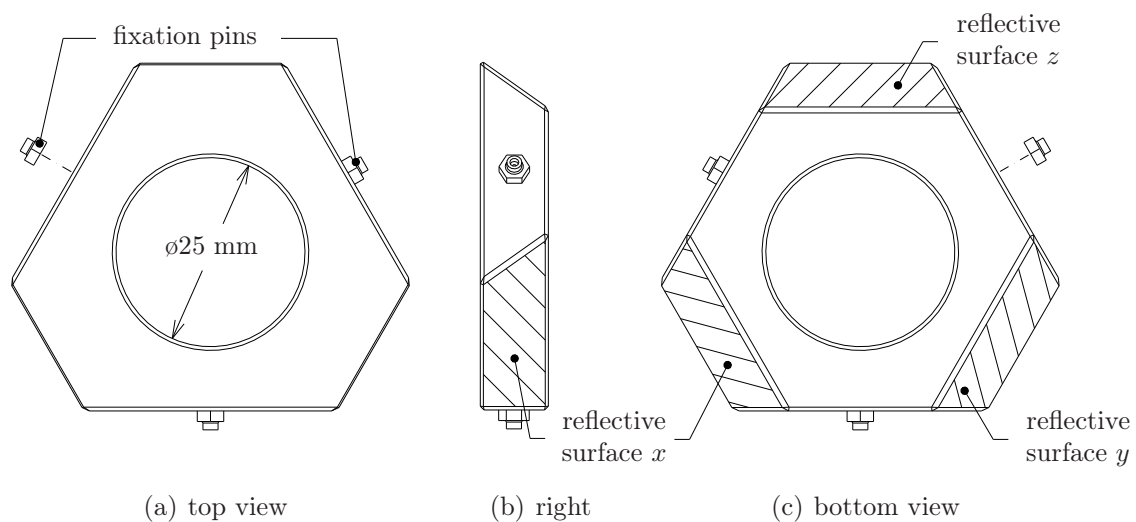


Figure 5.27 / The moving target mirror (Zerodur®) with three mutually orthogonal reflective surfaces (hatched areas). The mirror is 9 mm thick, weighs 25 g and has an estimated eigenfrequency of 10.8 kHz. Three Invar® fixation pins connect the mirror to the sample table.

The moving target mirror has three mutually orthogonal, reflective surfaces. Three Invar® fixation pins connect the mirror to the sample table assembly (Figure 5.28 on the next page, see also Figure 3.3 on Page 32).

The mirror is made from Zerodur® for maximal thermal stability. The fabrication starts with a Zerodur® cube (Figure 5.29(a)). Three adjacent sides of the cube are first made mutually orthogonal within ± 90 arcsec (see below) and then polished. The block is then cut to free the mirror (Figure 5.29(b)). Next, a hole $\varnothing 25$ mm is drilled to reduce the mirror's mass. All edges are then beveled to minimize the risk of chipping. A dielectric coating is applied to the reflective surfaces in the final step.

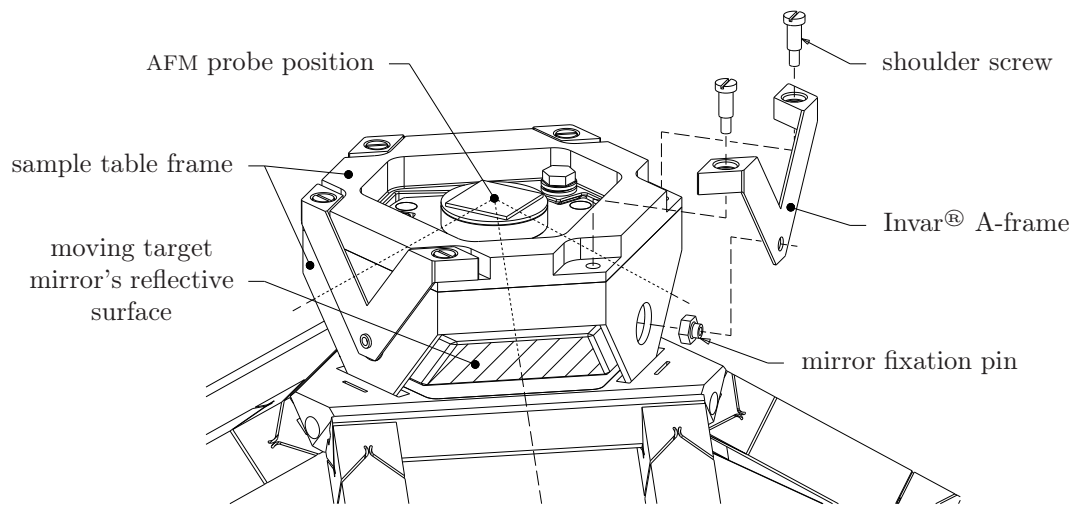


Figure 5.28 / Moving target mirror support. Three Invar[®] A-frames fully constrain the mirror to the sample table frame. See also Page 32.

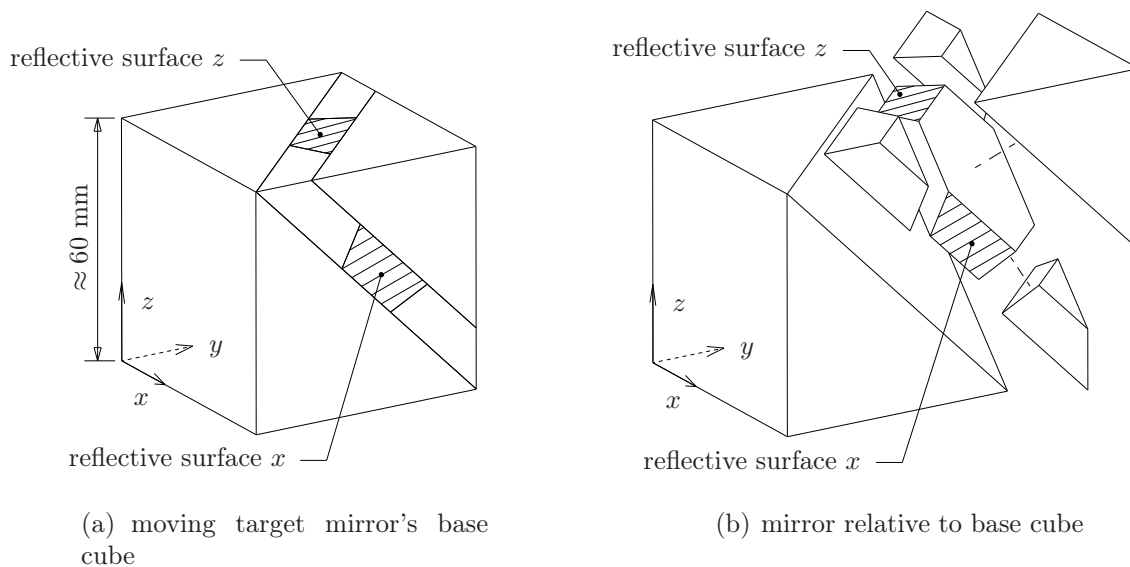
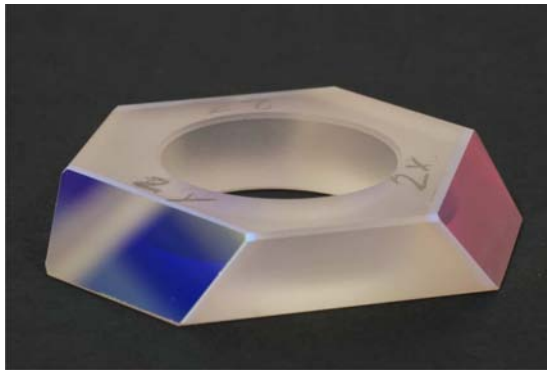


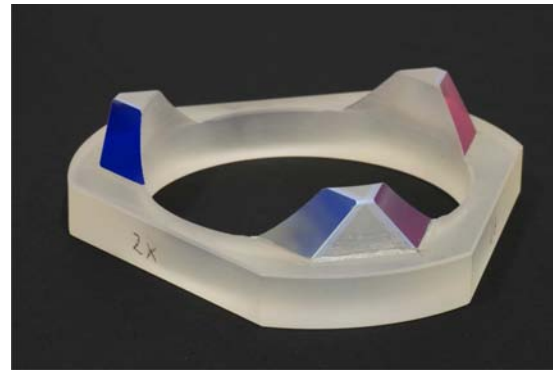
Figure 5.29 / The moving target mirror is machined from a Zerodur[®] cube. The mirror's reflective surfaces are hatched.

Fabricating a rather flat component like the moving target mirror from a cube gives relatively large offcuts, but has several advantages. Firstly, to make a cube accurately orthogonal is less difficult than grinding three faces towards mutual orthogonality on a flat component. Secondly, because the mirror's reflective surfaces are close to the centers of the cube's sides, typically the flattest area on a polished surface, it is relatively easy to achieve a high surface flatness.

Since the mirror's orthogonality will be calibrated anyway, it is not economical to specify very strict orthogonality tolerances. The deviations must, however, be within the measurement range of the calibration set up [103]. As the calibration set up at VSL can measure deviations of up to ± 100 arcsec, a ± 90 arcsec orthogonality tolerance is specified. The reflective surface flatness is, in close consideration with VSL, specified at $\lambda/10$ @ 633 nm. Apart from the reflective surfaces, there are, by design, no strict dimensional tolerances or surface quality requirements.



(a) moving target mirror



(b) stationary reference mirror

Figure 5.30 / The moving target mirror and the stationary reference mirror (discussed in Section 5.3.2). Both mirrors are shown upside down and differently scaled. The reflective surfaces are dielectrically coated for normal incidence.

Figure 5.30(a) shows a photograph of the mirror. The mirror's orthogonality and flatness are traceably measured at VSL. Table 5.2 summarizes the measurement results.

angle	orthogonality error (arcsec)	reflective surface	flatness ^a (<i>p-p</i>)
$x - z$	0.2 ± 0.1	x	$\lambda/25$
$y - x$	3.5 ± 0.1	y	$\lambda/20$
$z - y$	-2.7 ± 0.1	z	$\lambda/15$
^a $\lambda = 633$ nm			

Table 5.2 / Measured orthogonality and flatness of the moving target mirror. Specifications: orthogonality error $\leq \pm 90$ arcsec, flatness $\leq \lambda/10$ @ 633 nm. Measured at VSL.

The mirror's orthogonality and surface flatness are better than specified.

5.3.2 Stationary reference mirror

The stationary reference mirror is also made from Zerodur® (Figure 5.31).

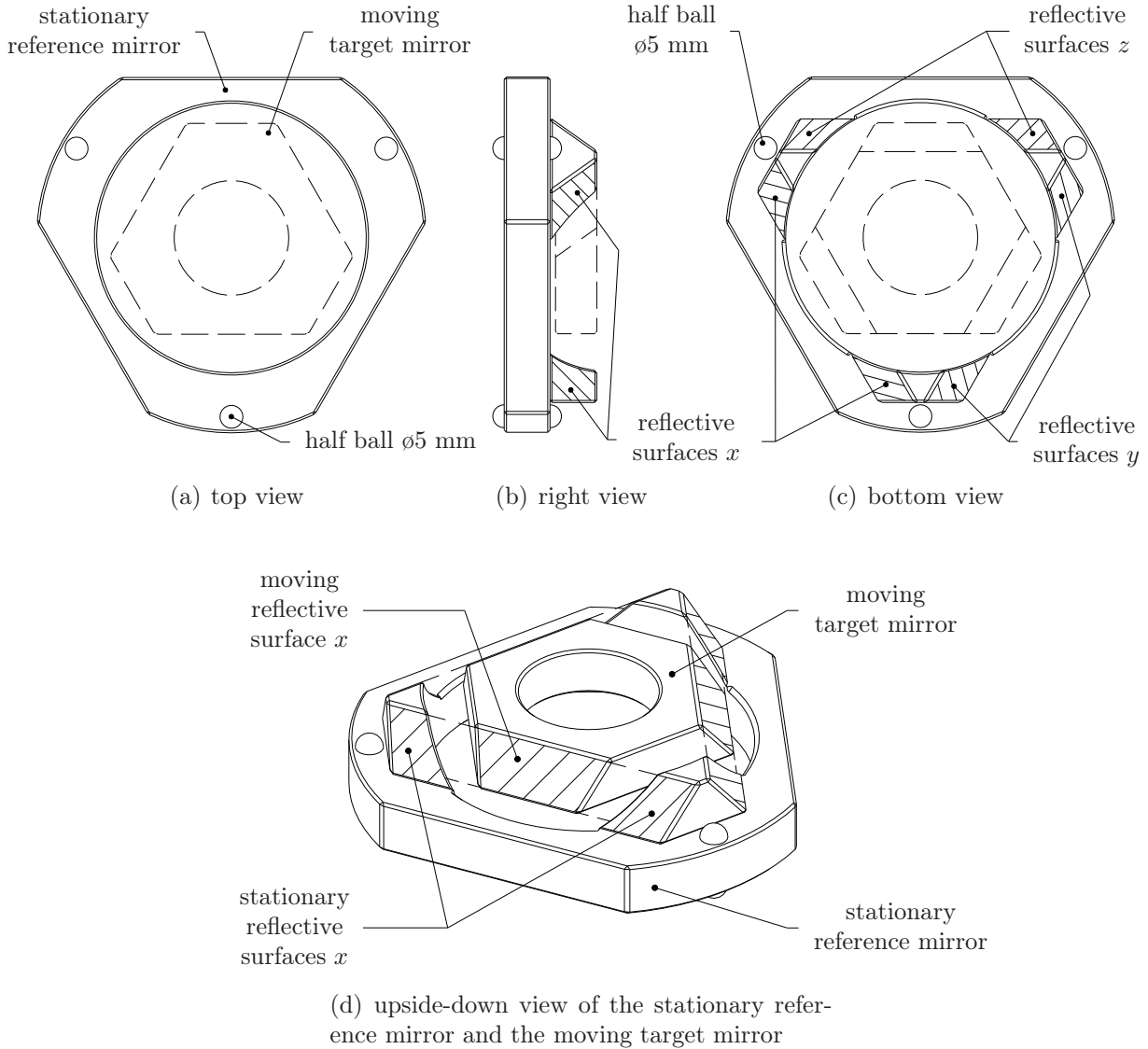


Figure 5.31 / The stationary reference mirror (Zerodur®). The mirror's mass is 65 g, the first eigenmode is estimated at 3.4 kHz. The three ø5 mm half balls on the top side mesh with the AFM head while the three half balls at the underside locate the mirror on the instrument. The stationary reference mirror's reflective surfaces align with the moving target mirror's reflective surfaces (d).

The stationary reference mirror's reflective surfaces align with the moving target mirror's reflective surfaces for minimal dead path error [113] (Figure 5.31(d)). Three Al_2O_3 half balls (ø5 mm) glued to the stationary reference mirror's underside, mesh

with three tungsten carbide v-groove contacts on the instrument base (Figure 5.32). This kinematic connection simplifies the mirror's periodic cleaning and inspection, because the mirror can be reinstalled on the instrument without requiring re-alignment (measured repositioning error < 1 arcsec).

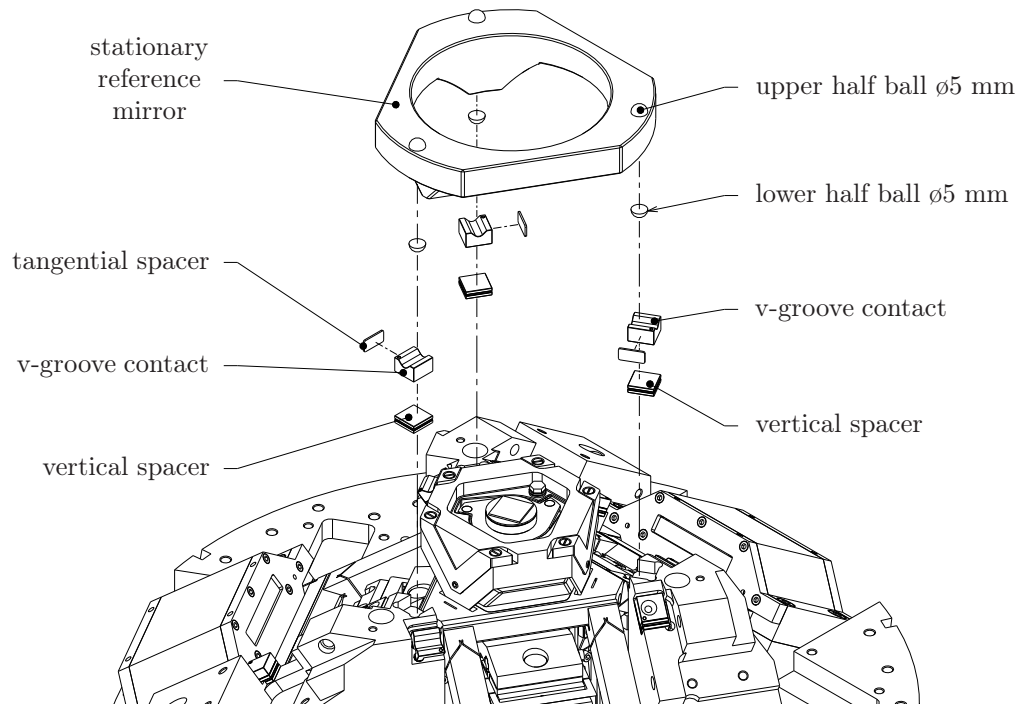


Figure 5.32 / The stationary reference mirror's lower three half balls mesh with three v-groove contacts on the instrument base. Three tangential spacers and three vertical spacers locate the v-groove contacts on the instrument. The spacer thicknesses are adjusted to align the stationary reference mirror.

The AFM head meshes to the three half balls on the mirror's top side. The three half balls on the top are directly above the three half balls at the underside to minimize the bending moments on the mirror.

The stationary reference mirror and the moving target mirror can be fabricated out of the same Zerodur[®] base cube. However, this is, for simplicity, not shown in the stationary reference mirror's fabrication procedure (Figure 5.33).

The orthogonal, polished base cube shown in Figure 5.33(a) is cut to separate the mirror section (Figure 5.33(b)). In the third step (Figure 5.33(c)), the mirror section is glued onto a Zerodur[®] support disc. A hole $\varnothing 60$ mm is then drilled through the mirror section and support disc (Figure 5.33(d)). Next, all edges are slightly beveled

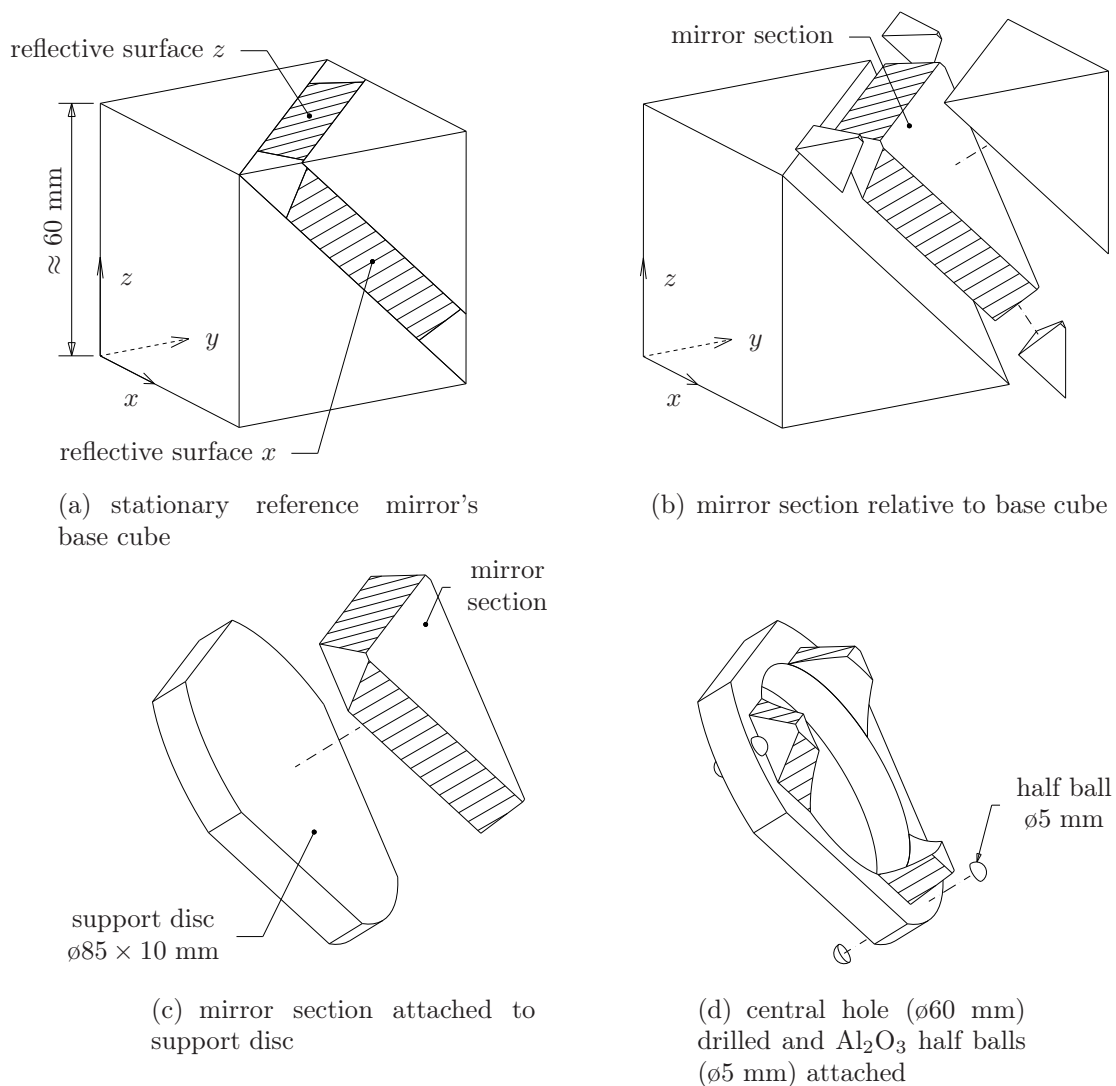


Figure 5.33 / Fabrication steps of the stationary reference mirror. The mirror is machined from a Zerodur[®] cube and attached to a Zerodur[®] support disc. The six Al_2O_3 half balls ø5 mm are glued onto the support disc in the last step.

and the reflective coating applied. Finally, the six Al_2O_3 half balls ø5 mm are glued to the support disc.

Figure 5.30(b) on Page 120 gives a photograph of the stationary reference mirror. Joining the mirror section to the support disc with adhesive before drilling the hole ø60 mm, keeps the reflective surfaces mutually aligned.

The stationary reference mirror's reflective surfaces extend nearly towards the edges of the base cube, which is disadvantageous for the surface flatness. Fortunately, the stationary reference mirror flatness is less critical because the interferometer reference beams do not actually move over the mirror's reflective surfaces.

Orthogonality differences between the stationary reference mirror and the moving target mirror, affect the beam paths in the interferometer and are therefore specified 'as small as reasonably possible'. The specified reflective surface flatness is identical for both mirrors.

For the stationary reference mirror, only the manufacturer's measurement data is available (Table 5.3). The data is considered reliable because the manufacturer's data for the moving target mirror agreed well with the VSL measurement results.

angle	orthogonality error (arcsec)	difference ^a (arcsec)	reflective surface	flatness ^b ($p-p$)
$x - z$	-3	-1	x	$\lambda/11$
$y - x$	2	-1	y	$\lambda/11$
$z - y$	0	-1	z	$\lambda/12$
^a between moving and stationary mirror			^b $\lambda = 633 \text{ nm}$	

Table 5.3 / Measured orthogonality and flatness of the stationary reference mirror. Data provided by manufacturer [8]. Indicated orthogonality differences between the moving target mirror and the stationary reference mirror are based on the manufacturer's data.

The stationary reference mirror's orthogonality agrees to within a few arcsec with the moving target mirror's orthogonality. The stationary reference mirror's reflective surface flatness is, as expected, slightly lower than the moving target mirror's flatness.

Figure 5.34 shows a photograph of the stationary reference mirror and the moving target mirror installed in the instrument.

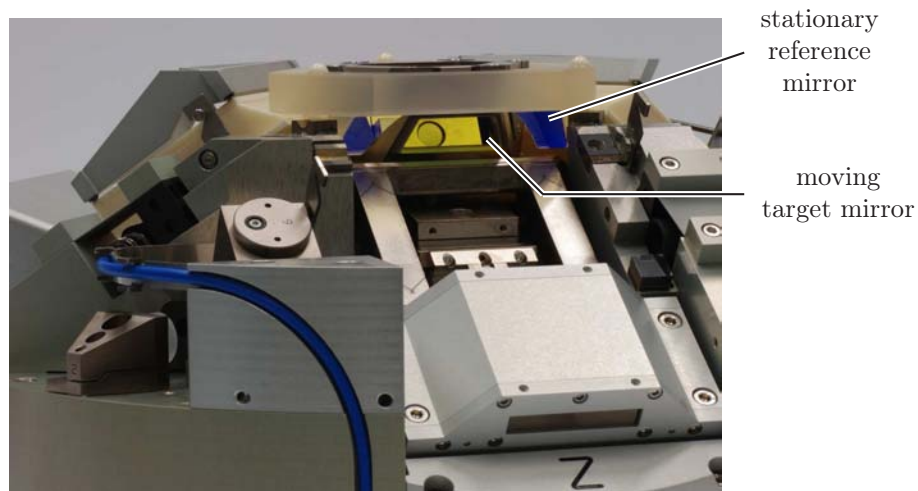


Figure 5.34 / The moving target mirror and the stationary reference mirror installed in the instrument.

5.4 Beam delivery

The beam delivery system divides the laser source's beam into three equal-intensity beams and reflects these beams towards the three interferometers. Fiber optic pickups and cables, guide the laser beams towards the measurement electronics after the beams have passed through the interferometers. The beam delivery system and the fiber optics are integrated into the instrument for maximum thermal and mechanical stability and minimal instrument footprint.

The beam delivery system is discussed first, the fiber optic components are described from Page 130 onward.

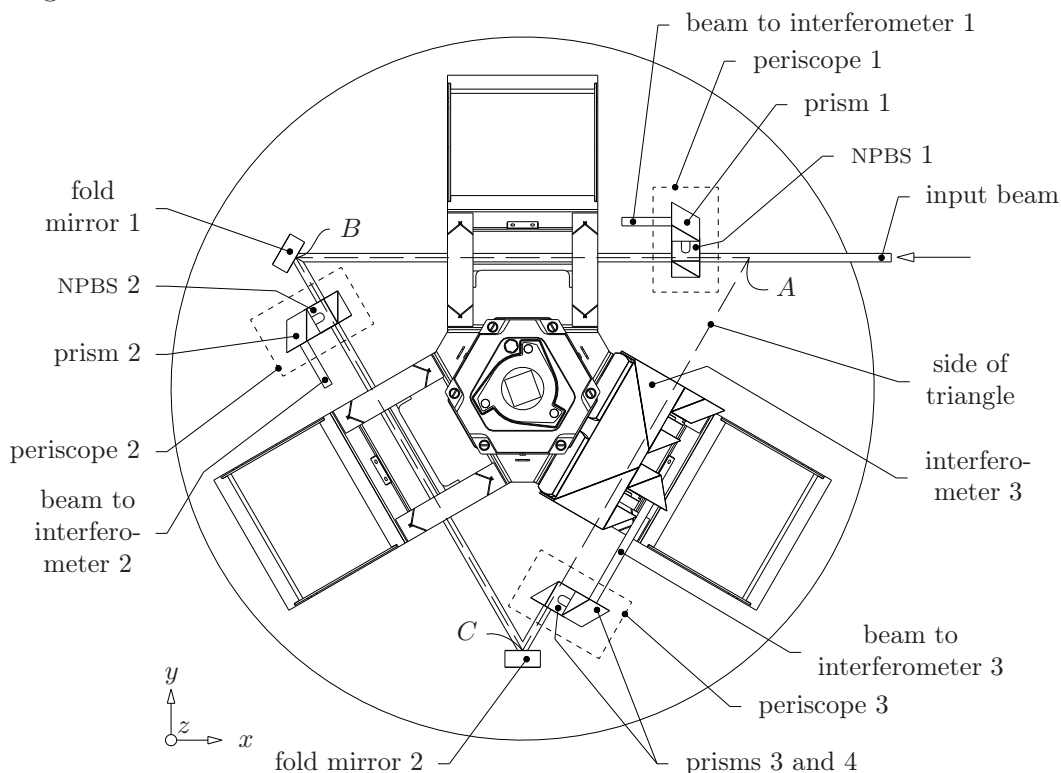


Figure 5.35 / Top view of the beam delivery optics (schematic). The input beam from the laser reflects twice to form an equilateral triangle $\triangle ABC$. A periscope in each of the triangle's legs reflects a portion of the beam towards the interferometer. Interferometers 1 and 2 are not shown.

Figure 5.35 gives a schematic top view of the beam delivery optics. Fold mirrors 1 and 2 reflect the input beam twice over 60° to give a triangular light path ($\triangle ABC$). This equilaterally triangular light path runs below the straight guide struts. The non-polarizing beamsplitter 1 (NPBS 1) in triangle section AB reflects one third of the light towards prism 1 and transmits two-thirds towards fold mirror 1. Prism 1

reflects the light towards interferometer 1. NPBS 1 and prism 1 together form the first periscope. A similar periscope is placed in the triangle section BC . The third periscope reflects all remaining light towards the third interferometer.

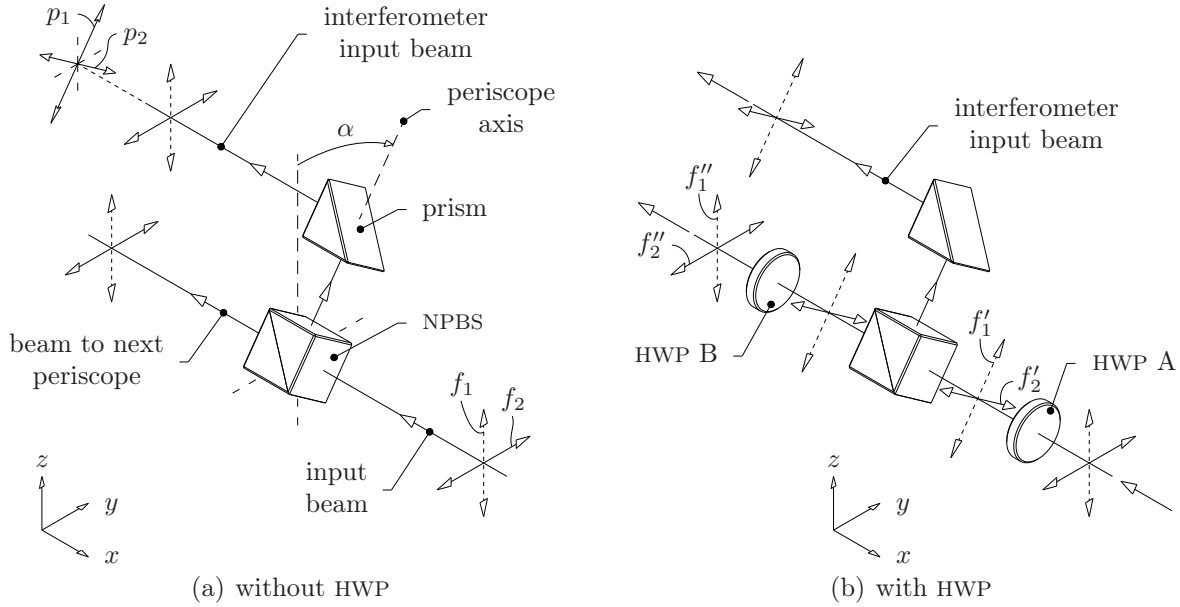


Figure 5.36 / The interferometer's polarization directions p_1, p_2 are not aligned to the laser beam's polarizations f_1, f_2 . The half-wave plate A (HWP A) rotate the polarizations to the correct orientation. The periscope makes an angle $\alpha \approx 35.3^\circ$ with the vertically oriented polarization f_1 .

The periscope axis in Figure 5.36(a) makes an angle α of about 35.3° with the laser input beam's vertically oriented polarization direction f_1 . The interferometer polarization states p_1 and p_2 , defined by the interferometer's input polarizing beamsplitter (Figure 5.11 on Page 103), are parallel and perpendicular to the periscope axis.

The angular misalignment between the laser polarizations f_1, f_2 and the interferometer polarizations p_1, p_2 results in partial mixing of the interferometer's measurement beam and reference beam [12]. This, in turn, leads to non-linearities in the displacement measurement, e.g. there is no strictly linear relation between the measured displacement and the actual OPD between the interferometer's measurement beam path and reference beam path [111]. Furthermore, the NPBS's symmetry planes are not aligned to the laser polarizations so any birefringence in the NPBS coating or glass results in elliptically polarized, instead of linearly polarized, exit beams [48]. Because of the elliptical polarization, the interferometer's measurement beam and reference beam mix and this leads to non-linearities.

A half-wave plate (HWP) is inserted into the beam between the laser source and the NPBS (Figure 5.36(b)). The HWP A aligns the polarizations f'_1, f'_2 of its output beam to the NPBS's symmetry planes and to the interferometer's polarization directions p_1, p_2 for minimal non-linearities.

HWP B rotates the NPBS's transmitted beam polarizations back to the laser beam polarization directions so the beam is polarized perpendicular to, and parallel with, the fold mirror surface. This minimizes the beam's polarization change upon reflection [55].

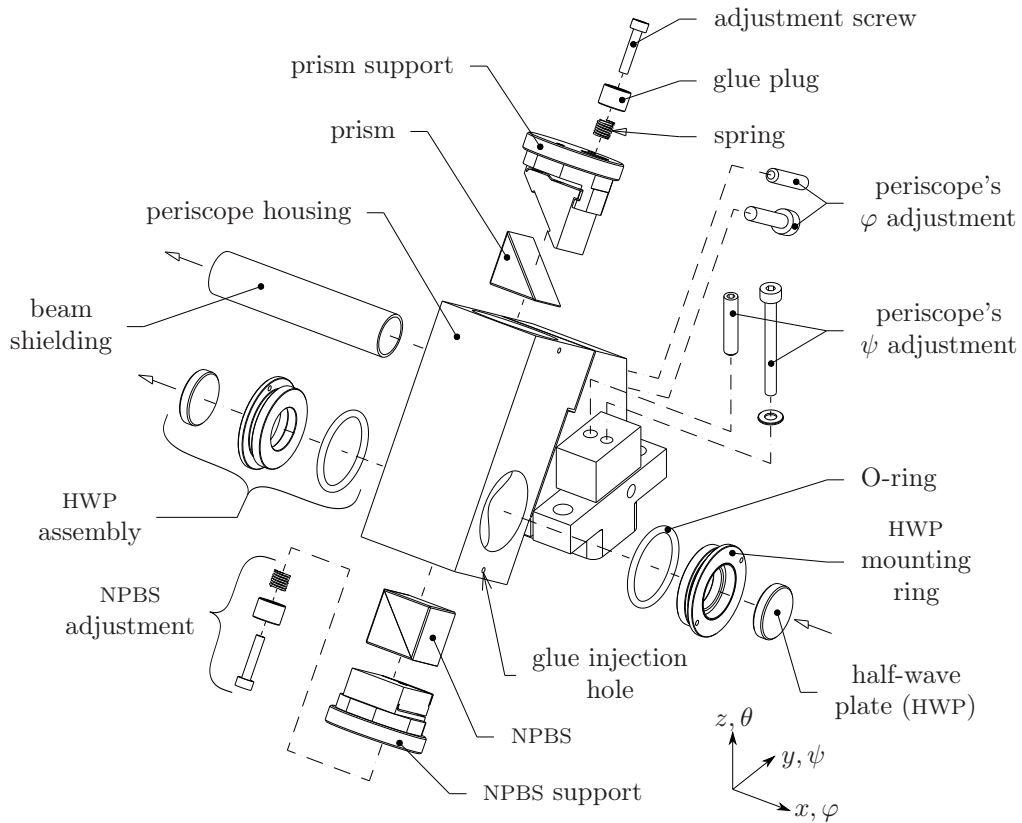


Figure 5.37 / Exploded view of the beam delivery periscope 1 or 2. A prism replaces the NPBS in periscope 3. The periscope housing shields the prism, NPBS and the inner surfaces of the HWPs from dust.

The two HWPs, the NPBS and the prism are integrated into one periscope assembly for maximum stability and protection against dust. Figure 5.37 gives an exploded view of the periscope.

The prism and NPBS are glued onto adjustable supports which, in turn, are installed in the periscope housing. The HWPs $\varnothing 10 \times 2$ mm are glued to the HWP mounting rings. Rubber O-rings hold the HWP mounting rings temporarily in place during the HWP alignment procedure. After alignment, the HWP mounting rings are permanently

secured to the periscope housing with glue.

Two elastic hinges with push-pull screws make the periscope's φ and ψ orientation adjustable. The θ orientation is adjusted in the periscope-to-instrument interface.

The periscope alignment procedure is divided into two steps. First the prism and NPBS are adjusted so the periscope's two output beams are parallel to the periscope's mounting faces. Then the periscope is installed on the instrument and aligned to the interferometer.

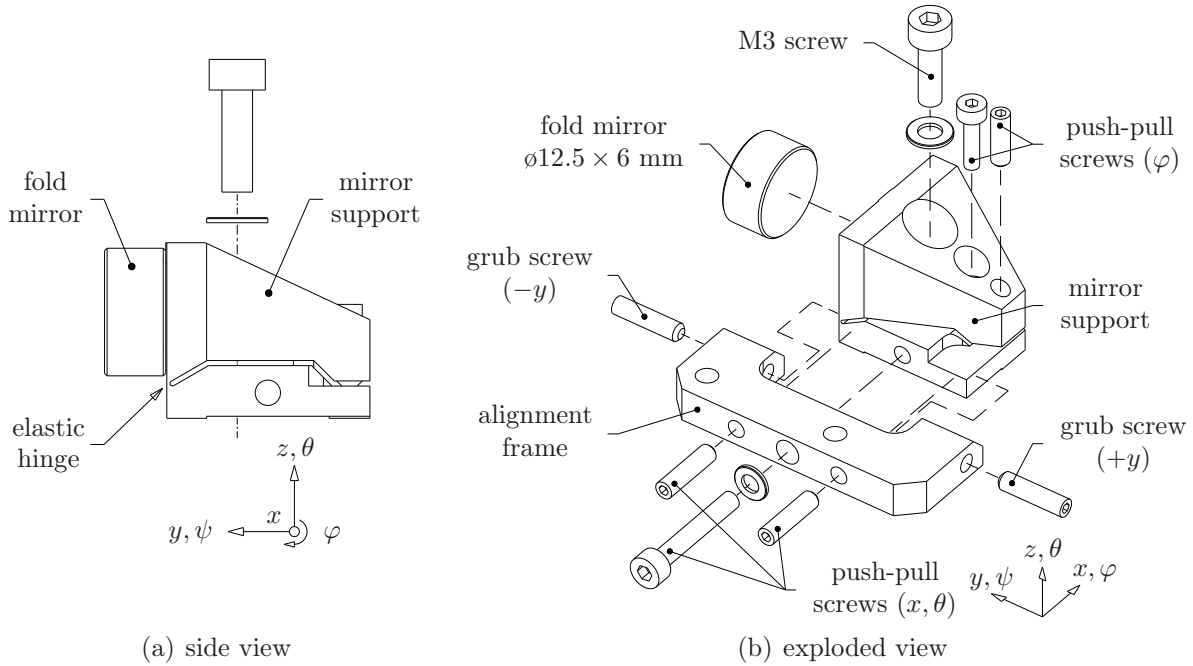


Figure 5.38 / Side view and an exploded view of the fold mirror assembly. The mirror's φ orientation is adjusted with push-pull screws on the mirror support. The alignment frame is temporarily installed on the instrument base and simplifies the fold mirror alignment in x, y and θ .

Figure 5.38 gives a side view and an exploded view of the fold mirror assembly. The dielectrically coated fold mirror is glued to the mirror support. This mirror support has an elastic hinge and a set of push-pull screws for mirror adjustments in φ . The mirror's θ orientation, as well as the x and y position, are adjusted by moving the mirror over the instrument base. A temporarily installed alignment frame with push-pull screws and grub screws simplifies this alignment.

Figure 5.39 indicates the position of the fold mirrors and the periscopes on the instrument base. A photograph of the fold mirror and the periscope is given in Figure 5.40. One of the three tubes that shield the laser beam from air turbulence is also partially visible in the photograph.

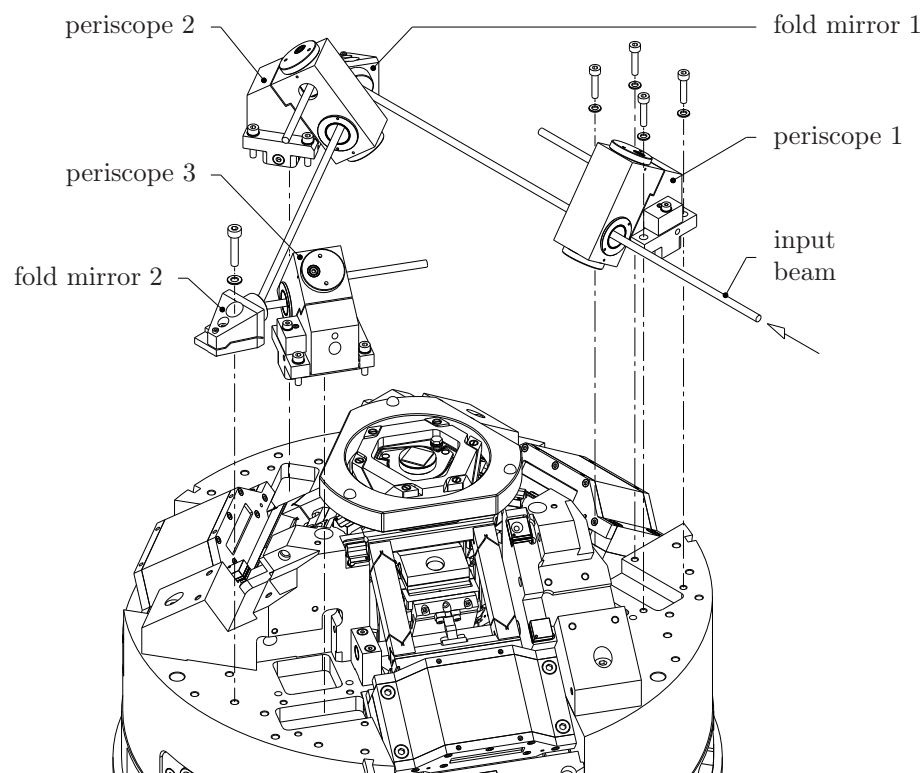


Figure 5.39 / The periscopes and fold mirrors attach directly to the instrument base.

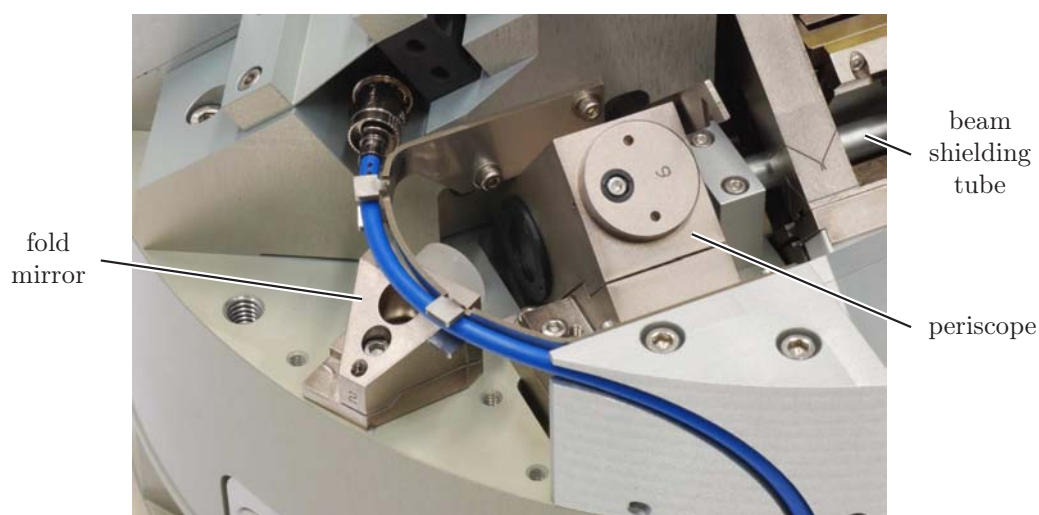


Figure 5.40 / A fold mirror and a periscope installed on the instrument. One of the tubes that shield the laser beam from air turbulence is partially visible (see also Figure C.2 on Page 149).

Fiber optics

The beam delivery system distributes the laser beam over the three interferometers. Each interferometer splits the beam into a measurement beam and a reference beam and reflects the beams towards their respective mirror. After reflection, the beams are recombined and directed towards a commercial fiber optic pickup. A linear polarizer in the pickup combines the orthogonally polarized measurement beam and reference beam into one interference beat signal [25]. This signal is then coupled into a $\varnothing 400\text{ }\mu\text{m}$, multi mode, optical fiber and transported to a fiber optic receiver on the measurement electronics board (Section 5.5).

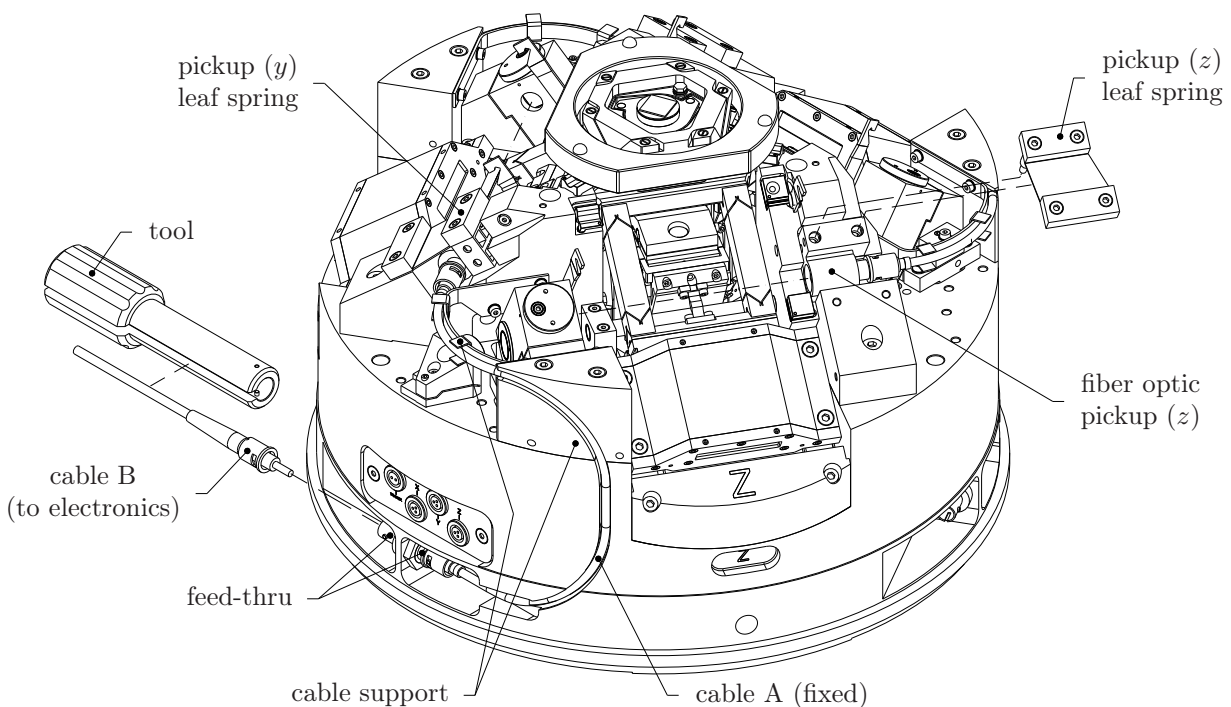


Figure 5.41 / A commercial fiber optic pickup converts the interferometer's output beams into an interference beat signal. A leaf spring fastens the pickup to the instrument. Two fiber optic cables transfer the interference signal of each pickup to the measurement electronics.

A leaf spring fastens the pickup to the instrument base (Figure 5.41). Two serially connected, fiber optics cables link each pickup to the measurement electronics. Cable A connects to the pickup and is permanently installed on the instrument. The second cable, cable B, connects to the measurement electronics and interfaces with cable A at a feed-thru connector at the instrument's base (Figure 5.41).

Cable B can be connected and disconnected from the feed-thru without affecting the

pickup alignment. A tool simplifies the otherwise impractical connection procedure.

The fiber optic cable A is tightly bent so the cable does not project beyond the instrument circumference. Additionally, the fiber optic connector's strain relief boot is removed so the cable bend can start as close as possible to the connector (Figure 5.42(a)).

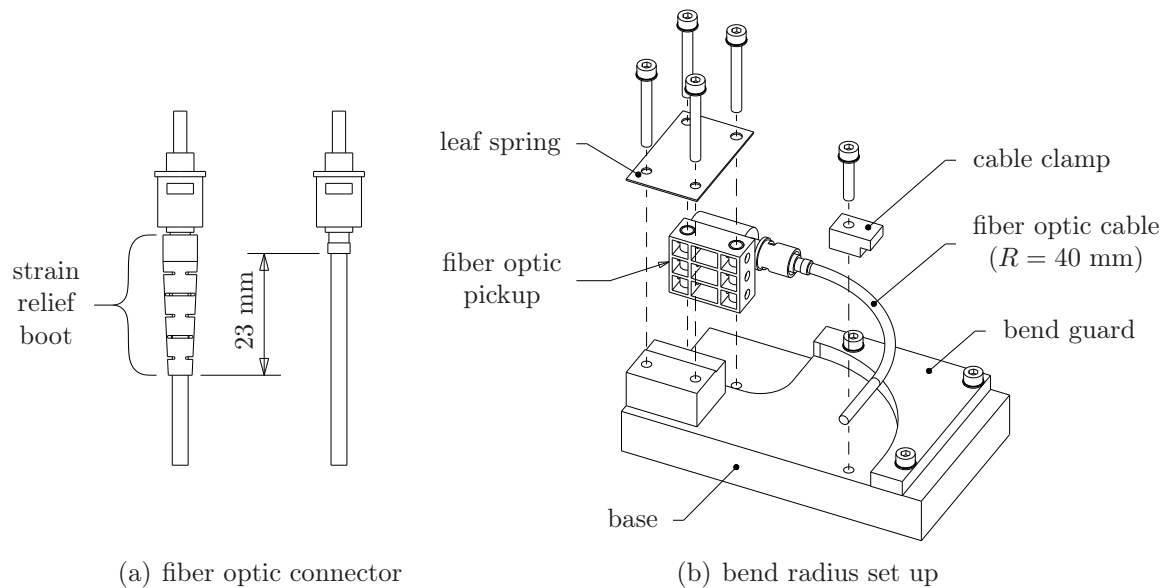


Figure 5.42 / Removing the connector's strain relief boot makes the connector axially more compact. Figure (b) shows the set up to test if the fiber optic cable can be bent to the recommended minimal bend radius even when the connector's strain relief boot is removed. The recommended minimal bending radius is 40 mm.

The effect of sharply bending the fiber optic cable without the strain relief boot in place, is tested at VSL. In this experiment, an optical interference signal is split into two equal-intensity parts by a non-polarizing beamsplitter. One part is coupled into a standard, unmodified fiber optic cable, the other part is coupled into a sharply bent cable without strain relief boot (Figure 5.42(b)). Both cables are connected to a measurement electronics board (Zygo[®] ZMI2000) which compares the output signals. The comparison showed no difference in optical signal quality between the unmodified fiber optic cable and the sharply bend cable without strain relief boot.

Figure 5.43 gives a photograph of the instrument with the fiber optic pickups and the fiber optic cable A.

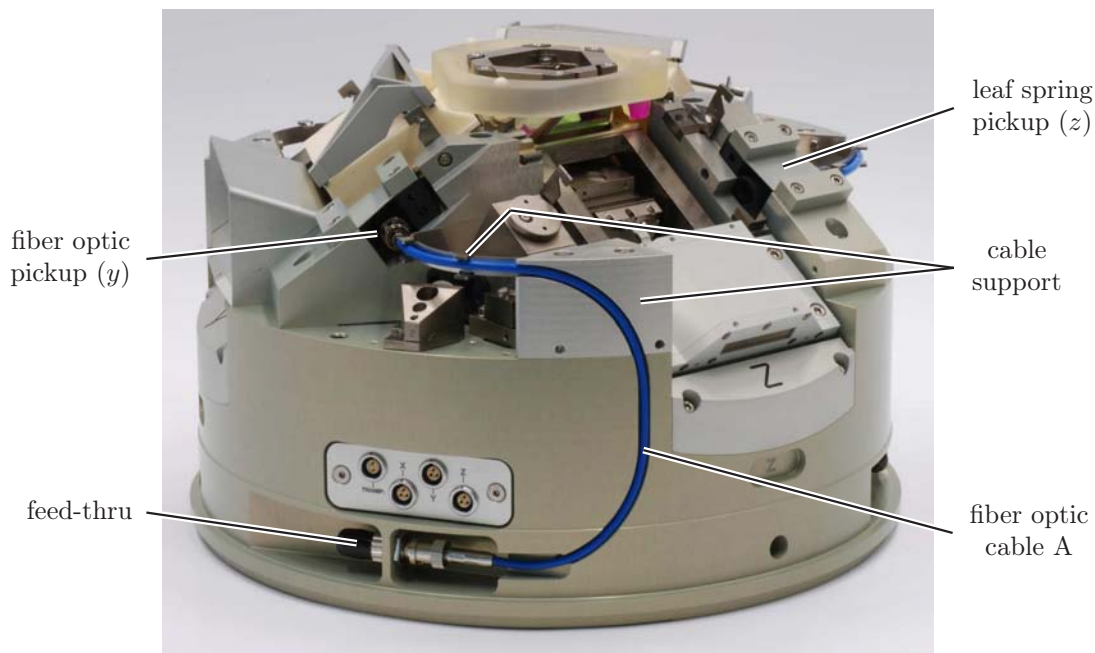


Figure 5.43 / The fiber optic pickups and cables on the instrument.

5.5 Measurement electronics

Figure 5.44(a) shows a photograph [116] of the commercial measurement electronics board (Zygo® ZMI4004™) used in the instrument's measurement system. The 160×233 mm circuit board is installed in the instrument electronics box (Figure 5.44(b)).

The fiber optic cables from the three interferometer pickups and the laser head, connect to fiber optic receivers on the measurement electronics board. The receivers convert the sinusoidal optical interference signals into electric signals [101]. The measurement electronics then measure the phase differences between the three interferometer signals and the laser head signal.

The phase change between two consecutive phase measurements is proportional to the OPD change in the interferometer during that time interval. Consequently, (electronic) summation of the phase changes gives the interferometer's OPD change since initialization or zeroing [25].

The phase measurements of the measurement board's four axes are digitally synchronized to within a ± 2 ns time window [115]. This synchronization mechanism, or data-age adjuster, automatically compensates for optical path length differences and electronic component differences between the measurement axes for maximum dynamic measurement accuracy [25].



(a) ZMI4004™ [116]



(b) installation in electronics box

Figure 5.44 / The fiber optic cables from the pickups and the laser, connect to sockets at the front of the Zygo® ZMI4004™ measurement board (a). The electric connectors for the communication with the instrument control computer, are located at the back of the board. Figure (b) shows the measurement board installed in the electronics box (see also Section 4.1.3 on Page 55).

Table 5.4 summarizes the measurement board specifications.

position resolution	nm	0.15
velocity range	m/s	± 2.55
maximum acceleration	<i>g</i>	100
data age uncertainty	ns	± 0.2
noise ^a (3σ)	nm	± 0.45
number of axes		4
communication		32-bit P2bus
^a with minimum optical power at receiver		

Table 5.4 / Specifications of the Zygo® ZMI4004™ measurement board when used with a double-pass interferometer [115].

5.6 Concluding remarks

The measurement system traceably measures the sample's displacements relative to the stationary AFM probe in three orthogonal directions. The system has three identical displacement measuring interferometers (DMIs), each measures the displacement in one direction.

The DMI's high resolution, high accuracy and large measurement range make it the most appropriate displacement sensor type for the new metrological AFM. A differential interferometer layout minimizes the measurement system's sensitivity to temperature variations. Because sufficiently small differential plane mirror interferometers (DPMIs) are not commercially available, a custom, compact and optically balanced DPMI is designed. This interferometer is kinematically mounted on the instrument for easy removal and reinstallation.

The three DPMIs use one monolithic, Zerodur[®] moving target mirror and one single, Zerodur[®], stationary reference mirror. Integration of the three mutually orthogonal moving target mirror surfaces into one single component, maximizes the mirror's thermal and mechanical stability. Additionally, the moving target mirror support is athermalized, e.g. the mirror's thermal center of expansion (TC) coincides with the AFM probe position, both radially and axially.

A beam delivery system integral to the instrument, distributes the input laser beam over the three interferometers. Commercial measurement electronics with fiber optic receivers and a specified 0.15 nm position resolution, complete the translation stage's displacement measurement system.

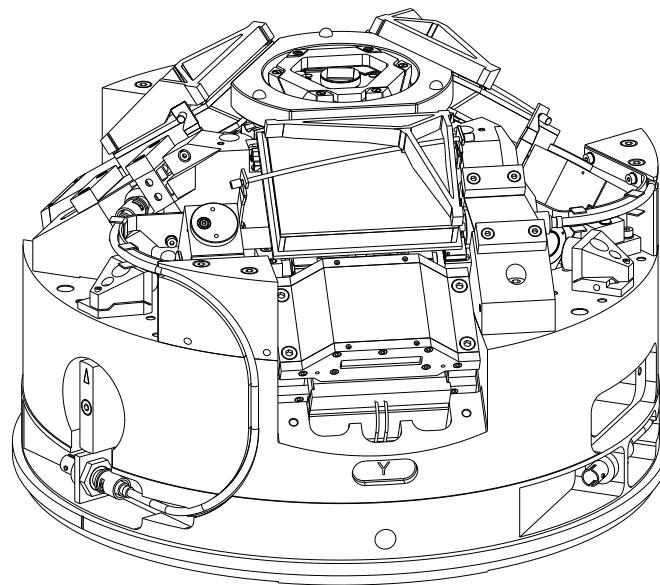


Figure 5.45 / Instrument design as discussed in Chapters 3, 4 and 5.

CHAPTER SIX

Conclusions

Most current or near-future appearing metrological AFMs (mAFMs) have a scanning range of about $100 \times 100 \times 10$ to $20 \mu\text{m}$. Extending the scanning range of mAFMs to the millimeter range while maintaining nanometer range uncertainty, reduces the calibration uncertainty through better measurement statistics and therefore helps to improve nanometer scale metrology. Additionally, increasing the scanning range makes mAFMs better suited for, for example, semiconductor critical dimension metrology. For these reasons, a long-range mAFM was developed with a scanning range of $1 \times 1 \times 1 \text{ mm}$, a sub-nanometer position resolution and a foreseen nanometer-range measurement uncertainty. The instrument was developed within the Metrology Stages Cluster of NanoNed, a national nanotechnology program.

The new, long-range mAFM has a stationary AFM head and a separate, three-DOF, sample translation stage.

The AFM head is designed for constant force, contact mode AFM and uses optical beam deflection to detect the AFM probe's movements. The AFM head kinematically connects to the sample translation stage.

The sample which needs scanning, is fixed on the translation stage's sample table via a kinematic sample holder. This sample holder allows off-line sample alignment and fast sample loading and thereby reduces the thermal disturbances on the instrument. The sample table design is optimized towards maximum eigenfrequency and fast settling after temperature changes.

Three identical, elastic parallel guides support the sample table. Each guide has a pair of parallel, cross-hinge type struts which, in turn, are placed on a stiffened leaf spring parallelogram.

Symmetry in the sample translation stage design, reduces the influence of gravity and vertical temperature gradients on the sample motions.

The straight guide's first eigenfrequency is predicted at 1.4 kHz. The estimated maximum reproducing sample table rotation leads to a worst-case estimated (Abbe) position measurement error of $\pm 3 \text{ nm}$. After calibration, this systematic error

expectedly reduces to a ± 0.5 nm position measurement uncertainty. Similarly, the estimated maximum, random, position measurement errors caused by actuator forces and temperature gradients are ± 0.7 nm and ± 0.2 nm respectively. These errors are well within the specified range.

Three identical Lorentz actuators drive the translation stage. The duo-motor type actuators have moving, copper coils, and stationary rare-earth magnets. The actuator coils closely align to the sample table's COG for minimal sample table rotations.

The actuator is designed towards maximum efficiency, e.g. minimal power dissipation per generated unit of actuation force. The actuator's measured maximum (continuous) force is about ± 1.5 N with a force constant of 57.8 ± 1.8 N/A.

A dedicated PC/104 based control system, controls the linear current amplifiers for the three actuators.

Stiffness compensation and weight compensation mechanisms reduce the actuator's static load to minimize the heat production within the instrument.

The weight compensation mechanism uses a low-stiffness tension spring and a 1:10 ratio to generate a nearly constant gravity opposing compensation force.

The elastic stiffness compensation mechanism measurably reduces the required maximum (static) actuator force from ± 2.10 N to ± 0.07 N. Consequently, the maximum power dissipation within the actuator reduces by over 99% from 0.48 W to below 0.6 mW.

The sample stage measurement system has three identical, custom, mutually orthogonal, differential plane mirror interferometers (DPMIs) which measure the sample's translations relative to the stationary AFM probe. The interferometers align to the AFM probe position for minimal Abbe error. The differential interferometer layout minimizes the measurement system's sensitivity to temperature variations. The DPMI design is optically balanced for maximum thermal stability.

The three DPMIs together use one single, monolithic, Zerodur[®], moving target mirror and one Zerodur[®], stationary reference mirror. Integration of the three mutually orthogonal moving target mirror surfaces into one single component, maximizes the mirror's thermal and mechanical stability. Additionally, the moving target mirror support is athermalized, e.g. the mirror's TC coincides with the AFM probe position, both radially and axially.

A beam delivery system distributes the input laser beam over the three interferometers. Commercial measurement electronics with fiber optic receivers and a specified 0.15 nm position resolution, complete the translation stage's displacement measurement system.

The sample translation stage is realized (Figure 6.1) and the AFM head designed. The

interferometers have not been assembled at the time of writing.

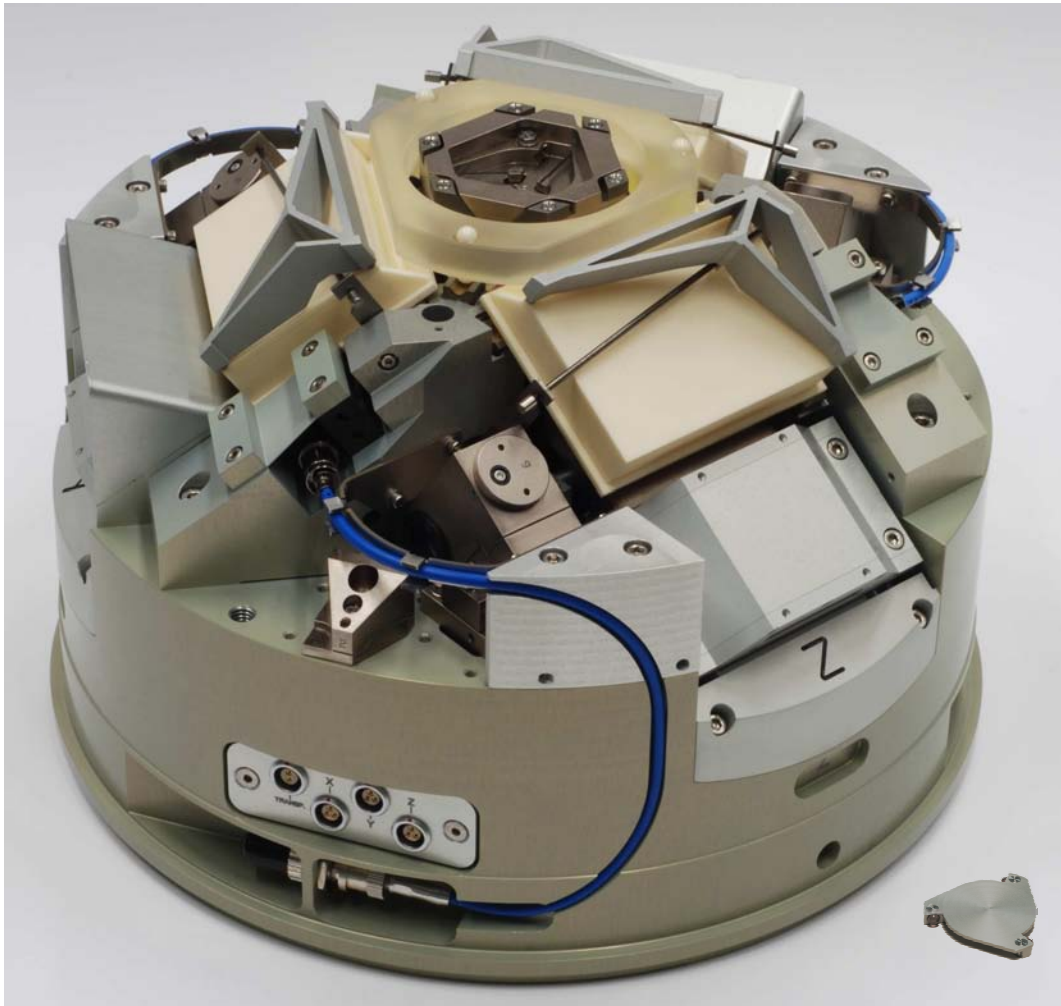


Figure 6.1 / The realized sample translation stage with kinematic sample holder (lower right).

Current metrological AFMs and transfer standards

Table A.1 on the next page summarizes the specifications of the current and near-future appearing metrological AFMs (mAFMs). A shorter version of the table is presented in Section 1.3 (Page 6).

Table A.2 on Page 141 gives the specifications of commercially available transfer standards for AFM. The data represent the state of affairs in 2005.

Figure A.1 shows the pattern of an one-dimensional and a two-dimensional transfer standard.

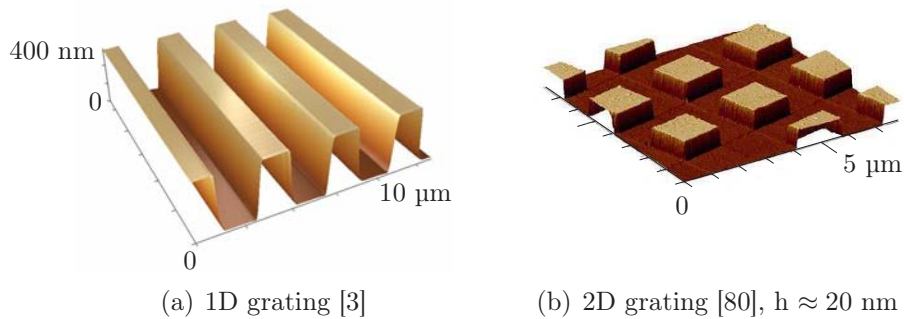


Figure A.1 / Typical transfer standard patterns for AFM. Repeat from Figure 1.3.

institute	scan volume	scan motions				displacement measurement			AFM		source
		DOF	actuator	tip	sample	type	resol. (nm)	uncert. (nm)	type	mode	
iNRiM	$30 \times 30 \times 18 \text{ }\mu\text{m}$	5	PZT	fixed	x,y	het-DMI ^a	0.2	note <i>b</i>	STM	-	[81]
					z, φ , ψ	CPS	0.4				
LNE	$50 \times 50 \times 5 \text{ }\mu\text{m}$	3	PZT	fixed	x,y,z	dif-DMI ^c	-	1 ^d	OBD	-	[86–88]
PTB	$70 \times 15 \times 15 \text{ }\mu\text{m}$	3	PZT	fixed	x,y,z	hom-DMI ^e	1.24	-	OBD	C	[21]
NPL	$100 \times 100 \times 5 \text{ }\mu\text{m}$	3	PZT	z	x,y	dif-DMI	≈ 0.1	2 ^{f,g}	-	-	[45, 64]
KRISS	$100 \times 100 \times 12 \text{ }\mu\text{m}$	3	PZT	z		CPS	0.36	see source	OBD	-	[54]
					x,y	het-DMI	1.24				
MIKES	$100 \times 100 \times 12 \text{ }\mu\text{m}$	4	PZT	z	x,y,z	het-DMI	-	-	OBD	-	[58, 59, 61]
NMIJ	$100 \times 100 \times 12 \text{ }\mu\text{m}$	3	PZT	fixed	x,y,z	dif-DMI	0.04	0.2 ^f	OBD	C,NC	[74]
VSL	$100 \times 100 \times 20 \text{ }\mu\text{m}$	3	PZT	fixed	x,y,z	het-DMI	0.15	1 ^d	OBD	C	[26, 56]
NMIA	$100 \times 100 \times 25 \text{ }\mu\text{m}$	3	PZT	fixed	x,y,z	dif-DMI	-	$\leq 1^d$	QTF ^h	NC	[47, 62]
FPS-SMD	$100 \times 100 \times 100 \text{ }\mu\text{m}$	3	PZT	fixed	x,y,z	het-DMI	-	1 ^d	OBD	-	[82–84]
NIM	$200 \times 200 \times 6 \text{ }\mu\text{m}$	9	-	x,y,z	x,y,z φ , ψ , θ	hom-DMI	0.088	-	OBD	-	[67]
CMI	$200 \times 200 \times 10 \text{ }\mu\text{m}$	4	PZT	z	x,y,z	hom-DMI	0.13	-	OBD	-	[63]
METAS	$800 \times 800 \times 200 \text{ }\mu\text{m}$	7	PZT	z		-	-	-	OBD	C,NC	[69]
					x,y,z	dif-DMI					
					φ , ψ , θ	-					
TU/e-VSL	$1 \times 1 \times 1 \text{ mm}$	3	lorentz	fixed	x,y,z	dif-DMI	0.15	-	OBD	C	[107–109]
PTB	$25 \times 25 \times 5 \text{ mm}$	6	lorentz + PZT	fixed	x,y,z	hom-DMI	0.08	-	OBD	C	[19, 22, 23]
					φ , ψ	AC	-				
NRC	$40 \times 40 \times 6 \text{ mm}$	12	PZT	z		CPS	0.05	1 ^d	QTF ^h	NC	[33]
					x,y,z	hom-DMI	0.5				
					φ , ψ , θ	AC	-				
NIST	$50 \times 50 \text{ mm} \times 5 \text{ }\mu\text{m}$	3	PZT	y	x	dif-DMI	-	$\leq 1^d$	STM	-	[60, 102]
				z		CPS					

^aheterodyne DMI^cdifferential DMI^ehomodyne DMI^gmeasurement of nominal 80 nm step height^b x,y : $3 \text{ nm} + 1 \cdot 10^{-3}l$, z : $2 \text{ nm} + 2 \cdot 10^{-3}h$ ($k=2$)^dspecification / goal^f $k=2$ ^hquartz tuning fork**Table A.1** / Overview of current and near-future appearing metrological AFMs.

manufacturer	series / type	pattern			dimensions (mm)		tracea- bility	source
		type	pitch (μm)	step height (nm)	effective area	sample		
Advanced Surface Microscopy	292UTC	1D-step	292 nm	30 – 40	-	4×3	PTB	[2]
	145TC		145 nm	90 – 110		6×4		
MikroMasch	TGZ-01/02/03	1D-steps	3	20, 100, 500	3×3	5×5	NIST	[73]
	TGZ-11		10	1500			-	
	TGF-11	1D-trapezoidal		$1.75 \mu\text{m}$				
NanoDevices	16460	2D-step	10 ± 0.04	200 ± 4	6×6	10×10	NIST	[76]
	16461			20 ± 4				
	16462	1D-step	2 ± 0.04	200 ± 4				
		2D-step	10 ± 0.04					
	16463	1D-step	2 ± 0.04	20 ± 4				
		2D-step	10 ± 0.04					
	NanoGauge NGS	1D-step (2×) + 2D-step	2 ± 0.02	200 ± 5	$1.6 \times 1.6 (3\times)$	7×4	[66]	
	10 ± 0.10							
Nanosensors	2D300	2D-step	$300 \pm 3 \text{ nm}$	≈ 70	$100 \times 100 \mu\text{m}$	5×7	PTB	[78]
NT-MDT	TGZ-1	1D-step	3 ± 0.05	19 ± 1	3×3	5×5	VIIMS?	[80]
	TGZ-2			105 ± 1.5				
	TGZ-3			540 ± 2				
	TGG-1	1D-triangle		$1.5 \mu\text{m}$				
	TGQ-1	2D-step		19.5 ± 1.5				
VLSI	STS-2	2D-step	$1.8, 3, 5$	18, 44, 100, 180	1×0.27	12×8	NIST	[106]
	STS-3		$3, 10, 20$					

Table A.2 / Overview of commercial transfer standards (2005).

APPENDIX B

AFM head design¹

The long-range mAFM uses a custom, compact AFM head (Figure B.1). This AFM head [92] is optimized towards mechanical and thermal stability and a such differs considerably from commercially available AFMs.

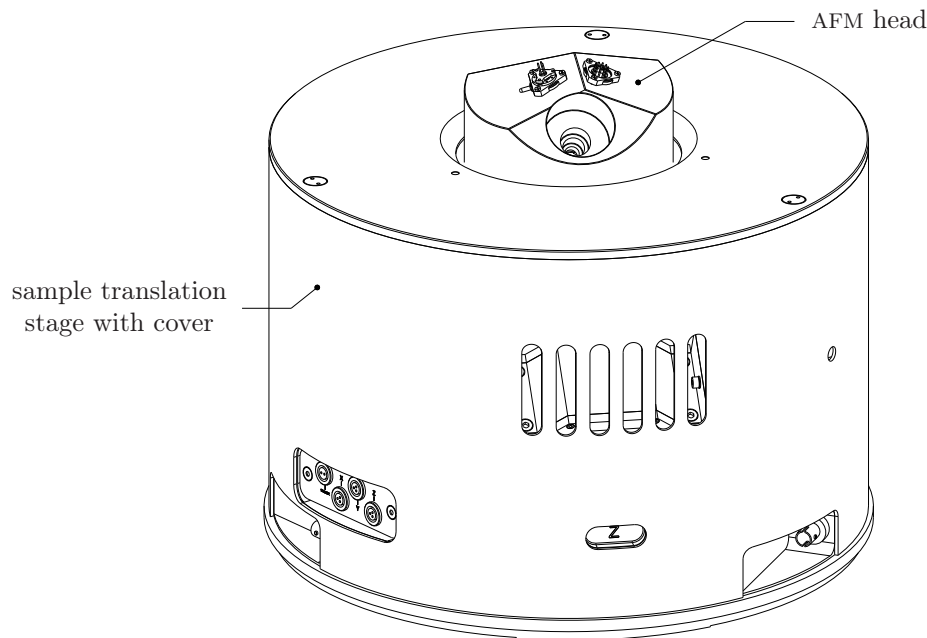


Figure B.1 / The AFM head is kinematically connected to the sample translation stage. The cantilever observation cameras are not visible.

The AFM head is designed for constant force, contact mode AFM and uses optical beam deflection (OBD) to detect the AFM probe's movements. Figure B.2 on the next page gives an exploded view.

¹I. de Rijk, CST-TU/e

The laser source is a $\varnothing 5.6$ mm, 635 nm wavelength, laser diode (Figure B.3(a)). The laser's optical power is adjustable to maximize the PSD's signal-to-noise ratio. Commercial beam shaping optics, focus the diode's output beam into a $\approx \varnothing 10$ μm spot. The laser diode is thermally isolated from the AFM head for maximum thermal stability. Furthermore, the laser diode assembly's TC coincides with the diode's emit point for high beam pointing stability.

A low noise, four-quadrant PSD detects the reflected beam movements (Figure B.3(b)). The PSD assembly is spring loaded onto the AFM head.

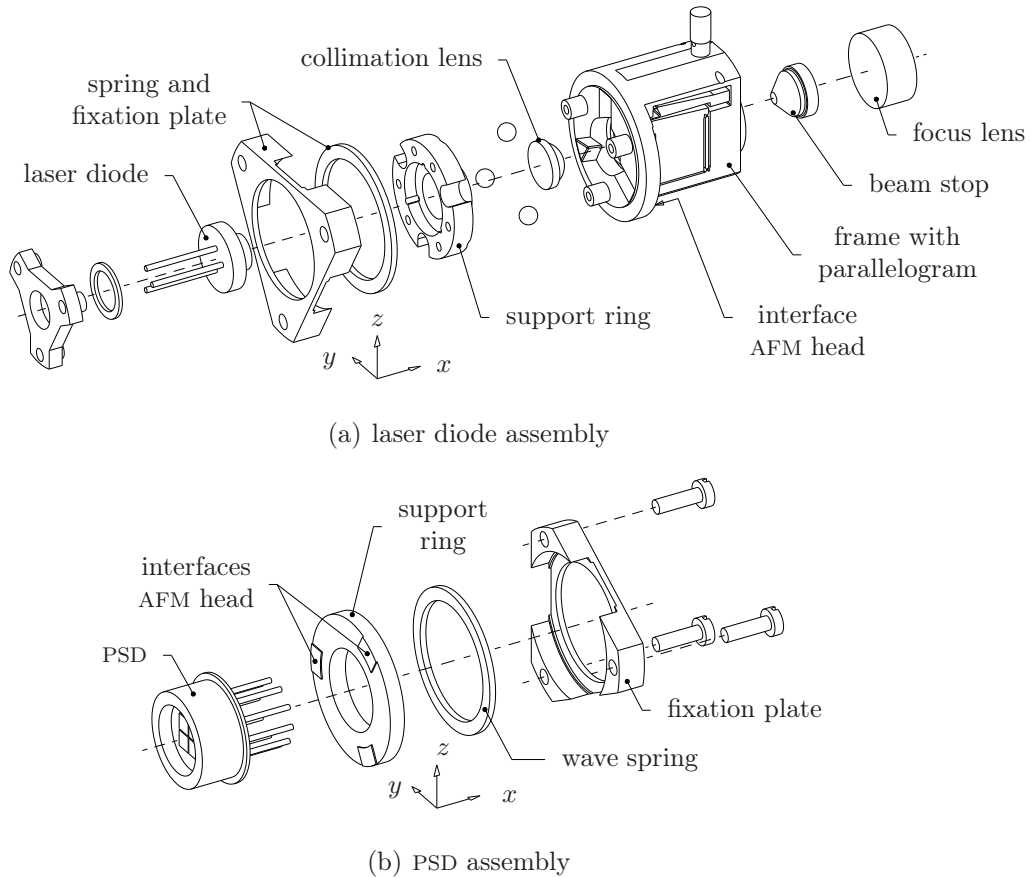


Figure B.3 / Two lenses focus the laser diode's beam onto the cantilever. The diode is thermally isolated from the AFM head. The laser diode assembly and the PSD assembly can laterally (y, z) move over the AFM head for beam alignment.

Two, compact, CMOS cameras with $20\times$ objectives, monitor the cantilever (Figure B.2). A separate frame supports the cameras. This minimizes the AFM head mass and keeps the AFM head's COG close to the stationary reference mirror for good dynamical performance.

Table B.1 on the next page, summarizes the AFM head specifications.

characteristics	
mode	contact mode
thermal center	coincides with AFM probe position
resolution ^a	$\approx 0.1 \text{ nm}$
range ^a	$\approx \pm 300 \text{ nm}$
laser	
type	diode
wavelength	$635 \pm 5 \text{ nm}$
optical power	0 - 5 mW
spot on cantilever	$\approx \varnothing 10 \text{ }\mu\text{m}$
PSD	
type	four-quadrant
active area	$3 \times 3 \text{ mm}$
spot on PSD	$\varnothing 1.8 \text{ mm}, 0.25 \text{ mW}$
cantilever observation	
camera	CMOS, 1280×1024
objective	20 \times magnification
system resolution	$\approx 1.3 \text{ }\mu\text{m}$

^avertically at tip, with a $l = 200 \text{ }\mu\text{m}$ cantilever

Table B.1 / AFM head specifications.

Base material and instrument base

Differences in thermal material properties between the instrument's main components, can increase the instrument's sensitivity to temperature variations. To minimize these differences, all (important) components are machined from the same, certified, aluminium bar stock.

Figure C.1 shows the main components within the extruded Al7075-T6 bar stock. The layout within the bar stock minimizes the differences within each set of three identical components, e.g. similar grain size distribution, internal stresses and risk of material defects.

VSL measured the bar stock's CTE to allow accurate thermal length compensation (Pages 17 and 30, $\alpha = 22.6 \pm 0.3 \mu\text{m/m/K}$).

The $\varnothing 248 \times 90$ mm instrument base (Figure C.2) is machined in one set up as much as possible to minimize fabrication tolerances.

The three interferometer and stationary reference mirror supports, see Figure C.2, bolt directly to the instrument base for high stiffness. Heat shields direct the (minimal) actuator heat away from the interferometric displacement measurement system and out of the instrument through ventilation openings in the instrument cover (Figure C.3).

Figure C.4 on Page 151 shows the instrument and the laser source set up on an optical breadboard table.

Figure C.5 shows photographs of the instrument base fabrication and instrument assembly.

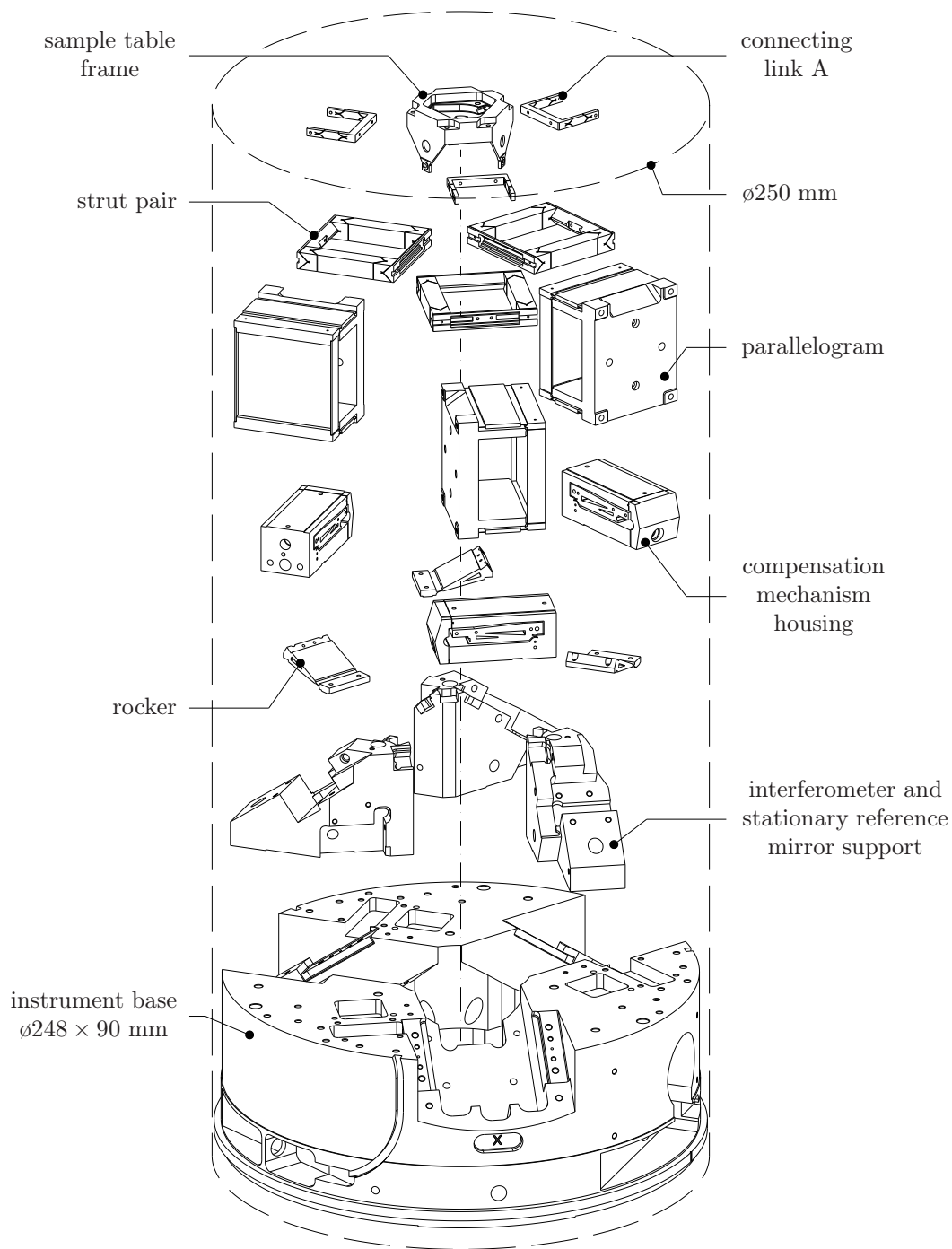


Figure C.1 / Instrument components within the ø250 mm bar stock. The length of the bar is exaggerated for clarity (actual length about 300 mm or half the length shown). Not all component's shown, the actual position (not orientation) of some components differs slightly from the figure.

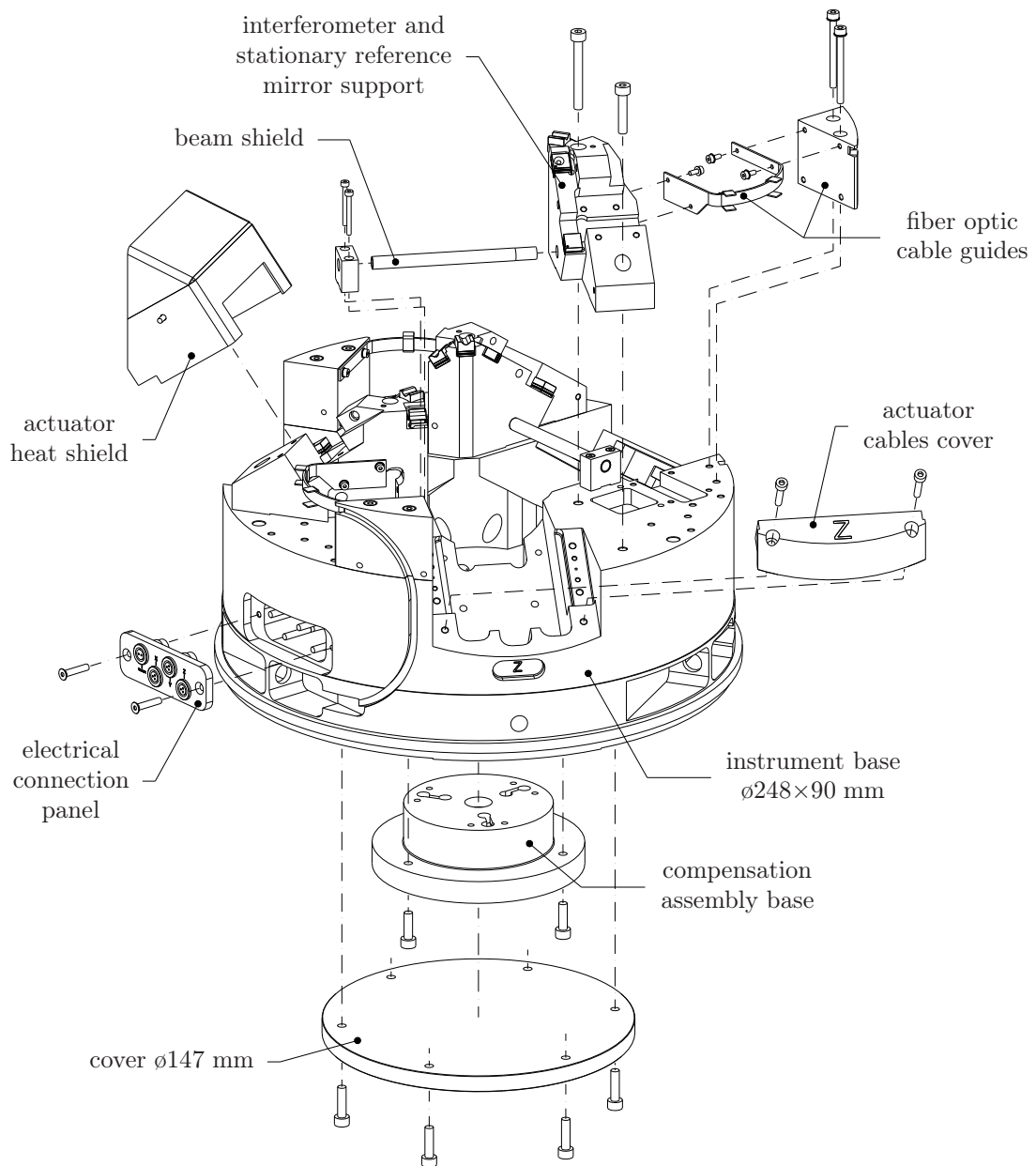


Figure C.2 / Exploded view of the instrument base assembly.
Figure C.3 shows the assembled instrument base assembly.

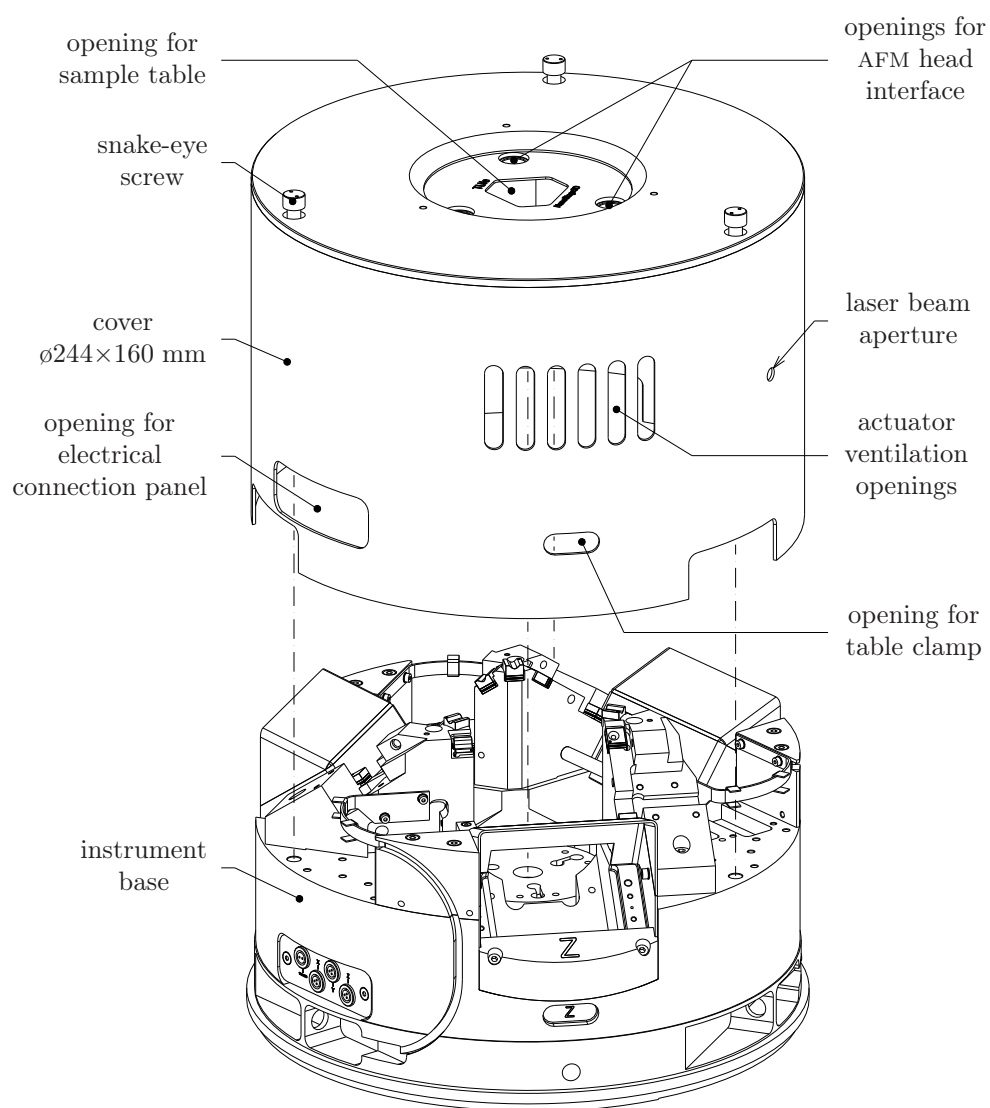


Figure C.3 / Instrument cover (permanently installed).

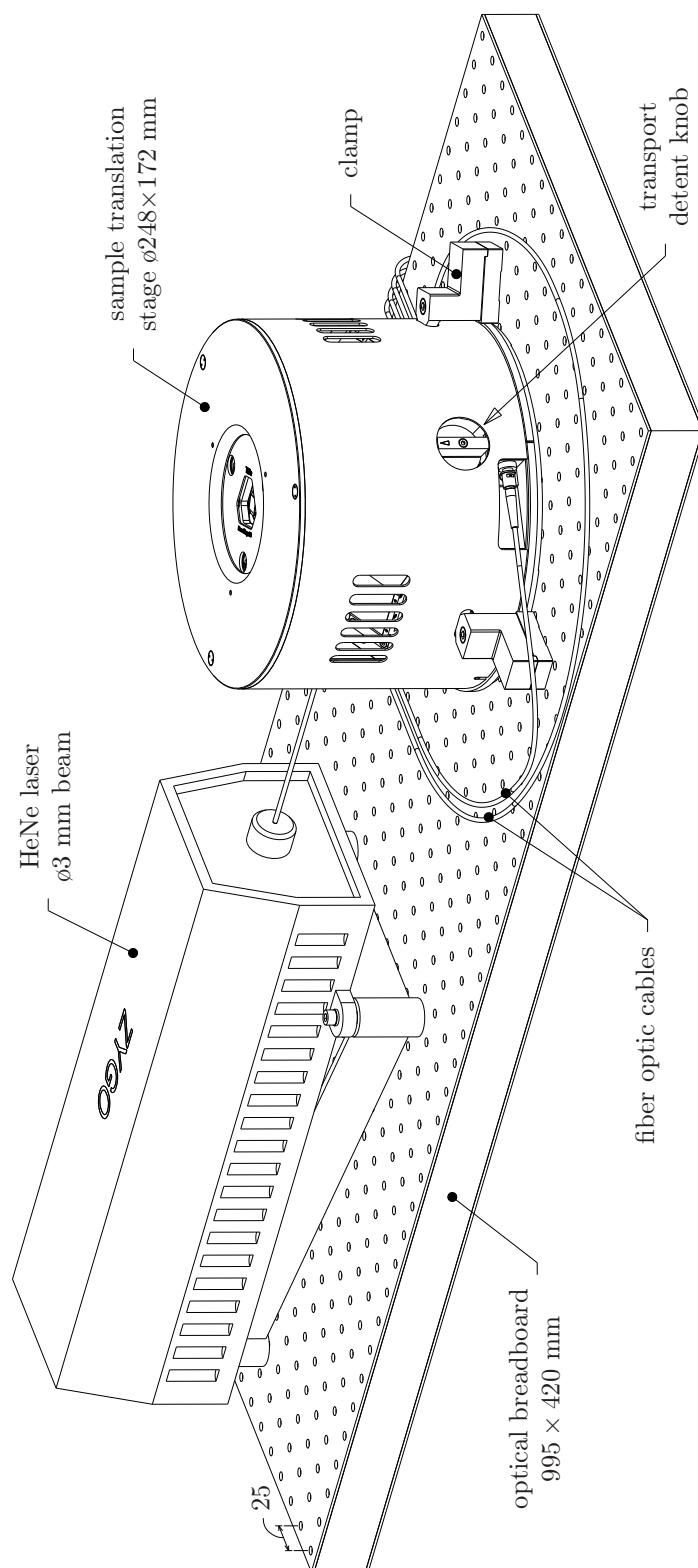
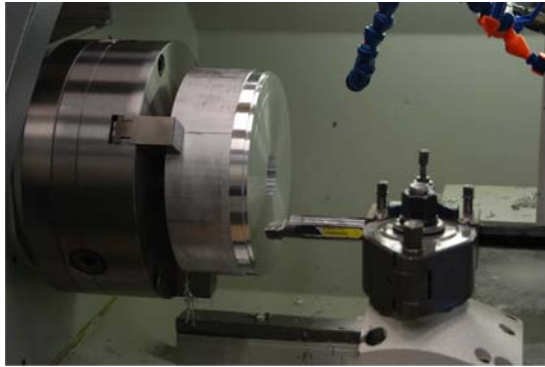
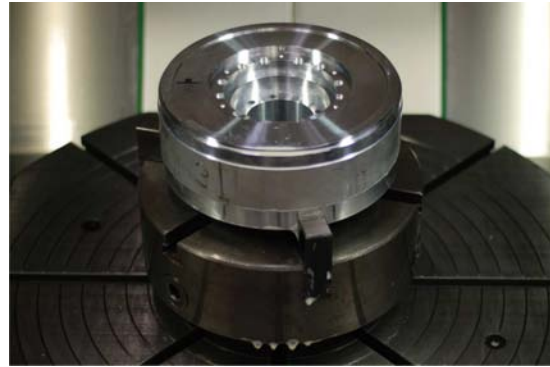


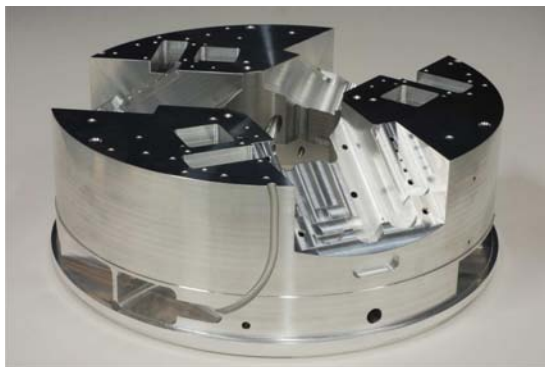
Figure C.4 / Sample translation stage and laser source installed on an optical breadboard. The AFM head and instrument electronics box are not visible.



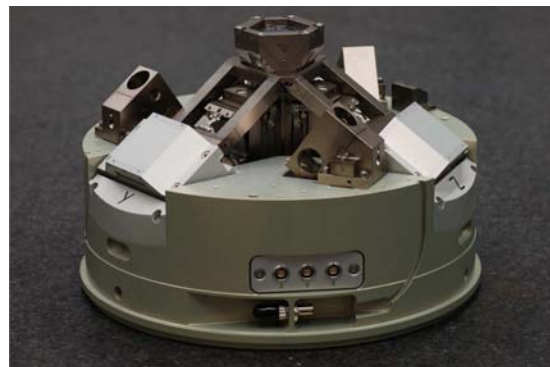
(a) rough CNC turning of the instrument base



(b) CNC milling (underside)



(c) instrument base before anodizing



(d) instrument partly assembled



(e) instrument fully assembled



(f) instrument cover installed

Figure C.5 / Instrument base fabrication and instrument assembly.

Intermediate optimization

Figure D.1 shows the eigenfrequency development during the sample table and strut optimization (Section 3.1). A few of the intermediate designs are given in Figure D.2.

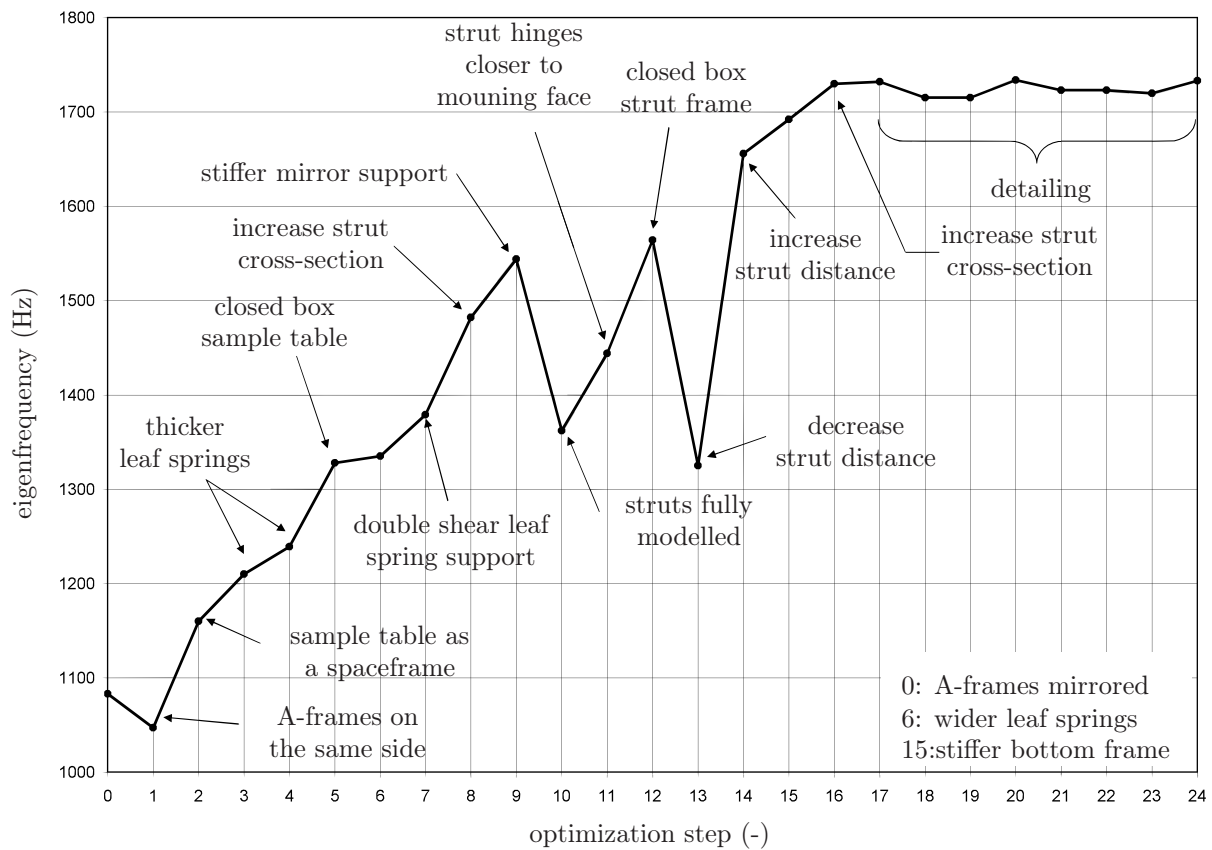


Figure D.1 / Optimization steps of the sample table and the struts.

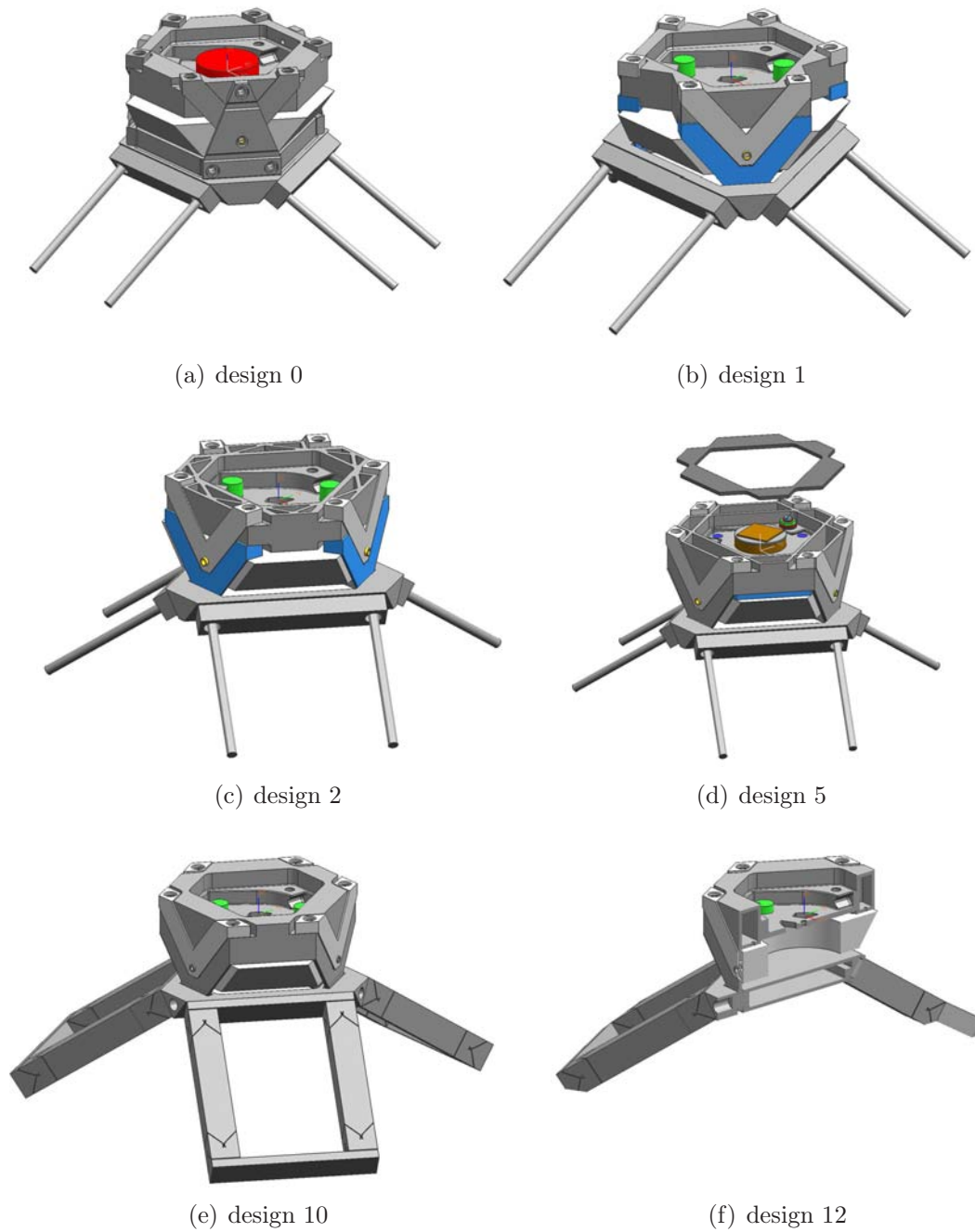


Figure D.2 / Several intermediate designs. The design's number correspond with the optimization step number in Figure D.1.

APPENDIX E

Actuator details

Table E.1 summarizes the actuator properties. Section 4.1.2 on Page 50 discusses the actuator design, the actuator measurements are described in Section 4.3.2 (Page 82).

performance ^a			
max force ^b	$F_{max,c}$	N	$\pm 1.5 \pm 0.1$
force constant	K_f	N/A	57.6 ± 1.8
motor constant	K_m	N/ \sqrt{W}	3.0 ± 0.1
coil			
wire diameter	d_w	mm	0.1
wire length	l_w	m	≈ 156
wire length, effective	l_e	m	≈ 90
turns	N	-	1500
space factor	-	%	≈ 62
resistance ^a	R	Ω	≈ 360
mass ^a	m_c	g	11.4
inductance ^c	L_c	mH	≈ 80
max current	i_{max}	mA	25
max current density	J_{max}	A/mm ²	3
max voltage drop	ΔV_c	V	9.0
magnets			
material and number	-		8× NdFeB (2 × 4)
dimensions	-	mm	15 × 15 × 5 (8×)
mass, per magnet	m_m	g	8.5
air gap flux density	B_g	T	0.60 ^d / 0.55 ^e
air gap	l_g	mm	4.2 (2×)
yoke and pole shoes ^f			
mass yoke	m_y	g	78
pole shoe thickness	-	mm	1

^ameasured, ^bcontinuous, ^cestimate [39, 75],

^dAnsoft Maxwell®, ^eEquation (4.9) on Page 49, ^fArmco®

Table E.1 / Actuator specifications. The values are calculated unless indicated differently.

Figures E.1 and E.2 on the next page show the pole shoe's influence on the magnetic field (field estimated with Ansoft Maxwell® version 9).

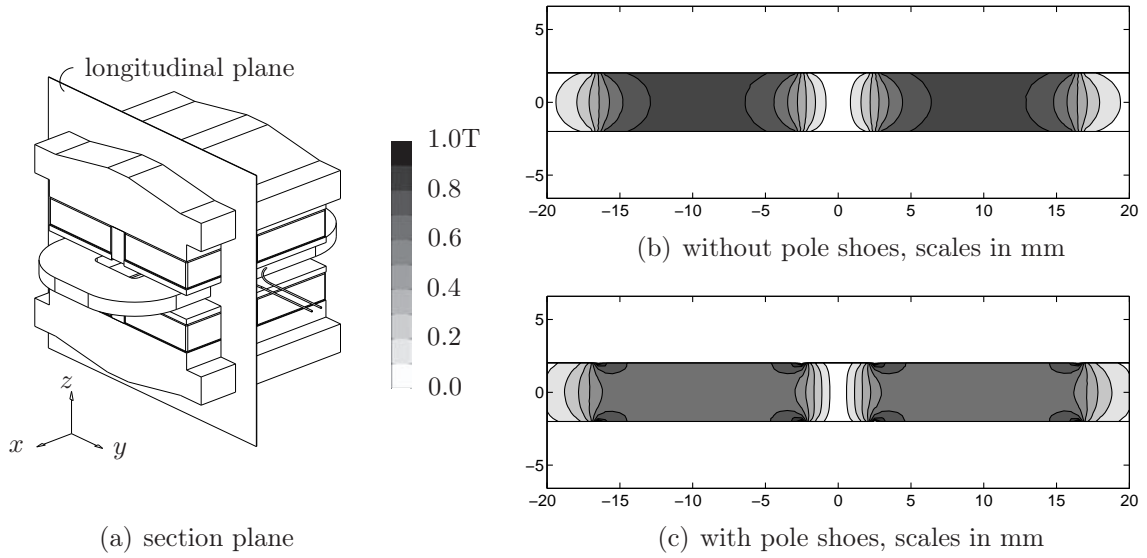


Figure E.1 / Magnetic field within the air gap (longitudinal plane). Average value over the coil's working area with pole shoes is about 0.60 T (without ≈ 0.64 T). The coil translates in the y -direction.

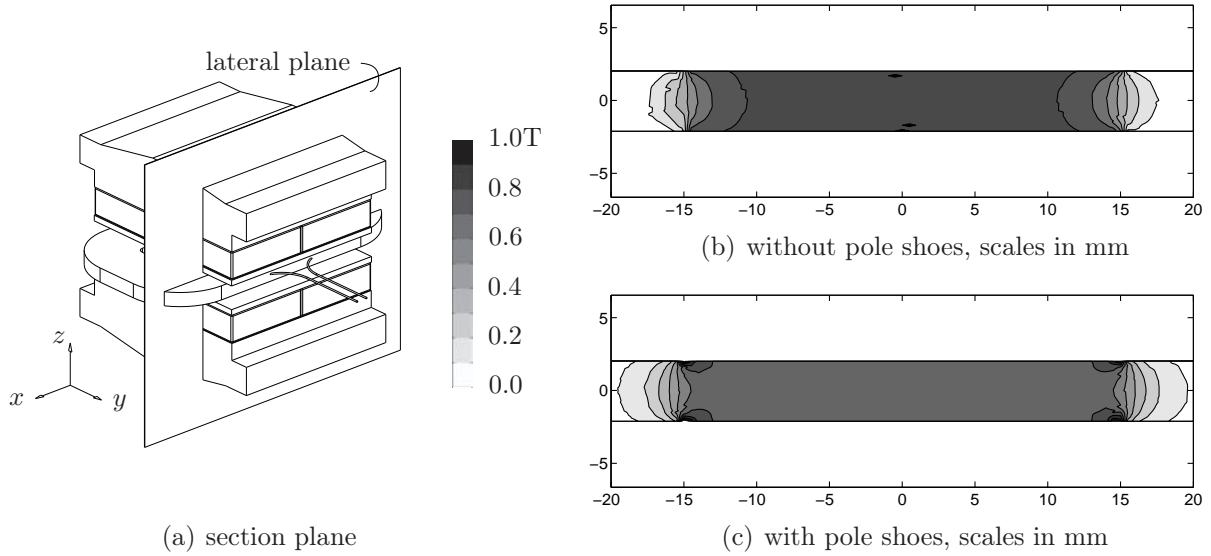


Figure E.2 / Magnetic field within the air gap (lateral plane). The gap between the magnets (at $x = 0$) changes the field locally (b). The pole shoes homogenize the field, the gap between magnets is no longer visible in the magnetic field (c).

The pole shoes increase the field's homogeneity at the cost of a slight reduction in average field strength ($\approx -7\%$).

APPENDIX F

Interferometer assembly

The interferometer assembly procedure has twenty-two steps. The steps which are already explained in Section 5.2.3 (Page 105), are repeated here for completeness.

The interferometer's top surface attaches to the optics support box. The interferometer is assembled upside-down on a flat surface on the jig to ensure no component extends above this mounting face. To prevent confusion during assembly, the images in the procedure represent the components 'as seen' during the assembly and are therefore mirrored compared to the figures in Chapter 5. Figure F.1 repeats the interferometer component names.

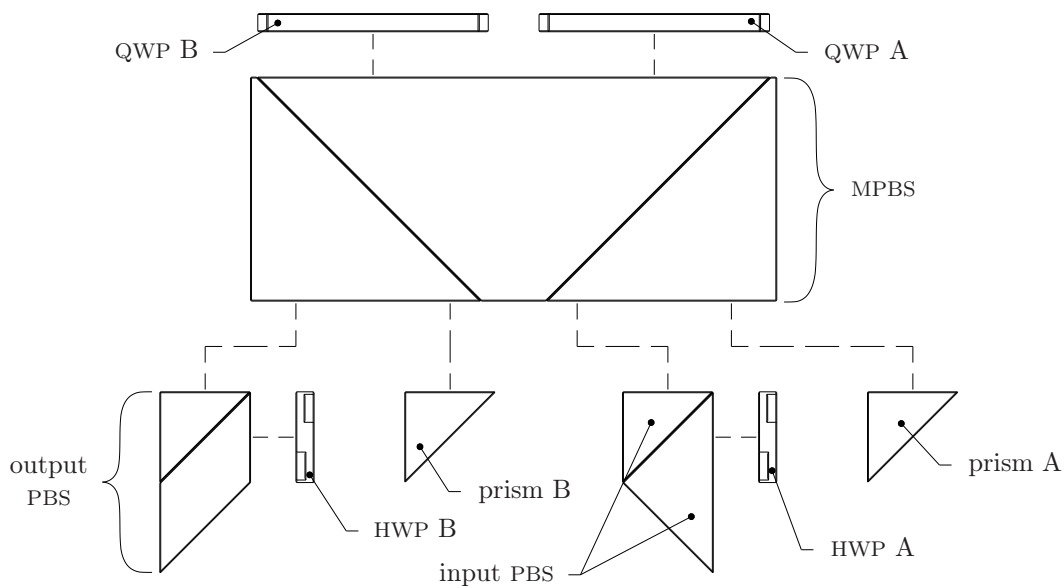
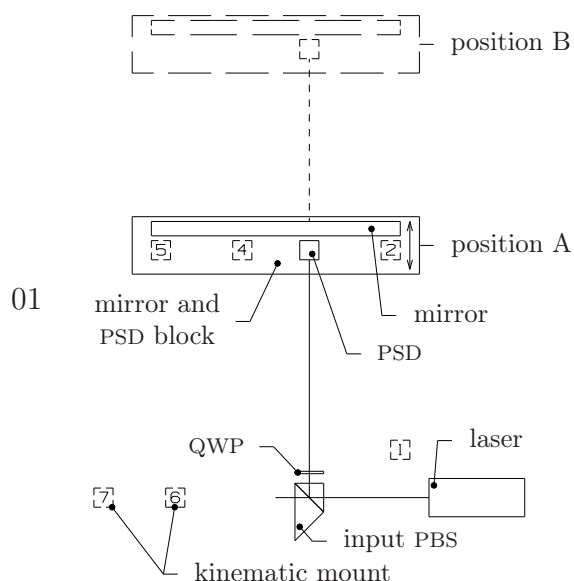
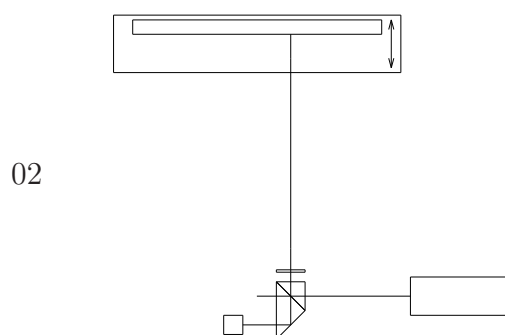


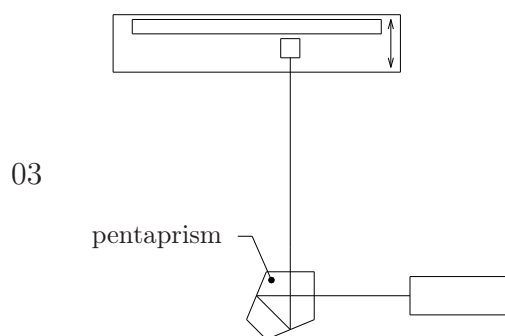
Figure F.1 / Interferometer component names. The interferometer is shown upside-down compared to Figure 5.11, e.g. the input beam enters the interferometer from the right instead of from the left.



- align laser source's beam parallel to the table
- adjust the kinematic PSD mounts 1, 6 and 7 so the sensor center's is the same height above the table as the laser beam
- install mirror and PSD block on position A (Figure 5.14)
- align mirror so it is perpendicular to the table using an autocollimator
- move mirror and PSD block to position B. Adjust mount B using an autocollimator until the mirror is parallel in both positions
- install input PBS and QWP, align so laser centers on PSD

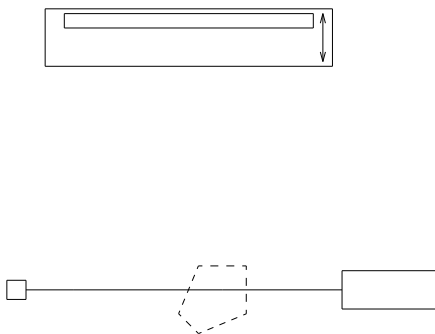


- move PSD behind input PBS
- rotate mirror on block around the table normal so the reflected beam centers on PSD
- move mirror block to other position and check alignment. If necessary repeat adjustment
- check mirror is perpendicular to table (autocollimator)



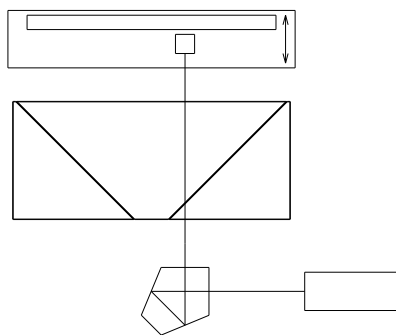
- move PSD to mirror and PSD block
- install pentaprism
- align laser source with the PSD
- perform step c at both mirror block positions. Laser is now perpendicular to the line through positions A and B

04



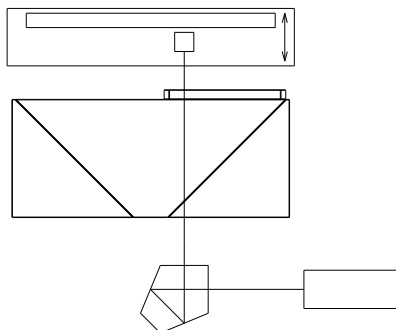
- a. remove pentaprism
- b. move PSD to kinematic mount nr 6 and position mount so the laser beam is centered on the sensor
- c. repeat for kinematic mount nr 7
- d. reinstall pentaprism

05



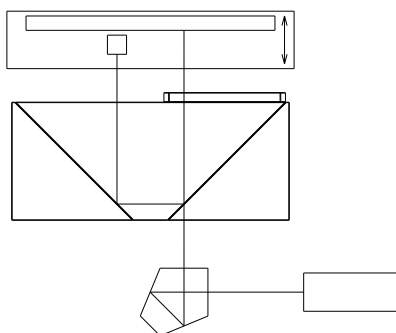
- a. install main polarizing beamsplitter (MPBS)
- b. check MPBS's influence on laser beam by flipping and rotating the component
- c. align MPBS front (QWP mounting surface) parallel to the mirror

06

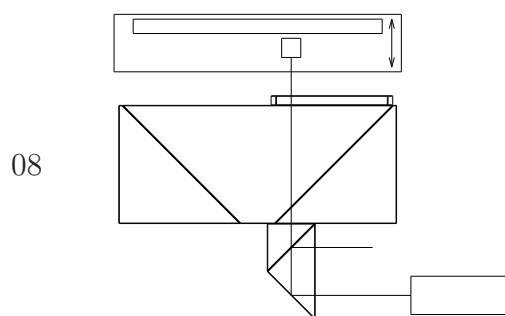


- a. temporarily install QWP A and check its influence on the beam path
- b. the three intermediate steps to correct for any beam deviation are not discussed

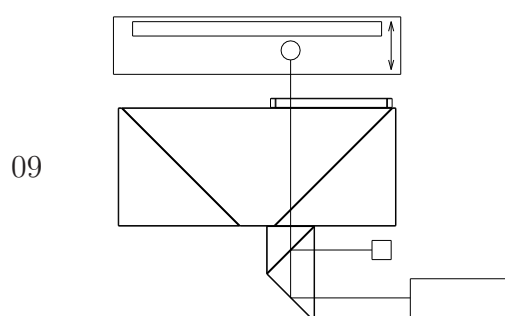
07



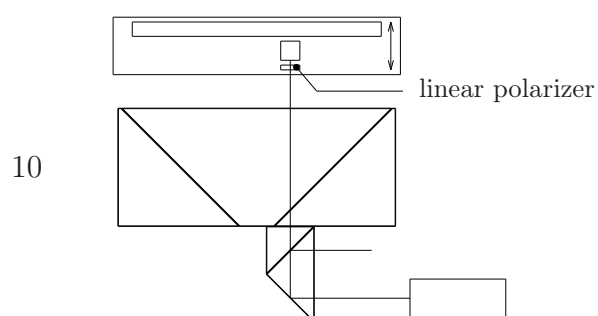
- a. move the PSD to kinematic mount nr 4
- b. check if reflected measurement beam centers on the PSD. If so then the beams are properly spaced
- c. if necessary translate MPBS sideways to correct for incorrect beam spacing
- d. reset PSD to kinematic mount nr 3



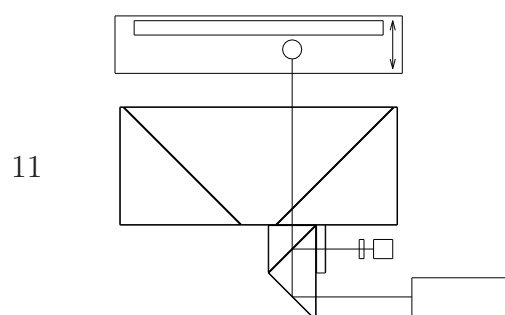
- a. install and move the input PBS until the beam centers on the PSD
 - b. if necessary reposition the laser source to get the beam centered
- this step is also described as step 1 on Page 107 (Figure 5.15)



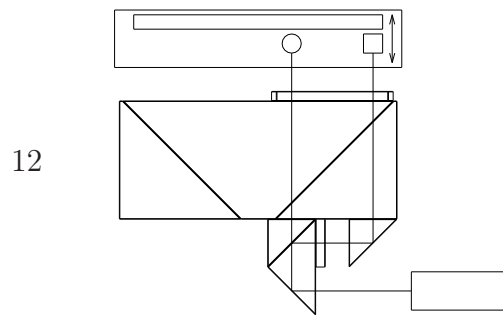
- a. move PSD to kinematic mount nr 1
- b. rotate the input PBS until the beam centers on the PSD



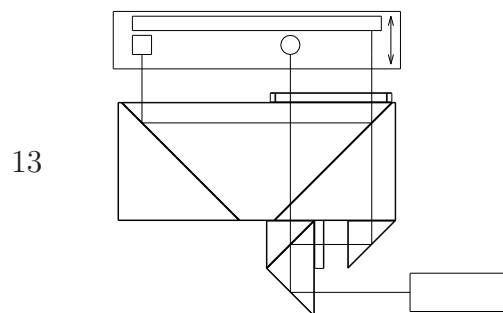
- a. move the PSD to kinematic mount nr 3
- b. install a linear polarizer in the beam and rotate until the light intensity on the PSD is maximal



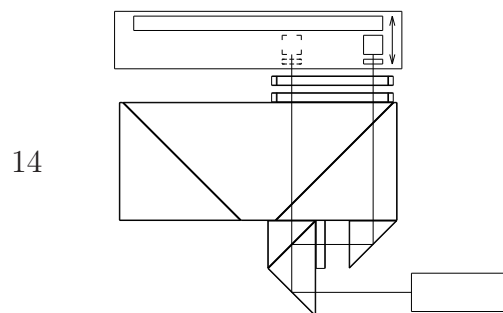
- a. move PSD and linear polarizer to kinematic mount nr 1
 - b. install HWP A against the input PBS
 - c. rotate HWP until the light intensity at PSD is maximal
- this step is also described as step 2 on Page 108 (Figure 5.16)



- a. move PSD to kinematic mount nr 2
- b. install prism A and adjust its position until the beam centers on the PSD
- this step is also described as step 3 on Page 109 (Figure 5.17)

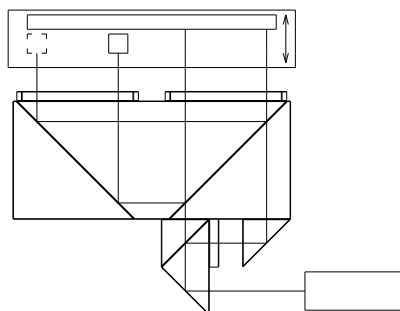


- a. move the PSD to kinematic mount nr 5
- b. check if the reference beam spacing is correct (first order only)



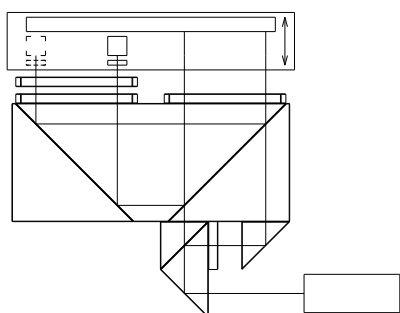
- a. move the PSD to kinematic mount nr 2
- b. temporarily install an extra QWP between the mirror and QWP A
- c. install the linear polarizer and measure beam intensity
- d. move PSD and polarizer to kinematic mount nr 3 and measure beam intensity
- e. if the two intensities differ considerably: rotate HWP to correct the polarization alignment error between the beams
- f. remove extra QWP

15



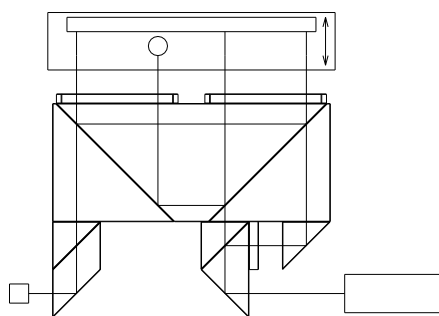
- a. move PSD to kinematic mount nr 4
- b. install QWP B
- c. check beam parallelism by moving mirror block from position A to B while measuring beam displacement on the PSD
- d. repeat with PSD at position 5

16



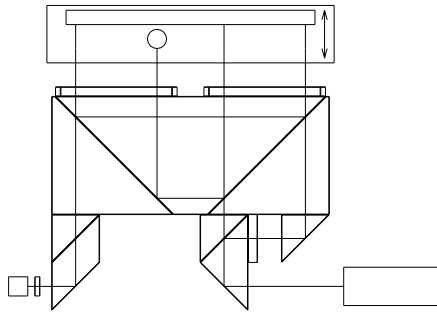
- a. temporarily install an extra QWP between the mirror and QWP B
- b. repeat measurements described in step 14 (check only)

17



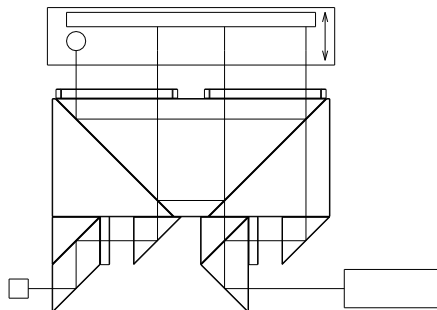
- a. move the PBS to position 6
 - b. add the output PBS and move until the output beam centers on the PSD
 - c. determine output beam's parallelism to the table by moving the PSD to position 7
 - d. install the beam stop in the measurement beam
- this step is also described as step 4 on Page 110 (Figure 5.18)

18



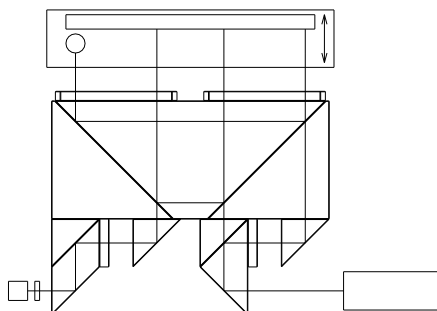
- a. install the linear polarizer in the output beam and rotate until beam intensity on PSD is maximum
- b. rotate the polarizer over 90 degrees and remove from the beam

19

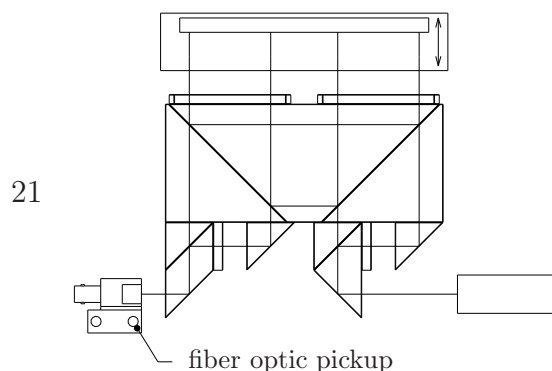


- a. move the beam stop to the reference beam
 - b. add prism B and HWP B
 - c. align prism so the beam centers on the PSD
 - d. repeat step b with the PSD at kinematic mount nr 7. The reference beam and measurement beam now overlap
- this step is also described as step 5 on Page 110 (Figure 5.19)

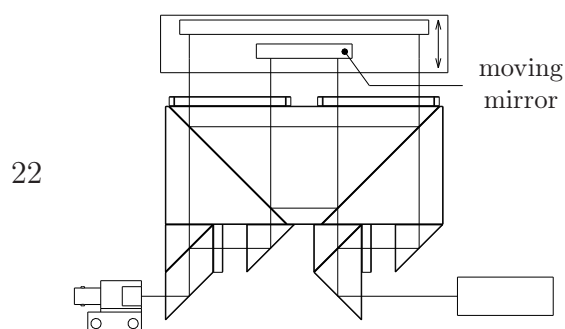
20



- a. reinstall the previously aligned linear polarizer
- b. rotate the HWP B until the light intensity at the PSD is maximal



- a. remove the beam stop
- b. place the fiber optic pickup in the output beam and use the measurement electronics's adjustment procedure [115] to fine adjust the prism B and HWP B position (if necessary)



- a. install a moveable mirror on the mirror and PSD block. A CPS measures the mirror's displacement
 - b. translate the mirror and compare the interferometer output with the CPS signal to determine the interferometer's linearity
 - c. remove the moving mirror. Determine the interferometer's stability by using one mirror as a target. Any measured displacement originates from the interferometer itself or drift and noise in the measurement electronics
 - d. remove the manipulators and repeat steps b and c
 - e. remove interferometer from the jig and install onto the optics box, see Section 5.2.4 on Page 113
- this step is also described as step 6 on Page 112 (Figure 5.20)

Transport accessories

The following accessories protect the instrument during transport:

transport detent mechanism (Page 165) to constrain the translation stage's sample table and straight guides,

mirror preload mechanism (Page 168) to preload the stationary reference mirror onto its kinematic mount,

transport cover and transport case (Page 169).

Transport detent

The manually operated detent mechanism is located on the instrument centerline and is controlled via a knob at the instrument circumference (Figure G.1).

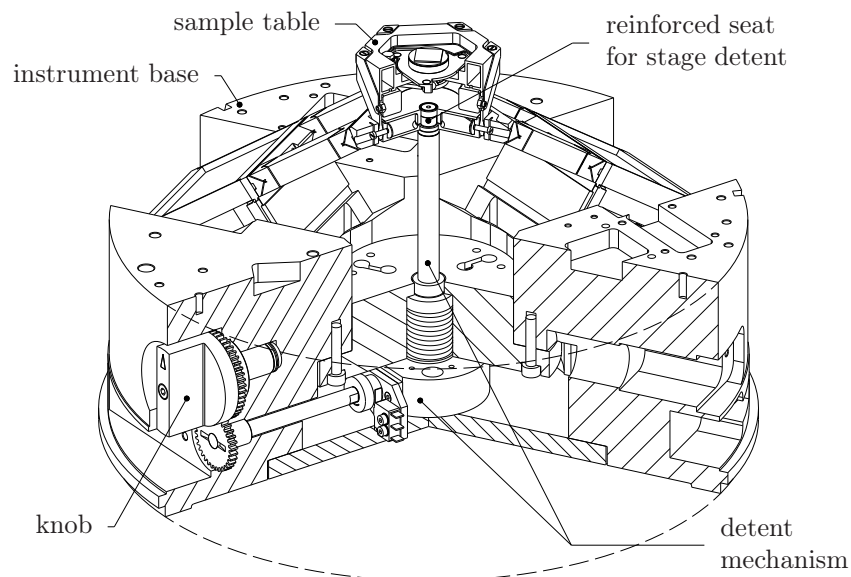


Figure G.1 / Cutaway view. The transport detent mechanism is located on the instrument centerline and is controlled via a knob at the instrument circumference.

The detent locates the sample table in the center of its motion range so all elastic straight guide elements are minimally stressed.

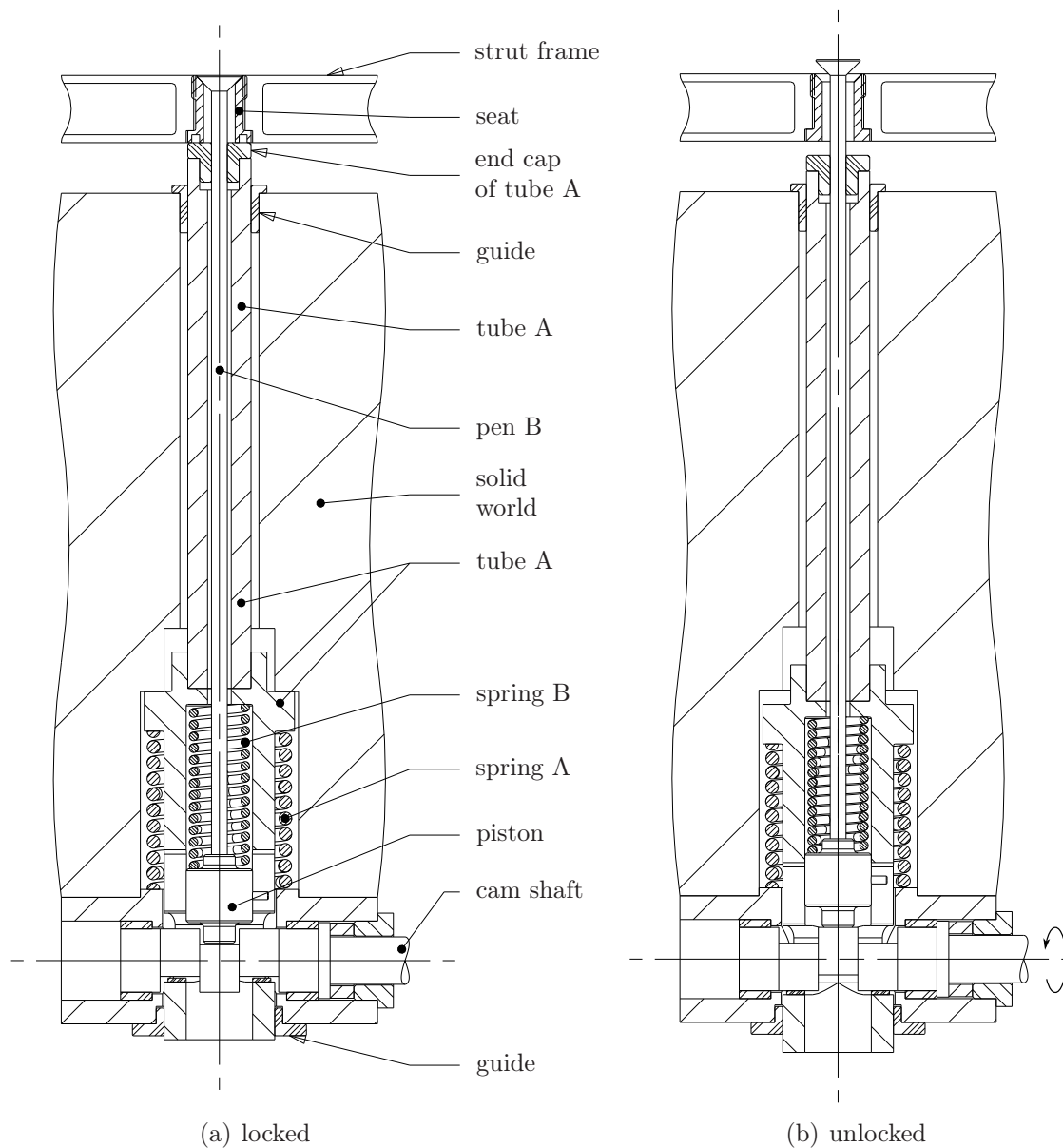


Figure G.2 / Cross-section of the transport detent mechanism. The mechanism is located on the instrument centerline. The solid world is drawn schematically.

Figure G.2(a) shows the detent mechanism in the closed position. The end cap of tube A provides a vertical reference or stop for the strut frame. Spring loaded pen B pulls the strut frame onto tube A's end cap, the pen's conical head horizontally centers the strut frame.

Rotating the cam shaft over 180° , opens the detent (Figure G.2(b)). The cam shaft's two outer cams synchronously pull tube A downward while the central cam pushes pen B upwards. The cam shaft decouples the detent's locking force from the torque needed to control the detent. The detent's clamping force loop is closed within the mechanism for minimal distortion of the sample table frame and the instrument base. Figure G.6(a) at the end of this appendix, gives a photograph of the detent mechanism.

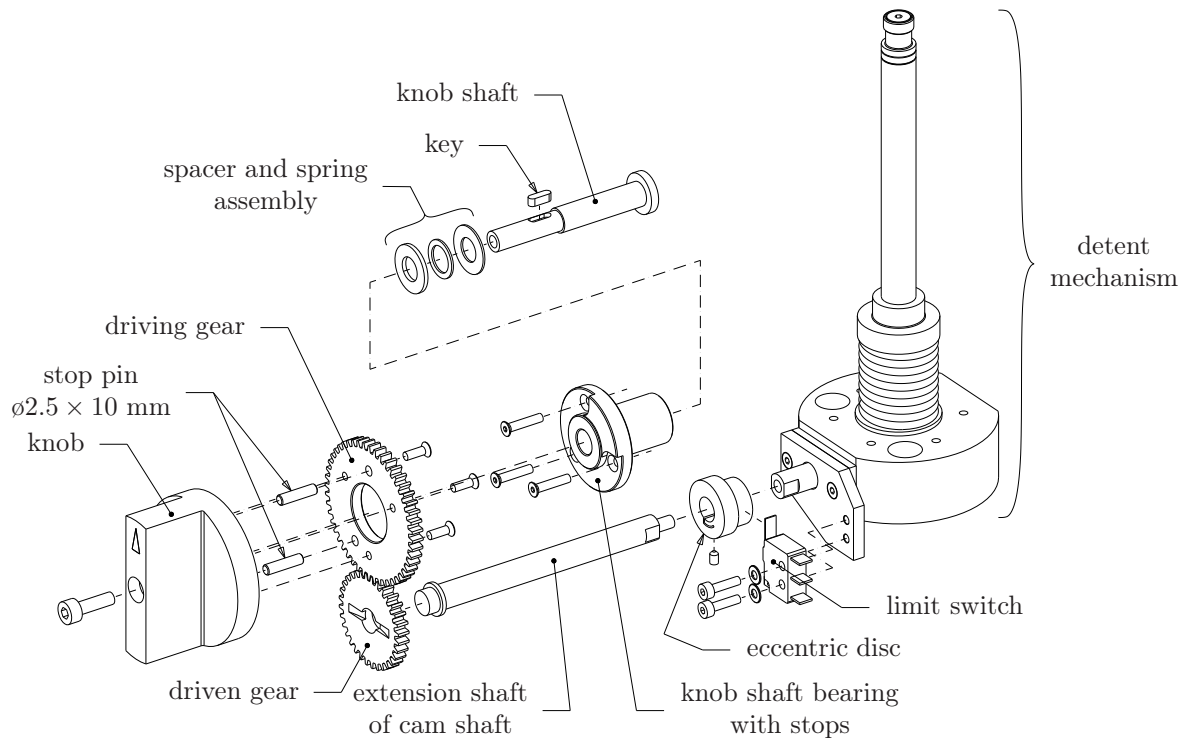


Figure G.3 / Exploded view of the transportation detent's knob assembly. The knob is located at the instrument's outer circumference, the detent mechanism at the instrument centerline.

Figure G.3 shows the detent knob assembly. The detent mechanism's knob drives the cam shaft through two steel gears. The driving gear is directly attached to the knob for high stiffness. Pins at the back of the knob, define the detent's end positions so the operator can clearly feel when the end positions are reached. A spring eliminates axial backlash in the knob bearing for a high-quality feel.

A limit switch detects the detent position (open/closed). This information is used during the interferometer initialization on instrument startup.

Reference mirror preload mechanism

The AFM head preloads the stationary reference mirror (Page 121) onto its kinematic mount during measurements. A separate preload mechanism replaces the AFM head during transport. Figure G.4 gives an exploded view of this stationary reference mirror preload mechanism.

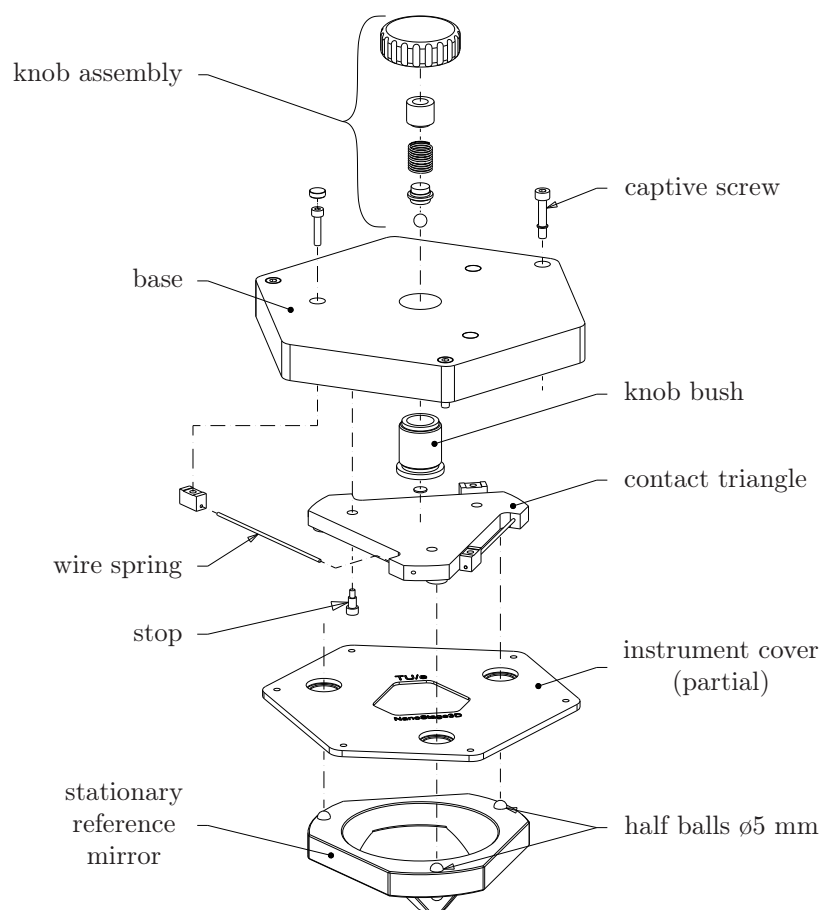


Figure G.4 / The stationary reference mirror preload mechanism preloads the reference mirror to the instrument during transport.

Three flat surfaces on the contact triangle's underside, mesh with the stationary reference mirror's three upper half balls. Three tangential wire springs connect the contact triangle to the preload mechanism's base and constrain the remaining DOFs. The mechanism's base, in turn, is fastened to the instrument cover by three captive screws. A preloaded compression spring in the knob assembly generates the preload force on the contact triangle.

Figure G.6(c) on Page 171 shows the reference mirror preload mechanism installed on the instrument cover.

Transport cover and transport case

Figure G.5 gives an exploded view of the instrument's transport cover. The reference mirror preload mechanism and the foam-lined transport case are also shown.

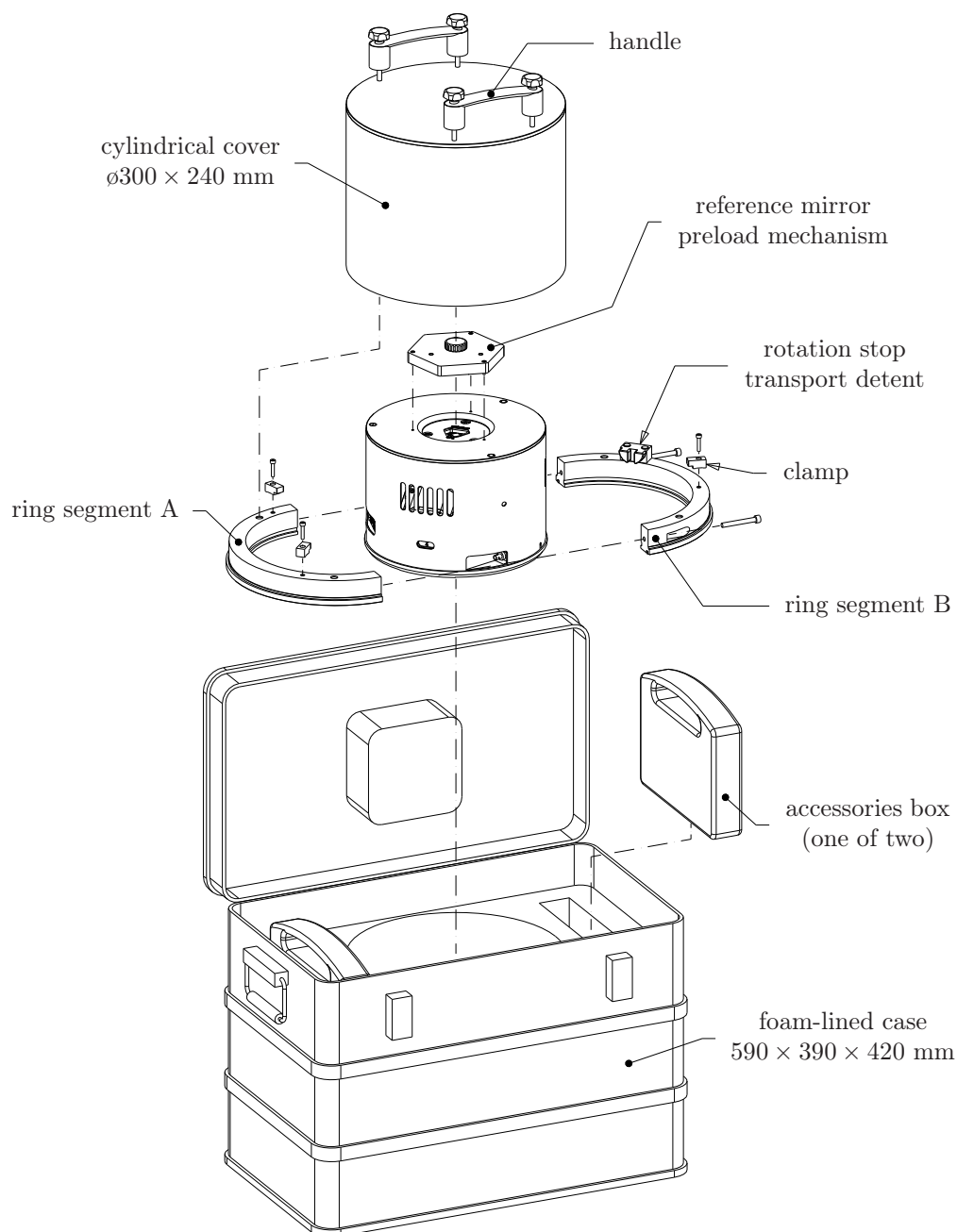


Figure G.5 / A dustproof transport cover and a foam-lined aluminium case, protect the instrument during transport.

The transport cover has an cylindrical aluminium cover $\varnothing 300$ mm and a two-segment ring. The two ring segments mesh with a flange on the instrument base. Four screws fasten the cylindrical cover to the ring segments.

Three clamps on the ring segments, eliminate the play between the ring and the instrument. A rotation stop on ring segment B secures the transport detent's knob against rotation. Rubber inserts in the ring underside, reduce the impact when the instrument is (unevenly) put down.

The cylindrical cover's four screws also secure the handles to the cover so it is, as a precaution, only possible to lift the instrument when the cover is properly fastened to the ring segments.

Figure G.6(b) gives a photograph of the assembled transport cover.

The aluminium transport case's foam lining is machined to a precision fit by waterjet cutting and has recesses for two accessories boxes. Figures G.6(d), G.6(e) and G.6(f) show photographs of the transport case and the accessories boxes.

The transport detent, the transport cover and the transport case were successfully put to the test on a 2500 km round trip from Eindhoven to San Sebastian, where the instrument was displayed at the Euspen 2009 conference [108].



(a) transport detent mechanism



(b) instrument, transport cover and several accessories



(c) reference mirror preload mechanism on instrument cover



(d) accessories box A (235 × 185 × 48 mm) with spare kinematic sample holders



(e) transport case (590 × 390 × 420 mm)



(f) accessories box B (235 × 185 × 48 mm) with instrument installation tools

Figure G.6 / The transport detent and the reference mirror preload mechanism constrain sample stage and the stationary reference mirror, respectively. The transport cover and transport case protect the instrument from dust and vibrations.

Bibliography

- [1] E. Abbé. Meßapparate für Physiker. *Zeitschrift Für Instrumentenkunde*, 10:446–8, 1890.
- [2] Advanced Surface Microscopy Inc., April 2005. <http://www.asmicro.com>.
- [3] AIST-NT, May 2009. <http://www.aist-nt.com>.
- [4] W. Augustyn and P. Davis. An analysis of polarization mixing errors in distance measuring interferometers. *J. Vac. Sci. Techno.*, 8(6):2032–6, 1990.
- [5] R. C. Barrett and C. F. Quate. Optical scan-correction system applied to atomic force microscopy. *Rev. Sci. Instrum.*, 62(6):1393–9, 1991.
- [6] A. G. T. M. Bastein, R. H. Bergmans, K. R. Koops, P. H. J. Schellekens and H. Haitjema. NanoNed project report, Flagship Nano-instrumentation, cluster 3: Metrology Stages, WP2: realization of a stage for SPM. 2004.
- [7] S. J. Bennett. A double-passed Michelson interferometer. *Optics Communications*, 4(6):428–30, 1972.
- [8] Berliner Glas KGaA Herbert Kubatz GmbH & Co., Waldkraiburger Straße 5, D-12347 Berlin. <http://www.berlinglas.de>.
- [9] G. Binnig, C. F. Quate and C. Gerber. Atomic force microscope. *Phys. Rev. Lett.*, 56(9):930–3, 1986.
- [10] G. Binnig, H. Rohrer, C. Gerber and E. Weibel. Surface studies by scanning tunneling microscopy. *Phys. Rev. Lett.*, 49(1):57–61, 1982.
- [11] N. Bobroff. Critical alignments in plane mirror interferometry. *Precis. Eng.*, 15(1):33–8, 1993.
- [12] N. Bobroff. Recent advances in displacement measuring interferometry. *Meas. Sci. Techno.*, 4:907–26, 1993.
- [13] R. Breil, T. Fries, J. Garnaes, J. Haycocks et al. Intercomparison of scanning probe microscopes. *Precis. Eng.*, 26:296–305, 2002.
- [14] J. B. Bryan. The Abbé principle revisited: an updated interpretation. *Precis. Eng.*, 1(3):129–32, 1979.
- [15] J. C. Compter. *The design and applications of industrial linear motors (lecture notes)*. Number 5EP10. Technische Universiteit Eindhoven, 2010.
- [16] J. C. Compter. Electromechanical Precision Drives Design Group, Technische Universiteit Eindhoven. Private communication, Sept 2010.
- [17] J. C. Compter, E. A. Lomonova and J. Makarovic. Direct 3-D method for performance prediction of a linear moving coil actuator with various topologies. *IEE Proc.-Sci. Meas. Technol.*, 150(4):183–91, 2003.
- [18] S. J. A. G. Cosijns. *Displacement laser interferometry with sub-nanometer uncertainty*. PhD thesis, Technische Universiteit Eindhoven, 2004.

- [19] G. Dai, T. Dziomba, M. Xu, L. Koenders and G. Wilkening. Accurate and traceable 3D calibration of nanoscale standards. In *Euspen 2005 - Conference Proceedings*, volume 1, pages 141–4, 2005.
- [20] G. Dai, L. Koenders, F. Pohlenz, T. Dziomba and H. U. Danzebrink. Accurate and traceable calibration of one-dimensional gratings. *Meas. Sci. Technol.*, 16:1241–9, 2005.
- [21] G. Dai, F. Pohlenz, H. U. Danzebrink, K. Hasche and G. Wilkening. Improving the performance of interferometers in metrological scanning probe microscopes. *Meas. Sci. Technol.*, 15:444–50, 2004.
- [22] G. Dai, F. Pohlenz, H. U. Danzebrink, M. Xu, K. Hasche and G. Wilkening. Metrological large range scanning probe microscope. *Rev. Sci. Instrum.*, 75(4):962–69, 2004.
- [23] G. Dai, H. Wolff, F. Pohlenz and H. U. Danzebrink. Further improvements of the measurement capabilities of a metrological large range AFM. In *Euspen 2010 - Conference Proceedings*, volume 1, pages 55–8, 2010.
- [24] H. U. Danzebrink, L. Koenders, G. Wilkening, A. Yacoot and H. Kunzmann. Advances in scanning force microscopy for dimensional metrology. *Annals of the CIRP*, 55:841–78, 2006.
- [25] F. C. Demarest. High-resolution, high-speed, low data age uncertainty, heterodyne displacement measuring interferometer electronics. *Meas. Sci. Technol.*, 9:1024–30, 1998.
- [26] K. Dirscherl and K. R. Koops. Developments on the NMi-VSL traceable scanning probe microscope. In *Proceedings of SPIE*, volume 5190, pages 173–7, 2003.
- [27] M. J. Downs. A proposed design for an optical interferometer with sub-nanometric resolution. *Nanotechnology*, 1:27–30, 1990.
- [28] M. J. Downs and J. W. Nunn. Verification of the sub-nanometric capability of an NPL differential plane mirror interferometer with a capacitance probe. *Meas. Sci. Technol.*, 9:1437–40, 1998.
- [29] M. J. Downs and W. R. C. Rowley. A proposed design for a polarization-insensitive optical interferometer with subnanometric capability. *Precis. Eng.*, 15(4):281–6, 1993.
- [30] J. N. Dukes and G. B. Gordon. A two-hundred-foot yardstick with graduations every microinch. *Hewlett-Packard J.*, 21(2):2–8, 1970.
- [31] T. Dziomba, L. Koenders and G. Wilkening. Entwicklung einer Kalibrierrichtlinie für Rastersondenmikroskope. *Technisches Messen*, 72(5):295–307, 2005.
- [32] J. van Eijk. *On the design of plate-spring mechanisms*. PhD thesis, Technische Universiteit Delft, 1985.
- [33] B. J. Eves. Design of a large measurement-volume metrological atomic force microscope (AFM). *Meas. Sci. Technol.*, 20(084003), 2009.
- [34] G. Friedbacher and H. Fuchs. Classification of scanning probe microscopies. *Pure Appl. Chem.*, 71(7):1337–57, 1999.
- [35] F. J. Giessibl. Advances in atomic force microscopy. *Rev. Mod. Phys.*, 75(3):949–83, 2003.
- [36] S. Gonda, T. Doi, T. Kurosawa, Y. Tanimura et al. Real-time, interferometrically measuring atomic force microscope for direct calibration of standards. *Rev. Sci. Instrum.*, 70(8):3362–8, 1999.

- [37] J. E. Griffith and D. A. Grigg. Dimensional metrology with scanning probe microscopes. *J. Appl. Phys.*, 74(9):R83–R109, 1993.
- [38] J. E. Griffith, G. L. Miller, C. A. Green, D. A. Grigg and P. E. Russell. A scanning tunneling microscope with a capacitance-based position monitor. *J. Vac. Sci. Technol. B*, 8(6):2023–7, 1990.
- [39] F. W. Grover. *Inductance calculations; working formulas and tables*. Dover, New York, 1973.
- [40] H. Haitjema, P. H. J. Schellekens and S. F. C. L. Wetzels. Calibration of displacement sensors up to 300 μm with nanometre accuracy and direct traceability to a primary standard of length. *Metrologia*, 37:25–33, 2000.
- [41] P. Hammond. *Electromagnetism for Engineers - An Introductory Course*. Oxford University Press, New York, fourth edition, 1997.
- [42] P. K. Hansma, J. P. Cleveland, M. Radmacher, D. A. Walters, P. E. Hillner et al. Tapping mode atomic force microscopy in liquids. *Appl. Phys. Lett.*, 64(13):1738–40, 1994.
- [43] A. G. Hardenbol, B. Kruizinga and D. de Bruijn. TNO Science and Industry. Private communications, 2008 - 2009.
- [44] W. Häßler-Grohne and H. Bosse. An electron optical metrology system for pattern placement measurements. *Meas. Sci. Technol.*, 9:1120–8, 1998.
- [45] J. Haycocks and K. Jackson. Traceable calibration of transfer standards for scanning probe microscopy. *Precis. Eng.*, 29:168–75, 2005.
- [46] W. C. Heerens. Application of capacitance techniques in sensor design. *J. Phys. E: Sci. Instrum.*, 19:897–906, 1986.
- [47] J. Herrmann, M. Lawn, C. Freund, J. Miles, V. Coleman and Å. Jämtning. Development of a scanning probe microscope for traceable nanoscale length metrology. In *Euspen 2010 - Conference Proceedings*, volume 1, pages 152–5, 2010.
- [48] W. Hou and X. Zhao. Drift of nonlinearity in the heterodyne interferometer. *Precis. Eng.*, 16(1):25–35, 1994.
- [49] A. Humphris, P. Atherton, D. Catto, C. Vasilev and J. Hobbs. Video rate atomic force microscopy. In *Euspen 2005 - Conference Proceedings*, volume 1, pages 145–8, 2005.
- [50] Interferomet Ltd, 2005. <http://www.interferomet.com>.
- [51] G. Jäger, E. Manske, T. Hausotte and H. J. Büchner. Nanomessmaschine zur abbefehlerfreien Koordinatenmessung. *Technisches Messen*, 67(7-8):319–23, 2000.
- [52] M. H. C. Janssen. Datasheet 'Audio Current Amplifier with OPA541' GTD-TU/e.
- [53] K. L. Johnson. *Contact mechanics*. Cambridge University Press, 1985.
- [54] J. Kim, J. W. Kim, B. C. Park and T. B. Eom. Measurement of microscope calibration standards in nanometrology using a metrological atomic force microscope. *Meas. Sci. Technol.*, 17:1792–800, 2006.
- [55] D. S. Klinger, J. W. Lewis and C. E. Randall. *Polarized light in optics and spectroscopy*. Academic Press, San Diego, 1990.
- [56] K. R. Koops and K. Dirscherl. Nanometrology standards in the Netherlands: the traceable scanning probe microscope. In *Euspen 2002 - Conference Proceedings*, volume 1, pages 525–8, 2002.

- [57] V. I. Korotkov, S. A. Pulkin, A. L. Vitushkin and L. F. Vitushkin. Laser interferometric diffractometry for measurements of diffraction grating spacing. *Applied Optics*, 35(24):4782–6, 1996.
- [58] V. Korpelainen and A. Lassila. Calibration of a commercial AFM: traceability for a coordinate system. *Meas. Sci. Technol.*, 18:395–403, 2007.
- [59] V. Korpelainen, J. Seppä and A. Lassila. Design and characterization of the MIKES metrology atomic force microscope. In *Euspen 2009 - Conference Proceedings*, volume 2, pages 239–42, 2009.
- [60] J. A. Kramar. Nanometre resolution metrology with the molecular measuring machine. *Meas. Sci. Technol.*, 16:2121–8, 2005.
- [61] A. Lassila and V. Korpelainen. Design of an interferometrically traceable AFM at MIKES. In *Proceedings of Nanoscale 2004*, 2004.
- [62] M. Lawn, J. Herrmann, C. H. Freund, J. R. Miles, M. Gray et al. Traceable nanoscale length metrology using a metrological Scanning Probe Microscope. In *Proceedings of SPIE*, volume 7729, 2010.
- [63] J. Lazar, P. Klapetek, O. Číp, M. Čížek and M. Šery. Local probe microscopy with interferometric monitoring of the stage nanopositioning. *Meas. Sci. Technol.*, 20(084007), 2009.
- [64] R. Leach, J. Haycocks, K. Jackson, A. Lewis, S. Oldfield and A. Yacoot. Advances in traceable nanometrology at the National Physical Laboratory. *Nanotechnology*, 12:R1–R6, 2001.
- [65] R. K. Leach. Traceable measurement of surface texture at the National Physical Laboratory using NanoSurf IV. *Meas. Sci. Technol.*, 11:1162–72, 2000.
- [66] LOT-Oriel, April 2005. <http://www.lotoriel.de>.
- [67] M. Lu, S. Gao, Q. Jin, J. Cui, H. Du and H. Gao. An atomic force microscope head designed for nanometrology. *Meas. Sci. Technol.*, 18:1735–9, 2007.
- [68] Y. Martin, C. C. Williams and H. K. Wickramasinghe. Atomic force microscope-force mapping and profiling on a sub 100-Å scale. *J. Appl. Phys.*, 61(10):4723–9, 1987.
- [69] F. Meli. Design of a new 3D-metrology AFM at METAS using differential Jamin type interferometers. In *NanoScale 2008. Programme and Short Abstracts*, 2008.
- [70] F. Meli, R. Thalmann and P. Blattner. High precision pitch calibration of gratings using laser diffractometry. In *Conf. on Precision Engineering and Nanotechnology*, volume 2, pages 252–5, 1999.
- [71] J. P. Merlet. Direct kinematics of parallel manipulators. *IEEE transactions on robotics and automation*, 9(6):842–6, 1993.
- [72] G. Meyer and N. M. Amer. Novel optical approach to atomic force microscopy. *Appl. Phys. Lett.*, 53(12):1045–7, 1988.
- [73] Mikromasch, April 2005. <http://www.spmtips.com>.
- [74] I. Misumi, S. Gonda, Q. Huang, T. Keem, T. Kurosawa et al. Sub-hundred nanometre pitch measurements using an AFM with differential laser interferometers for designing usable lateral scales. *Meas. Sci. Technol.*, 16:2080–90, 2005.
- [75] S. Moshier. Inductance Calculator version 0.2. Computer program, 2006.
- [76] Nanodevices, May 2005. <http://www.pelcoint.com/probes/calibgrt.html>.

- [77] NanoNed. <http://www.nanoned.nl>.
- [78] Nanosensors, April 2005. <http://www.nanosensors.com/2D300.html>.
- [79] Nanostage3D. <http://www.nanostage3D.nl>.
- [80] NT-MDT, April 2005. <http://www.ntmdt-tips.com/catalog/gratings>.
- [81] G. B. Picotto and M. Pisani. A sample scanning system with nanometric accuracy for quantitative SPM measurements. *Ultramicroscopy*, 86:247–54, 2001.
- [82] J. Piot. Micro & Precision Engineering Group, Katholieke Universiteit Leuven. Private communication, Sept 2009.
- [83] J. Piot, J. Qian, H. Pirée, G. Kotte, J. Petry et al. Design of a sample holder for a metrological atomic force microscope. In *Euspen 2010 - Conference Proceedings*, volume 1, pages 2241–4, 2010.
- [84] J. Piot, J. Qian, H. Pirée, G. Kotte, C. van Haesendonck et al. Design of a thermally and mechanically stable metrological atomic force microscope at KULeuven. In *Euspen 2009 - Conference Proceedings*, volume 2, pages 227–30, 2009.
- [85] P. V. Pistecky. *Micro-techniek constructie-elementen 1: lagers (lecture notes, in Dutch)*. Number wb5409. Technische Universiteit Delft, 1987.
- [86] B. Poyet and S. Ducourtieux. Advances in the development of the LNE metrological atomic force microscope. In *Proceedings of SPIE*, volume 7718, 2010.
- [87] B. Poyet, S. Ducourtieux, J. David and L. Lahousse. Design of the LNE metrological atomic force microscope. In *Euspen 2009 - Conference Proceedings*, volume 2, pages 263–6, 2009.
- [88] B. Poyet, S. Ducourtieux, J. David, L. Lahousse and S. Leleu. Development of a new high guidance quality XYZ flexure scanner for the LNE metrological AFM. In *NanoScale 2008. Programme and Short Abstracts*, 2008.
- [89] PTB, Arbeitsgruppe 5.15, Quantitative Rastersondenmikroskopie, May 2008. <http://www.ptb.de>.
- [90] K. W. Raine and M. J. Downs. Beam-splitter coatings for phase quadrature interferometer optics. *Optica Acta*, 25(7):549–58, 1978.
- [91] A. M. Rankers. *Machine dynamics in mechatronic systems - an engineering approach*. PhD thesis, Universiteit Twente, 1997.
- [92] I. de Rijk. Design of a metrological atomic force microscope head. Master's thesis, Technische Universiteit Eindhoven, Dec 2008.
- [93] P. C. J. N. Rosielle and E. A. G. Reker. *Constructieprincipes 1 - bedoeld voor het nauwkeurig bewegen en positioneren (lecture notes, in Dutch)*. Number 4007. Technische Universiteit Eindhoven, 2000.
- [94] D. Sarid. *Scanning force microscopy : with applications to electric, magnetic and atomic forces*. Oxford University Press, rev. ed edition, 1994.
- [95] D. Sarid, D. Iams, V. Weissenberger and L. S. Bell. Compact scanning-force microscope using a laser diode. *Optics Letters*, 13(12):1057–9, 1988.
- [96] P. van Schendel. NanoSurf AG - SPM introduction. Presentation, 2006.
- [97] I. Schmidt, T. Hausotte, U. Gerhardt, E. Manske and G. Jäger. Investigations and calculations into decreasing the uncertainty of a nanopositioning and nanomeasuring machine (NPM-Machine). *Meas. Sci. Technol.*, 18:482–6, 2007.

- [98] J. Schneir, T. H. McWaid, J. Alexander and B. P. Wilfley. Design of an atomic force microscope with interferometric position control. *J. Vac. Sci. Techno.*, B 12(6):3561–6, 1994.
- [99] J. K. van Seggelen. *A 3D coordinate measuring machine with low moving mass for measuring small products in array with nanometer uncertainty*. PhD thesis, Technische Universiteit Eindhoven, 2007.
- [100] R. Solberg. *Data acquisition system AFM (type no. P09008)*. IME Technologies, Den Dolech 2 - WL 1.56, 5612 AZ Eindhoven, Dec 2009. <http://www.imetechnologies.nl>.
- [101] G. E. Sommargren. A new laser measurement system for precision metrology. *Precis. Eng.*, 9(4):179–84, 1987.
- [102] E. C. Teague. The National Institute of Standards and Technology molecular measuring machine project: metrology and precision engineering design. *J. Vac. Sci. Techno.*, 7(6):1898–902, 1989.
- [103] M. G. A. van Veghel and K. R. Koops. VSL - Dutch Metrology Institute. Private communications, 2008.
- [104] J. P. M. B. Vermeulen. *Ceramic optical diamond turning machine*. PhD thesis, Technische Universiteit Eindhoven, 1999.
- [105] M. M. P. A. Vermeulen. *High-precision 3D-coordinate measuring machine - design and prototype-development*. PhD thesis, Technische Universiteit Eindhoven, 1999.
- [106] VLSI Standards Inc., April 2005. <http://www.vlsistd.com>.
- [107] C. Werner, P. C. J. N. Rosielle and M. Steinbuch. Design and realization of a long stroke translation stage for SPM. In *NanoScale 2008 - Programme and Short Abstracts*, 2008.
- [108] C. Werner, P. C. J. N. Rosielle and M. Steinbuch. Design and realization of a long stroke translation stage for metrological AFM. In *Euspen 2009 - Conference Proceedings*, volume 1, pages 176–9, 2009.
- [109] C. Werner, P. C. J. N. Rosielle and M. Steinbuch. Design of a long stroke translation stage for AFM. *Int. J. Mach. Tool. Manu.*, 50(2):183–90, 2010.
- [110] P. West and B. Weeks. Scanning 2005. In *Short course: introduction to atomic force microscopy*, 2005.
- [111] C. M. Wu and R. D. Deslattes. Analytical modeling of the periodic nonlinearity in heterodyne interferometry. *Applied Optics*, 37(28):6696–700, 1998.
- [112] A. Yacoot. NPL Center for Basic Thermal and Length Metrology. Private communication, April 2006.
- [113] C. Zanoni. Differential interferometer arrangements for distance and angle measurements: principles, advantages and applications. *VDI Berichte*, (749):93–106, 1989.
- [114] Q. Zhong, D. Inniss, K. Kjoller and V. B. Elings. Fractured polymer/silica fiber surface studied by tapping mode atomic force microscopy. *Surface Science Letters*, 290:L688–92, 1993.
- [115] Zygo[®] Corporation, Laurel Brook Road, Middlefield, Connecticut, USA. *Operating Manuals OMP-0329B (7702 laser head), OMP-0460Q (ZMI4000 measurement board), OMP-0429H (ZMI510 interferometer system)*.
- [116] Zygo[®] Metrology Solutions Division, 2008. <http://www.zygo.com/met>.

Nomenclature

Symbol	Description	Unit
A	area	m^2
B	magnetic flux density	T
B_r	magnet remanence	T
c	speed of light	m/s
c	stiffness	N/m
c_p	specific heat	$\text{J}/(\text{kg K})$
d	diameter	m
E	energy	J
E	modulus of elasticity	N/m^2
F	force	N
f	frequency	Hz
f_{eig}	first resonance frequency	Hz
g	gravitational acceleration	m/s^2
H	coercive field strength	A/m
H_c	magnet coercivity	A/m
i	current	A
i	ratio	-
J	current density	A/m^2
K_f	force constant	N/A
K_m	motor constant (\sqrt{S})	$\text{N}/\sqrt{\text{W}}$
L	inductance	H
l	length	m
N	turns	-
P_{diss}	power loss	W
R	radius	m
R	reflection coefficient	-
R	resistance	Ω
r	relative spring compression	-
S	steepness (K_m^2)	N^2/W
s	stroke	m

Symbol	Description	Unit
T	temperature	K
T	transmission coefficient	-
v	speed	m/s
V	volume	m ³
W	work	J
x, y, z	cartesian coordinate system	-

Greek	Description	Unit
α	angle	rad
α	coefficient of thermal expansion	m/(m K)
Δf	frequency difference	Hz
ΔT	temperature difference	K
ΔV	voltage drop	V
$\Delta x, \Delta y, \Delta z$	displacement in x, y or z	m
θ	rotation around z axis	rad
λ	thermal conductivity	W/(m K)
λ	wavelength	m
μ	friction coefficient	-
μ	permeability	H/m
ρ	density	kg/m ³
ϱ	specific resistance	Ω m
φ	magnetic circuit flux	Wb
φ	rotation around x axis	rad
ψ	rotation around y axis	rad

Subscript	Description	Subscript	Description
a	axial	o	unstressed
c	coil, compensation	p	parallel
e	effective	r	residual, reaction
g	gap, weight compensation	s	stage, stroke, sample
h	horizontal	t	tangential
l	lateral	v	vertical
m	magnet	w	wire
n	nominal, normal	y	yoke

Abbreviation	Description
AC	autocollimator, autocollimation
ADC	analog-to-digital converter
AFM	atomic force microscope / microscopy
AIMS™	Adaptive Interferometric Metrology System, homodyne, differential plane mirror interferometer, trademark of Interferomet Ltd
AR	anti-reflection
Armco®	soft-iron, registered trademark of AK Steel
c-AFM	contact mode AFM
CFM	constant force mode
CHM	constant height mode
CNC	computer numerical control
CMI	Czech Metrology Institute
CMOS	complementary metal-oxide-semiconductor image sensor
COG	center of gravity
CPS	capacitive position sensor
CST	Control Systems Technology Group TU/e
CTE	coefficient of thermal expansion
DAC	digital-to-analog converter
DMI	displacement measuring interferometer
DOF	degree of freedom
DPMI	differential plane mirror interferometer
EDM	electrical discharge machining
FEA	finite element analysis
FPS-SMD	FPS Economy - SMD Metrology Division (Belgium)
FRF	frequency response function
GTD	Gemeenschappelijke Technische Dienst TU/e
HSPMI	high stability plane mirror interferometer
HWP	half-wave plate
iNRiM	Istituto Nazionale di Ricerca Metrologica (Italy)
Invar®	low-expansion metal, registered trademark of ArcelorMittal
KRISS	Korea Research Institute of Standards and Science
LNE	Laboratoire National de Métrologie et d'Essais (France)
LR-SPM	Large-Range SPM (PTB's mAFM)
mAFM	metrological AFM
Matlab Simulink®	modeling and simulation software for dynamic systems, registered trademark of The MathWorks, Inc.
Maxwell®	electromagnetic field simulation software, registered trademark of Ansoft Corporation

Abbreviation	Description
METAS	Swiss Federal Office of Metrology and Accreditation
MIKES	Centre for Metrology and Accreditation (Finland)
MPBS	main polarizing beamsplitter
nc-AFM	non-contact mode AFM
NIM	National Institute of Metrology (China)
NIST	National Institute of Standards and Technology (USA)
NMI	national metrology institute
NMIA	National Metrology Institute Australia
NMIJ	National Metrology Institute of Japan
NMM	NanoMeasuringMachine, SIOS Meßtechnik GmbH
NPBS	non-polarizing beamsplitter
NRC	National Research Council of Canada
NX Nastran [®]	finite element analysis (FEA) software tool, registered trademark of UGS Corp.
OBD	optical beam deflection
OPD	optical path difference
PBS	polarizing beamsplitter
Pen-VAC [®]	bellow-type vacuum gripper, registered trademark of Sipel Electronic S.A.
PMI	plane mirror interferometer
PSD	position sensitive detector
PTB	Physikalisch-Technische Bundesanstalt (Germany)
PZT	polycrystalline ceramic material with piezoelectric properties, also used to refer to a piezoelectric actuator
QWP	quarter-wave plate
SEM	scanning electron microscope / microscopy
SPM	scanning probe microscope / microscopy
STM	scanning tunneling microscope / microscopy
Tappingmode [®]	intermittent contact mode AFM technique, registered trademark of Veeco Metrology Group
TC	thermal center of expansion
VNIIMS	Russian research Institute for Metrological Service
VSL	Metrology Institute of the Netherlands
Zerodur [®]	low-expansion ceramic, registered trademark of Schott AG
ZMI4004 [™]	heterodyne interferometry measurement electronics, trademark of Zygo Corporation

Summary

The Atomic Force Microscope (AFM) is a widely used, high resolution surface imaging instrument. Making accurate nanometer-scale measurements with an AFM requires calibration of the instrument against the standard of length. In this calibration, grating samples are used and these grating samples are in turn calibrated using a traceable, metrological AFM (mAFM). Extending the scanning range of mAFMs from the current tens of micrometers to the millimeter range, while maintaining nanometer range uncertainty, reduces the calibration uncertainty through better measurement statistics and therefore helps to improve nanometer scale metrology. For these reasons, a long-range mAFM is developed with a scanning range of $1 \times 1 \times 1$ mm, a sub-nanometer position resolution and a foreseen nanometer-range measurement uncertainty.

The new long-range mAFM has a stationary AFM head and a separate, three-DOF, sample translation stage to move the grating sample.

The kinematically mounted AFM head is designed for constant force, contact mode AFM and uses optical beam deflection to detect the AFM probe's movements.

Three identical, elastic parallel guides support the translation stage's sample table. Each guide has a pair of parallel, cross-hinge type struts which, in turn, are placed on a stiffened leaf spring parallelogram. The translation stage design's first resonance frequency is 1.4 kHz.

Symmetry in the sample stage design, reduces the influence of gravity and vertical temperature gradients on the sample motions. The estimated maximum reproducing sample table rotation leads to a worst-case estimated (Abbe) position measurement error of ± 3 nm. After calibration, this systematic error expectedly reduces to a ± 0.5 nm position measurement uncertainty. Similarly, the estimated maximum, random, position measurement errors caused by actuator forces and temperature gradients are ± 0.7 nm and ± 0.2 nm respectively. These errors are well within the specified range.

The grating sample is fixed on the translation stage via a kinematic sample holder. This kinematic mount allows off-line sample alignment and fast sample loading and thereby reduces the thermal disturbances on the instrument.

Three duo-motor type, Lorentz actuators drive the translation stage. The actuators are designed towards maximum efficiency, e.g. minimal power dissipation per generated unit of actuation force. Three identical, elastic, stiffness compensation and weight compensation mechanisms reduce the actuator's maximum static power dissipation from 0.48 W to below 0.6 mW.

Three identical and mutually orthogonal differential plane mirror interferometers, measure the movements of the sample table. The interferometers align to the AFM probe position for minimal Abbe errors. The differential interferometer layout minimizes the measurement system's sensitivity to temperature variations.

The three, mutually orthogonal, moving target mirror surfaces for the interferometers are integrated into one monolithic, Zerodur® component for maximum thermal and mechanical stability. Additionally, the moving target mirror's support is athermalized. The stationary reference mirror surfaces are combined into one single component as well.

Beam delivery optics distribute the laser input beam over the three interferometers. Commercial fiber optic receivers and measurement electronics complete the translation stage's measurement system.

Samenvatting

De Atomic Force Microscope (AFM) kan oppervlakken met atomaire resolutie in beeld brengen. Om een AFM voor betrouwbare lengtemetingen op nanometer-schaal te kunnen gebruiken, moet deze AFM gekalibreerd worden tegen de lengtestandaard. Voor deze kalibratie worden referentiestandaarden gebruikt die veelal gekalibreerd zijn met een herleidbare, metrologische AFM (mAFM).

De huidige mAFMs hebben een scanbereik van enkele tientallen micrometers. Als dit meetbereik, met behoud van de huidige meetonzekerheid, tot het millimeterbereik vergroot kan worden, dan kunnen referentiestandaarden statistische gezien met een lagere onzekerheid worden gekalibreerd. Deze lagere kalibratieonzekerheid is belangrijk voor de ontwikkeling van de metrologie op nanometer-schaal. Vanwege dit belang, is er een nieuwe lange-slag mAFM ontwikkeld met een meetbereik van $1 \times 1 \times 1$ mm, een subnanometer positieresolutie en een voorziene meetonzekerheid richting het nanometerbereik.

De nieuwe lange-slag mAFM bestaat uit een stilstaande AFM en een drie-assige translatietafel om het sample te bewegen. De AFM is ontworpen voor constant-force, contact-mode AFM. De verplaatsingen van de AFM probe worden via het optical beam deflection principe gemeten.

Voor de rechtgeleiding van de translatietafel worden drie identieke, elastische parallelgeleidingen gebruikt. Iedere geleiding bestaat uit twee gelijke, parallelle sprieten en een enkel parallellogram met verstijfde bladveren. De laagste resonantiefrequentie van de translatietafel is 1.4 kHz (FEA). Symmetrie in de parallelgeleiding opstelling, beperkt de invloed van verticale temperatuurgradiënten en de zwaartekracht op de bewegingen van de translatietafel. De verwachte maximale, reproducerende, rotatie van de translatietafel geeft een Abbe meetfout van ± 3 nm. Deze systematische fout reduceert na kalibratie tot een ± 0.5 nm meetonzekerheid. De niet-reproducerende rotaties, veroorzaakt door aandrijfkrachten en temperatuurgradiënten, resulteren in een geschatte meetfout van respectievelijk ± 0.7 nm en ± 0.2 nm. De afwijkingen door rotaties van de translatietafel vallen binnen de specificaties.

Het sample dat gescand moet worden, wordt via een kinematische samplehouder op de translatietafel bevestigd. De houder maakt offline sample uitlijning mogelijk en helpt daarmee de thermische belasting op het instrument te beperken.

De translatietafel wordt aangedreven door drie identieke Lorentz actuatoren. De actuatoren zijn ontworpen voor minimale warmteontwikkeling. Het verliesvermogen

in de actuatoren is verder geminimaliseerd door toepassing van gewicht- en stijfheidcompensatie. Door deze compensaties daalt het maximale, statische, verliesvermogen per actuator van 0.48 W tot minder dan 0.6 mW.

Drie identieke, differentiële vlakke-spiegel interferometers, meten de verplaatsingen van het sample. De interferometers zijn opgelijnd met de AFM probe positie om de Abbe fout te minimaliseren. De differentiële interferometer lay-out resulteert in een korte, stabiele meetlus. De drie, onderling haakse, bewegende doelspiegels zijn geïntegreerd in een enkele, monolithische Zerodur[®] doelspiegel voor maximale thermische en mechanische stabiliteit. De ophanging van de doelspiegel is thermisch gecompenseerd in radiale en axiale richting. De drie stilstaande referentiespiegels zijn eveneens samengevoegd tot een enkelvoudige Zerodur[®] component.

Vast in het instrument opgestelde optieken, verdelen de ingaande laserstraal gelijkelijk over de drie interferometers. Na interferentie worden de optische signalen door commerciële meetelectronica verwerkt.

Dankwoord

Geenszins heb ik het werk alleen gedaan. Oprechte dank aan:

VSL, voor het leveren van de probleemstelling. Met name wil ik Richard Koops, Marijn van Veghel, Rob Bergmans en Gerard Kotte bedanken, ik heb dankzij jullie over de theorie en de praktijk van lengtemetingen geleerd.

NanoNed. Een woord van dank aan de Flagshipcaptains Ton Bastein en Michael Engelmann en Program Officer Rens Vandeberg is hier op z'n plaats.

Nick Rosielle. Beste Nick, ik ben dankbaar dat ik het prachtige vak construeren van jou heb mogen leren. Daarnaast bedankt voor je inbreng in het project. Ik heb de samenwerking naast leerzaam ook als prettig ervaren.

Maarten Steinbuch. Beste Maarten, een betere promotor kan een AIO zich niet wensen; bedankt voor je begeleiding, je laat ruimte als het kan en bent kritisch als het moet. Ook je aanstekelijke enthousiasme en je support op onzekere momenten was aangenaam.

Dave Bax. Beste Dave, bedankt voor je eersteklas instrumentmakerswerk. Je hoge standaard van werken, je rust op de meest spannende momenten van fabricage en montage en je vakkennis zijn bewonderenswaardig. Het samen monteren en uitlijnen was naast leerzaam ook leuk.

Rinus Janssen, Mariëlle Dirks-Smit, René Henselmans, Paul de Laat en Peter Minten (allen GTD) wil ik hierbij hartelijk bedanken voor hun bijdragen in de realisatie. De aansturing is ontworpen en opgebouwd door Ramon Solberg (IME Technologies), waarvoor dank.

Ivo de Rijk. Beste Ivo, bedankt voor het AFM-kop ontwerp dat je hebt gemaakt tijdens je afstuderen. Het was, ondanks de tijdsdruk, altijd leuk om met je samen te werken.

De leden van de kerncommissie, professor Compter (TU/e), professor Munnig Schmidt (TU Delft) en professor Urbach (TU Delft) wil ik bedanken voor het constructieve commentaar op het conceptproefschrift.

Ook de collega's van Constructies en Mechanismen en van Control Systems Technology wil ik vriendelijk bedanken voor de discussies, ideeën en oplossingen. Met name wil ik Ron Hendrix bedanken voor de constructieve gesprekken en hulp met elektronica en software, en Roel Merry voor het regelaarontwerp.

Petra Aspers, Lia Neervoort, Inge van Marion en Lucienne Dado, bedankt voor de ondersteuning, zowel op de TU/e als ver daarbuiten.

Als laatste een woord van dank aan m'n ouders en zus. Beste Ans en Manfred, zonder jullie steun en vertrouwen over de jaren was het niet gelukt, bedankt daarvoor. Astrid, ik heb je steun erg gewaardeerd. Je bent een fijne zus waar ik trots op ben!

Eindhoven, oktober 2010.

Curriculum Vitae

Chris Werner was born in Dussen, the Netherlands, on December 23, 1979.

- 1992-1998 Secondary school, Dongemond College, Raamsdonksveer.
- 1998-2004 Mechanical Engineering at Technische Universiteit Eindhoven.
Graduated (cum laude) within the Constructions & Mechanisms group.
- 2002 Internship at Centre for Precision Metrology,
University of North Carolina at Charlotte, USA.
- 2003-2004 Master thesis project at Drivetrain Innovations bv, Eindhoven.
- 2004-2010 PhD candidate at Technische Universiteit Eindhoven,
Department of Mechanical Engineering, Control Systems
Technology group.
- 2010- Co-founder of Entechna Engineering, Breda.

